

32nd conference with international participation



BOOK OF EXTENDED ABSTRACTS

October 31 - November 2, 2016

HOTEL HORIZONT, ŠPIČÁK
CZECH REPUBLIC



Central European Association
for Computational Mechanics

BOOK OF EXTENDED ABSTRACTS

32nd conference with international participation **Computational Mechanics 2016**

ISBN 978-80-261-0647-0

Published by

University of West Bohemia, Univerzitní 8, 306 14 Plzeň, Czech Republic, IC 49777513

Edited by

Vítězslav Adámek

Alena Jonášová

Martin Zajíček

Conference secretariat

Monika Nocarová

Department of Mechanics

Faculty of Applied Sciences

University of West Bohemia

Univerzitní 8

306 14 Plzeň

Czech Republic

phone: +420 377 632 301

e-mail: vm@kme.zcu.cz

Copyright © 2016 University of West Bohemia, Plzeň, Czech Republic

PREFACE

The Book of Extended Abstracts contains 76 two-page abstracts presented at the 32nd conference **Computational Mechanics 2016**, which was held at the Hotel Horizont in Špičák, Czech Republic, on October 31 – November 2, 2016. This annual conference, which was attended by nearly one hundred participants from the Czech Republic, Slovakia and from abroad, was organised by the Department of Mechanics, Faculty of Applied Sciences of the University of West Bohemia under the auspices of

- Miroslav Lávička, the Dean of the Faculty of Applied Sciences,
- Jiří Struček, the Vice-President of the Pilsen Region for Education, Sport, Culture and Tourism,
- Czech Society for Mechanics,
- Czech National Committee of IFToMM,
- Central European Association for Computational Mechanics.

The main objective of this traditional conference is to bring together academicians, researchers and industrial partners interested in relevant disciplines of mechanics including

- solid mechanics,
- dynamics of mechanical systems,
- mechatronics and vibrations,
- reliability and durability of structures,
- fracture mechanics,
- mechanics in civil engineering,
- fluid mechanics and fluid-structure interaction,
- thermodynamics,
- biomechanics,
- heterogeneous media and multiscale problems,
- experimental methods in mechanics,

to create an opportunity for meeting, discussion and collaboration among the participants. As in the previous years, the three best papers presented at this conference were awarded the Czech Society for Mechanics Award for young researchers under 35 years of age.

To all conference participants, we offer the possibility to publish their peer-reviewed full papers in the international journal **Applied and Computational Mechanics**, which has been published by the University of West Bohemia since 2007 (see <http://www.kme.zcu.cz/acm/>).

We would like to express our gratitude to all the invited speakers for their significant contribution to the conference and the time and effort they put. Considerable acknowledgement belongs also to the members of the Organising Committee for their important work.

We strongly believe that all participants of the CM2016 enjoyed their stay in the beautiful nature of the Šumava region in a meaningful way. Finally, we want to invite you all to come to the next conference CM2017.

Jan Vimmr
University of West Bohemia
Chairman of the Scientific
Committee

Vítězslav Adámek
University of West Bohemia
Chairman of the Organising
Committee

SCIENTIFIC COMMITTEE

Chairman:

Jan Vimmr

University of West Bohemia, Faculty of Applied Sciences, Czech Republic

Members:

Miroslav Balda

Research and Testing Institute Plzeň, Czech Republic

Jiří Burša

Brno University of Technology, Faculty of Mechanical Engineering, Czech Republic

Jan Dupal

University of West Bohemia, Faculty of Applied Sciences, Czech Republic

Václav Dvořák

Technical University of Liberec, Faculty of Mechanical Engineering, Czech Republic

Jiří Fürst

Czech Technical University in Prague, Faculty of Mechanical Engineering, Czech Republic

Miroslav Holeček

University of West Bohemia, Czech Republic

Jaromír Horáček

Institute of Thermomechanics, Czech Academy of Sciences, Czech Republic

Michal Kotoul

Brno University of Technology, Faculty of Mechanical Engineering, Czech Republic

Jiří Křen

University of West Bohemia, Faculty of Applied Sciences, Czech Republic

Vladislav Laš

University of West Bohemia, Faculty of Applied Sciences, Czech Republic

Justín Murín

Slovak University of Technology in Bratislava, Faculty of Mechanical Engineering, Slovak Republic

Milan Naď

Slovak University of Technology in Bratislava, Faculty of Materials Science and Technology in Trnava, Slovak Republic

Jiří Náprstek

Institute of Theoretical and Applied Mechanics, Czech Academy of Sciences, Czech Republic

Miloslav Okrouhlík

Institute of Thermomechanics, Czech Academy of Sciences, Czech Republic

Luděk Pešek

Institute of Thermomechanics, Czech Academy of Sciences, Czech Republic

Jindřich Petruška

Brno University of Technology, Faculty of Mechanical Engineering, Czech Republic

Jiří Plešek

Institute of Thermomechanics, Czech Academy of Sciences, Czech Republic

František Pochylý

Brno University of Technology, Faculty of Mechanical Engineering, Czech Republic

Pavel Polach

Research and Testing Institute Plzeň, Czech Republic

Eduard Rohan

University of West Bohemia, Faculty of Applied Sciences, Czech Republic

Josef Rosenberg

University of West Bohemia, Faculty of Applied Sciences, Czech Republic

Milan Růžička

Czech Technical University in Prague, Faculty of Mechanical Engineering, Czech Republic

Milan Sága

University of Žilina, Faculty of Mechanical Engineering, Slovak Republic

Petr Sváček

Czech Technical University in Prague, Faculty of Mechanical Engineering, Czech Republic

Zbyněk Šika

Czech Technical University in Prague, Faculty of Mechanical Engineering, Czech Republic

Michael Valášek

Czech Technical University in Prague, Faculty of Mechanical Engineering, Czech Republic

Jaroslav Zapoměl

VŠB – Technical University of Ostrava, Faculty of Mechanical Engineering, Czech Republic

Vladimír Zeman

University of West Bohemia, Faculty of Applied Sciences, Czech Republic

Table of Contents

Bartošák M., Jurenka J., Růžička M., Doubrava K.: <i>Calculation of the sound power in the inlet of the aero-engine based on the analytical prediction</i>	1
Beneš P., Volech J., Šika Z., Hajžman M., Kraus K.: <i>Control synthesis of a planar multi-level manipulator</i>	3
Brůha J., Zeman V.: <i>Dynamic properties of a turbine blade couple: Analysis of the contact force effects</i>	5
Bublík O., Vimmr J., Pecka A., Pešek L.: <i>Assessment of flutter origin in simplified blade cascade with prescribed harmonic motion</i>	7
Cimrman R., Lukeš V., Rohan E.: <i>Hierarchical numerical modelling of porous media in SfePy</i>	9
Čečrdle J.: <i>Whirl flutter optimisation-based solution of twin turboprop aircraft using full-span model</i>	11
Červená O., Hajžman M., Mrštík J.: <i>Vibration of turbine rotors considering foundation excitation</i>	13
Dupal J.: <i>Statics and dynamics of cable structures</i>	15
Fürst J.: <i>On the application of LU-SGS scheme for turbomachinery flows</i>	17
Hába A., Zelenka J., Kohout M.: <i>Experimental analysis of railway vehicle passing over turnout frog</i>	19
Had J.: <i>Damage prediction with coupled fatigue and creep mechanism applied on generator turbine</i>	21
Hájek P., Švancara P., Horáček J., Švec J. G.: <i>FE modelling of the influence of the lamina propria properties on the vocal folds vibration and produced sound for specific Czech vowels</i>	23
Hajžman M., Bulín R., Zavřel J., Šika Z., Polach P.: <i>Dynamics of a parallel multilevel mechanism</i>	25
Havelková L., Krofta L., Sindhvani N.: <i>Stress distribution in pelvic floor structures depending on real fetus head molding and trajectory during vaginal delivery</i>	27
Havlásek M., Pochylý F.: <i>Interaction of the rigid journal with incompressible fluid</i>	29
Holman J.: <i>Numerical solution of 3D flow through turbine cascade using modified EARSIM model</i>	31
Hora P.: <i>The use of the Chebyshev interpolation in elastodynamic problems</i>	33
Horáček J., Radolf V., Bula V., Košina J., Vampola T., Dušková M.: <i>Experimental investigation of phonation using artificial models of human vocal folds and vocal tract</i>	35
Hračov S., Náprstek J.: <i>Vibration analysis of visco-elastically coupled beams</i>	37
Hynek P., Vampola T.: <i>Search algorithm for centerlines inside complex branched channels</i>	39

Chamrad J., Marcián P., Borák L., Wolff J.: <i>Stress – strain analysis of cranial implant</i> . . .	41
Janoušek J., Holmström S., Pohja R., Führer U.: <i>Creep-fatigue behaviour of steel P91</i> . . .	43
Jansová M., Malotín T., Křen J., Votápek P., Lobovský L., Hynčík L.: <i>Finite element analysis of supracondylar periprosthetic femoral fracture treatment</i>	45
Juárez-Luna G., Tenorio-Montero E.: <i>Frame elements with embedded discontinuities for modelling hinges in reinforced concrete prismatic elements</i>	47
Kašpárek M., Nováková L., Novotný J.: <i>The flow field and the pressure drop in multiple stenoses</i>	49
Klečková J., Hamza J.: <i>CFD method of prediction of turbine blade flutter</i>	51
Klesa J.: <i>Aerodynamic design of the propeller for low-speed indoor UAV</i>	53
Kohout M., Michálek T., Vágner J., Zelenka J.: <i>Yaw dampers in construction of rail vehicles</i>	55
Kouba J., Nožička J.: <i>Design of open combustion chamber for LIF measurements</i>	57
Kovář F., Valášek M., Švéda J.: <i>Measurement of the end point by laser tracker which is mounted on a slide</i>	59
Král R.: <i>Investigation of aeroelastic bridge instabilities using the multidimensional Fokker-Planck equation and wind-tunnel experiment</i>	61
Kraus K., Beneš P., Šika Z., Polach P.: <i>Experimental redundantly actuated cable-driven manipulator</i>	63
Kutiš V., Jakubec J., Paulech J., Gálik G., Murín J., Hrabovský J.: <i>Parametric CFD analyses of coolant flow in nuclear reactor VVER 440</i>	65
Lašová Z., Zemčík R.: <i>Determination of velocity of propagation of Lamb waves in aluminium plate using piezoelectric transducers</i>	67
Lepš M., Šmejkal M.: <i>Computational aspects of RBFN meta-models for reliability problems</i>	69
Lindstedt L., Vychytil J., Dziewonski T., Hynčík L.: <i>Numerical simulation of a human body in aircraft crash scenarios</i>	71
Lobovský L., Mandys T., Sklenička J., Bublík O., Vimmr J.: <i>Validation tests for gravity casting simulations</i>	73
Louda P.: <i>Some results of simulations of flows with internal permeable walls</i>	75
Lukeš V., Jiřík M.: <i>Semi-automatic finite element mesh generation using medical imaging data</i>	77
Moravcová F., Lukeš V., Rohan E.: <i>Surface sensitivities computation for turbine blades using OpenFOAM</i>	79
Mračko M., Tkachuk A., Kolman R., Plešek J., Gabriel D.: <i>Comparison of local and global critical time step size estimators in explicit dynamics</i>	81

Murín J., Aminbaghai M., Hrabovský J.: <i>Non-uniform torsion modal analysis of thin-walled open cross-sections with effect of axial force</i>	83
Nad' M.: <i>Structural dynamic modification of the vibrating beam structures</i>	85
Náhlík L., Štegnerová K., Majer Z., Hutař P.: <i>Subcritical micro-crack growth in particulate ceramic composite with residual stresses</i>	87
Nováková N., Habán V., Hudec M.: <i>Computational simulation of additional effects in the sealing gap</i>	89
Padovec Z., Zbojovský M.: <i>Experimental analysis of steering shaft with focus on the strength of the bonded joint</i>	91
Pašek M., Šašek, J.: <i>Single core model in VPS with respect to non-linear static, crashworthiness and internal acoustic</i>	93
Pecka A., Bublík O., Vimmr J.: <i>Simple parallel implementation of an implicit CFD solver using the Schwarz domain decomposition method</i>	95
Pečínka L., Svoboda J., Zeman V.: <i>Friction and fretting wear coefficients between the key and the groove in the lower part of the WWER 440-213 reactor pressure vessel.</i>	97
Plánička S., Vimmr J.: <i>Numerical simulation of free surface flows using a three-equation model for two-phase flows</i>	99
Poduška J., Hutař P., Kučera J., Sadílek J., Frank A., Náhlík L.: <i>The influence of residual stress on fracture behavior of the CRB test specimen</i>	101
Polach P., Bulín R., Beneš P., Šika Z., Hajžman M.: <i>Approaches to the computational modelling of the mechanical systems with cables</i>	103
Půst L., Pešek L.: <i>Free vibration modal spectrum of planetary gearing box</i>	105
Radolf V., Horáček J., Laukkanen A. M.: <i>Effect of a soft tissue on vocal tract acoustic resonance properties in vocal exercises using phonation into tubes</i>	107
Rohan E., Cimrman R.: <i>Modelling of wave propagation in phononic plates in frequency and time domain</i>	109
Rosenberg J., Adámek V.: <i>Contribution to the analysis of higher dimensional dynamical systems</i>	111
Sága M., Handrik M., Kopas P., Vaško M., Tropp M.: <i>Numerical and experimental study of induction bending of large diameter pipes</i>	113
Sapietová A., Dekýš V., Šulka P.: <i>Modelling vibration sources of rotating device using MSC.ADAMS</i>	115
Sváček P., Valášek J.: <i>Numerical simulations of flow induced vocal folds vibrations</i>	117
Šedlbauer D.: <i>Wang tiles with adaptive edges in material engineering</i>	119
Šika Z., Krejza R., Beneš P., Hromčík M.: <i>Planar mechatronic structures with distributed collocated actuators and sensors</i>	121

Špička J., Vychytil J., Hynčák L., Maňas J.: <i>Numerical analysis of a pedestrian to car collision: Effect of variations in walk</i>	123
Špirk S.: <i>Simulations of terminal ballistics phenomena</i>	125
Štorkán J., Vampola T.: <i>Influence of geometric configuration of the acoustic-structural system on deformation characteristics</i>	127
Tonar Z., Kubíková T., Kochová P., Witter K.: <i>Microscopic structural analysis of biological tissues and biomaterials</i>	129
Tran Xuan T., Cirkl D.: <i>Simulation model of seat with implemented pneumatic spring with consideration of variable pressure in air reservoir</i>	131
Turjanicová J., Rohan E., Lukeš V.: <i>Multiscale modeling of ionic transport in deformable porous media</i>	133
Uruba V.: <i>On stability of 2D flow-field</i>	135
Valkovič V., Jančo R., Frydrýšek K.: <i>Influence of random factors on pipeline systems</i>	137
Vampola T., Horáček J.: <i>Influence of the velopharyngeal opening on human voice quality</i>	139
Vaško M., Handrik M., Kopas P., Sága M.: <i>Analysis of stress concentration near graphite particles in globular graphite cast iron</i>	141
Voltr P.: <i>Calculation of locomotive traction force in transient rolling contact</i>	143
Zavřel J., Šika Z., Volech J., Dupal J.: <i>Modeling of drive of cable driven mechanism</i>	145
Zavřelová T., Mareš T.: <i>The influence of the slenderness ratio of the composite beam on its bending stiffness</i>	147
Zeman V., Hlaváč Z.: <i>Eigenfrequency analysis of nuclear reactor with clearances in couplings</i>	149
Žák J.: <i>Dimensioning of the take-up bar on a weaving loom using Winkler's model of soil</i>	151

Calculation of the sound power in the inlet of the aero-engine based on the analytical prediction

M. Bartošák^a, J. Jurenka^a, M. Růžička^a, K. Doubrava^a

^aFaculty of Mechanical Engineering, CTU in Prague, Technická 4, 166 07 Prague, Czech Republic

Tone noise radiated through the inlet of a turbofan is mainly due to rotor and stator interactions at subsonic regimes and due to the generated shock waves at transonic fan tip speeds. The paper is focused on the calculation of the 3D ducted acoustic field using FEM. Rotor in transonic conditions is analyzed. Analytical prediction of the harmonic sound power is proposed. Method is an alternative to a direct numerical computation and leads to a very fast calculation. Estimation of the initial pressure jump of the shock waves in the rotor plane is based on normal shock wave equation and is used as the acoustic loading in the FEM model. All blades are assumed to be identical and only the blade passing frequency and its harmonics are generated.

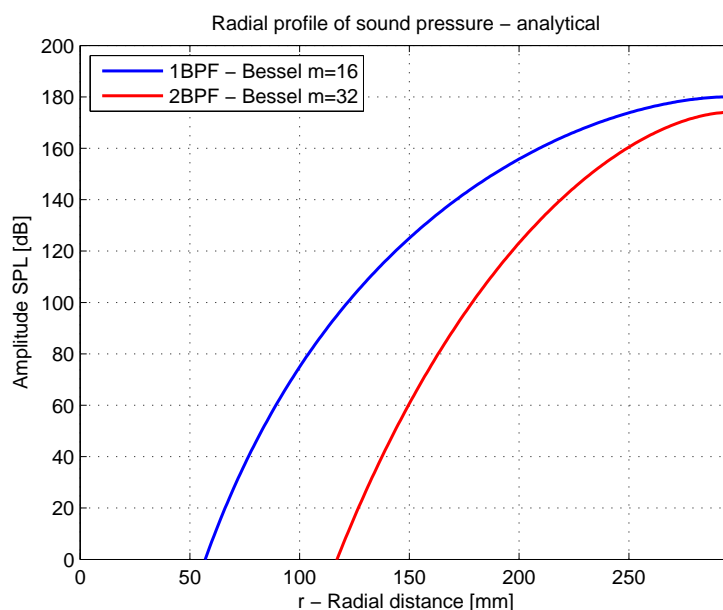


Fig. 1. Radial profile of sound pressure based on analytical prediction

This approach consists of the following steps. First, normal shock wave equation is used for the calculation of the initial pressure jump just ahead of rotor [1, 2]. Radial profile of the the sound pressure in the circular section of the duct is considered in the form of the Bessel function. The profile for the first two blade passing frequencies is shown in Fig. 1.

Subsequently, analytical results are used as the pressure loading in the rotor section in the finite element analysis of the ducted air. Pressure boundary condition is prescribed in the user

subroutine. ABAQUS is selected for the numerical calculations. Sound pressure is calculated from the transient and steady-state dynamics FEM. Primarily blade passing frequencies are investigated. Linear acoustics equations are assumed. Calculated sound pressure for the first blade passing frequency is shown in Fig. 2.

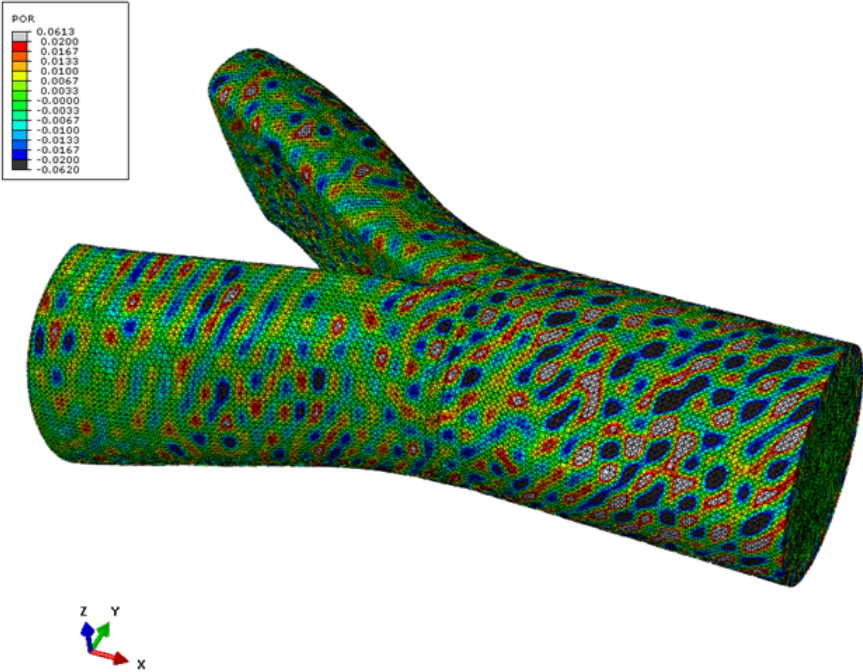


Fig. 2. Harmonic response analysis of sound pressure

Finally, calculated sound pressure will be subsequently used in the acoustic-structural analysis. Results will be used to design the composite duct. Proposed method is alternative to numerical computation using RANS and it is very suitable for design calculations.

Acknowledgements

The authors would like to acknowledge the support from the Technology Agency of the Czech Republic, grant No. TE02000032.

References

- [1] Lewy, S., Polacsek, C., Barrier, R., Analytical and numerical prediction of harmonic sound power in the inlet of aero-engines with emphasis on transonic rotation speeds, *Journal of Sound and Vibration* 333 (26) (2014) 7165-7182.
- [2] McAlpine, A., Fisher, M. J., On the prediction of buzz-saw noise in aero-engine inlet ducts, *Journal of Sound and Vibration* 248 (1) (2001) 123-149.

Control synthesis of a planar multi-level manipulator

P. Beneš^a, J. Volech^a, Z. Šika^a, M. Hajžman^b, K. Kraus^a

^a Faculty of Mechanical Engineering, CTU in Prague, Technická 4, 160 00 Praha 6, Czech Republic

^b Faculty of Applied Sciences, University of West Bohemia, Univerzitní 8, 306 14 Plzeň, Czech Republic

Multi-level manipulators consist of the main movable platform and at least one superimposed active structure. The main platform should primarily cover large workspace while the superimposed one is capable to perform smaller but highly dynamic maneuvers. For that purposes the parallel cable manipulators are usually used at the first level. They are capable to cover large workspace, they are lightweight and relatively cheap and easy to build. However, the nature of cables limits these manipulators to the area of low frequencies. Therefore, the higher frequencies should be covered by the superimposed structure that provides smaller but rapid movements. This structure could be driven by e.g. piezo elements or voice coils.

The simulation model is in Fig. 1. The basis is the redundant parallel cable driven manipulator with three degrees of freedom (DOF) controlled by four cables. Cables driven by linear actuators are connected to the corners of the platform. The configuration could be easily changed, but in order to get the best maneuverability the one in Fig. 1 was chosen. Cables are modelled as elastic, both linear and non-linear cable stiffness [3] has been simulated. The active structure connected to the platform has 3 DOFs on its own and it is driven by three piezo actuators.

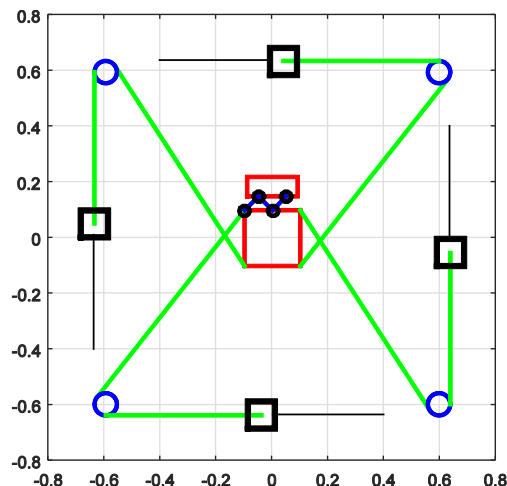


Fig. 1. Matlab visualization of the simulated multi-level manipulator

The control synthesis deals with two main problems. The first one is the control of redundantly actuated basis platform using flexible cables. The second one is the splitting of motion between two levels of manipulator. The control of the superimposed structure itself is easier as it is not redundant.

Several approaches have been applied to control redundantly actuated cable driven platform. The simplest one is the control of three cables with respect to position while the

forth one is force-controlled to ensure that all cables are under tension. The more advanced approach is the sliding mode control with primary objective in accurate positioning and secondary objective in the anti-backlash control (positive tension in cables) [4]. Another tested approach is based on the centralized model control [2].

The splitting of the motion between manipulator's levels is mainly the matter of frequencies. The simulated approach is based on the same strategy as so called washout-algorithms (WA) used by driving simulators [1]. Basically the main idea is the filtration of the desired signal with respect to manipulator's modal capabilities and reachable workspace of its particular motion levels. The best results are obtained if the desired trajectory is known in advance and the filtration could be non-causal, Fig. 2.

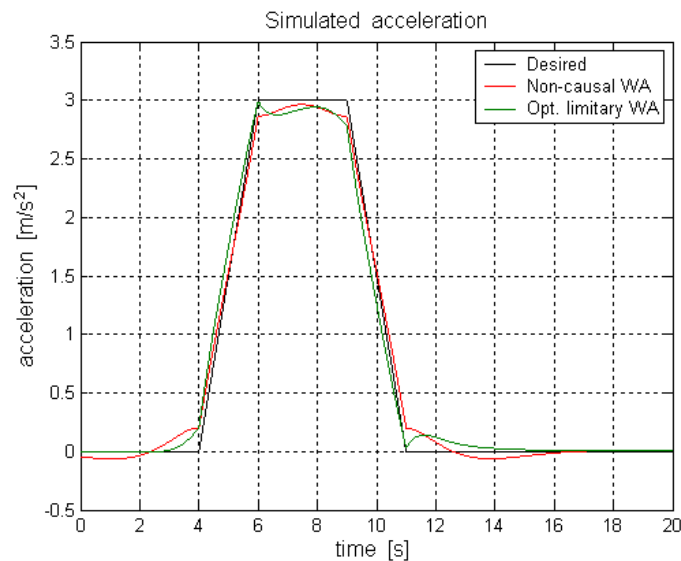


Fig. 2. Motion splitting – comparison of different washout algorithms

The presented planar manipulator is used just for the test of different modelling and control strategies. The results will be further applied to two spatial mechanisms with three and six DOFs that are available in CTU laboratories.

Acknowledgements

The work has been supported by the Czech Science Foundation project GA15-20134S - Multi-Level Light Mechanisms with Active Structures.

References

- [1] Beneš, P., Simulator of vehicle, Diploma thesis, CTU in Prague, 2004.
- [2] Kraus, K., Redundantly actuated cable-driven manipulator, Diploma thesis, CTU in Prague, 2016.
- [3] Kraus, W., Force control of cable-driven parallel robots, Dr-Ing. thesis, Universität Stuttgart, 2015.
- [4] Procházka, F., Valášek, M., Šika, Z., Robust sliding mode control of redundantly actuated parallel mechanisms with respect to geometric imperfections, *Multibody System Dynamics* 36 (3) (2016) 221-236.

Dynamic properties of a turbine blade couple: Analysis of the contact force effects

J. Brůha ^{a, b}, V. Zeman ^{a, b}

^a Department of Mechanics, Faculty of Applied Sciences, University of West Bohemia, Univerzitní 8, 306 14 Plzeň, Czech Republic

^b NTIS – New Technologies for the Information Society, Faculty of Applied Sciences, University of West Bohemia, Univerzitní 8, 306 14 Plzeň, Czech Republic

The contribution is concerned with modelling of a harmonically excited turbine blade couple with frictional contact of shrouds and analysing the effects of compressive normal and tangential friction forces on dynamic properties of the blades. The turbine twisted blades (that are considered to be clamped into a rotating rigid disk) are modelled by means of the finite element method using Rayleigh beam elements with varying cross-sectional parameters and six degrees of freedom in each of nodes (Fig. 1) [1, 2]. The rhomboid-shaped shrouds are considered to be rigid. The modelling of interactions at the contact surfaces is carried out using a multi-point frictional contact model [3, 4] with constant normal contact stiffness. In such a case, the total contact area of interacting blade shrouds is divided into a set of elementary contact areas and both compressive normal forces and tangential friction forces are distributed among them (see Fig. 1). The considered dry friction characteristic is smooth and includes the micro- and macro-slip phases. The presented method was tested on the blades of the MTD30 stage HP15 type [5].

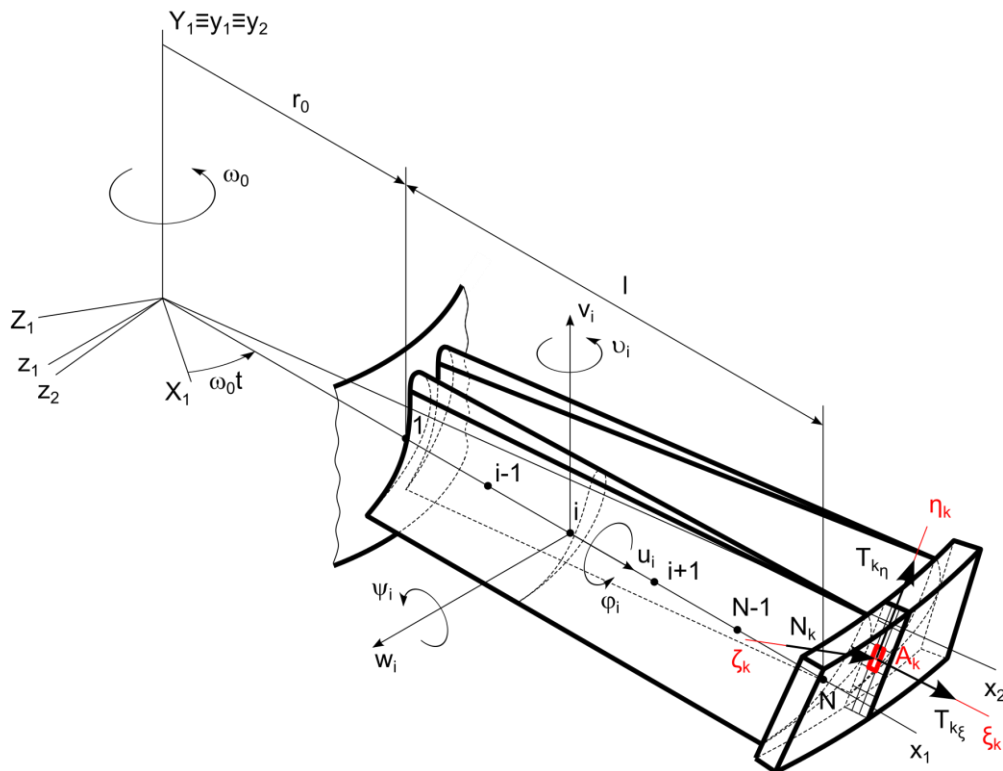


Fig. 1. Rotating blade couple with frictional contact of shrouds

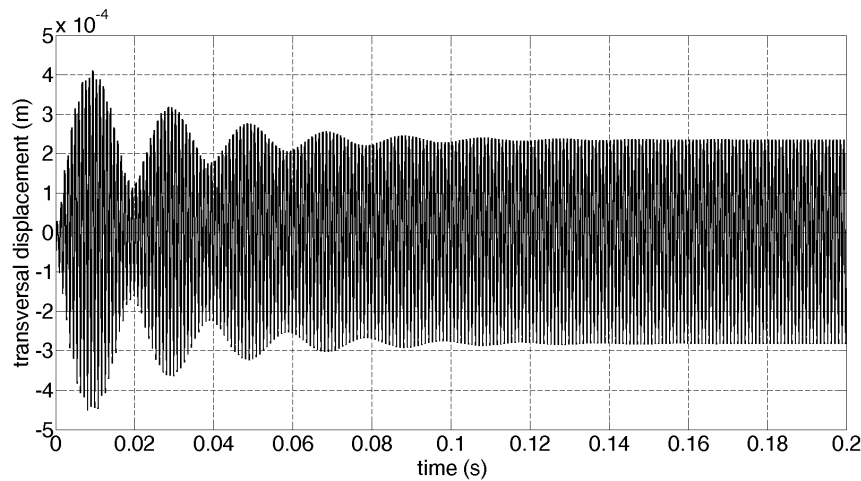


Fig. 2. Simulated transversal displacement of the first blade: frictionless contact of shrouds

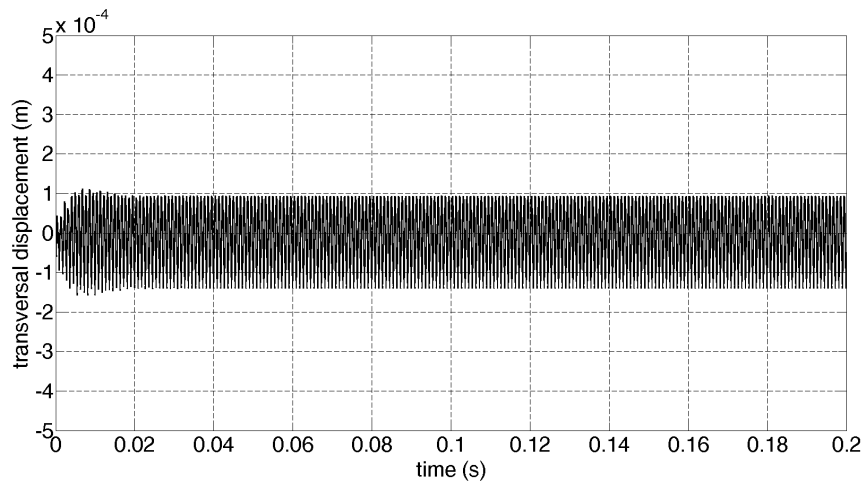


Fig. 3. Simulated transversal displacement of the first blade: frictional contact of shrouds

The developed in-house code in MATLAB computing environment is capable to analyse the effects of friction (as an important source of damping, see Figs. 2 and 3), compressive normal forces, and normal contact stiffness at the contact between the shrouds on dynamic response of the blade couple.

Acknowledgements

This work was supported by the project LO1506 of the Ministry of Education, Youth and Sports and by the grant project SGS-2016-038 of the University of West Bohemia.

References

- [1] Brůha, J., Rychecký, D., Modelling of rotating twisted blades as 1D continuum, *Applied Mechanics and Materials* 821 (2016) 183-190.
- [2] Brůha, J., Zeman, V., Numerical analysis of the modal properties of a shrouded turbine blading, *Book of full texts of the 22nd international conference Engineering Mechanics 2016*, Institute of Thermomechanics AS CR, Prague, 2016, pp. 94-97.
- [3] Hajžman, M., Byrtus, M., Zeman, V., Solution of the mutual contact in the finite element analysis of twisted blades, *Colloquium Dynamics of Machines 2012*, Prague, pp. 51-58.
- [4] Hajžman, M., Rychecký, D., Multipoint contact approach to the analysis of interacting flexible bodies vibration, *Advances in Mechanisms Design* 8 (2012) 181-186.
- [5] Kubín, Z., Hlous, J., Measurement of rhombic bladed disk, *Research report*, Doosan Škoda Power, Pilsen, 2013.

Assessment of flutter origin in simplified blade cascade with prescribed harmonic motion

O. Bublík^a, J. Vimmr^a, A. Pecka^a, L. Pešek^b

^a*NTIS – New Technologies for the Information Society, Faculty of Applied Sciences, University of West Bohemia, Univerzitní 8, 306 14 Pilsen, Czech Republic*

^b*Institute of Thermomechanics, Academy of Sciences of the Czech Republic, Dolejškova 1402/5, 182 00 Prague, Czech Republic*

A dynamic instability of blades in blade cascade caused by fluid flow, formally known as flutter, is still a subject of interest [1, 5]. Modern turbines are designed to maximize efficiency and power. This leads to high operational temperature and high flow rate, which can cause the loss of blades stability. Depending on the phase angle between the vibrating blade and aerodynamic forces acting on the blade, the two following cases can occur:

- i) kinetic energy of the blade is transmitted to the flow,
- ii) the energy of the flow is absorbed into the blade.

In the first case, we talk about damped vibration from the aero-elasticity point of view. In the second case, where the flow adds the energy to blades and their amplitudes increase, we talk about unstable excited vibration, i.e. flutter. It has been shown [7] that the critical flutter point, i.e. the highest aero-dynamical excitation, arises for a particular inter-blade phase angle. Most of aerodynamic studies are based on the so called travelling wave mode of vibration, where one assumes that all blades vibrate with the same frequency, amplitude and inter-blade phase angle.

For the purpose of this study, we choose the travelling wave mode approach for the numerical modelling of the unsteady flow and flutter analysis in the simplified blade cascade formed by three flat plates, see Fig. 1 (left). Each plate performs kinematic harmonic motion in the y -direction $y = A \sin(2\pi ft + \phi)$ for the upper plate, $y = A \sin(2\pi ft)$ for the middle plate and $y = A \sin(2\pi ft - \phi)$ for the bottom plate. The amplitude and the frequency of the harmonic motion are $A = 0.003$ m and $f = 20$ Hz, respectively. Thus, all flat plates in the cascade vibrate and their mutual movement creates the travelling waves in the cascade. The aim of this numerical study is to determine aerodynamic forces acting on the flat plates in the cascade and the flutter origin, when the harmonic motion with inter-blade phase angle is prescribed.

As a mathematical model, the system of Navier-Stokes equations, which describes the flow of compressible viscous fluid, was considered. To include the influence of turbulent fluctuations on the mean flow a one-equation turbulence model of Spalart and Allmaras [8] was used. The numerical simulation was performed using developed in-house CFD software based on the discontinuous Galerkin finite element method [3, 4]. To capture the blade motion, the equations were considered in ALE (Arbitrary Lagrangian-Eulerian) form [2, 6].

The numerical simulations were performed for four different inter-blade phase angles $\phi = \{\frac{\pi}{2}, \frac{\pi}{4}, -\frac{\pi}{4}, -\frac{\pi}{2}\}$. The obtained y -components of forces acting on the middle blade were analysed for all inter-blade phase angles and the aerodynamic damping parameter

$$\sigma = -\frac{c_w}{\pi A^2},$$

was determined. The variable c_w denotes the work of aerodynamic force performed per one cycle of harmonic motion. The resulting parameter σ depending on inter-blade phase angle ϕ is shown in Fig. 1 (right). The positive value of parameter σ means that the kinetic energy of the flat plate is transmitted to the flow and thus the flutter phenomena does not occur.

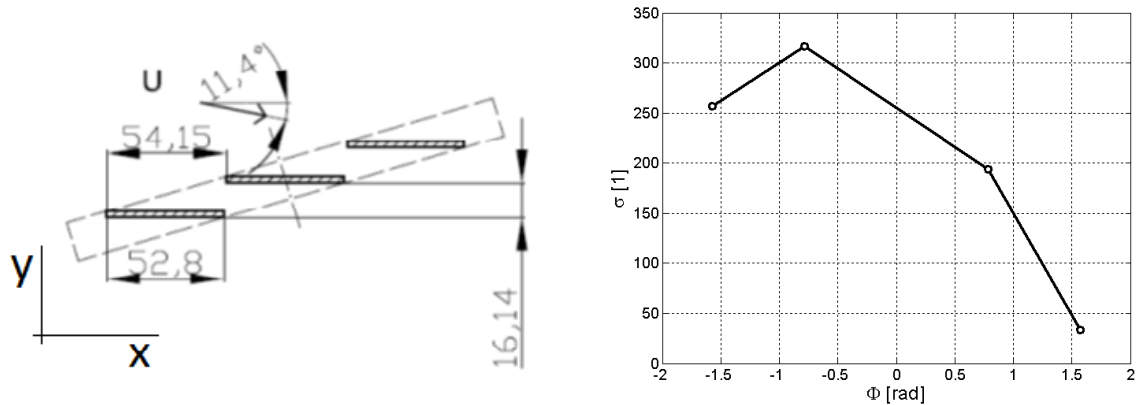


Fig. 1. Flat plates cascade configuration (*left*); parameter σ depending on the inter-blade phase angle ϕ (*right*)

Acknowledgement

The authors appreciate the kind support by the grant GA 16-04546S "Aero-elastic couplings and dynamic behaviour of rotational periodic bodies" of the Czech Science Foundation.

References

- [1] Armstrong, E. K., Stevenson, R. E., Some practical aspect of compressor blade vibration, Journal of the Royal Aeronautical Society 64 (1960) 117-130.
- [2] Bublík, O., Vimmr, J., Jonášová, A., Comparison of discontinuous Galerkin time integration schemes for the solution of flow problems with deformable domains, Applied Mathematics and Computation 267 (2015) 329-340.
- [3] Cockburn, B., Shu, C.-W., RungeKutta discontinuous Galerkin methods for convection-dominated problems, Journal of Scientific Computing 16 (3) (2001) 173-261.
- [4] Feistauer, M., Česenek, J., Space-time discontinuous Galerkin finite element method for convection-diffusion problems and compressible flow, Numerical Methods and Applications 6046 (2011) 1-13.
- [5] Owens, H. M., Trumpler, W. E., Mechanical design and testing of long steam turbine blading, ASME Paper No. 49-A-64, 1949.
- [6] Persson, P.-O., Bonet, J., Peraire, J., Discontinuous Galerkin solution of the Navier-Stokes equations on deformable domains, Computer Methods in Applied Mechanics and Engineering 198(17-20) (2009) 1585-1595.
- [7] Schlaflí, D., Experimental investigation of transient flow in oscillating ring lattices, Ph.D. thesis, École polytechnique fédérale de Lausanne, Lausanne, 1989, doi: 10.5075/epfl-thesis-800. (in German)
- [8] Spalart, P. R., Allmaras, S. R., A one-equation turbulence model for aerodynamic flows, AIAA Paper No. 92-439, 1992.

Hierarchical numerical modelling of porous media in SfePy

R. Cimrman^a, V. Lukeš^b, E. Rohan^b

^a*New Technologies Research Centre, University of West Bohemia, Univerzitní 8, 306 14 Plzeň, Czech Republic*

^b*NTIS – New Technologies for the Information Society, Faculty of Applied Sciences, University of West Bohemia, Univerzitní 8, 306 14 Plzeň, Czech Republic*

Materials with different levels of porosity at different scales [1, 4] can be found in nature as well as in technical practice. The theory of homogenization [3, 5] provides a natural way of upscaling a lower level description to higher levels of porosities in a sense that effective material coefficients (stiffness, permeability, Biot coefficients etc.) at a higher level are obtained by applying homogenization to the lower level. This leads to a suitable hierarchical description of the porous medium, where all the different porosities are taken into account [6]. However, such a description involves solving many sub-problems in complex relationships. In the contribution we discuss our method of tackling this complexity using the homogenization engine implemented in the open source finite element package SfePy [2].

The homogenization technique, when applied to a problem, results in a set of homogenized coefficients that can be evaluated using one or several characteristic response (aka corrector) functions. The characteristic response functions are solutions to subproblems, related to the original problem, solved on a periodic representative volume cell. The homogenization engine in SfePy allows to:

- define the subproblems for the characteristic response functions;
- define the homogenized coefficients as functions of the characteristic response functions;
- express and automatically resolve the mutual dependencies among the characteristic response functions as well as the homogenized coefficients.

The above framework can be used to compute on-demand the homogenized macroscopic material parameters in a macroscopic domain.

Acknowledgements

This work was supported the project GACR 16-03823S of the Czech Science Foundation, and by the project LO1506 of the Czech Ministry of Education, Youth and Sports.

References

- [1] Auriault, J. L., Boutin, C., Deformable porous media with double porosity. Quasi-statics. I: Coupling effects, *Transport in Porous Media* 7 (1992) 63-82.
- [2] Cimrman, R., SfePy – write your own FE application. In: Pierre de Buyl and Nelle Varoquaux, editors, *Proceedings of the 6th European Conference on Python in Science (EuroSciPy 2013)*, Brussels, 2014, pp. 65-70.

- [3] Cioranescu, D., Damlamian, A., Griso, G., The periodic unfolding method in homogenization, *SIAM Journal on Mathematical Analysis* 40 (4) (2008) 1585-1620.
- [4] Ene, H.I., Poliřevski, D., Model of diffusion in partially fissured media, *Zeitschrift für angewandte Mathematik und Physik* 53 (2002) 1052-1059.
- [5] Griso, G., Rohan, E., On the homogenization of a diffusion-deformation problem in strongly heterogeneous media, *Ricerche di matematica* 56(2) (2007) 161-188.
- [6] Rohan, E., Cimrman, R., Hierarchical numerical modelling of nested poroelastic media, In: B. H. V. Topping, editor, *Proceedings of the 11th International Conference on Computational Structures Technology*, Stirlingshire, Civil-Comp Press, 2012, doi:10.4203/ccp.99.250.

Whirl flutter optimisation-based solution of twin turboprop aircraft using full-span model

J. Čečrdle ^a

^a *Aeronautical Research and Test Institute, Beranových 130, 199 05 Praha, Czech Republic*

Whirl flutter is a specific type of flutter instability, relevant for turboprop aircraft, caused by the effect of rotating parts as a propeller or a gas turbine engine rotor. The instability is driven by motion-induced unsteady aerodynamic propeller forces and moments acting on the propeller plane. Whirl flutter may cause unstable vibration of a propeller mounting, or even a failure of an engine installation or a whole wing. The optimisation-based analytical procedure was prepared to make the analysis possible at an aircraft early development phase. The method allows determination of the whirl flutter stability margins for the speed, which is set by regulations as the certification speed. The solution employs gradient-based algorithm and includes modal-based and flutter-based design responses. Design variables are represented by the engine attachment stiffness parameters.

For the purpose of aeroelastic analyses, simple dynamic beam structural models (stick models) are used. In the most cases, the half-span model with either symmetric or antisymmetric boundary conditions is sufficient. However, application of a full-span model is necessary in some specific cases. The typical example is the whirl flutter of the usual twin wing-mounted tractor engine aircraft, for which whirl flutter stability characteristics are influenced also by the directions of rotation of both propellers. In the case of the full-span model, both symmetric and antisymmetric engine vibration modes must be modelled. For this purpose, the special modelling pattern employing spring elements and rod elements is used.

The solution includes four design variables: 1) effective stiffness of the engine attachment for symmetric pitch; 2) effective stiffness of the engine attachment for antisymmetric pitch; 3) effective stiffness of the engine attachment for symmetric yaw; and 4) effective stiffness of the engine attachment for antisymmetric yaw. These design variables are related to the spring constants of two grounded spring elements and to the torsional stiffness of the two pairs of rod elements. Three frequency ratios are defined: 1) pitch frequency ratio (VFR), 2) yaw frequency ratio (HFR) and, finally 3) critical frequency ratio (CFR). VFR and HFR are set according the ground vibration test results or are guessed. CFR is a ratio of flutter critical modes, i.e. those modes, whose combination causes flutter instability. The choice of the critical modes is mainly dependent on the mode order on the relation of directions of rotation of the two propellers. In the cases with the identical directions, the critical modes are symmetric pitch and antisymmetric yaw or antisymmetric pitch and symmetric yaw. However, in cases with the inverse directions, the critical modes are symmetric pitch and symmetric yaw or antisymmetric pitch and antisymmetric yaw.

The first preparatory optimisation step is performed to set the initial design variables for the main optimisation. The design constraint includes the requirement to maintain the frequency of the engine mode of the highest frequency at the selected frequency value (using $\pm 2\%$ band). The objective function is defined as the minimization of the frequency ratio error and is expressed as minimisation of sum of squares of VFR, HFR and CFR errors.

The main optimisation is started from the values of design variables set in the preparatory step. The design constraint includes the requirement to maintain the frequency ratios (VFR, HFR, CFR), for which the $\pm 2\%$ band is used. Also, the constraint of flutter stability (i.e., negative damping) at the selected certification speed V_{cert} is applied to all modes included into the solution. The objective function is defined as the minimization of the sum of frequencies, including both symmetric and antisymmetric engine pitch and yaw vibration modes.

The output quantities include the values of design variables, for which the flutter speed is equal to the specified certification speed and the specified frequency ratios are equal to the specified target values. The described procedure is then repeated for a several CFRs to obtain enough points to construct a stability margin curve. The cross-orthogonality correlation analysis of modes before and after the each optimisation iteration is performed and mode re-ordering is performed in the case of the mode switching.

The described methodology is demonstrated on a model of a twin engine commuter aircraft. For the purpose of demonstrating the method, the simplified model with four degrees of freedom representing both the symmetric and antisymmetric engine pitch and yaw vibrations was used. The residual structure was considered to be rigid and the control surface and tab actuation drives were blocked. Fig. 1 presents the resulting stability margins for the cases of symmetric revolution of both propellers for both identical and inverse directions.

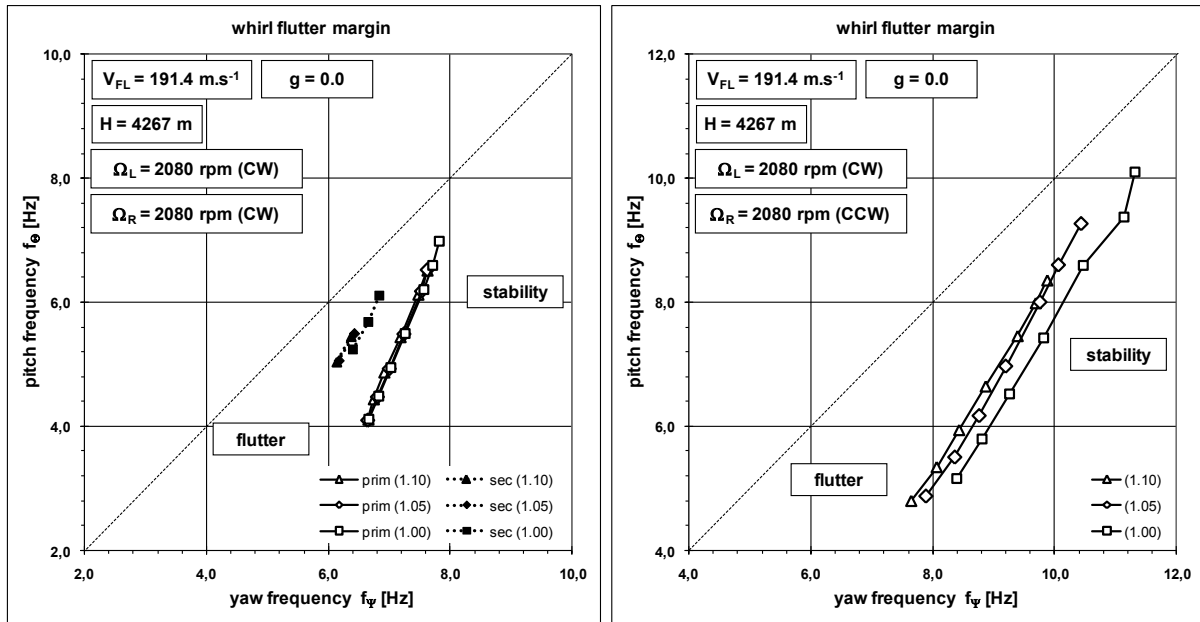


Fig. 1. Whirl flutter stability margins - symmetrical revolutions, identical and inverse directions

For the case of identical directions of propeller revolutions, two mechanisms of the whirl flutter appear: 1) a combination of symmetric pitch and antisymmetric yaw modes (primary flutter), and 2) a combination of antisymmetric pitch and symmetric yaw modes (secondary flutter). The required engine pitch and yaw frequency is higher for the primary flutter mechanism. In the case of the inverse directions of propeller revolutions, the instability is caused by the combination of antisymmetric pitch and antisymmetric yaw modes. Compare to the previous case, the required engine pitch and engine yaw frequencies are considerably higher. The future work will be focused on the assessment of the downwash effect, which represents the aerodynamic interference between propeller, nacelle and wing.

References

- [1] Čečrdle, J., Whirl flutter of turboprop aircraft structures, Woodhead Publishing, Cambridge, 2015.

Vibration of turbine rotors considering foundation excitation

O. Červená^a, M. Hajžman^a, J. Mrštík^a

^aVýzkumný a zkušební ústav Plzeň s.r.o., Tylova 1581/46, 301 00 Plzeň, Czech Republic

Power plants (in particular nuclear power plants) have to be carefully designed with respect to various undesirable problems and phenomena, which also include a seismic excitation [3, 4]. This paper deals with the dynamics of large turbine rotors common in power plants including the effects of moving foundation and stator parts. The whole turboset system [1] can be divided into two basic parts – a foundation including all stator (non-rotating) components of a turbine and a rotor train (see Fig. 1).

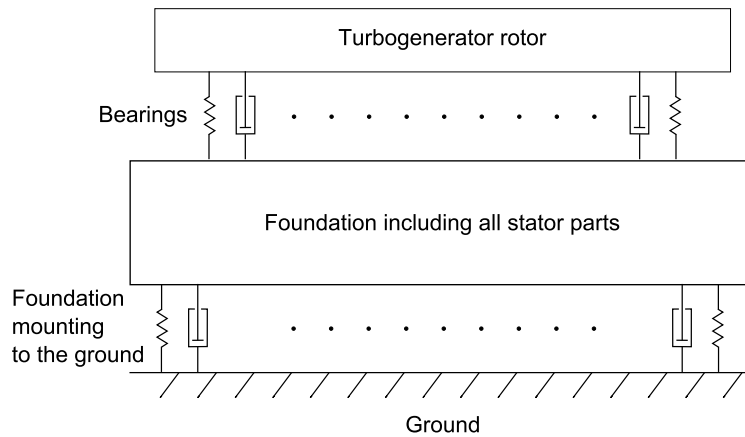


Fig. 1. General scheme of a whole turboset system

For the sake of mathematical modelling the model is divided into a rotor train (described by vector of generalized coordinates \mathbf{q}_R) and a non-rotating foundation part (described by \mathbf{q}_F)

$$\begin{bmatrix} \mathbf{M}_F & \mathbf{0} \\ \mathbf{0} & \mathbf{M}_R \end{bmatrix} \begin{bmatrix} \ddot{\mathbf{q}}_F \\ \ddot{\mathbf{q}}_R \end{bmatrix} + \left(\begin{bmatrix} \mathbf{B}_F + \mathbf{B}_G & \mathbf{0} \\ \mathbf{0} & \mathbf{B}_R + \omega_0 \mathbf{G}_R \end{bmatrix} + \mathbf{B}_B \right) \begin{bmatrix} \dot{\mathbf{q}}_F \\ \dot{\mathbf{q}}_R \end{bmatrix} + \left(\begin{bmatrix} \mathbf{K}_F & \mathbf{0} \\ \mathbf{0} & \mathbf{K}_R \end{bmatrix} + \mathbf{K}_B \right) \begin{bmatrix} \mathbf{q}_F \\ \mathbf{q}_R \end{bmatrix} = \begin{bmatrix} \mathbf{f}_F \\ \mathbf{f}_R + \mathbf{f}_u \end{bmatrix}, \quad (1)$$

where \mathbf{M}_F and \mathbf{M}_R are the mass matrices of the foundation and the rotor, \mathbf{B}_F and \mathbf{B}_R are the material damping matrices, \mathbf{K}_F and \mathbf{K}_R are the stiffness matrices of the foundation and the rotor, \mathbf{B}_G is the damping matrix representing the GERB elements between the foundation and the ground, $\omega_0 \mathbf{G}_R$ is the matrix of gyroscopic effects, \mathbf{B}_B and \mathbf{K}_B are the damping and the stiffness of the bearings (generally dependent on rotor angular velocity ω_0), \mathbf{f}_F and \mathbf{f}_R are the vectors of arbitrary external excitation and \mathbf{f}_u is the vector representing unbalance excitation, which can be expressed in a complex form $\mathbf{f}_u(t, \omega) = \mathbf{f}(\omega)e^{i\omega t}$.

In case of a seismic excitation the vectors of external excitation can be formulated as

$$\begin{bmatrix} \mathbf{f}_F \\ \mathbf{f}_R \end{bmatrix} = \begin{bmatrix} -\mathbf{m}_F \ddot{u}_g(t) \\ -\mathbf{m}_R \ddot{u}_g(t) \end{bmatrix} = \begin{bmatrix} -\mathbf{M}_F \mathbf{q}_{st} \ddot{u}_g(t) \\ -\mathbf{M}_R \mathbf{q}_{st} \ddot{u}_g(t) \end{bmatrix}, \quad (2)$$

where \mathbf{m}_F and \mathbf{m}_R are the vectors of mass parameters of the foundation and the rotor, u_g is the ground displacement in general direction given by unit vector \vec{e} and \mathbf{q}_{st} is the vector of static displacement of the system caused by unit ground displacement in direction \vec{e} . Displacement u_g can be particularly considered to be a kinematic excitation defined using three orthogonal displacements of the ground in global coordinate system $u_j, j = 1, 2, 3$. The vectors of external excitation can be written in the form

$$\begin{bmatrix} \mathbf{f}_F \\ \mathbf{f}_R \end{bmatrix} = \begin{bmatrix} -\sum_{j=1}^3 \mathbf{m}_{F,j} \ddot{u}_j(t) \\ -\sum_{j=1}^3 \mathbf{m}_{R,j} \ddot{u}_j(t) \end{bmatrix}, \quad (3)$$

where $\ddot{u}_j(t)$ are accelerations of the ground in the j -th direction axes of the global coordinate system. Illustrative seismic excitation in a chosen direction is shown in Fig. 2.

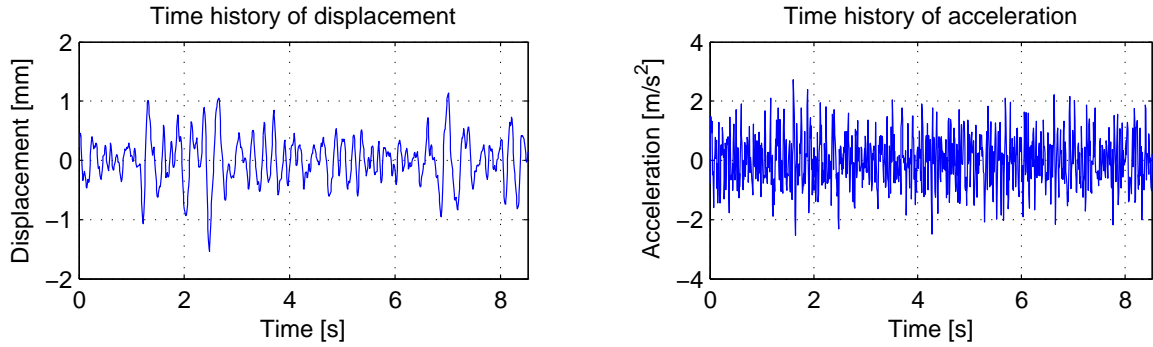


Fig. 2. Example of seismic excitation

The created mathematical model of a rotor and a foundation including seismic excitation can be further formulated in the condensed form [2] in order to reduce the number of the system degrees of freedom. The model in such a form is suitable for the solution using the numerical integration. An in-house software was developed based on the proposed modelling methodology and its performance is demonstrated by means of the particular real turbine example.

Acknowledgements

The paper has been originated in the framework of institutional support for the long-time conception development of the research institution provided by Ministry of Industry and Trade of the Czech Republic.

References

- [1] Adams, M. L., Rotating machinery vibration: From analysis to troubleshooting, Marcel Dekker, New York, 2001.
- [2] Byrtus, M., Hajžman, M., Zeman, V., Dynamics of rotating systems, University of West Bohemia, Plzeň, 2010. (in Czech)
- [3] Chopra, A. K., Dynamics of structures, University of California, Berkeley, 2012.
- [4] Su, W-C., Hernried, A.G., Yim, S.C.S., Seismic response of rotating machines–structure–RFBI systems, Earthquake Engineering & Structural Dynamics 29 (2000) 213-240.

Statics and dynamics of cable structures

J. Dupal ^a

^a Faculty of Applied Sciences, University of West Bohemia, Univerzitní 8, 306 14 Plzeň, Czech Republic

Cables became very important components of special cable robot or manipulator driving parts. It was ensured that lateral and longitudinal cable vibrations significantly influence behaviour of the end-effector of such cable appliance. The paper deals with the first stage of simulation-modelling and numerical simulation of strongly nonlinear vibration of one cable. The new mathematical model of cable takes into account dissipative effect of Kelvin-Voight material and air resistance during cable vibration.

To describe the cable behaviour and obtain Eq. of motion we can use Hamilton's principle in form

$$\delta \int_0^t (W_N + E_K - V) dt = 0, \quad (1)$$

where W_N , E_K , V is work of non-conservative external forces, kinetical energy and potential energy, respectively. Kinetical energy of cable can be written in form

$$E_K = \frac{1}{2} \int_0^L \mu \dot{\mathbf{r}}^T \dot{\mathbf{r}} ds, \quad (2)$$

where $\mathbf{r}(s, t)$ is radius-vector of arbitrary cable point, dot marks time differentiation, μ is mass of one meter of cable, s is length cable coordinate and L is total cable length. Variation of kinetical energy integral can be expressed after some arrangements as

$$\delta \int_0^t E_K dt = - \int_0^t \int_0^L \mu \dot{\mathbf{r}}^T \delta \mathbf{r} ds dt. \quad (3)$$

Potential energy of cable consist of gravitational and strength part [1]

$$V = \frac{1}{2} \int_0^L \left(\frac{1}{2} EA \varepsilon^2 - \mu g \mathbf{r}^T \mathbf{e}_3 \right) ds dt = \frac{1}{2} \int_0^L \left[\frac{1}{2} EA (\|\mathbf{r}'\| - 1)^2 - \mu g \mathbf{r}^T \mathbf{e}_3 \right] ds dt, \quad (4)$$

variation of potential energy integral after arrangements can be written in form

$$\begin{aligned} \delta \int_0^t V dt = \int_0^t \left\langle EA h \left\{ \|\mathbf{r}'_L\| - 1 \right\} \frac{\|\mathbf{r}'_L\| - 1}{\|\mathbf{r}'_L\|} \mathbf{r}'_L{}^T \delta \mathbf{r}'_L - EA h \left\{ \|\mathbf{r}'_0\| - 1 \right\} \frac{\|\mathbf{r}'_0\| - 1}{\|\mathbf{r}'_0\|} \mathbf{r}'_0{}^T \delta \mathbf{r}'_0 - \right. \\ \left. - \int_0^L EA h \left\{ \|\mathbf{r}'\| - 1 \right\} \left(\mathbf{r}'' - \frac{\mathbf{r}''}{\|\mathbf{r}'\|} + \frac{\mathbf{r}'{}^T \mathbf{r}''}{\|\mathbf{r}'\|^3} \mathbf{r}' \right)^T \delta \mathbf{r} ds + \int_0^L \mu g \mathbf{e}_3^T \delta \mathbf{r} ds \right\rangle dt. \end{aligned} \quad (5)$$

Individual symbols in relations (4) and (5) correspond to: \mathbf{e}_3 - unit vector having direction of gravitation, \mathbf{r}_L and \mathbf{r}_0 -radius-vector of cable end and origin point, E -Young modulus, A -cable cross section area, g -gravitation constant, $h\{\}$ -Heaviside unit step function. In case when the boundary cable points are stationary, the first two terms of (5) drop out.

Virtual work of external non-conservative forces includes air resistance and inner damping of material. Air resistance virtual work can be expressed in form

$$\delta W_A = -\eta_o (\mathbf{n}^T \dot{\mathbf{r}}) \mathbf{n}^T \delta \mathbf{r}, \quad (6)$$

where \mathbf{n} is unit normal vector of cable and η_o is coefficient of resistance. Normal vector can be expressed in form

$$\mathbf{n} = \frac{\frac{\mathbf{r}^{\parallel}}{(\mathbf{r}^{\perp T} \mathbf{r}^{\perp})^{\frac{1}{2}}} - \frac{\mathbf{r}^{\perp T} \mathbf{r}^{\perp}}{(\mathbf{r}^{\perp T} \mathbf{r}^{\perp})^{\frac{3}{2}}} \mathbf{r}^{\perp}}{\left[\frac{\mathbf{r}^{\perp T} \mathbf{r}^{\parallel}}{\mathbf{r}^{\perp T} \mathbf{r}^{\perp}} - \frac{(\mathbf{r}^{\perp T} \mathbf{r}^{\perp})^2}{(\mathbf{r}^{\perp T} \mathbf{r}^{\perp})^2} \right]^{\frac{1}{2}}}. \quad (7)$$

Variation of integral of virtual work of viscous forces (Kelvin-Voight material) can be written down in form

$$\delta \int_0^t W_{KV} dt = \int_0^t \int_0^L \eta_v EA \dot{\varepsilon} \delta \varepsilon ds dt, \quad (8)$$

where η_v is coefficient of viscous damping, $\dot{\varepsilon}$ is speed of deformation which can be expressed in form

$$\dot{\varepsilon} = \frac{\dot{\mathbf{r}}^{\perp T} \mathbf{r}^{\perp}}{(\mathbf{r}^{\perp T} \mathbf{r}^{\perp})^{\frac{1}{2}}}. \quad (9)$$

After substitution (9) into (8) and integrating per-partes we can write

$$\delta \int_0^t W_{KV} dt = - \int_0^t \int_0^L \frac{\partial}{\partial s} \left(\eta_v EA \frac{\dot{\mathbf{r}}^{\perp T} \mathbf{r}^{\perp}}{(\mathbf{r}^{\perp T} \mathbf{r}^{\perp})} \mathbf{r}^{\perp T} \right) \delta \mathbf{r} ds dt. \quad (10)$$

Comparing terms staying at $\delta \mathbf{r}$ in relations (3), (5), (6) and (10) and put it equal to zero we can come to the Eq. of motion of one cable in form

$$\begin{aligned} \ddot{\mathbf{r}} = & h \left\{ \|\mathbf{r}^{\perp}\| - 1 \right\} \frac{EA}{\mu} \left(\mathbf{r}^{\parallel} - \frac{\mathbf{r}^{\parallel}}{\|\mathbf{r}^{\perp}\|} + \frac{\mathbf{r}^{\perp T} \mathbf{r}^{\perp}}{\|\mathbf{r}^{\perp}\|^3} \mathbf{r}^{\perp} \right) + \\ & + h \left\{ \|\mathbf{r}^{\perp}\| - 1 \right\} \frac{\eta_v EA}{\mu} \left[\frac{\dot{\mathbf{r}}^{\perp T} \mathbf{r}^{\perp}}{\mathbf{r}^{\perp T} \mathbf{r}^{\perp}} \mathbf{r}^{\perp} + \frac{\dot{\mathbf{r}}^{\perp T} \mathbf{r}^{\parallel}}{\mathbf{r}^{\perp T} \mathbf{r}^{\perp}} \mathbf{r}^{\perp} - \frac{2(\dot{\mathbf{r}}^{\perp T} \mathbf{r}^{\perp})(\mathbf{r}^{\perp T} \mathbf{r}^{\perp})}{(\mathbf{r}^{\perp T} \mathbf{r}^{\perp})^2} \mathbf{r}^{\perp} + \frac{\dot{\mathbf{r}}^{\perp T} \mathbf{r}^{\perp}}{\mathbf{r}^{\perp T} \mathbf{r}^{\perp}} \mathbf{r}^{\parallel} \right] + g \mathbf{e}_3 - \eta_o (\mathbf{n}^T \dot{\mathbf{r}}) \mathbf{n}. \end{aligned} \quad (11)$$

Conclusion: This equation of motion was solved by means of Galerkin's method leading to strongly non-linear system of ordinary differential equations which can be solved by some appropriate method e.g. Runge-Kutta continuation.

Acknowledgements

The paper has originated in the framework of solving No. 15-20134S project of the Czech Science Foundation entitled "Multi-level Light Mechanisms with Active Structures".

References

- [1] Jingli, D., Sunil, K.A., Dynamic modeling of cable-driven parallel manipulators with distributed mass flexible cables, *Journal of Vibration and Acoustics* 137 (2) (2015) 021020 (8 pages).

On the application of LU-SGS scheme for turbomachinery flows

J. Fůrst^a

^a*Faculty of Mechanical Engineering, CTU in Prague, Karlovo nám. 13, 121 35 Praha, Czech Republic*

The contribution deals with the development of coupled solver for compressible flows using the OpenFOAM package. The OpenFOAM package [4] is a widely spread open CFD source library. The ready made CFD solvers contained in the library are mainly based on the segregated pressure-based methodology which is appropriate for incompressible or weakly compressible flows. In the case of transonic or supersonic flows the coupling between the pressure, density, and temperature becomes more important and the efficiency of segregated approach is highly impaired. The coupled (density-based) solvers based on the approximate Riemann fluxes become much more efficient. So for the only coupled density based solver in the standard OpenFOAM distribution is *rhoCentralFoam* which uses an explicit central-upwind scheme of Kurganov and Tadmor. There exist also another projects through the OpenFOAM community (e.g. the *densityBasedTurbo* or *aeroFoam*) which use the AUSM family or Roe fluxes combined with explicit Runge-Kutta integration in time. Nevertheless all the above mentioned density based solvers suffer from the stability restriction and are therefore not very suitable for the calculation of viscous turbulent flows.

The matrix-free LU-SGS (lower-upper symmetric Gauss-Seidel) implicit scheme [1] offers a very simple implicit method with memory requirements comparable to the explicit method. The article [3] gives detailed description of the implementation of the LU-SGS scheme for the case of inviscid flows. We follow the same methodology and we extend the solver for the case of viscous turbulent flows including multiple rotating frames of reference. The update step of the LU-SGS is realized in two subsequent sweeps through the mesh in increasing and decreasing order

$$D_i \Delta W_i^* = -R_i^n - \frac{1}{2} \sum_{j \in N_i, j < i} \left[(\Delta \vec{F}_c^*)_j \vec{S}_{ij} + r_j \Delta W_j^* \right], \quad (1)$$

$$D_i \Delta W_i^n = D_i \Delta W_i^* - \frac{1}{2} \sum_{j \in N_i, j > i} \left[(\Delta \vec{F}_c^n)_j \vec{S}_{ij} - r_j \Delta W_j^n \right], \quad (2)$$

where N_i is the set of neighbor cell indices, $\Delta W_i^* = W_i^* - W_i^n$, $\Delta W_i^n = W_i^{n+1} - W_i^n$, $(\Delta \vec{F}_c^*)_j = \vec{F}_c(W_j^*) - \vec{F}_c(W_j^n)$, $(\Delta \vec{F}_c^n)_j = \vec{F}_c(W_j^{n+1}) - \vec{F}_c(W_j^n)$ (here \vec{F}_c is the convective flux vector). The spectral radius of the flux Jacobian including viscous contribution is approximated as (see [1])

$$r_j = \omega \left(|\vec{u}_j \cdot \vec{S}_{ij} + c_j| \|\vec{S}_{ij}\| + \frac{\|\vec{S}_{ij}\|}{\|\vec{x}_i - \vec{x}_j\|} \left(\frac{\nu}{Pr} + \frac{\nu_T}{Pr_T} \right) \max\left(\frac{4}{3}, \gamma\right) \right) \quad (3)$$

with $\omega = 1.2$. The diagonal term is $D_i = |\Omega_i| / \Delta t_i + \frac{\omega}{2} \sum_{j \in N_i} r_j$.

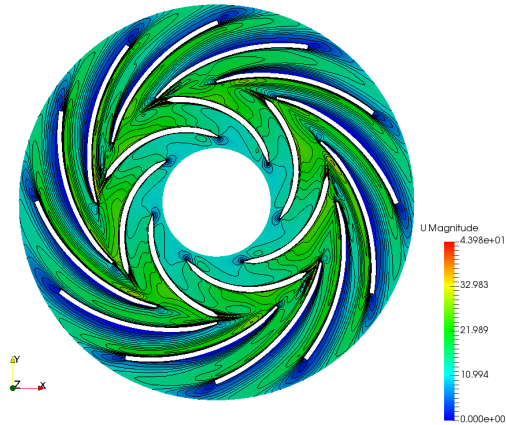


Fig. 1. Velocity magnitude in the ERCOF-TAC centrifugal pump

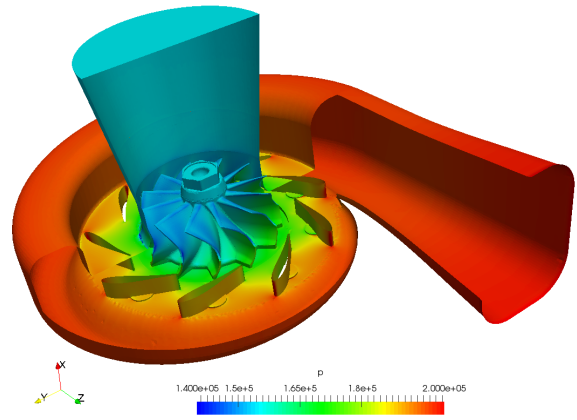


Fig. 2. Pressure distribution in the radial turbine

Fig. 1 shows the distribution of velocity magnitude in the ERCOFTAC centrifugal pump, see [2] for details. The 2D numerical simulation has been done with the above mentioned LU-SGS method where the residual R_i^n was evaluated using AUSM+up scheme and two frames of reference were assumed (the so called frozen rotor method). The comparison with results in [2] shows that the LU-SGS method gives similar results as the segregated solver for incompressible flows based on SIMPLE loop.

Fig. 2 shows the result of the calculation of 3D turbulent flow through the radial turbine. The rotor speed is set to 90 000 rpm and the total to static pressure ratio was 1.3. The rotor tip speed is about 250 m/s (i.e. $M = 0.45$) and therefore the compressibility becomes more important. The calculation has been performed using LU-SGS scheme with HLLC fluxes and the unstructured mesh contained approximately 8 000 000 cells.

The above mentioned cases prove that the LU-SGS scheme can be used for the solution of compressible turbulent flows including flows in complex geometry.

Acknowledgements

This work has been supported by the grant TACR TE01020020.

References

- [1] Blazek, J., Computational fluid dynamics: principles and applications, Elsevier, 2005.
- [2] Petit, O., Nilsson, H., Numerical investigations of unsteady flow in a centrifugal pump with a vaned diffuser, International Journal of Rotating Machinery 2013 (2013) 1-14, doi: 10.1155/2013/961580.
- [3] Shen, C., Xia, X., Wang, Y., Yu, F., Jiao, Z., Implementation of density-based implicit LU-SGS solver in the framework of OpenFOAM, Advances in Engineering Software 91 (2016) 80-88.
- [4] Weller, H.G., Tabor, G., Jasak, H., Fureby, C., A tensorial approach to computational continuum mechanics using object oriented techniques, Computers in Physics 12 (1998) 620-631.

Experimental analysis of railway vehicle passing over turnout frog

A. Hába^a, J. Zelenka^a, M. Kohout^a

^a Jan Perner Transport Faculty, University of Pardubice, Nádražní 547, 560 02 Česká Třebová, Czech Republic

In the course of a vehicle passing over a simple turnout, the increased dynamical response (especially in vertical direction) is indicated due to the crossing of the rails in the turnout frog area (see Fig. 1). This fact results in a quick degradation of appropriate turnout components. To service life maximizing of these components, there is necessary to concern to vehicle-track interaction in the course of passing over a turnout.

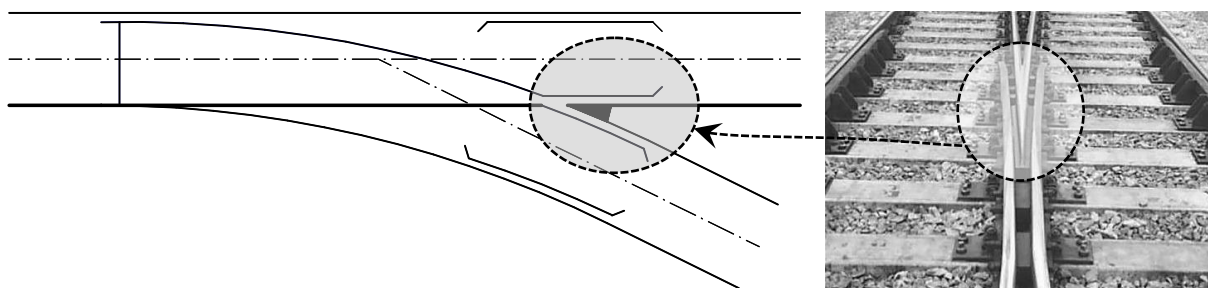


Fig. 1. Diagram of the simple turnout and view of the frog area

The experimental determination of the vertical dynamical response of a vehicle passing over a turnout is based on a vertical acceleration measurement on the wheelset axle box [2]. For the sufficient description of the vehicle dynamical response in the course of passing over a turnout at the speed up to 160 kmph, the minimum sampling rate of the recorded data shall be set to 10 kHz. With regard to the frequency of the wheel vertical motion in the course of passing over the turnout frog area, the measured acceleration course is then filtered by the bench-pass filter. The typical course of the vertical acceleration measured on the wheelset axle box is shown in Fig. 2 [3].

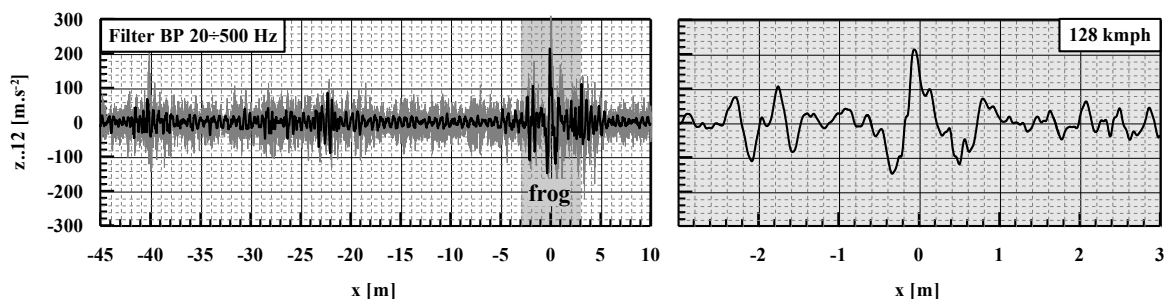


Fig. 2. Typical acceleration course measured on the axle box of the first vehicle wheelset in the course of passing over a whole turnout (left); filtered acceleration course corresponding to passing over the frog area (right)

The origin of the horizontal axis of both graphs in Fig. 2 is situated to the position of the maximum vertical deflection of the wheel, which always corresponds to the instant when wheel passes from the wing rail to the frog tip or conversely (according the passing

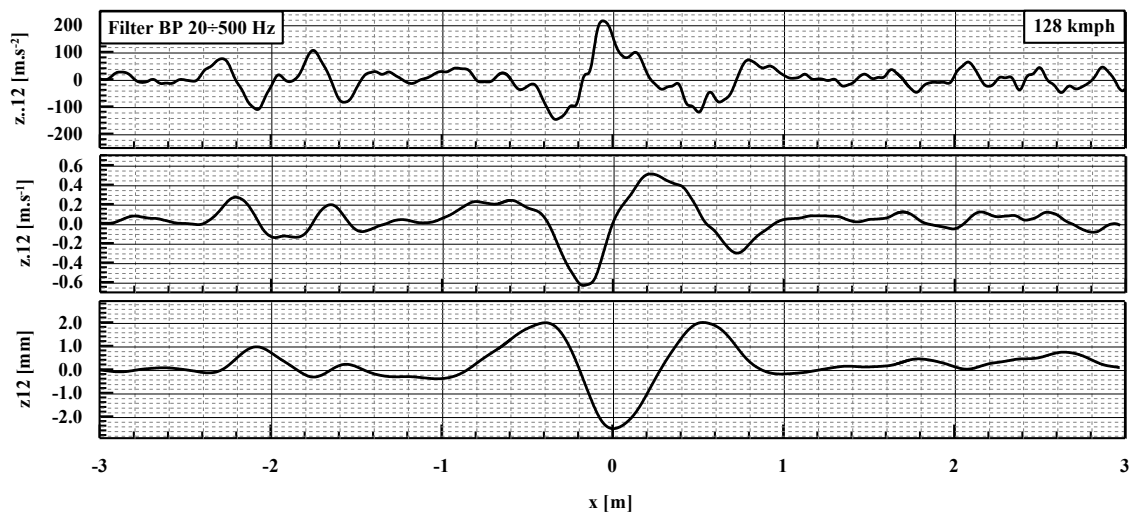


Fig. 3. The graphs presents (from the top): the acceleration course measured on the axle box of the first vehicle wheelset in the course of passing over a turnout frog area; the vertical wheel velocity obtained by the integration of the measured vertical acceleration; the vertical wheel deflection obtained by the integration of the vertical wheel velocity

direction) [1]. This extreme of the wheel vertical deflection corresponds to the zero value of the vertical velocity. The courses of the wheel vertical velocity and the deflection are obtained by the integration of the measured vertical acceleration (see Fig. 3).

The vehicle dynamical response in the course of passing over the turnout frog area is regarded by the equivalent loading, which value is determined as a total of the static wheel load and the dynamic response of the inertia force of the unsuspended mass per a wheel [2]. The Fig. 4 presents the courses of the equivalent loading of the same turnout during its 1 year operation.

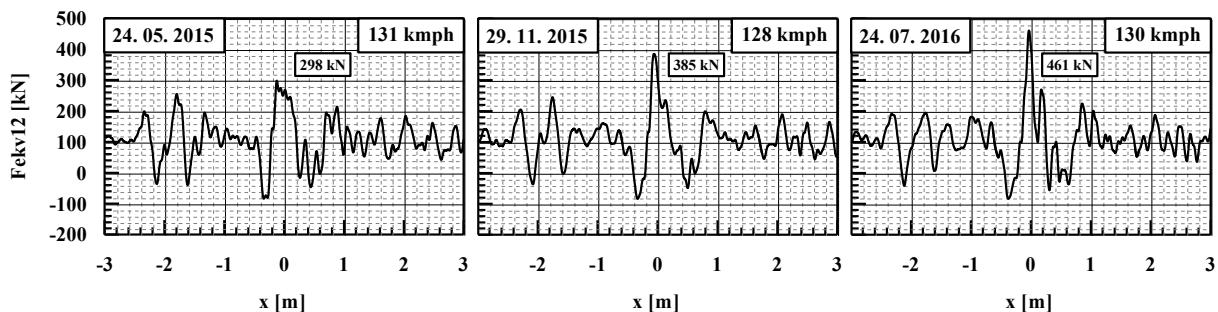


Fig. 4. Courses of the equivalent loading of the same turnout during its 1 year operation

In the course of vehicle passing over the turnout frog area, the vertical wheel deflection is caused not only by changes of the wheel-rail kinematical relation but also by the vertical deflection of the rail. By this reason, the value of the equivalent loading cannot be understood as an absolute value of the wheel-rail force. Although there is possibility to correct this assessment by the rail vertical response measurement, there is necessary to take to account also the impact process of passing over the turnout frog for determination of the real value of the wheel-rail force.

References

- [1] Grin, G., Verschleiß und Belastung von Weichenherzstücken, Diploma Thesis, Technische Universität Dresden, 2013.
- [2] Zelenka, J., Hába, A., Kohout, M., Determination of equivalent loading of railway turnout frog area in the course of vehicle passing based on EN 14363 approaches, Certified methodology, 2014.
- [3] Zelenka, J., Hába, A., Kohout, M., Vyhodnocení měření zrychlení na lokomotivě řady 380 při průjezdu vybranými výhybkami stanice Ústí nad Orlicí, Research report DP-03-15, 2015. (in Czech)

Damage prediction with coupled fatigue and creep mechanism applied on generator turbine

J. Had^a

^a National center for research, development and testing in aerospace, a.s., Beranových 130 Praha 9, Prague, Czech Republic

During the service of an engine, a multitude of material damage such as foreign object damage, erosion, high cycle fatigue, low cycle fatigue, fretting, hot corrosion/oxidation, creep, and thermo-mechanical fatigue is induced in these parts. The mechanical loading and effects based on the temperature gradient were stated as the most important factors.

Change of both mechanical loading and temperature distribution occurs during the common engine service. Changing temperature during the loading cycles has influence on stress-strain state and therefore it causes closure problem of stress-strain hysteresis loop. Temperature dependent fatigue properties brings additional aspects to deal with. Moreover high temperature field can induces creep and it causes interaction with pure fatigue (ϵ^{pl} induced mechanism). The way how both mechanism can be considered is described in further paragraphs.

Damage calculated from fatigue parameter influenced by actual temperature is proposed in paper [1]. Actual damage is calculated in every step of loading history. Evolution of fatigue damage can be calculated cheap and very quickly using widely available isothermal fatigue curves. Proposed concept overcame hysteresis loop closure problems. The closure problem is solved by identification of origin of hysteresis loop to current analyzing point. Temperature dependent damage is based on interpolation of experimental fatigue data for the current temperature. Actual fatigue damage is evaluated with SWT damage operator. Prandtl-Ishlinskii model of hysteresis (finite number of spring-slider models connected in series) is applied on interpolated iso-thermal fatigue curves for current temperature. Actual fatigue damage is get as the sum of elemental contributions from each individual spring-slider sub-models.

It is known that the fatigue and creep damages depend on elasto-plastic strain and stress respectively. If the life prediction is based on the instantaneous values, both fatigue and creep damages should be overestimated for positive mean stress due to relaxation. For this purpose visco-plasticity strain component must be evaluated and affected final elasto-plastic strain and stress respectively. In order to cover viscoplasticity spring-slider model was extended to the nonlinear Maxwell model by adding nonlinear damper in series according to [2], see Fig. 1.

In whole procedure stress tensor serves as a preprocessed input into the assessment. For this purpose elastic FEM analysis was performed and all necessary inputs are calculated from elastic stress tensor. In the case of low cycle fatigue, both stress and strain must be known. Elasto-plastic stress is calculated with Neuber's approximation from FEM elastic stress. For strain approximation stress-controlled Prandtl-Ishlinskii model can be used to cover elasto-plasticity. For stepwise stress history elasto-plastic and viscoplastic strain component are gain independently solving one after another. Elasto-plastic and viscoplastic strain component are linked together with the principle of superposition and viscoplastic component is taken into consideration only if actual temperature in current time step is higher than creep temperature. Elasto-plastic strain component is calculated from extrapolated stabilized cyclic deformation

curve for strain rate $\dot{\epsilon} \rightarrow \infty$. Viscoplastic strain is evaluated according to law of perfect viscoplasticity with elastic domain with temperature dependent material parameters fitted from tensile creep curves. Creep and fatigue damage are calculated according to proposed method described in [1] and [2]. Total damage is supposed as the summation of fatigue and creep damage. Sequential block scheme of described approach is depicted in Fig. 3.

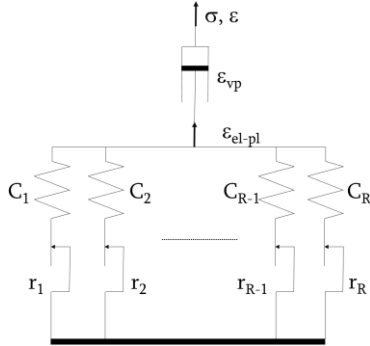


Fig. 1. Model of viscoplasticity

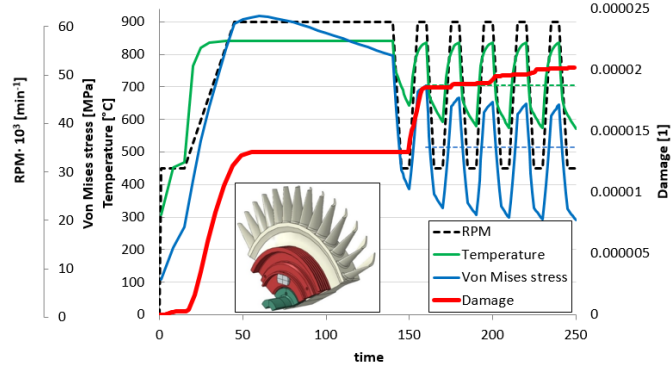


Fig. 2. Evolution of damage during the simplified loading sequence

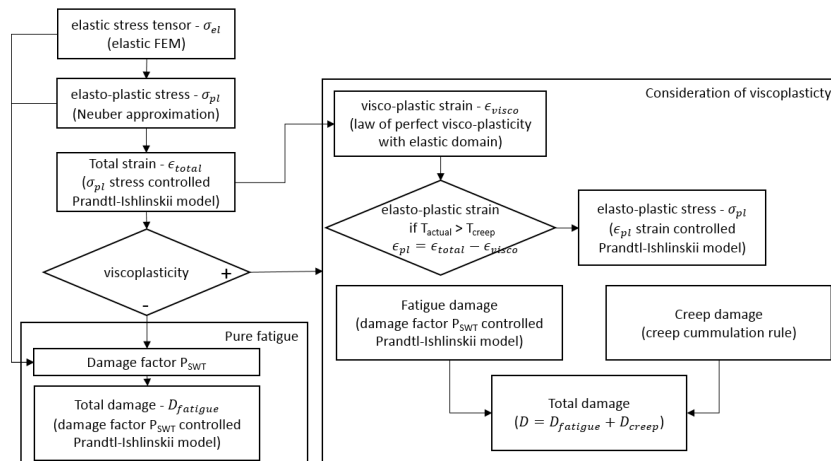


Fig. 3. Block scheme of consideration of both fatigue and creep damage mechanisms

Damage operator approach was applied to fatigue assessment of generator turbine. Heat transport analysis was performed, at first, to solve convection and conduction of heat from gas to structural parts. Temperature field is assumed from previous heat analysis as a boundary condition in subsequent structural analysis. Stress and temperature results in crucial point as well as predicted damage progression are shown in Fig. 2.

Presented paper briefly described promising approach for continuous damage calculation during the non-isothermal loading of generator turbine. Presented concept is computational cheap and very effective using only widely available material data from isothermal tests.

Acknowledgements

This work was supported by National center for research, development and testing in aerospace, a.s. in project TMF, project number IP4408.

References

- [1] Nagode, M., Hack, M., Fajdiga, M., Low cycle thermos-mechanical fatigue: damage operator approach, *Fatigue & Fracture of Engineering Materials & Structures* 33 (3) (2010) 149-160.
- [2] Nagode, M., Fajdiga, M., Coupled elastoplasticity and viscoplasticity under thermomechanical loading, *Fatigue & Fracture of Engineering Materials & Structures* 30 (6) (2007) 510-519.

FE modelling of the influence of the lamina propria properties on the vocal folds vibration and produced sound for specific Czech vowels

P. Hájek^a, P. Švancara^{a,b}, J. Horáček^b, J. G. Švec^c

^aInstitute of Solid Mechanics, Mechatronics and Biomechanics, Brno University of Technology, Technická 2896/2, 616 69, Brno, CZ

^bInstitute of Thermomechanics, Academy of Sciences of the Czech Republic, Dolejškova 1402/5, 182 00, Prague, CZ

^cDepartment of Biophysics, Palacky University Olomouc, 17. listopadu 12, 771 46, Olomouc, CZ

Vowel production is a physical process including interaction between exhaling air (fluid), vibrating vocal folds (structure) and phonation (acoustics). Each environment affects one another, e.g. moving boundary of the vocal folds (VF) represents set of acoustic sources and initiated acoustic pressure influences the VF back. Such a mutual influence is apparent while comparing results obtained from computational modelling of different vowels.

Presented two-dimensional (2D) finite element (FE) model of the flow-induced self-oscillation of the human VF enables solving fluid-structure-acoustic interaction occurring during phonation. The aim is to analyze the influence of stiffness of superficial lamina propria (SLP) on VF vibrations for vocal tracts (VT) shaped for particular Czech vowels. Such a symmetrical or unsymmetrical variation of the SLP properties accompanies diverse VF pathologies.

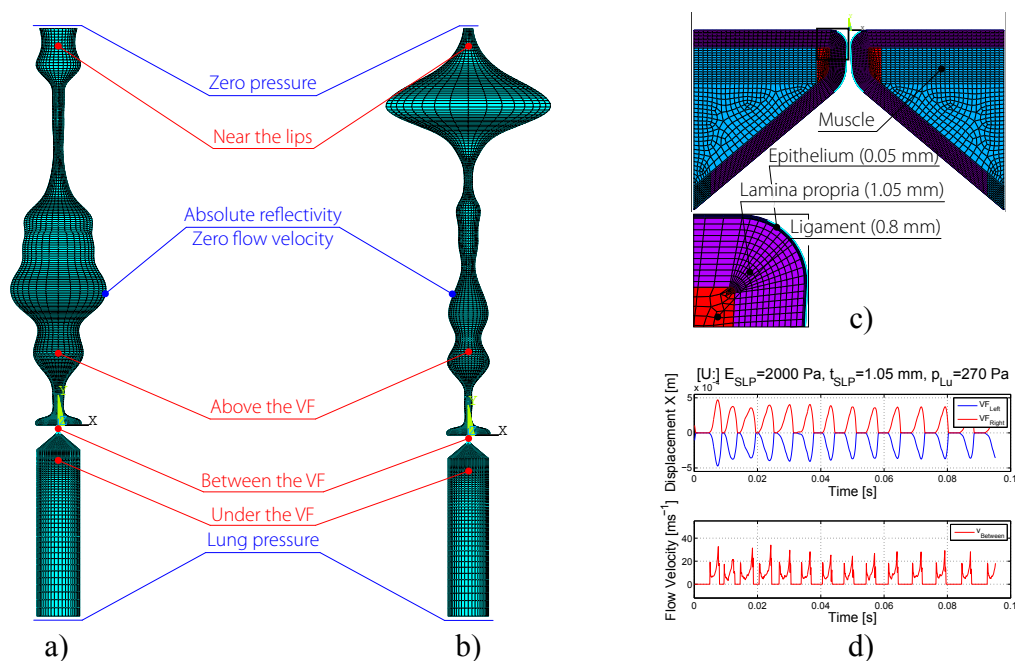


Fig. 1. a) Fluid FE model of the acoustic spaces of the trachea and the VT for Czech vowel [i:] and b) [u:] vowel, c) structural FE model of the four-layered tissue of the VF and d) example of simulated VF displacements and flow velocity in glottis in time domain for vowel [u:]

Similar FE model has been developed in previous work of the authors [1] with the VT shaped for Czech vowel [a:]. This paper presents results of effect of stiffness of SLP on VF vibration for VT shaped for Czech vowels [i:] and [u:].

The 2D FE model includes setting to phonatory position, large deformation of VF tissues and their contact and unsteady viscous compressible airflow separated during glottal closure described by the Navier-Stokes equations. The fluid mesh morphs according to the VF motion (solved by Arbitrary Lagrangian-Eulerian approach). Geometric data of the VT were converted from MRI [2] (see Fig. 1a) and b)), the VF employ Scherer's M5 geometry [3] (see Fig. 1c)). The airflow (36 °C) was considered in the acoustic spaces, the VF have homogenous isotropic linear-elastic material properties. Details of FE models and algorithms could be found in [1].

Several variants of computations were performed for rising Young's modulus of lamina propria E_{SLP} and for lung pressure $p_{Lu} = 270$ Pa. Fig. 1d) shows example of computed displacement in x (lateral) direction of selected nodes in the middle of the VF and flow velocity in selected node between VF, both obtained for vowel [u:] with default settings $E_{SLP} = 2000$ Pa and $p_{Lu} = 270$ Pa. There is a comparison between maximal width of glottis WG_{max} , vibration frequency f , open quotient OQ and closing quotient CIQ for [i:] and [u:] vowel in Table 1.

Table 1. Computed characteristics of VF oscillation depending on E_{SLP} for $p_{Lu} = 270$ Pa

E_{SLP} [Pa]	p_{Lu} [Pa]	Vowel [i:]				Vowel [u:]			
		WG_{max} [mm]	f [Hz]	OQ [-]	CIQ [-]	WG_{max} [mm]	f [Hz]	OQ [-]	CIQ [-]
2000	270	0.51	143	0.46	0.17	0.56	127	0.43	0.10
2500		0.49	141	0.46	0.14	0.49	133	0.49	0.09
3000		0.46	139	0.49	0.15	0.42	119	0.55	0.07
3500		0.35	97	0.34	0.07	0.38	99	0.62	0.07

Change of VT shape or more precisely acoustics of the VT causes variation in structural results and reveals functional fluid-structure-acoustic interaction. The stiffer lamina propria causes a decrease of WG_{max} and f in most cases, similarly to the vowel [a:] as in [1]. Values of OQ are about 0.5, which corresponds to clinical results [1]. The developed FE model could be employed in research of vowel production with impaired VF.

Acknowledgement

This research is supported by the Brno University of Technology by the project *Fond Vědy FV 16-09* and by the Grant Agency of the Czech Republic project No 16-01246S *Computational and experimental modelling of self-induced vibrations of vocal folds and influence of their impairments on human voice*.

Reference

- [1] Hájek, P., Švancara P., Horáček J., Švec J.G., Numerical simulation of the effect of stiffness of lamina propria on the self-sustained oscillation of the vocal folds, Proceedings of the conference Engineering Mechanics 2016, Svratka, 2016, pp. 182-185.
- [2] Radolf, V., Direct and inverse task in acoustics of the human vocal tract, Ph.D. Thesis, Czech Technical University in Prague, 2010.
- [3] Scherer, R.C., Shinwari, D., De Witt, K.J., Zhang, C., Kucinschi, B.R., Afjeh, A.A., Intraglottal pressure profiles for a symmetric and oblique glottis with a divergence angle of 10 degrees, The Journal of the Acoustical Society of America 109 (4) (2011) 1616-1630.

Dynamics of a parallel multilevel mechanism

M. Hajžman^a, R. Bulín^a, J. Zavřel^b, Z. Šika^b, P. Polach^a

^aDepartment of Mechanics, Faculty of Applied Sciences, University of West Bohemia, Univerzitní 8, 306 14 Plzeň, Czech Republic
^bDepartment of Mechanics, Biomechanics and Mechatronics, Faculty of Mechanical Engineering, Czech Technical University in Prague, Technická 4, 166 07 Praha, Czech Republic

This paper describes the creation of a computational model of a cable manipulator with added active piezo-structure (so called multilevel mechanism). Multilevel mechanisms with hierarchical motion control can be advantageously used in specific cases where several levels of various motions have to be controlled.

Particularly the spherical redundantly actuated tilting mechanism is considered (see Fig. 1). It is primarily actuated by four fibres and performs a spherical motion with three degrees of freedom [4]. The four fibres lead over pulleys to sliders with servo-drives (see Fig. 2). Active structure with six piezoactuators is integrated between the end-effector platform and auxiliary platform suspended and moved by four fibres [2]. The piezoactuators are mounted in the cubic configuration. The central spherical joint (Cardan universal joint) equipped with rotational incremental sensors simultaneously ensures the measurement of the end-effector platform position. The large lower frequency components of motion can be controlled by the servo-drives through the fibres, whereas the small high frequency components of motion can be controlled by the piezoactuators.

The idea behind the hierarchical motion control of lightweight multilevel mechanisms consists of the large motion level realized by cable driven parallel mechanisms [1] and the small motion levels realized using active structures [3]. The superimposed active structures can im-

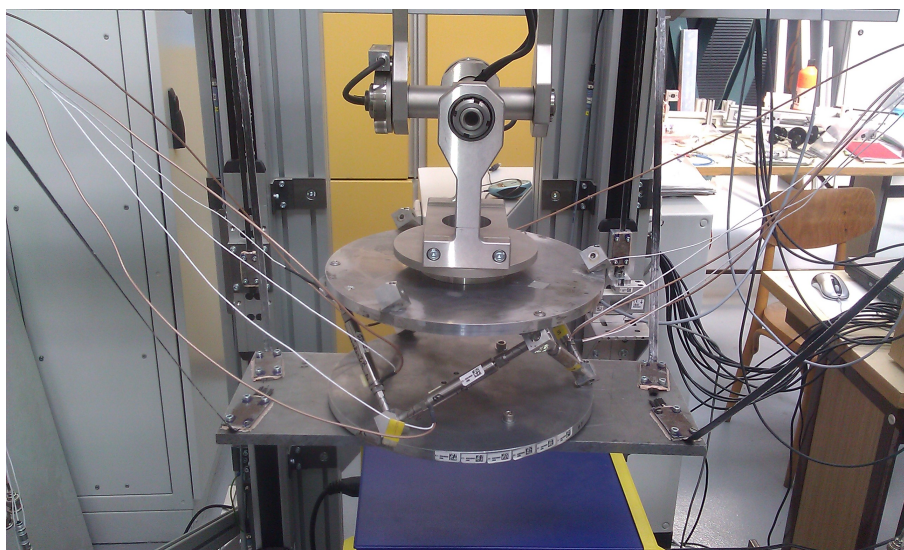


Fig. 1. Real Quadrosphere mechanism with the active piezo-structure

prove the positioning accuracy and operational speed of the end-effectors of recently developed cable driven parallel mechanisms of different types.

The mechanism is composed of a rigid manipulator with three degrees of freedom, added active structure with piezo-elements and a platform driven by four fibres (Fig. 2). The multi-body dynamics approaches are a suitable way in order to create the mechanism model. Two different models are presented — the MSC.ADAMS model and the in-house MATLAB model. The fibre system was created using MSC.ADAMS/Machinery Cable module. This module offers two methods for the modelling of cables — the simplified one and the discretized one. The simplified method is the force based method (implemented also in the in-house MATLAB model). The discretized method is based on the point-mass model and is intended for cables with not negligible mass.

The basic model verification was done using the modal analysis of a linearized model. Various numerical simulations and result comparisons were performed.

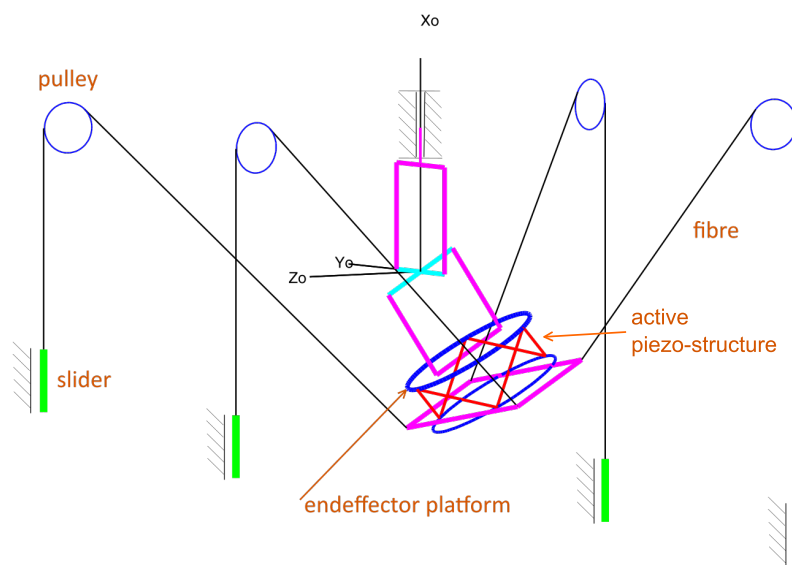


Fig. 2. Scheme of the Quadrosphere driven by cables with the active piezo-structure

Acknowledgement

The paper has originated in the framework of solving No. 15-20134S project of the Czech Science Foundation entitled “Multi-level Light Mechanisms with Active Structures”.

References

- [1] Duan, X., Qiu, Y., Duan, Q., Du, J., Calibration and motion control of a cable-driven parallel manipulator based triple-level spatial positioner, *Advances in Mechanical Engineering* 6 (2014), doi: 10.1155/2014/368018.
- [2] Hajžman, M., Bulín, R., Šika, Z., Svatoš, P., Usage of the particle swarm optimization in problems of mechanics, *Applied and Computational Mechanics* 10 (1) (2016) 15-26.
- [3] Svatoš, P., Optimization and motion control of cable-driven parallel mechanisms, Ph.D. thesis, Czech Technical University, Prague, 2016. (in Czech)
- [4] Svatoš, P., Šika, Z., Valášek, M., Bauma, V., Polach, P., Optimization of anti-backlash fibre driven parallel kinematical structures, *Bulletin of Applied Mechanics* 8 (31) (2012) 40-44.

Stress distribution in pelvic floor structures depending on real fetus head molding and trajectory during vaginal delivery

L. Havelková^a, L. Krofta^b, N. Sindhvani^c

^aNew Technologies - Research Centre, University of West Bohemia, Univerzitní 8, 306 14 Plzeň, Czech Republic

^bInstitute for the Care of Mother and Child, Podolské nábřeží 157, 147 00 Praha 4 - Podolí, Czech Republic

^cOrgan Systems, University of Leuven, Oude Markt 13, 3000 Leuven, Belgium

Pelvic floor dysfunctions such as urinary/fecal incontinence or pelvic organ prolapse are very often associated with the tissue injuries during vaginal delivery. Nevertheless, it is recognized that the understanding of the process of pelvic floor damage is still very limited [4]. Therefore, the sophisticated computer models represent the suitable tool how to improve that. In the literature, there are many studies focused on the computational analysis of the pelvic floor. Most of them model the fetus head as an rigid body or as the structure with the stiff material [2]. However, during the vaginal delivery in the vertex position, the fetus head is molded into an ellipsoid shape caused by pressure in birth canal. This occurs because the bones are separated by sutures and fontanelles ensuring its flexibility [4]. To our knowledge, only few studies simulate the head as a deformable body with adjusted materials [3] or including the cranial sutures [1]. Nevertheless, in those works, the analysis is based on the first stage only or the head molding is estimated using the Lapeers index [1]. Therefore, the aim of this work was to analyze the stress distribution in levator ani muscle (MLA) using the FE model of female pelvic floor and the deformable fetal head respecting dynamic MRI obtained during the second stage of labor.

The 3D virtual model was developed. The model consists of the female pelvis, the levator ani muscle (MLA), the obturator muscle and the fetal head. The geometry was based on real MRI data of the young woman (25 years, nulliparous, height 171 cm, weight 64 kg) and of the neonate (1 day, 3600 g), both high-resolution axial 3T MRI scans (Phillips Achieva TX series). The initial geometric model was reconstructed using 3D Slicer (BWH, 3.0, Boston). The final geometry was modified by HyperMesh software (Altair, 11.0, Michigan). The initial and boundary conditions were considered to simulate the actual initial position and rotation of all observed components and to represent the structure of surrounding support. The pelvis was fixed for all degrees of freedom to fit the model in space. The fetal head follows the curve of Carus respecting the anatomy of birth canal. The pelvis was modeled by rigid body. The muscles were represented by hyperelastic Ogden material model enabling the huge deformations during vaginal birth. The samples of porcine levator ani muscles were used to identify the model parameters. Twenty levator ani muscles extracted from eight female pigs were used. The muscles were removed surgically during general anesthesia. Each sample was loaded by the uniaxial tensile test (Zwick/Roell, Ulm, Germany) to record the tensile force and elongation changes. The material parameters were determined by the least-square minimization method using MATLAB software.

The main aim was to model the deformable fetal head. The head consists of 7 bones (parietal, frontal, occipital - each right and left, face), of sutures and fontanelles, see Fig. 1.

The bones are modeled by rigid bodies. The sutures and fontanelles are composed of shell elements represented by null material type as defined in Virtual Performance Solution (9.0, ESI Group, Paris, France). This material is convenient and economic tool for modeling of surfaces when internal forces and deformations are not of interest. In this model, these components represent just the connection between the rigid bones. In reality, these objects are either very soft cartilages or holes. The trajectories during second stage of labor are defined for each bone separately. The motion data are based on real-time dynamic MR images recorded during vaginal delivery occurring over 2 contractions [5]. And thus, the real head motion considering head molding as well as expulsion was ensured. The dynamic MR sequence allows visualization in the mid-sagittal plane only. Thus, only 2D dimensions of fetal head were fitted. However, based on the assumption of a constant total volume of fetal head, the third dimension at each time frame was also estimated.

The analysis of stress von Mises distribution in MLA during second stage of vaginal delivery was performed using VPS, see Fig. 1. Two models were compared: (1) one with the rigid fetal head and (2) the other with the deformable one. The results show that the deformable head leads to reduction of almost 20% of stress. The maximal stress was found: (1) in the left attachment to the pelvis - 54.41 MPa and (2) in lower part of MLA in the middle - 47 MPa, respectively. Quantitative evaluation of this model showed good agreement with other studies.

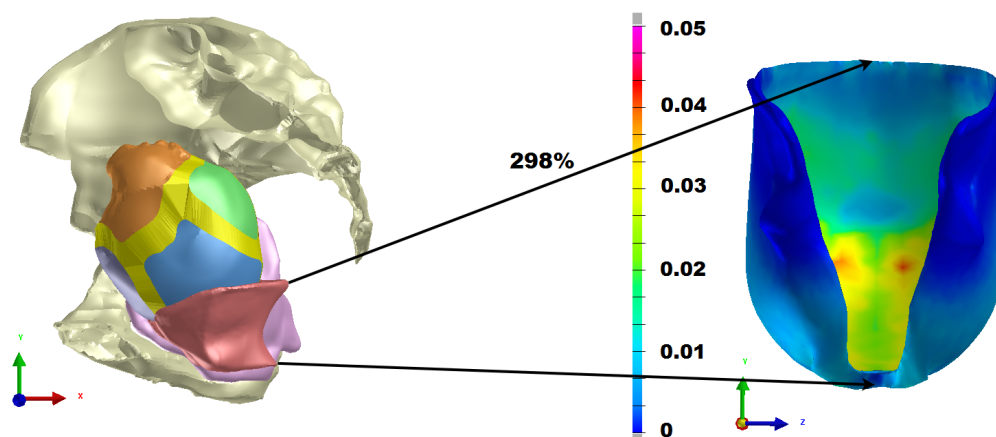


Fig. 1. The deformable fetal head based on real-time dynamic MRI (*left*); the stress distribution in MLA [GPa] - deformable head leaving the MLA area, maximal MLA elongation (*right*).

References

- [1] Lapeer, R., Prager, R., Fetal head moulding: finite element analysis of a fetal skull subjected to uterine pressure during the first stage of labour, *Journal of Biomechanics* 34 (2001) 1125-1133.
- [2] Li, X., Kruger, J., Chung, J., Nash, M., Nielsen, P., Modelling childbirth: Comparing athlete and non-athlete pelvic floor mechanics, *Medical Image Computing and Computer-Assisted Intervention* 11 (2008) 750-757.
- [3] Pu, F., Xu, L., Li, D., Li, S., Sun, L., Wang, L., Fan, Y., Effect of different labor forces on fetal skull molding, *Medical Engineering & Physics* 33 (2011) 620-625.
- [4] Silva, M.E.T., Oliveira, D.A., Roza, T.H., Brandao, S., Parente, M.P.L., Mascarenhas, T., Jorge, R.M.N., Study on the influence of the fetus head modling on the biomechanical behavior of the pelvic floor muscles, during vaginal delivery, *Journal of Biomechanics* 48 (2015) 1600-1605.
- [5] Sindhvani, N., Bamberg, C., Havelkova, L., Famaey, N., Callewaert, G., Dudenhausen, J.W., Teichgraber, U., Deprest, J.A., In vivo evidence of significant levator-ani muscle stretch on MR images of a live childbirth, *International Urogynecology Journal* 27 (Suppl. 1) (2016) 144-145.

Interaction of the rigid journal with incompressible fluid

M. Havlásek^a, F. Pochylý^a

^aBrno University of Technology, Faculty of Mechanical Engineering, V. Kaplan Department of Fluid Engineering, Technická 2896/2, Brno, Czech Republic

This paper deals with the problem of identification of added effects of incompressible fluid that impacts on the rigid journal performing translational motion. The main goal is to create mathematical model of squeeze film damper. Squeeze film damper is a lubricated component of mechanical systems which provides viscous damping. The lubrication of a damper is usually realized by magnetorheological fluids.

Presented mathematical model includes a methodology for identification of added mass, damping and stiffness matrices based on time dependence of resultant force impacted on rigid journal which is a result of CFD analysis.

Computational modeling is based on squeeze film damper with magnetorheological lubricant. For preliminary fluid flow modeling approach is used incompressible and newtonian liquid as the constitutive model for modeling lubricant in squeeze film damper. Physical properties of used fluid for modeling is specified in Table 1.

Table 1. Physical properties of fluid

Density	$\rho = 955 \text{ kg m}^{-3}$
Dynamic viscosity	$\eta = 0.3 \text{ Pa s}$

The journal is modeled as a rigid body performing translation motion and all points have circular orbit. It means that the motion of journal is a precessional. Trajectory of the journal centre of gravity has centre of rotation on stator axis and radius equal to eccentricity.

The problem of performing CFD analysis of incompressible fluid that impacts on the rigid journal performing translational motion was solved on two geometry variants. In the first variant of geometry shown in Fig. 1, there is no flow between bases of journal and stator. Second variant of geometry (Fig. 2) allows liquid to flow also in space between bases of journal and stator. For both variants of geometry, whole range of computations with different values of eccentricity were carried out. Result of computation were time dependent horizontal and vertical components of resultant force, which were evaluated on the part of journal side situated in the narrow gap.

Horizontal and vertical components of resultant force obtained from CFD analysis are converted to its radial and tangential components. These components are not time dependent. For every geometrical configuration (with specific eccentricity), five computations with different angular velocities of precession were carried out. Results of these computations were used as input data for regression analysis. The quadratic polynomial was used as regression function. Resultant function describes either radial or tangential component of resultant force and angular velocity dependence. Added mass, damping and stiffness matrices are determined on the

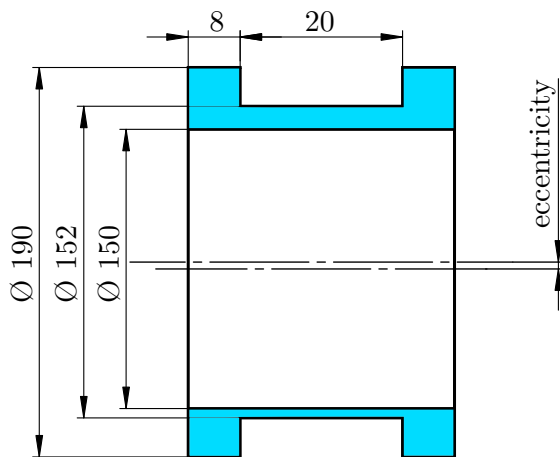


Fig. 1. First geometrical configuration

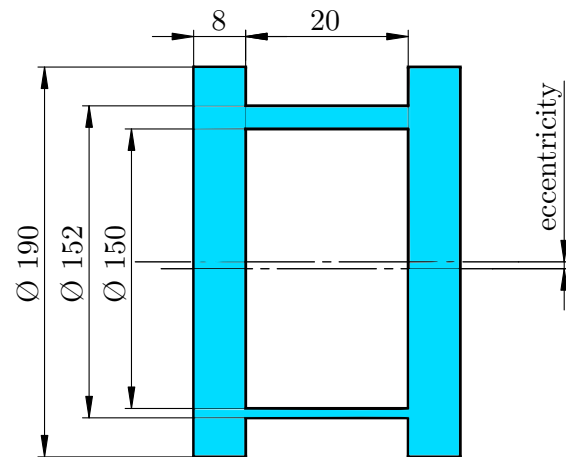


Fig. 2. Second geometrical configuration

basis of quadratic polynomials. All of them are square matrices of the second order. Described methodology for identification of added effects is based on mathematical model of sealing gap, presented in [1], and further on mathematical model presented in [2] and [3].

Presented methodology for identification of added effects could also be used for analysis of added effects in other mechanical systems, e.g. journal bearings, sealing gaps etc. It could be used for identification of added effects in cases when more general constitutive models are considered.

Acknowledgement

The research was supported by project of the Grant Agency of the Czech Republic, within the project GA101/15-06621S “Modeling intelligent damping elements of rotating systems using the physical properties of magneto-rheological fluids”.

References

- [1] Krutil, J., Pochylý, F., Fialová, S., Habán, V., The effects of a thin liquid layer on the hydrodynamic machine rotor, *International Journal of Mechanical, Aerospace, Industrial, Mechatronic and Manufacturing Engineering* 9 (5) (2015) 948-951.
- [2] Staubi, T., Bissing M., Numerically calculated rotor dynamic coefficients of a pump rotor side space, *Proceedings of the International Symposium on Stability Control of Rotating Machinery (ISCORMA)*, South Lake Tahoe, U.S.A., 2001.
- [3] Zagorul'ko, A., Gerasimiva, K., Altyncev, E., Numerical analysis of annular seals-bearings, *Proceedings of the 12th International Scientific and Engineering Conference HERVICON 2008*, Kielce-Przemysł, 2008, pp. 105-113. (in Russian)

Numerical solution of 3D flow through turbine cascade using modified EARSM model

J. Holman^a

^a*Faculty of Mechanical Engineering, CTU in Prague, Karlovo náměstí 13, 121 35 Praha 2, Czech Republic*

The article deals with the numerical simulation of turbulent flow of the compressible fluid through the TR-L-3 prismatic turbine cascade in the test section of the wind tunnel. The TR-L-3 turbine cascade is composed from prismatic extensions of rotor blade profiles (SE 1050, [1]) of the last stage of Škoda Power's steam turbine. The flow is influenced by the tunnel walls, where secondary flows coming from the development of the end-wall boundary layers cause additional losses and their non-trivial distribution [1].

Turbulent flow is modeled by the system of Reynolds averaged Navier-Stokes equations [5], which is closed by the explicit algebraic Reynolds stress model (EARSM) of Wallin and Johansson [4]. The EARSM model is based on the Kok's two-equation TNT¹ $k - \omega$ model. Closure model constants of the TNT model were modified especially for conjunction with the EARSM model constitutive relations [2]. The Navier-Stokes equations together with the model of turbulence are discretized by the finite volume method. Inviscid fluxes are approximated by the HLLC Riemann solver with piece-wise linear WENO reconstruction. Viscous fluxes are discretized by the central differencing with the aid of dual mesh. Resulting system of ordinary differential equations is then solved by the explicit two-stage TVD Runge-Kutta method with point implicit treatment of the source terms of turbulence model [2].

From Figs. 1 and 2 one can see very good qualitative agreement between 2D and 3D simulations. The energy losses were evaluated to be 2.76% in the case of 2D simulation and 3.12% in the symmetry plane ($z = 80$ mm) of 3D simulation (see Fig. 4). Figs. 3 and 4 shows three-dimensional character of the flow field. Moreover, distribution of energy losses is also strongly influenced by the inlet boundary conditions [1]. On Fig. 4 is clearly visible different position and magnitude of the local maximum of energy losses. The constant inlet velocity profile causes shift of the local maximum towards the wall and decrease of magnitude of energy losses compared to the formed inlet velocity profile. The results obtained using the EARSM model are in good agreement with the experiment. Furthermore, one can observe good agreement between above described in-house finite volume method solver and freely available software OpenFOAM which are completely different numerical solvers.

Acknowledgements

The work was supported by the Grant no. GAP101/12/1271 and Grant no. P101/10/1329 of the Grant Agency of Czech Republic.

¹TNT - Turbulent Non-Turbulent. The name is related to the analysis of the model near the outer edge of the boundary layer [3].

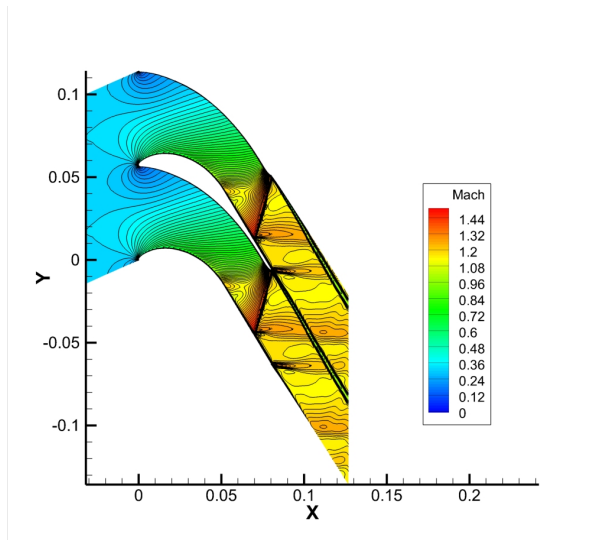


Fig. 1. 2D simulation

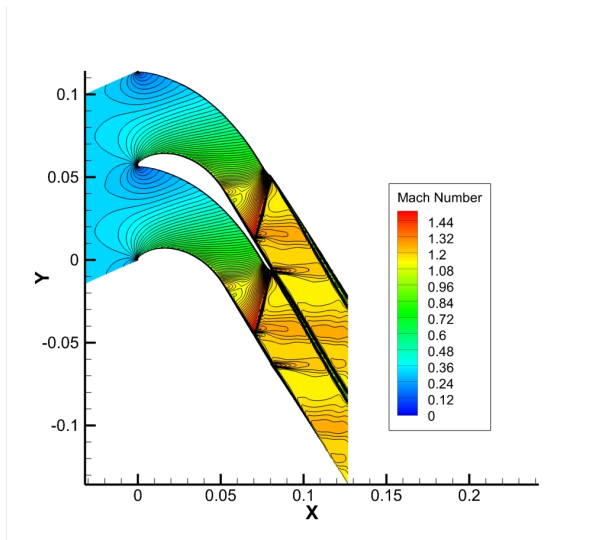


Fig. 2. 3D simulation, $z = 80$ mm

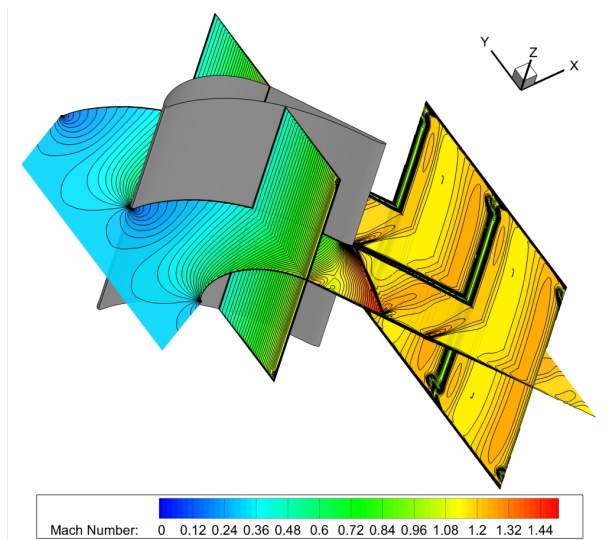


Fig. 3. 3D simulation

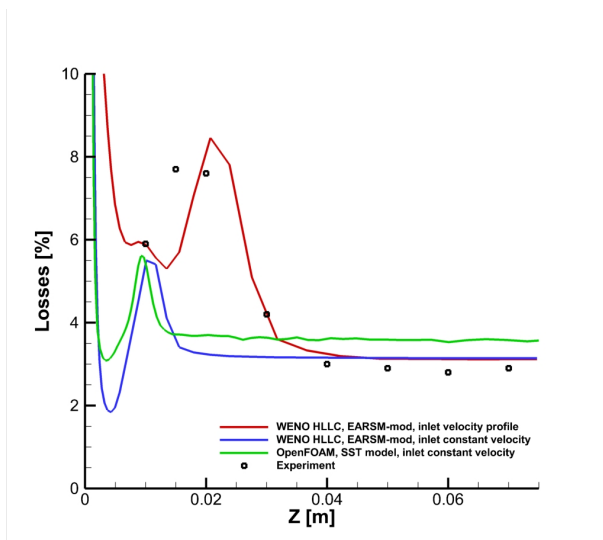


Fig. 4. Distribution of losses along the blade

References

- [1] Fürst, J., Luxa, M., Šimurda, D., The spanwise distributions of losses in prismatic turbine cascade with non-uniform inlet velocity profile, *Engineering Mechanics* 21 (2) (2014) 135-141.
- [2] Holman, J., Numerical solution of steady and unsteady turbulent flow, dissertation thesis, CTU in Prague, 2015. (in Czech)
- [3] Kok, J. C., Resolving the dependence on freestream values for $k - \omega$ turbulence model, *AIAA Journal* 38 (7) (2000) 1292-1295.
- [4] Wallin, S., Engineering turbulence modeling for CFD with focus on explicit algebraic Reynolds stress models, dissertation thesis, Royal Institute of Technology, 2000.
- [5] Wilcox, D. C., *Turbulence modeling for CFD*, DCW Industries, Inc., La Canada, California, 1994.

The use of the Chebyshev interpolation in elastodynamic problems

P. Hora^a

^a*Institute of Thermomechanics, Czech Academy of Sciences, Veleslavínova 11, 301 14 Plzeň, Czech Republic*

For the analytical solution of the thick bar impact problem it is needed to evaluate a complicated oscillating integrals for displacements and stresses. The integration along the dispersion curve is generally calculated by means of trapezoid or Simpson's rule numerical integration (i.e. methods with equally spaced points).

This dispersion relation $f(x, \gamma a)$ (see Fig. 1 (left)) is defined as

$$(2 - x^2)^2 J_0(\gamma a A) J_1(\gamma a B) + 4AB J_1(\gamma a A) J_0(\gamma a B) - \frac{2x^2}{\gamma a} A J_1(\gamma a A) J_1(\gamma a B) = 0,$$

where a is radius of the semi-infinite bar, γ is wavenumber, x is the ratio of the phase velocity and the shear wave velocity, κ means the ratio of the squares of the phase velocities for the bar's material, $A = \sqrt{\kappa x^2 - 1}$, $B = \sqrt{x^2 - 1}$ and J is the Bessel function of the first kind.

For the purpose of the speed up calculation, the dispersion curves are precalculated in equidistant points of γa .

The disadvantages of this process are: 1. impossibility to integrate from zero, 2. problematic choice of γa -step.

In order to remove the first restriction, another form of the dispersion relations is used. After making the substitution, $z = x\gamma a$, the dispersion relation $g(z, \gamma a)$ (see Fig. 1 (right)) is defined as

$$(2\gamma a^2 - z^2)^2 J_0(A) J_1(B) + 4\gamma a^2 AB J_1(A) J_0(B) - 2z^2 A J_1(A) J_1(B) = 0,$$

where $A = \sqrt{\kappa z^2 - \gamma a^2}$ and $B = \sqrt{z^2 - \gamma a^2}$.

In order to remove the second restriction, the integration method with unequally spaced points is used. For non-periodic functions, methods with unequally spaced points such as Gaussian quadrature and Clenshaw-Curtis quadrature are generally far more accurate. For using of these integration methods, the dispersion curves were approximated by the Chebyshev polynomials [2].

In Table 1 the properties of Chebyshev approximation for given curves are shown (vertical scale, total length of polynomial). For comparison, 100 curves for γa from 0.001 to 100 with step 0.001 take the 80MB file. 100 curves for γa from 0 to 100 created by the Chebyshev approximation take only the 1.3MB file.

While using the Gaussian or Clenshaw-Curtis quadrature, the calculation time has provided a 100x speedup over the original.

For numerical experiments were used MATLAB's toolbox CHEBFUN [1] and Julia's package ApproxFun [3].

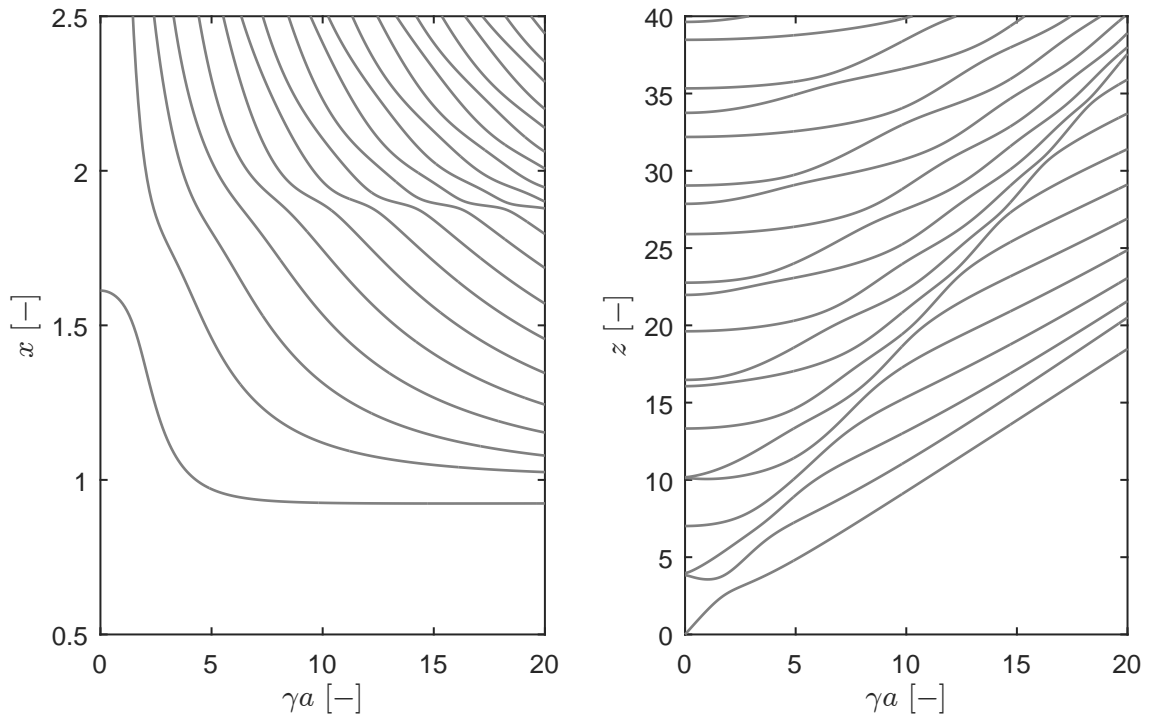


Fig. 1. Dispersion curves: $x - \gamma a$ form (left) and $z - \gamma a$ form (right)

Table 1. The Chebyshev approximation properties for any dispersion curves

Curve #	Vertical scale	Length (splitting=off)	Length (splitting=on)
1	93	396	168
2	100	454	218
3	100	455	209
10	100	1821	301
20	120	4226	597
30	140	6527	729

Acknowledgement

The work was supported by the institutional support RVO:61388998.

References

- [1] Driscoll, T.A., Hale, N., Trefethen, L.N., editors, Chebfun Guide, Pafnuty Publications, Oxford, 2014.
- [2] Snyder, M.A., Chebyshev methods in numerical approximation, Prentice-Hall, 1966.
- [3] <http://github.com/ApproxFun/ApproxFun.jl.git>

Experimental investigation of phonation using artificial models of human vocal folds and vocal tract

J. Horáček^a, V. Radolf^a, V. Bula^a, J. Košina^a, T. Vampola^b, M. Dušková^c

^a Institute of Thermomechanics ASCR, Dolejškova 1402/5, 182 00 Prague, Czech Republic

^b CTU Faculty of Mechanical Engineering Dept. of Mechanics, Biomechanics and Mechatronics, Technická 4, Prague, Czech Republic

^c Institute of Macromolecular Chemistry, ASCR, Heyrovského nám. 1888/2, Prague, Czech Republic

The contribution presents results of in vitro measurements of voicing performed on originally developed models of the human vocal folds and vocal tract. The designed models are based on CT and MRI measurements of human subject during phonation. The measured phonation (aerodynamic, vibration and acoustic) characteristics are comparable with values found in humans; however, obtaining reliably some of such characteristics, like for example pulsations of air pressure in subglottal, intraglottal and supraglottal spaces, from in vivo measurements is usually very problematic or nearly impossible.

Comparing to the previous studies [1, 2] the measurements were performed with an innovative three layer vocal folds model. Silicon wedge modelling a vocal fold body was added inside the vocal fold reducing the space of the liquid layer under the silicon cover. This modification substantially reduced the airflow rate of phonation onset below $Q=0.1$ l/s and the fundamental phonation frequency below $F_0=90$ Hz. Installation of pressure transducers in the vocal tract cavity enabled to obtain more information on magnitudes of pressure fluctuations in laryngeal and oral parts of the vocal tract. Usage of the high-speed camera enabled to study vibration amplitudes of the vocal folds and to determine the opening and closing phases related to the acoustic and pressure data measured in time domain, see Figs. 1 and 2.

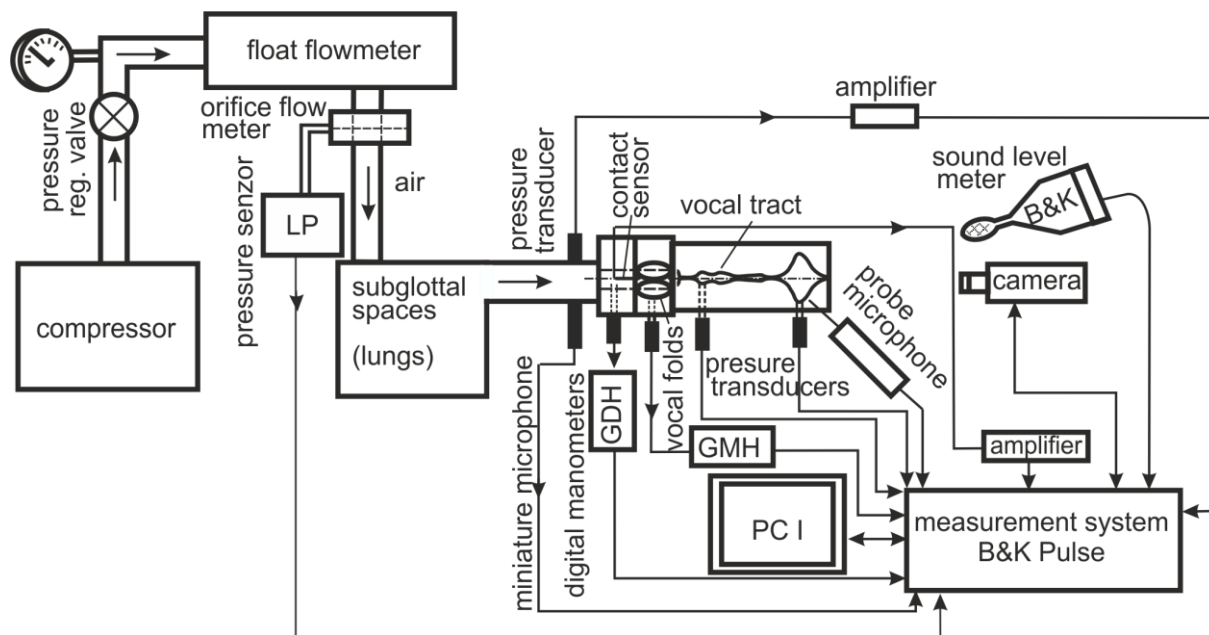


Fig. 1. Scheme of the measurement set up

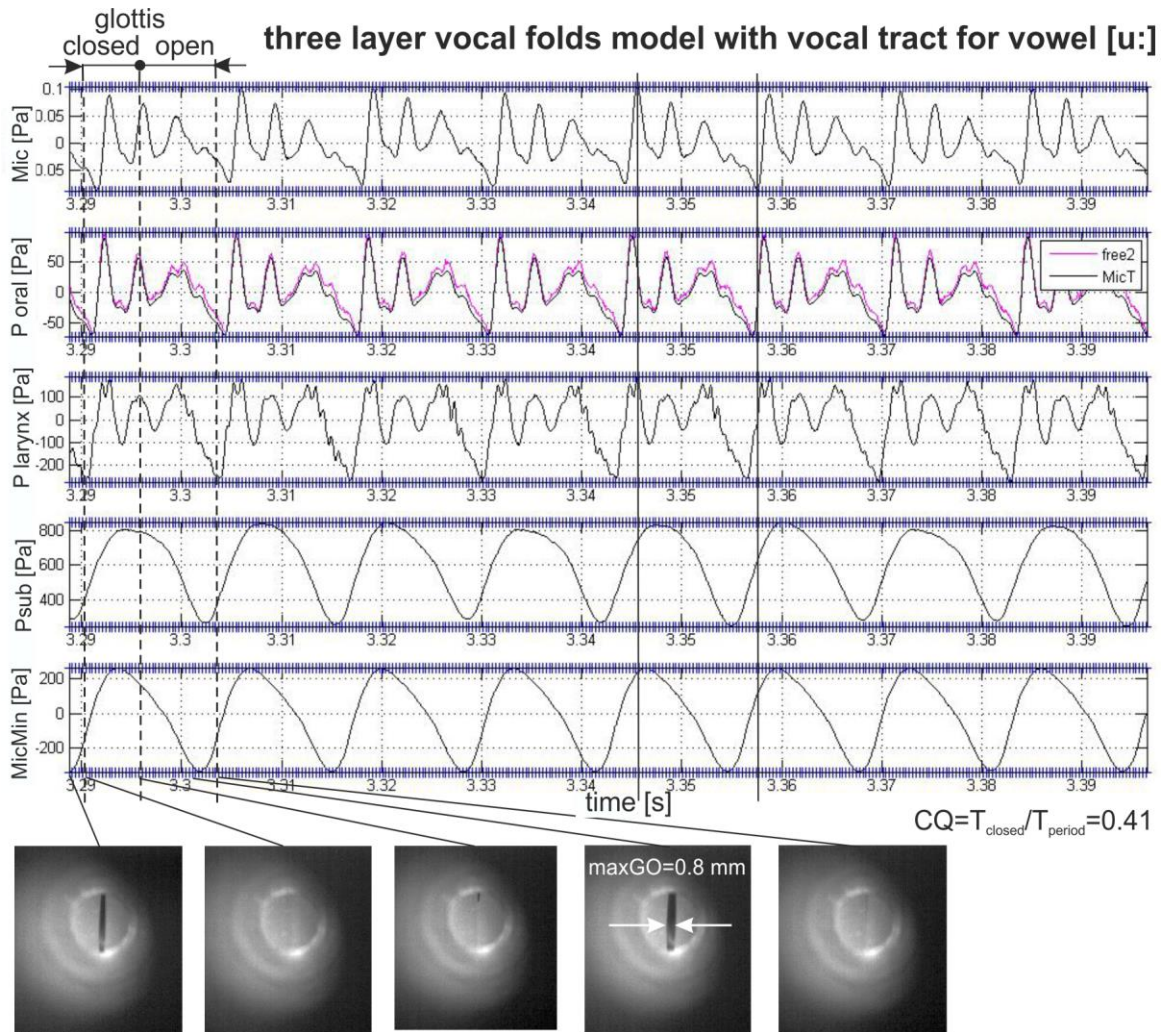


Fig. 2. Example of the measured pressure signals and snapshots of the vocal folds vibration ($Q=0.04$ l/s)

Fig. 2 shows typical signals of the subglottal pressure ($MicMin$, P_{sub}) recorded just below the vocal folds, the laryngeal pressure just above the vocal folds (P_{larynx}), the oral pressure in the mouth cavity (P_{oral}) and sound signal outside the vocal tract together with 5 images taken during 1 period of the vocal folds vibration. The glottis was closed for 41% of the time period followed by the maximum of the glottis opening $maxGO=8$ mm. Maximum peaks of the generated sound level (Mic) appear just after the glottis closure. The pressure waveforms inside and outside the vocal tract (P_{larynx} , P_{oral} , Mic) are similar, only slightly time shifted due to the limited sound propagation velocity and containing resonance frequencies (formants) of the vocal tract model for vowel [u:].

Acknowledgements

The work has been supported by the grant project GACR No 16-01246S.

References

- [1] Horáček, J., Bula, V., Košina, J., Radolf, V., Phonation characteristics of self-oscillating vocal folds replica with and without the model of the human vocal tract, Proceedings of Engineering Mechanics 2016, Svratka, Praha: Ústav termomechaniky AV ČR, 2016, pp. 214-217.
- [2] Horáček, J., Vampola, T., Bula, V., Radolf, V., Dušková, M., Experimental investigation of airflow, acoustic and vibration characteristics of a liquid filled self-oscillating vocal folds model, Flow-Induced Vibration & Noise, FIV 2016. Delft: TNO, 2016, pp. 23-30.

Vibration analysis of visco-elastically coupled beams

S. Hračov^a, J. Náprstek^a

^a*Institute of Theoretical and Applied Mechanics, ASCR v.v.i., Prosecká 76, CZ-190 00 Praha, Czech Republic*

The paper presents a dynamic analysis of two parallel beams with continuously distributed parameters that are interconnected by a massless visco-elastic layer. This system can be applicable for suppressing the excessive vibrations of the buildings [1, 2] as well as the towers, the chimneys and the pipelines. It can be also used in case of dynamically sensitive details of various industrial structures. The vibration energy of the primary beam is absorbed by an additional system consisting of the secondary beam and the interlayer that works as a dynamic damper. The equations of motion of the complete system can be written in the form

$$\begin{aligned}
 EJ_1 u_1'''' + b_1 \dot{u}_1 + b(\dot{u}_1 - \dot{u}_2) + c(u_1 - u_2) + \mu_1 \ddot{u}_1 &= f(x, t), \\
 k_{EJ} EJ_1 u_2'''' + k_b b_1 \dot{u}_2 + b(\dot{u}_2 - \dot{u}_1) + c(u_2 - u_1) + k_\mu \mu_1 \ddot{u}_2 &= 0.
 \end{aligned} \tag{1}$$

The beams of Euler-Bernoulli type with prismatic cross sections are assumed. The geometric and physical parameters of the beams and the interlayer are considered constant independent on the length coordinate. The following nomenclature in Eq. (1) is adopted: EJ_i - bending stiffness of i -th beam ($i = 1, 2$), μ_i - mass/length of the adequate beam, b_i , b - viscous damping/length of adequate beam or interlayer respectively, c - normal stiffness of the interlayer/length, $f(x, t)$ - harmonic excitation force/length. Furthermore, the following ratios of the structural parameters are used: $k_{EJ} = EJ_2/EJ_1$, $k_b = b_2/b_1$, $k_\mu = \mu_2/\mu_1$. The detailed study of the system (1) regardless the boundary conditions can be found in [3]. In this paper, the main focus lies in the analysis of the system of two coaxial cylindrical consoles, see Fig. 1.

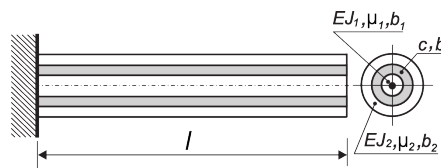


Fig. 1. Scheme of the cantilever beam pair coupled by visco-elastic interlayer

As only stationary processes are investigated in the meaning of eigenvibration or forced vibration due to stationary excitation in the form $f(x, t) = F(x)e^{i\omega t}$, then space and time coordinates in functions u_1 , u_2 can be separated as $u_j(x, t) = v_j(x) \cdot e^{i\omega t}$, $j = 1, 2$. The solution of the beam pair vibration is determined analytically for all frequency ranges of the excitation frequency ω . The form of the solution depends on the relation of the excitation frequency ω to frequency $\omega_b^2 = c(1 + k_\mu)/\mu_1$. From the practical point of view the most important frequency interval represents the frequencies $\omega > \omega_b$. In this case, the eigenfrequencies of the system can be determined from the characteristic equation

$$\eta \frac{\mu_1^2}{(EJ_1)^2} \omega^4 - \left[\rho_j^4 (\eta + 1) \frac{\mu_1}{EJ_1} + c \frac{\mu_1}{(EJ_1)^2} \left(\eta + \frac{1}{k_{EJ}} \right) \right] \omega^2 + \rho_j^8 + \rho_j^4 \frac{c}{EJ_1} \left(1 + \frac{1}{k_{EJ}} \right) = 0, \tag{2}$$

where $\eta = k_\mu/k_{EJ}$ and ρ_j is the j -th root of the equation

$$1 + \cos \rho l \cdot \cosh \rho l = 0. \quad (3)$$

Two positive real roots of the characteristic equation (2) corresponding to each ρ_j represent the eigenfrequencies of the system $\omega_{j,(1,2)}$. The eigenvectors related to this pair of eigenfrequencies can be expressed as

$$\begin{vmatrix} v_{1,j,(i)}(x) \\ v_{2,j,(i)}(x) \end{vmatrix} = \begin{vmatrix} V_{1,j,(i)} \\ V_{2,j,(i)} \end{vmatrix} \cdot \left[\cos \rho_j x - \cosh \rho_j x + C(\sin \rho_j x - \sinh \rho_j x) \right], \quad i = 1, 2, \quad (4)$$

where $C = \frac{\sin \rho_j l - \sinh \rho_j l}{\cos \rho_j l + \cosh \rho_j l}$.

The shapes of both coupled eigenvectors are similar, but the eigenvectors differ in the ratio between the corresponding coordinates related to particular beams i.e. in the ratio between elements of the vector V

$$\frac{V_{1,j,(i)}}{V_{2,j,(i)}} = 1 + \frac{EJ_1 k_{EJ}}{c} \left[\rho_j^4 - \eta \frac{\mu_1}{EJ_1} \omega_{j,(i)}^2 \right], \quad i = 1, 2. \quad (5)$$

The special combination of structural parameters, $\eta = 1$, allows to express eigenfrequencies $\omega_{j,(1,2)}$ as well as ratios (5) explicitly in the following favourable forms

$$\omega_{j,(1)}^2 = \frac{\rho_j^4 EJ_1}{\mu_1}, \quad \frac{V_{1,j,(1)}}{V_{2,j,(1)}} = 1, \quad \omega_{j,(2)}^2 = \frac{\rho_j^4 EJ_1 + c \left(1 + \frac{1}{k_{EJ}}\right)}{\mu_1}, \quad \frac{V_{1,j,(2)}}{V_{2,j,(2)}} = -k_{EJ}. \quad (6)$$

The first eigenfrequency is independent from the interlayer stiffness and identical with those of the individual beams. The equality between elements of vector V leads to the same amplitude as well as the phase of the corresponding points on both beams during the free vibration. The second eigenfrequency is equal to the eigenfrequency of the system represented by individual cantilever beam supported by an elastic layer, the stiffness of which is a function of the stiffness of the interlayer and of the ratio of the stiffness of the beams. The second eigenvector is also composed from the modes of individual beams. The phase between corresponding points on both beams is opposite and equal to a ratio of the stiffness of the beams.

The paper also presents a detail analysis of the forced vibration. The dynamic behaviour of the system is investigated parametrically to cover all possible effects of individual subsystems. Damping effectiveness is also analysed for several values of viscosity of the interlayer and damping of the particular beams. The recommendations and limitations for the application of the system are presented and discussed.

Acknowledgement

The kind support of the Czech Science Foundation project No. 15-01035S and of the RVO 68378297 institutional support are gratefully acknowledged.

References

- [1] Fu, T.S., Double skin facades as mass dampers, Proceedings of American Control Conference, ACC, Washington D.C., 2013, pp. 4749-4753.
- [2] Kyoung, S.M., Structural design of double skin facades as damping devices for tall buildings, Procedia Engineering 14 (2011) 1351-1358.
- [3] Náprstek, J., Hračov, S., Dynamics of beam pair coupled by visco-elastic interlayer, Applied and Computational Mechanics 9 (2015) 127-140.

Search algorithm for centerlines inside complex branched channels

P. Hynek ^a, T. Vampola ^a

^a Department of Mechanics, Biomechanics and Mechatronics, Faculty of Mechanical Engineering, Czech Technical University in Prague, Technická 4, Praha 6, Czech Republic

This contribution concerns itself with the algorithm for the search of centerlines of the complex branched channel, which is describe with the help of a surface mesh. The final centerlines are used as base for the computational model, which can be based on the finite element method (FEM), or finite volume method (FVM). A 3D model of a human lungs, which contain lung lobes, trachea, bronchi and bronchioles is used illustration in this case. The surface mesh is obtained by magnetic resonance imaging (MRI) and is formed by 0,5 mil. elements, as shown in Fig. 1.

The surface mesh must be formed by triangular elements \mathbf{E} (total amount $n\mathbf{E}$) and a corresponding number of \mathbf{N} nodes (number $n\mathbf{n}$). Before starting the search algorithm, it is necessary to set the input parameters that may affect precision of the final centerlines and total calculation time. The input parameters (along with a brief description) can be found in Table 1.

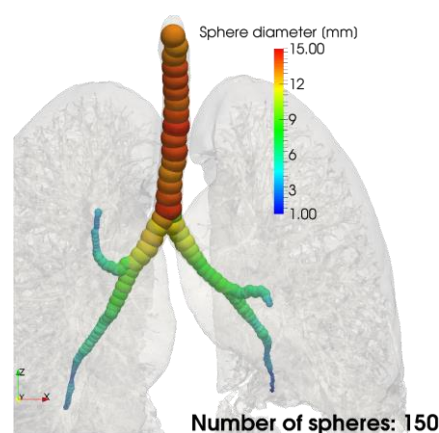


Fig. 1. Surface mesh of respiratory tract of a human

Table 1. Input (user) parameters for searching algorithm

C_0	Origin of the channel (first sphere center)
v_0	Initial direction (vector) for the centerline search
R	Number of discrete points on the sphere surface [2] (Fig. 2)
K_{max}, K_{min}	Ratio coefficient max. a min. for new sphere radius
D_{max}	The largest possible displacement of the sphere center
α_{max}	The largest possible angular deviation

The searching algorithm is created in the MATLAB enviroment using the optimization toolbox functions [1].

At the start the positions of the center of gravity \mathbf{T}_E for each element of surface mesh \mathbf{E} is calculated and using optimization functions the maximal diameter d_i for the placed sphere \mathbf{B}_i is found. Optimization parameters are the displacements $[d_x, d_y, d_z]$ of the sphere center in the individual direction of the global coordinate system. The requirements for the target function are:

$$F_c = \min \left(\frac{1}{d_i} \right), \quad d_i = 2 \cdot (\min(\overline{C_{iNew} T_E})), \quad C_{iNew} = C_i + [d_x, d_y, d_z],$$

$$D_{max} \geq \sqrt{(d_x^2 + d_y^2 + d_z^2)}$$

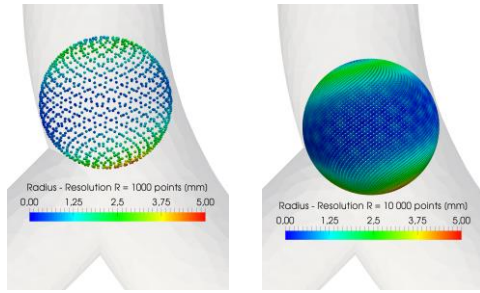


Fig. 2. Resolution of the sphere comparison

On the surface of the inscribed sphere \mathbf{B}_i with the center point \mathbf{C}_{iNew} , the diameter \mathbf{d}_i is created and the final number of discrete points determined (number \mathbf{R}) [2] (Fig. 2) and for each set point a maximal sphere diameter is found. The largest of these represents the potential center of the newly placed \mathbf{B}_{i+1} at the coordinates \mathbf{C}_{i+1} .

For maintaining of the fluency and direction of the centerline, it is necessary to control the angle of deviation α_i between the lines drawn between the centers inscribed spheres \mathbf{B}_{i-1} , \mathbf{B}_i and \mathbf{B}_{i+1} . This angle size can not exceed the maximal value α_{Max} defined by the user. The size of the placed sphere must be controlled by two coefficients, \mathbf{K}_{min} and \mathbf{K}_{max} . Both parameters are dependant on the sphere diameters (the percentage of deviation) and the distance from the beginning of the channel. This check is advantageous in the case, when the channel expands out into free space (e.g. bronchioles to the lung lobes in our case of surface mesh). If the inscribed sphere does not satisfy these conditions, this leads to the termination of the search in the current branch and a gradual search of the branch will start. Assuming that each inscribed sphere can be branched only once.

The following figures show the simply branched channel, which was used for debugging the searching algorithm as described above. The first picture shows the results of the branching, where the maximal distance (in defined direction) from a specific inscribed sphere to the surface mesh of the channel is calculated. The second picture shows all the inscribed spheres and the third show the final centerline of the branched channel.

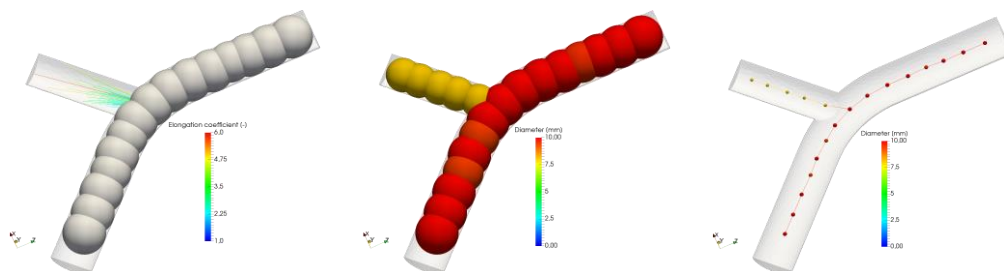


Fig. 3. Principle of centerline search algorithm. Branching (left), placed sphere (center), centerline (right)

The introduced algorithm for centerlines of branched channel searching is very robust and can be used on complex branched channels (e.g. human lungs, Fig. 1). In the case, when frequent change of the cross section and branching occurs, it is recommended to use a finer surface mesh. The reduction of the number of elements leads to the loss of geometrical information and it can lead to problems with searching the branch location.

Acknowledgements

The research is supported by the Grant Agency of the Czech Republic in project No 16-01246S Computational and experimental modelling of self-induced vibrations of vocal folds and the influence of their impairments on the human voice.

References

- [1] MATLAB and Optimization Toolbox Release 2015a, The MathWorks, Inc., Natick, Massachusetts, United States.
- [2] Swinbank, R., Purser, J., Fibonacci grids: A novel approach to global modelling, Quarterly Journal of the Royal Meteorological Society 132 (619B) (2006) 1769-1793.

Stress – strain analysis of cranial implant

J. Chamrad^a, P. Marcián^a, L. Borák^a, J. Wolff^b

^a Institute of Solid Mechanics, Mechatronics and Biomechanics, Faculty of Mechanical Engineering, Brno University of Technology, Technická 2896/2, 616 69 Brno, Czech Republic

^b Department of Oral and Maxillofacial Surgery, VU University Medical Center Amsterdam, Amsterdam; NL

Nowadays society is usually in the rush. People are using bicycles, motorbikes, scooters, in-line skates or doing adrenalin sports. It increases the number of accidents and also collisions with people, who are walking on the side of the roads.

These accidents, related to cycling or in-line skating are very dangerous, because in many cases head injury may occur (although the person is using helmet).

Skull consists of 28 bones and provides protection for the most important organ in the entire human body, brain. In some cases, when one of the bones is broken, is of vital importance to replace bone with implant (as shown in Fig. 1).

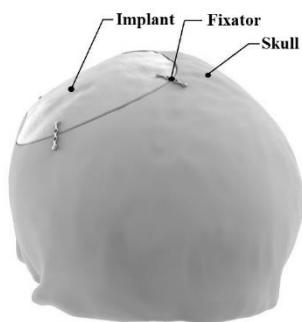


Fig. 1. System Skull – implant – fixators

Mechanical behavior of cranial implant is an important factor, which has an impact on its function. The function is influenced by external load from environment and by intracranial pressure. These loads can cause movement of implant and harm of bone tissue. An assessment of mechanical behavior may be determined either by experimental or computational modeling approach [2]. A computational approach is more effective in Biomechanics, because it provides us more opportunities for analysis. The most common method is Finite Element Method (FEM). All calculations were realized in software ANSYS 16.2.

The aim of this study is to assess different thicknesses of implants made from different materials using different amount of fixators.

Computational model can be divided into several models (model of geometry, materials, boundaries and loads) [2]. Model of geometry requires several steps. Data from Computed Tomography (CT) are transformed and adjusted in software STL Model Creator and saved as .stl format [4]. Than using CAD software, volume model is prepared and other modifications (e. g. hole for implant) is done. This part is done twice, for skull and for spongy part. 3 different thicknesses fixed by 3, 4 and 5 fixators were solved.

Submodels of materials are defined as homogeneous isotropic linear elastic materials (Hook's materials), which are defined by two parameters Young's modulus and Poisson ratio [4]. 3 different materials were analyzed (PMMA, PEEK and Titanium alloy Ti6Al4V).

Model of boundary conditions consists of loads, which interact on skull in normal condition and don't cause any effect to skull (not defected one). A force (50 N) corresponds to an approximate weight of the head (~5 kg [4]). In addition, the bone and implant were loaded with an ICP (4 kPa [1]). The models were fixed at the bottom side of the skull in the region where the spine is assumed.

Based on FEA of this specific implant (shown in Fig. 1) some features were observed:

- the highest stress in implant is in holes for screws, which are significant stress concentrators;
- the lowest equivalent (von Mises) stress is in implant, made from PMMA, the highest is in implant from Ti6Al4V for all thicknesses (as shown in Fig. 2);
- higher number of fixators significantly decreases loading of a bone tissue.

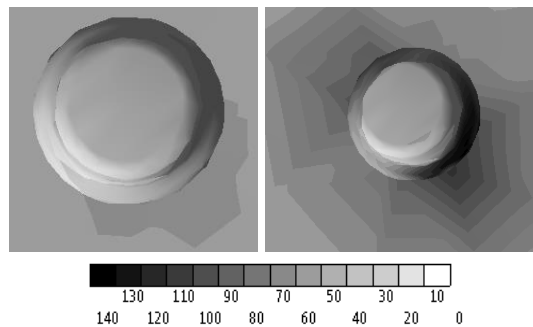


Fig. 2. Equivalent stress in PMMA (left) and Ti6Al4V (right) implant

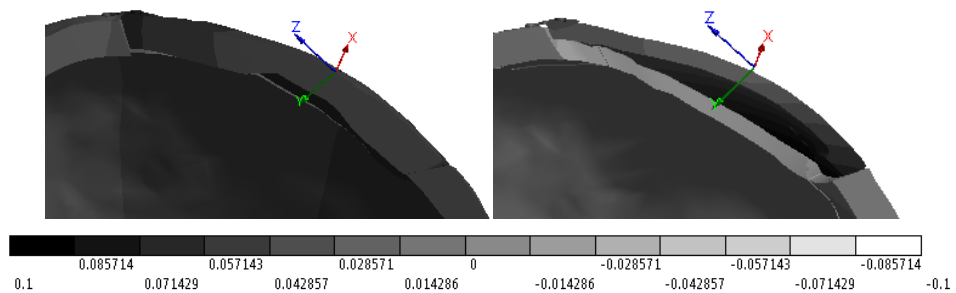


Fig. 3. Directional deformation for PMMA implant fixed by 3 (left) and 5 (right) fixators

The results of the study confirm that higher stresses are in materials with higher ultimate tensile strength. Higher directional deformation occurs in the position of loading force while using more fixators, because more fixators don't enable implant to move as a unit (maximum directional deformation is lower for more fixators – as shown in Fig. 3). Using more fixators for large implants decrease the value of HMH strain in skull under the threshold 0.003 (Frost's Mechanostat hypothesis [3]).

Acknowledgements

The research was supported by the Czech Science Foundation by grant No. GA16-08944S.

References

- [1] Czosnyka, M., Pickard, J.D., Monitoring and interpretation of intracranial pressure, *Journal of Neurology, Neurosurgery and Psychiatry* 75 (6) (2004) 813–821.
- [2] Janíček, P., Systémové pojetí vybraných oborů techniky, Akademické nakladatelství CERM, Brno, 2007. (in Czech)
- [3] Jee, W.S., Principles in bone physiology, Review Article, *Journal of musculoskeletal & neuronal interactions* 1 (2000) 11-13.
- [4] Ridwan-Pramana, A., Marcián, P., Borák, L., Narra, N., Forouzanfar, T., Wolff, J., Structural and mechanical implications of PMMA implant shape and interface geometry in cranioplasty – a finite element study, *Journal of Cranio-Maxillofacial Surgery* 44 (1) (2016) 34-44.

Creep-fatigue behaviour of steel P91

J. Janoušek ^a, S. Holmström ^b, R. Pohja ^c, U. Führer ^d

^a Research Centre Rez, Hlavní 130, 250 68 Husinec-Řež, Czech Republic

^b Joint Research Centre, Westerduinweg 3, NL-1755 LE Petten, The Netherlands

^c VTT Technical Research Centre of Finland Ltd, Vuorimiehentie 3, FI-02044, Espoo, Finland

^d Karlsruhe Institute of Technology, Institute for Applied Materials, Eggenstein-Leopoldshafen, Germany

This contribution corresponds with the round robin experiments which have been performed within European FP7 project MatISSE. The experimental programme deals with the issue of basic understanding and prediction of cyclic softening in tempered martensitic steels such as P91, which is a frequent choice for high temperature/pressure piping and heat exchangers in steam-based power plants [3]. This material together with steel 316L and 316L(N) are the main candidates for the construction of the planned research reactor concepts Myrrha, Astrid, Alfred and Allegro. The experiments are immensely important for validation of the models especially for effect of hold time on cyclic softening and hence on the damage behavior.

The supporting test effort will be focused on strain controlled low cycle fatigue tests with different tension, compression and tension-compression hold times. Especially long hold times are targeted. The evolving change of time-dependent inelastic strains (relaxed strain) during these tests is related to softening and the corresponding creep behavior (strain rates) and creep-fatigue life is directly affected [4, 5].

A lot of results were presented in [1] where the study was investigated by uniaxial low cycle fatigue tests with no hold time and compressive/tensile hold time 1 minute, 10 minutes, 1 hour and 3 hours at 550 °C for strain range $\Delta\varepsilon = 0.6\%$ up to 1.5%. Also the batch of material is different as it is possible to see chemical composition in [1] and [2]. The results are depicted in Fig. 1. The strain rate in cycling is 6 % per minute.

As it was describe in [2] the type of tests which are performed in laboratories of Research Centre Rez in Pilsen have symmetrical reversed strain i.e. strain ratio $R = -1$. Test matrix

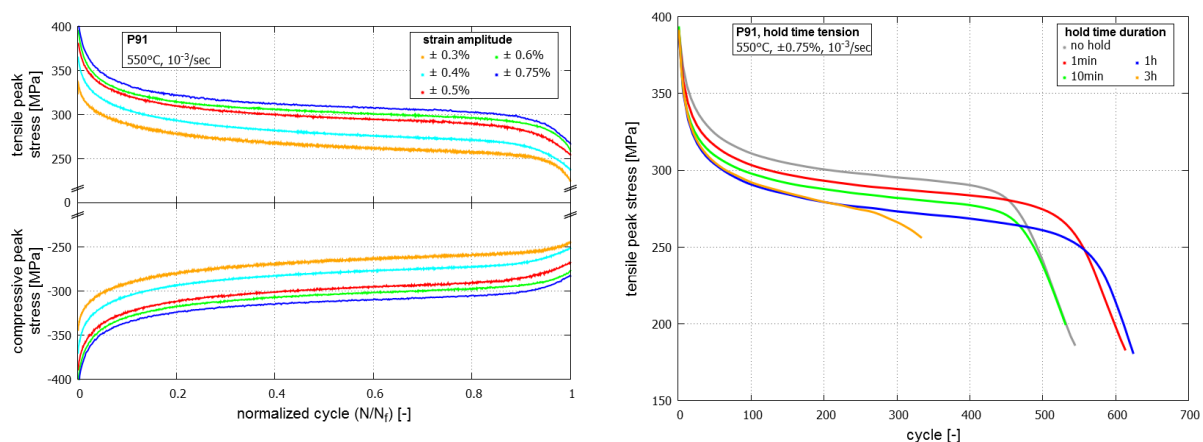


Fig. 1. Cyclic softening of P91 in LCF reference tests with strain range $\Delta\varepsilon = 0.6\%$ up to 1.5%. without hold time and for test with $\Delta\varepsilon = 1.5\%$ with tensile 1 minute, 10 minutes, 1 hour and 3 hours hold time at 550 °C

corresponds with strain range $\Delta\varepsilon = 0.5\%$, 0.7% and 0.9% with a tensile hold time 1 hour and 12 hours in every cycle. The stopped condition is after 1000 cycles, max 1500 cycles, alternatively after 50 cycles (for 12 hours hold time) or if a failure will occur. The cycle has a shape of triangle and temperature for all tests is $600\text{ }^{\circ}\text{C}$.

The first experiment was for strain range $\Delta\varepsilon = 0.5\%$ with 1 hour tensile hold time. Test was performed on electromechanical creep testing machine Kappa SS-CF and it was interrupted in 73 cycle due to bad tuning (P I values) and the testing system became unstable. Reached test results are shown in Fig. 2. The experimental programme was extended for servohydraulic testing machine.

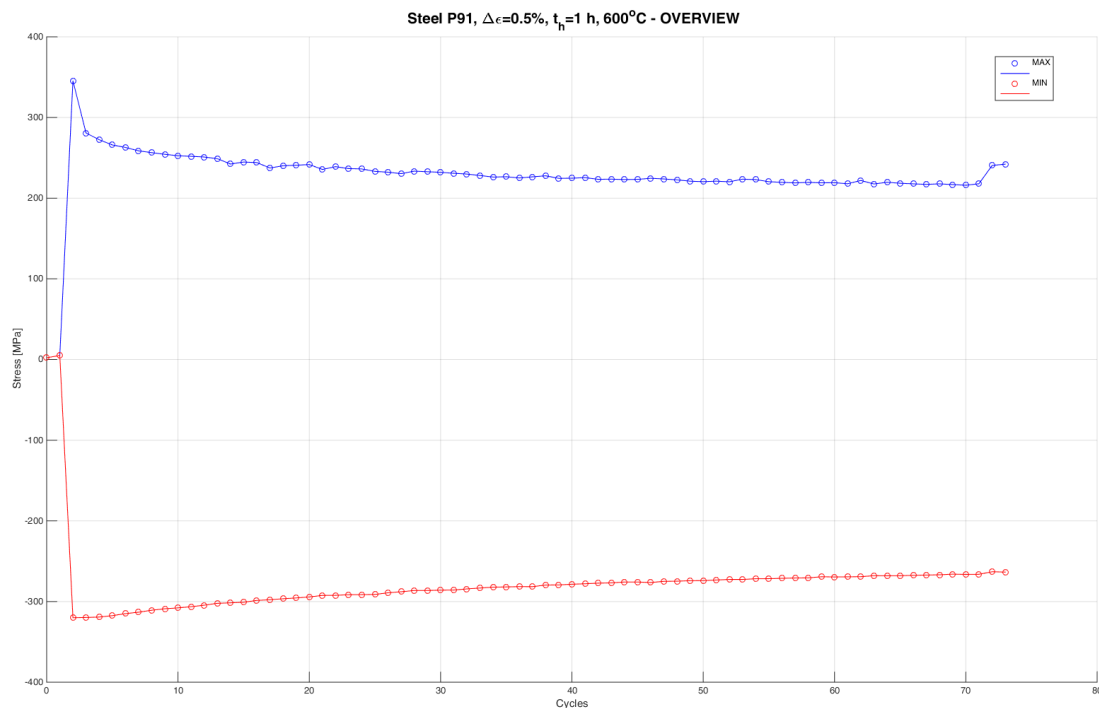


Fig. 2. Cyclic softening of P91 in LCF with strain range $\Delta\varepsilon = 0.5\%$ with tensile 1 hour hold time at $600\text{ }^{\circ}\text{C}$ – stop after 73 cycles by unstable testing system

Acknowledgements

This research work was financially supported by the Ministry of Education, Youth and Sport Czech Republic Project LQ1603 (Research for SUSEN). This work has been performed within the SUSEN Project in the framework of the European Regional Development Fund (ERDF) in the project CZ.1.05/2.1.00/03.0108 and MatISSE project, contract nr. 604862.

References

- [1] Führer, U., Aktaa, J., Creep-fatigue interaction and cyclic softening of ferritic-martensitic steels, Baltica X, Finland, 2016.
- [2] Janoušek, J., Holmström, S., Pohja, R., Cyclic softening of tempered ferritic-martensitic steel P91, Proceeding of the 31st Conference with International Participation Computational Mechanics 2015, Špičák, Czech Republic, 2015.
- [3] Swindeman, R.W., Santella, M.L., Maziasz, P.J., Roberts, B.W., Coleman, K, Issues in replacing Cr–Mo steels and stainless steels with 9Cr–1Mo–V steel, International Journal of Pressure Vessels and Piping 81 (2004) 507–512.
- [4] ASTM E606-92, Standard practice for strain-controlled fatigue testing.
- [5] ASTM E2714 – 13, Standard test method for creep-fatigue testing.

Finite element analysis of supracondylar periprosthetic femoral fracture treatment

M. Jansová^a, T. Malotín^b, J. Křen^a, P. Votápek^c, L. Lobovský^a, L. Hynčík^d

^aNTIS - New Technologies for the Information Society, Faculty of Applied Sciences, University of West Bohemia, Univerzitní 8, 306 14 Plzeň, Czech Republic

^bDepartment of Orthopaedics and Traumatology, Faculty of Medicine of Charles University and Faculty Hospital in Plzeň, alej Svobody 80, 304 60 Plzeň, Czech Republic

^cDepartment of Machine Design, Faculty of Mechanical Engineering, University of West Bohemia, Univerzitní 8, 306 14 Plzeň, Czech Republic

^dNew Technologies – Research Centre, University of West Bohemia, Univerzitní 8, 306 14 Plzeň, Czech Republic

An extra-articular fracture of distal femur is one of the less frequent complications following a total knee arthroplasty (TKA). This study deals with a simple extra-articular fracture (A1 according to Schewring and Meggitt [3]). There are several types of implants used by orthopedic surgeons for treatment of this type of fracture. In this study we compare a response under load for a distal femoral nail (DFN), a dynamic condylar screw (DCS) and an angled blade plate (ABP).

The finite element mesh of the model of human femur is based on model from Hynčík and Křen [2]. In order to obtain more biofidelic results the compact bone is modelled by 3D mesh instead of its simplification by one layer of 2D mesh. A 2mm wide gap in the femur models the A1 fracture (Fig. 1). This gap is filled in by 3D elements that simulate a partially healed fracture with a callus. The models of the TKA, the nail and the plates are based on a laser scan. The simplified models of a screw and a spiral blade are taken from Číhalová et al. [1]. The femoral condyles are cut according to the TKA placement. The created models with the placement of the DFN, the DCS and the ABP implants are shown in Fig. 1.

The material parameters of bones were obtained from available literature, the callus has material properties of a cartilage [4], the DFN is made of titanium alloy and the DCS and the ABP are made of steel.

A rigid body was formed at the surface of the femoral head. A force corresponding to the body mass of 70 kg was applied on its centre of gravity in a direction of mechanical axis and all other degrees of freedom were fixed. The distal part of the femoral component was fixed in all degrees of freedom.

The von Mises stress distribution in the implant and the displacement of femur in all three main directions were analysed for all three implants.

In case of the DFN there are no significant stress changes in the screws and an increased stress in the middle of the spiral blade where it is in contact with the nail. In the nail, there are three locations of higher stress values: the hole for the distal screw, the hole for the spiral blade and an area around the fracture. The latter one could be caused by the fact that it is also the narrowing of the nail. The displacement of femur in all axes shows that its mid-shaft bends laterally and ventrally.

Von Mises stress in the DCS implant reaches the highest values in the areas of the plate in contact with the screws whereas in the ABP it is the part between the first and the sixth hole from the distal end of the plate. Both for the DCS and the ABP the femoral mid-shaft bends

laterally and the part of femur just above the fracture moves ventrally as well as the proximal end of the plates of the DCS and the ABP implant. The whole femur above the fracture moves distally, compressing the callus.

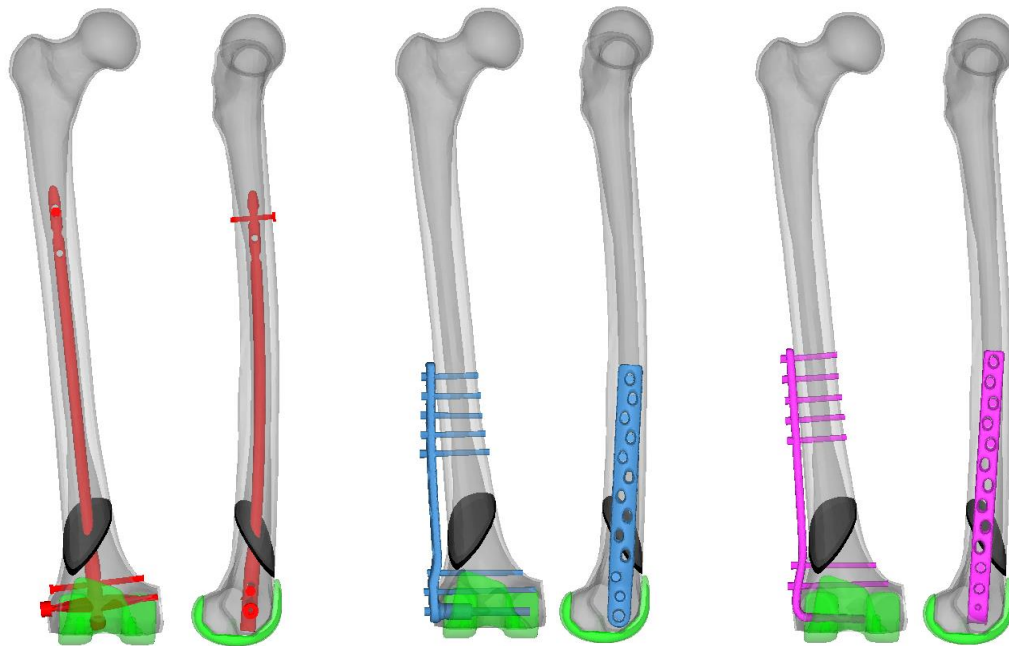


Fig. 1. The frontal (left) and lateral (right) view of the model of femur with the TKA (green), the callus in the area of an A1 fracture (black) and the implants: DFN (red), DCS (blue) and ABP (pink)

The response of the femur and the DFN, the DCS and the ABP implants under load was assessed by simulations using a finite element model of femur with an implemented TKA and a partially healed A1 fracture of the distal femur with a callus. The load during standing on one foot was imposed on the femoral head. The results show that the DCS and the ABP differ mainly in the von Mises stress distribution in the plate. The most significant difference between the model with the DFN and the other two plate-type models is in the displacement in the sagittal plane.

Acknowledgements

This study was supported by the project LO1506 of the Czech Ministry of Education, Youth and Sports and by projects SGS-2016-012 and SGS-2016-059 of the University of West Bohemia.

References

- [1] Číhalová, L., Křen, J., Matějka, J., Koudela, K., FE model of metaphyseal wedge fracture fixation in extra-articular part of distal femur, *Modelling and optimization of physical systems* 8 (2009) 11-16.
- [2] Křen, J., Hynčík, L., Stability of proximal femur nail fixating per-trochanteric fracture, *Proceeding of Computational Mechanics*, 2002, pp. 219-224.
- [3] Schewring, D.J., Meggitt, B.F., Fracture of the distal femur treated with the AO dynamic condylar screw, *Journal of bone and joint surgery* 74 (1) (1992) 122-125.
- [4] Wehner, T., Steiner, M., Ignatius, A., Claes, L., Prediction of the time course of callus stiffness as a function of mechanical parameters in experimental rat fracture healing studies-a numerical study, *PLoS One* 9:e115695, 2014, doi:10.1371/journal.pone.0115695.

Frame elements with embedded discontinuities for modelling hinges in reinforced concrete prismatic elements

G. Juárez-Luna ^a, E. Tenorio Montero ^{a,b}

^a Departamento de Materiales, Universidad Autónoma Metropolitana, San Pablo No. 180, Col. Azcapotzalco, 02200 México
^b Dirección General de Ingeniería y Arquitectura, Universidad Tecnológica de Panamá, Avenida Universidad Tecnológica de Panamá, Campus Metropolitano Víctor Levi Sasso, Panamá, Ciudad de Panamá

Frame elements with embedded discontinuities are formulated for modelling the development of hinges. In these elements, damage is modelled as the development of hinges with jumps in the axial displacement $[[u]]$, rotation $[[\theta]]$, transverse displacement $[[w]]$ or their combinations, as shown in Fig. 1. These finite elements were assigned with constitutive models to include the capacity of the flexural moment, shear force and normal force, whose formulations are based on damage mechanics theory and on experimental test reported in the literature, including the constitutive behaviour of the reinforced concrete. The finite elements and the constitutive models were implemented in a finite element program FEAP (Taylor 2008).

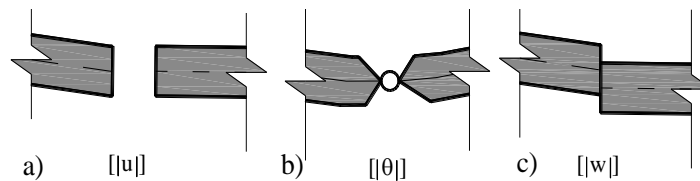


Fig. 1. Jumps in: a) axial displacement, b) rotation and c) transverse displacement

To show the capability of the frame elements with embedded discontinuities for modelling the occurrence and evolution of damage, a two-story reinforced concrete frame shown in Fig. 2a is studied. This frame has a span $L = 3.5$ m and story height $H = 2$ m, which columns are clamped at the bottom. The mechanical properties of the concrete are: Young's modulus of $E_c = 28.6$ GPa, Poisson ratio $\nu_c = 0.2$, ultimate compressive strength $\sigma_{cu} = 30$ MPa. The mechanical properties of the reinforcing steel are: Young's modulus $E_s = 192.5$ GPa, Poisson ratio $\nu_s = 0.3$ and yield stress $\sigma_y = 418$ MPa. Beam and columns have the same cross section, 30×40 cm, and the same area of longitudinal reinforcement area; however, these sections have different coverings, 4 and 3 cm, respectively, as shown in Fig. 2b. The beams and columns were discretized, as shown in Fig. 2c, with frame element with embedded discontinuities. In the numerical solution of this example, a continuous compression load of 700 kN are applied at the top of the columns, whereas a horizontal displacement was applied at the top of the frame. The reactions of the every applied displacements correspond to the force applied at the top of the frame.

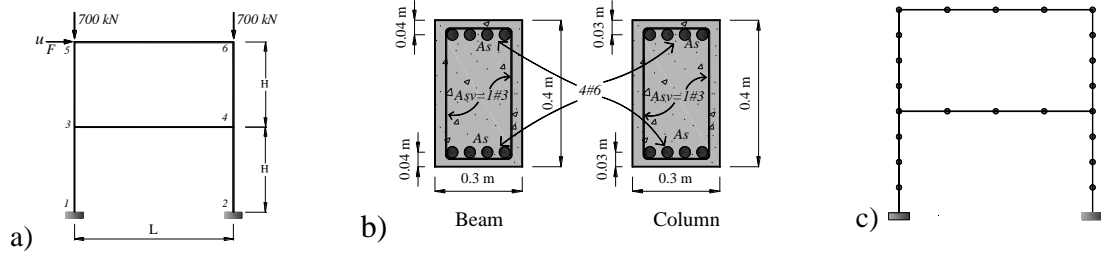


Fig. 2. Two story reinforced concrete frame: a) geometry, b) discretization and c) cross sections

The evolution of the occurrence of hinges is shown in Fig. 3a. First, two hinges occurred simultaneously at the ends of the first floor beam. Next, other two hinges occurred simultaneously at the ends of the second floor beam. Then, a hinge occurred at the bottom of the right column. Finally, a hinge occurred at the bottom of the left column. Fig. 3b shows the computed force vs displacement curve, which is compared with the experimental curve reported by Vecchio and Emara (1992) and with the numerical curve reported by Jukic (2013), who used beam elements with embedded discontinuities of the rotational jump. In the ascending part, the three curves are quite similar; however, they are different after 250kN, but the computed curve in this paper is closer to the experimental curve than the one computed by Jukic (2013).

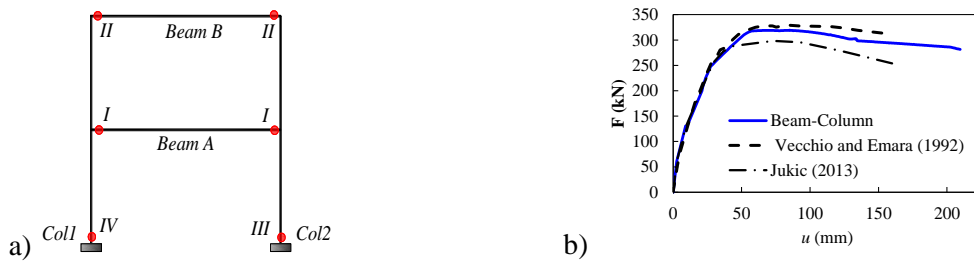


Fig. 3. a) occurrence of hinges and b) force vs displacement curve

Acknowledgements

The first author acknowledges the support given by the Universidad Autónoma Metropolitana and the financial support by the National Science and Technology Council of Mexico (Conacyt) under the agreement number I010/176/2012, in the context of the research project: “Analysis and design of concrete slabs”. The PhD fellowship granted to the second author by Conacyt is gratefully acknowledged.

References

- [1] Jukic, M., Finite element for modeling of localized failure in reinforced concrete, Dissertation, L’Ecole Normale Supérieure de Cachan, France, 2013.
- [2] Taylor, L.R., A finite element analysis program (FEAP) v8.2, Department of Civil and Environmental Engineering, University of California at Berkeley, Berkeley, CA, 2008.
- [3] Vecchio, F.J., Emara M.B., Shear deformations in reinforced concrete frames, ACI Structural Journal 89 (1) (1992) 46–56.

The flow field and the pressure drop in multiple stenoses





M. Kašpárek^a, L. Nováková^a, J. Novotný^a

^a Faculty of Mechanical Engineering, Czech Technical University in Prague, Technická 4, 166 07 Praha, Czech Republic

The wall of blood vessel is affected by all changes in internal pressure, flow field and wall shear stress [4]. These effects or mechanical damage may represent an initial factor in the development of atherosclerosis and therefore can lead to stenosis formation [2], [1]. Stenosis refers to localized narrowing of blood vessel. The severity of stenosis depends on many factors: length, percentage of narrowing, wall roughness and number of stenosis etc. Also, the development of double or multiple stenoses in a vessel can have serious consequences [3].

Four idealized rigid models of blood artery with stenosis were used in the experiment. All the models have identical geometry of narrowing, but different number and stenosis distance. The dimensions of the models are in Table 1. A flow field for three different regimes was measured for each model by PIV method (Particle Image Velocimetry). Subsequently the static pressure was measured for each model by special pressure sensors. The Reynolds number (Re) related to the tube diameter was set 210, 400 and 600 for PIV measurement and 175, 350, 438, 613, 788, 876 for static pressure measurement.

Table 1. The dimensions and scheme of the models

Model	Number of stenosis	Inner diameter of the tube D (mm)	Inner diameter of the narrowing d (mm)	Distance stenosis (mm, number diameter)	Scheme
1	1	14	7	-	
2	2	14	7	42, 3D	
3	2	14	7	56, 4D	
4	3	14	7	28, 2D	

In the experiment the special fluid with similar dynamic viscosity to human blood was used. Working fluid was the mixture of distilled water, glycerol and sodium iodide. The weight ratio was (distilled water:glycerol:sodium iodide) 47,38:36,94:15,68. The final mixture viscosity was $4,6 \cdot 10^{-3} \text{Pa}\cdot\text{s}$ and refractive index was 1,43. The change of refractive index was crucial for optical access quality of PIV method. The model was made from glass (refractive index 1,47). The similar refractive index of working fluid and model reduces optical distortion and deformation.

Fig. 1 shows axial velocity $U(\text{m/s})$ in stenotic and poststenotic region for regime of Reynolds number 210. The flow field shows the accelerating flow in the narrowing and the jet created behind the narrowing. The jet influences the flow within the distance of approximately 200 mm (exceeds 14 diameters of the tube).

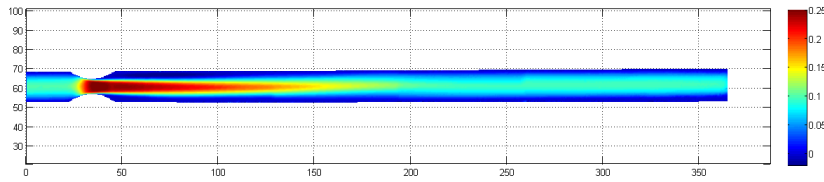


Fig. 1. Axial velocity U [m/s]

Fig. 2 represents the radial velocity V(m/s) for Reynolds number 210. The elevated values of V are located in the constricted section and in separation area.

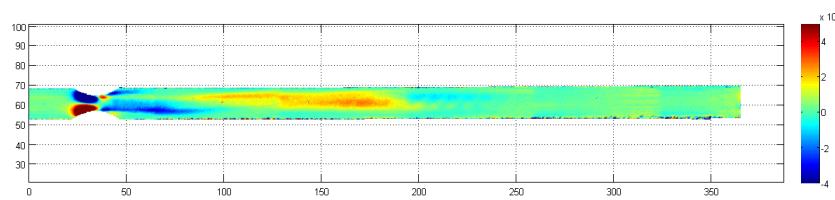


Fig. 2. Radial velocity V [m/s]

The graph in the Fig. 3 shows dependence of pressure drop coefficient on Reynolds number for all studied models. The pressure drop coefficient increases as the Reynolds number decreases. The lowest values of pressure drop coefficient are for the model 1 (single stenosis). The highest values of pressure drop coefficient are for the model 4 (three stenosis in series). The values of pressure drop coefficient for the model 3 and 4 show that the total length of multiple stenoses is also important. The model of double stenosis with longer distance has higher pressure drop coefficient. In our contribution we discuss the problem of correct pressure loss evaluation as well.

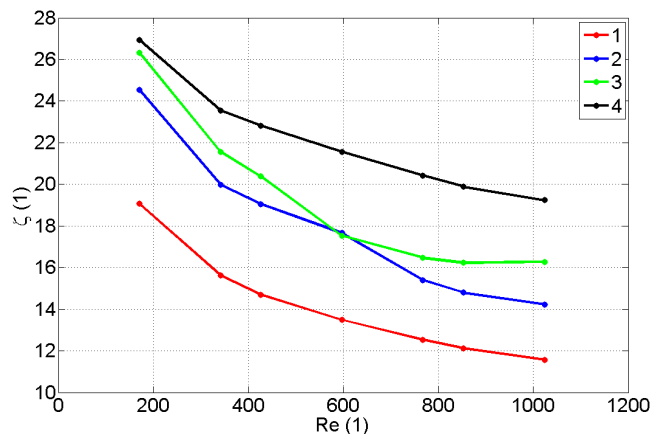


Fig. 3. Dependence of pressure drop coefficient on Reynolds number for all models

Acknowledgements

This work was supported by Grant Agency of the Czech Technical University in Prague, grant No SGS15/191/OHK2/3T/

References

- [1] Caro, C.G., Discovery of the role of wall shear in atherosclerosis, *Arteriosclerosis Thrombosis and Vascular Biology* 29 (2009) 158-161.
- [2] Glagov, S., Zarins, C.K, Giddens, D.P., Ku,D, N., Hemodynamics in atherosclerosis: insights and perspectives gained from studies of human arteries, *Archives of Pathology & Laboratory Medicine* 316 (1988) 1371–1375.
- [3] Lee, T.S., Liao, W., Low, H.T., Numerical simulation of turbulent flow through series stenoses, *International Journal for Numerical Methods in Fluids* 42 (7) (2003) 717–740.
- [4] McDonald, D.A., *Blood flow in the arteries*, Williams & Wilkins, Baltimore, Maryland, 1960.

CFD method of prediction of turbine blade flutter

J. Klečková^{a,b}, J. Hamza^b

^a Faculty of Applied Sciences, University of West Bohemia, Univerzitní 8, 306 14 Plzeň, Czech Republic

^b Research and Testing Institute Pilsen, Tylova 1581/46, 301 00 Plzeň, Czech Republic

This paper is devoted to the aeroelasticity phenomenon called “flutter” which has to be taken into account in the design of many industrial applications, where the self-excited oscillation could occur and can cause irreversible damage. This work is concentrating on developing the method of the quick prediction of flutter of a steam turbine blade. The work was inspired by a methodology which was designed by authors Kielb and Panovsky, [1], [2] and [3]. This method of stability prediction is based on CFD analysis of steam flow through passage of three neighboring turbine blades which vibrate with a range of phase angles called inter-blade phase angles (IPBA) between each pair of blades.

In Fig. 1 (left) there is the 3D model of a turbine blade colored by contours of total deformation obtained from modal analysis as the first eigen mode. For CFD analysis was created a 2D section at radial coordinate of 1461.9 mm (measured from the rotor center). All CFD computations were provided for domain with three profiles, Fig. 1 (right). The middle blade is referential and its number is zero. The neighboring blades are numbered ± 1 .

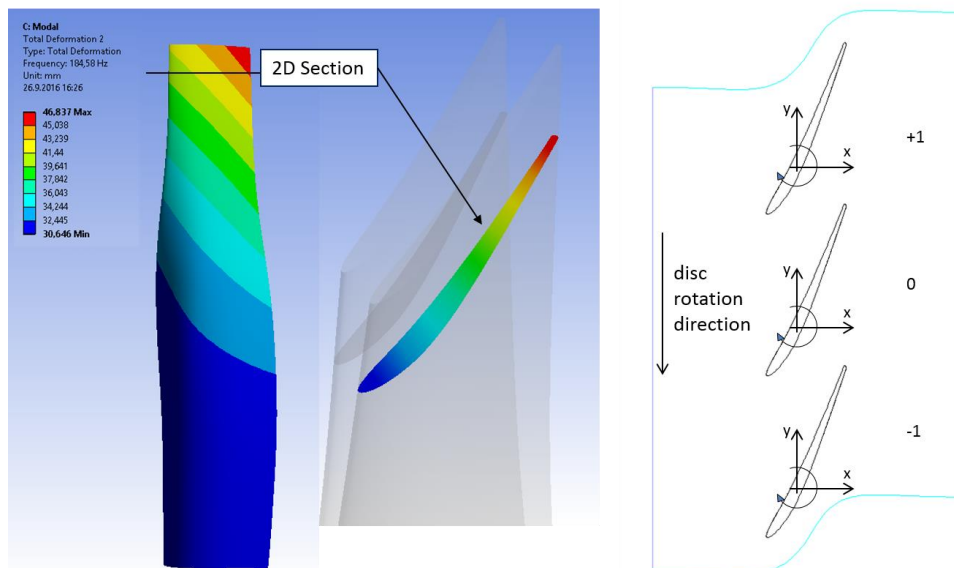


Fig. 1. 3D model of turbine blade colored by contours of total deformation, the first eigen mode (left), computational domain with three neighboring blade profiles (right)

Harmonic vibration motion of each blade was based on results of modal analysis and defined as the combination of displacement and the rotation with axis of rotation placed in the center of gravity of the blade. Structural eigen modes were obtained from ANSYS Mechanical. Vibrating motion was prescribed as a sinusoidal time-dependent function with a frequency corresponding to the first eigen frequency. Numerical simulations of a two-dimensional steam flow through the computational domain were accomplished by software

ANSYS Fluent for eighteen different IBPAs from interval $(-180^\circ, 180^\circ)$. SST k-omega turbulence model was used to solve the problem. The disc rotation was included using a moving reference frame model.

Aerodynamic work of fluid on the referential blade is computed as integral below, [2]

$$W = \int_{t}^{t+T} \int_A p \vec{v} \cdot \vec{n} dAdt,$$

where p is the unsteady pressure on the surface of the referential blade, \vec{v} is the local velocity vector, \vec{n} is the outer unit normal vector, A is surface area and T is the time period of oscillation. Dependence of aerodynamic work on IBPA is shown in Fig. 2.

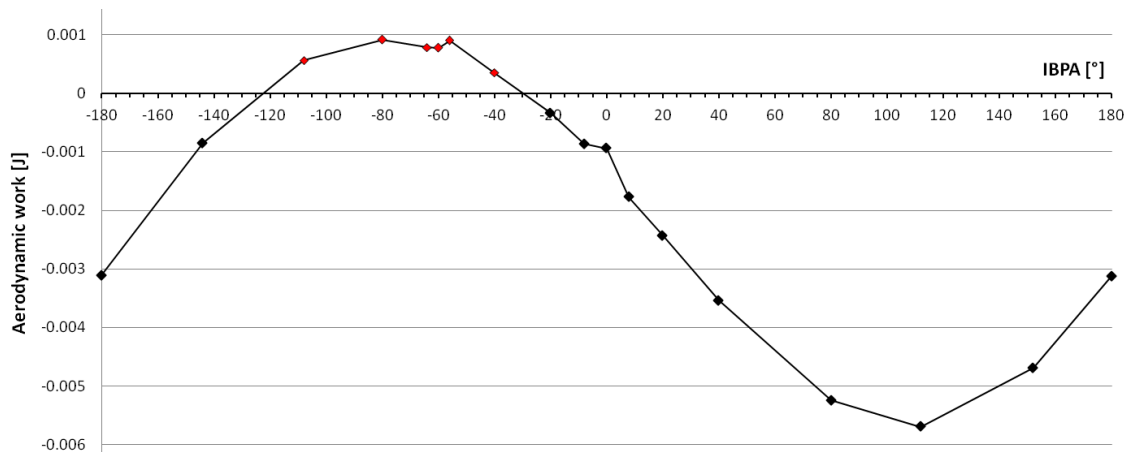


Fig. 2. Aerodynamic work of fluid on the referential blade surface in dependence on inter-blade phase angle

This presentation describes the methodology of the turbine blade flutter prediction based on 2D analysis of steam flow. Positive value of aerodynamic work means that the blade absorbs energy from the flow which leads to unstable blade behavior and negative work results in damped blade motion. According to the graph in Fig. 2, the unstable behavior could occur for IBPAs from interval $(-120^\circ, -30^\circ)$. Since numerical results are consistent with results of 3D analysis for one type of blade, future efforts will be devoted to proving accuracy of 2D analysis of other blades because of sparing computational time.

Acknowledgements

The work has been supported by the institutional support for a long-term conceptual development of the research institution and by the research project TA ČR n. TE01020068 “Center of research and experimental development of reliable energy production”.

References

- [1] Kielb, R.E., Barter, J., Chernysheva, O., Fransson, T., Flutter of low pressure turbine blades with cyclic symmetric modes: A preliminary design method, *Journal Of Turbomachinery-transactions Of The ASME* 126 (2) (2004) 306 – 309.
- [2] Panovsky, J., Flutter of aircraft engine turbine blades, Ph.D. thesis, University of Cincinnati, Cincinnati, OH, 1997.
- [3] Panovsky, J., Kielb, R.E., A design method to prevent low pressure turbine blade flutter, ASME Paper No. 98-GT-575, 2000.

Aerodynamic design of the propeller for low-speed indoor UAV

J. Klesa^a

^a*Faculty of Mechanical Engineering, CTU in Prague, Karlovo náměstí 13, 121 35 Praha 2, Czech Republic*

Aerodynamic design of propellers working at low Reynolds number brings many problems. Viscous forces have significant influence on the flow and cause high airfoil drag-to-lift ratio. This results in relatively low propeller efficiency compared with propellers for manned aircraft. Flow at low Reynolds numbers brings also problems with the flow stability and separation. All these makes the task extremely challenging.

The propeller will be used for the long endurance indoor unmanned aerial vehicle (UAV) developed at the Department of Aerospace Engineering of the Czech Technical University in Prague. It will be used especially for the propagation of the department. The requirement for the several hours of flight determines low flight speed. The propulsion system must be as efficient as possible to minimize the energy consumption. Table 1 contains input parameters for the propeller aerodynamic design. It is assumed that the aircraft weights 40g, aircraft lift coefficient is 0.5 with lift-to-drag ratio 5. The aircraft will be powered by an electric motor with gearbox. The unknown parameters are propeller RPM and diameter. This paper is focused on the analysis of their influence on the propeller efficiency.

Table 1. Propeller design parameters

number of blades	2
flight speed [m/s]	3.2
required thrust [N]	0.08
design lift coefficient [-]	0.75
design lift-to-drag ratio [-]	8

Design method used is based on [3]. It uses Betz's law [1]. More detailed description of propeller aerodynamic models can be found in [5]. Viscous losses are included by the means of the drag-to-lift ratio. Airfoil characteristics (i.e. airfoil drag-to-lift ratio) are based on the values from [4] and [2]. Propeller efficiency was computed for wide range of RPM and diameter.

Computed values of the efficiency are displayed in Fig. 1. Thick black line connects points with the maximum efficiency for given propeller diameter and thus represents optimal combinations of RPM and diameter for the required propeller performance. Fig. 2 shows dependence of efficiency on the propeller diameter for these optimal combinations. Fig. 2 shows that the increase of propeller diameter leads to higher efficiency as expected. However, increase of the diameter should be connected with the change of RPM. Otherwise can an increase of diameter leads to the decrease of efficiency. This very important information can not be found in the aerodynamic textbooks and represents the main achievement of this paper.

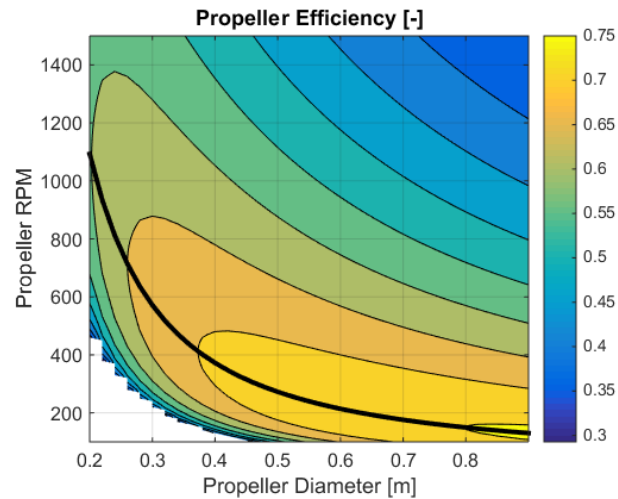


Fig. 1. Dependence of the propeller efficiency on the propeller diameter and on the propeller shaft RPM; the thick black line connects points with the maximum efficiency for given propeller diameter

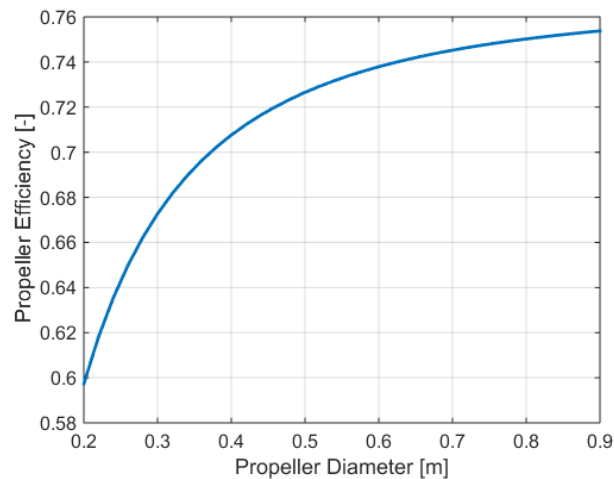


Fig. 2. Dependence of the propeller efficiency on the propeller diameter

References

- [1] Betz, A., Screw propeller with minimum energy loss, Nachrichten von der Gesellschaft der Wissenschaften zu Göttingen, Mathematisch-Physikalische Klasse 1919 (1919) 193-217. (in German)
- [2] Eder, H., All about indoor flying – From rubber drive to RC-micro-models, VTH, Baden-Baden, 2014. (in German)
- [3] Larrabee, E. E., Practical design of minimum induced loss propellers, Business Aircraft Meeting and Exposition, Society of Automotive Engineers, Warrendale, PA, April 1979, Paper 790595.
- [4] Sunada, S., Sakaguchi, A., Kawachi, K., Airfoil section characteristics at a low Reynolds number, Journal of Fluids Engineering 119 (1) (1997) 129-135.
- [5] Wald, Q. R., The aerodynamics of propellers, Progress in Aerospace Sciences 42 (2) (2006) 85-126.

Yaw dampers in construction of rail vehicles

M. Kohout^a, T. Michálek^a, J. Vágner^b, J. Zelenka^a

^a Jan Perner Transport Faculty, University of Pardubice, Nádrazní 547, 560 02 Česká Třebová, Czech Republic

^b Jan Perner Transport Faculty, University of Pardubice, Studentská 95, 532 10 Pardubice, Czech Republic

Dampers in the construction of rail vehicles are used for damping translational movements in running gears of the rail vehicle (primary and secondary suspensions - vertical, connection car body to bogie frame - lateral orientation). With the growth of the maximum operating speed on railways special types of dampers for damping rotational movement between bogie and car body have been developed (yaw damper - Fig. 1). These dampers are designed to prevent the development of unstable vehicle motion in a straight track [1] and preserve the running safety and low lateral force effects between the vehicle and the track.



Fig. 1. Yaw damper on locomotive

Properties of yaw dampers should allow two very different operation modes:

- vehicle run in straight track (required high damping force at low stroke) and
- run through transition curve and through curve (required low forces at high stroke).

To describe the characteristics of damper in the simplest form the velocity characteristic is used (dependence of the damping force on damper deformation velocity). Specific requirements for damping of rotational movements bogie against carbody in the straight track at the maximum speed (stroke 2÷5 mm, frequency 3÷8 Hz) lead to a very steep velocity characteristic (force increase already at velocities of around 10÷30 mm/s).

Total deformation and force of the damper is determined by the elastic deformation of the damper fixing elements (proportional to the rubber stiffness; doesn't participate in movement damping) and the damping force of the liquid (proportional to the velocity of the piston). The overall behavior depends usually on the stroke and the frequency of loading (Fig. 2).

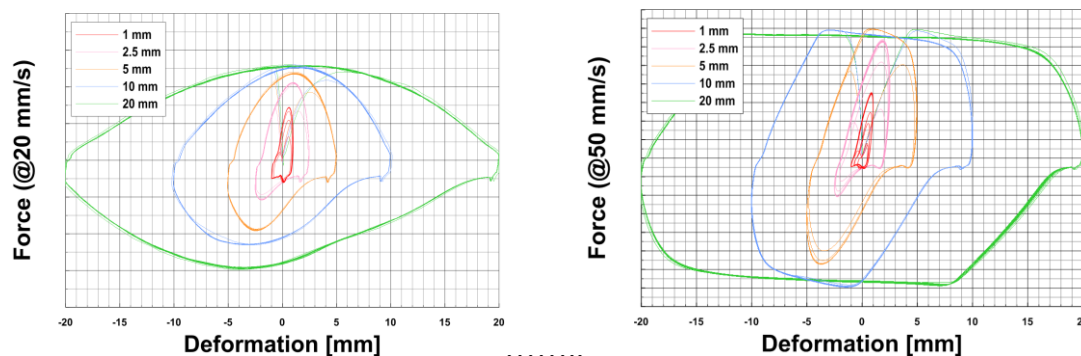


Fig. 2. Effect of stroke and frequency on shape of measured working characteristics of yaw damper

With regard to the damper construction and its condition, the damper may have an extra shock delay in the force increase (e.g. due to air bubbles) and therefore less ability to energy dissipation (Fig. 3). It is necessary to know in detail the behavior under various conditions and the degree of wear of the damper, even if this phenomenon did not occur.

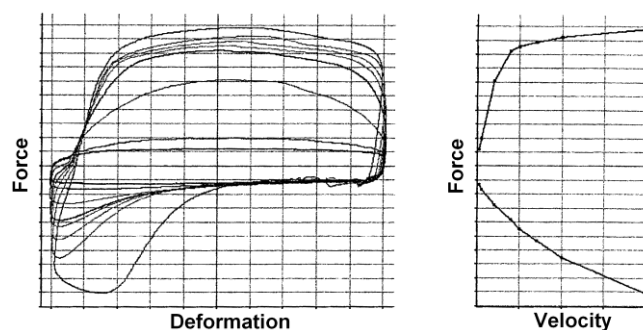


Fig. 3. Example of the damper characteristic with reduced damping ability

Damper in computational simulations can be replaced e.g. by Maxwell model, taking into account the stiffness of joints and inertial mass of the moving parts of the damper. Hydraulic dampers in railway applications is dedicated the standard EN 13802 [2], which among other things, defines the fundamental parameter method for determining dynamic stiffness and equivalent dynamic damping rate of the damper from test results. Both parameters can thus be defined as a function of the amplitude of the damper deformation.

Experiments in laboratory and in operation. In order to obtain input data for the calculation of spare model parameters in computational simulation, the test stand was designed and manufactured. Simultaneously they were produced dampers with an integrated force sensor and sensor of deformation so that it is possible to determine the operating conditions and compare the behavior of the damper in a laboratory, in an operation (Fig. 4) and in computational simulation.

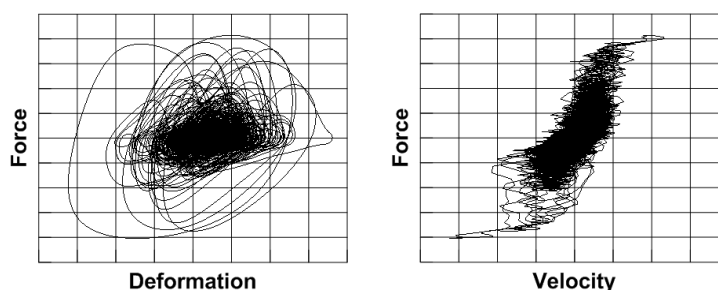


Fig. 4. Example of damper behavior under operating conditions (stochastic excitation, straight track)

Aim of work is to develop a methodology of laboratory tests in order to obtain data for the definition of the complex characteristic of the yaw damper and subsequent implementation of a suitable model into computational simulation of a rail vehicle run.

Acknowledgements

The work has been supported by the Technology Agency of the Czech Republic within the project No. TE 01020038.

References

- [1] Zelenka, J., Kohout, M., Michálek, T., Application of sensitivity analysis in design of characteristics of damping joints in locomotive running gear, *Engineering Mechanics* 20 (5) (2013) 369–378.
- [2] ČSN EN 13802:2014, Railway applications - Suspension components - Hydraulic dampers, Czech Office for Standards, Metrology and Testing, Praha, 2014.

Design of open combustion chamber for LIF measurements

J. Kouba ^a, J. Nožička ^a

^a Department of Fluid Dynamics and Thermodynamics, Faculty of Mechanical Engineering, Czech Technical University in Prague, Technická 4, 16607 Praha 6, Czech Republic

One of the most ecological types of combustion engine propellant is the natural gas. Nowadays, the usage of the natural gas in the automotive industry is probably the most discussed topic. The CNG (Compressed Natural Gas) is seen in the halfway between the conventional propellants (gasoline, diesel) and renewable ones. The main goal of the present-day development of the CNG engines is a more efficient way of the ignition and burning of the fuel mixture. In addition to the numerical simulations and measurements of the quantities related to the engine performance, the combustion process can also be measured by an optical method LIF, which could give us a deeper insight. However, due to the complex problematics of the LIF measurement and the problematics of combustion, an extensive knowledge across many fields, such as chemistry, thermodynamics, fluid mechanics, classical and quantum physics, is needed for a successful experiment to be carried out. That is why, before the actual measurement with the LIF method, there has to be a number of experiments and calculations and the data obtained from them are crucial for the complex measurement. Therefore, before measuring the closed chamber, it is far more convenient to start with an open one for many reasons. One of them being the lower cost. Due to the LIF's high demands on optical entries, a larger amount of expensive quartz glass has to be used in the case of a closed chamber. Due to the lower pressure in the combustion chamber, the decrease of the safety risks is another advantage of the open chamber. It can be designed only to hold the fuel mixture and to fix the ignition device. Because of this, the strength analysis of the combustion chamber, optical parts and the exhaust system is redundant.

The design is based on the capabilities of the measuring device and by the future measurements. The chamber has a rectangular shape with a square base that is of size 70x70mm. The height of the inner space is 30mm. On the sides of the chamber, there are two windows made of magnesium glass, which is UV transmitting, and therefore, the measurement with LIF is possible. The chamber has a one-way circular intake with diameter of 3mm for the fuel and an open output with the diameter of 30mm.

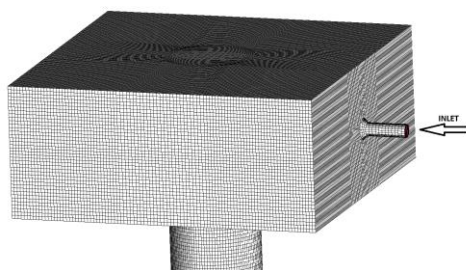


Fig. 1. Structured mesh of open combustion chamber

The fuel is premixed and consists of a stoichiometric compound of methane and air. This mixture was chosen, because the methane volume ratio in CNG is approximately 98%. The stoichiometric ratio was chosen for the reference measurement and because of the ability to ignite. Given the pressure of 101325Pa and the temperature of 20°C, the mass of the used methane ($m=9,3 \cdot 10^{-3} \text{g}$) was calculated from the stoichiometric equation. The overall density of the mixture is $\rho=1,1528 \text{ kg} \cdot \text{m}^3$, which means, due to the mixture being lighter than the air, that it is necessary to position the exhaust downwards.

The calculated mass of the methane is too low to be dosed in this scale, therefore, as mentioned above, the mixture is prepared in a bigger scale beforehand. The movement of the whole mixture is important if we focus on the burning aspect. The mixed combustion can be seen as a compound movement that involves movement of the fuel mixture and the laminar burning velocity. A numerical calculation of the residual movement of the fuel mixture after the closing of the intake is a part of this work. This issue is important because of two reasons. First one being the spreading of the flame front in the combustion chamber. Because this process influences the efficiency, power and the whole machine, the velocity of the spreading and the burning of the whole mixture are the main subject of interest in the field of the combustion chambers. The other reason for importance is the possibility to verify the properties of the mixed fuel using the flame speed that is dependent on the mixture composition, pressure and temperature.

The simulation was carried out on a simple structured mesh shown in Fig.1. The realisable k-epsilon model was used as a numerical model. The intake velocity of the fuel mixture is 15m/s. The regime of the calculation is non-stationary with a variable setting of the time step, with Courant number set to 2. Results of numerical simulation are shown in Fig 2-4.

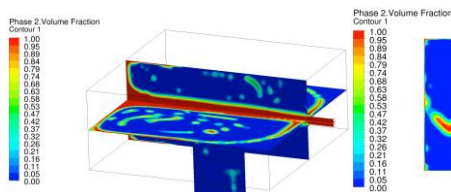


Fig. 2. Concentration of species before inlet closing

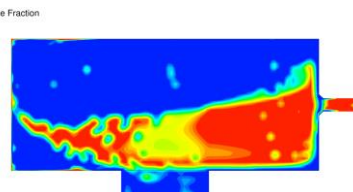


Fig. 3. Concentration at $t=0,45\text{s}$ after closing

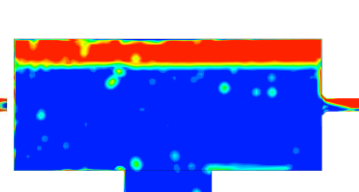


Fig. 4. Concentration at $t=6\text{s}$ after closing

Acknowledgements

This work was supported by the Grant Agency of the Czech Technical University in Prague, grant No. SGS15/148/OHK2/2T/12.

References

- [1] Bernard, P.S., Wallace, J.M., Turbulent flow: analysis, measurement, and prediction, John Wiley & Sons, Hoboken, NJ, 2002.
- [2] Versteeg, H.K., Malalasekera, W., An introduction to computational fluid dynamics: the finite volume method, Pearson Education Ltd., 2nd ed., New York, 2007.
- [3] Warnatz, J., Maas, U., Dibble, R.W., Combustion: physical and chemical fundamentals, modeling and simulation, experiments, pollutant formation, Springer, 2nd ed., New York, 1999.

Measurement of the end point by laser tracker which is mounted on a slide

F. Kovář^a, M. Valášek^a, J. Švéda^b

^aDepartment of Mechanics, Biomechanics and Mechatronic, Faculty of Mechanical Engineering, CTU in Prague, Technická 4, 160 00 Praha, Czech Republic

^bDepartment of Production Machines and Equipment, Faculty of Mechanical Engineering, CTU in Prague, Horská 3, 128 00 Praha, Czech Republic

Accuracy of distance measurement depends mainly on accuracy of measuring device and on quality of measuring method with commutating algorithm of measuring data. The quality of measuring method is closely linked to duration, which is mainly associated with thermal deformation.

If we need to measure a long distance space, we may appropriately use the laser tracker – laser contactless measure device. In the case when we need measurement with higher accuracy, in comparison with the laser tracker, we can use a redundant method. Ordinary redundant methods is time consuming or needs more laser trackers, it is too expensive. Described method is relatively fast, cheap, and well automated.

The basic scheme of the described method consists of a laser tracker (tracker) placed in the machine and set of reflectors of the laser beam (reflectors). The reflectors could be arbitrarily placed in the workspace on the machine frame or on the workpiece. The reflectors could be also placed outside the workspace, for example on the construction of a hall etc. This scheme is shown in Fig. 1 of the patent [2]. Fig. 1 shows us workspace – 1, spindle – 2, headstock – 3, machine – 4, reflectors – 5, laser beam – 6, platforms holding reflectors – 7.

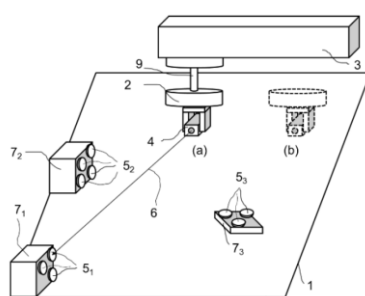


Fig. 1. Measurement scheme

Measurement procedure starts by moving of the end-effector (corresponds to position of tracker) to the first position (Fig. 1 position (a)). In this position, the tracker measure the relative position of all reflectors (it means x, y, z of reflectors). After that the end-effector moves into the second position. (Fig. 1 position (b)). In this position the tracker measures all reflectors again. Similarly we measure the reflectors from all desired positions. From the measurement of reflectors in one position we obtain the relative position of all reflectors and one position of the tracker. With each new end point location and subsequent measurement

we obtain redundancy. To determine the amount of redundancy we use formula:

$$E = \frac{v}{b}, \quad (1)$$

where E means redundancy, v means binding equations and b is number of searched parameters.

Computation of measured data is based on modified Newton method, which is described by expressions:

$$\begin{aligned} \mathbf{F}_s &= \mathbf{F}(\mathbf{R}_s, \mathbf{l}), \\ \mathbf{J}_s &= \mathbf{J}(\mathbf{R}_s, \mathbf{l}), \\ \Delta \mathbf{R}_s &= -\lambda (\mathbf{J}_s^T \mathbf{J}_s)^{-1} \mathbf{J}_s^T \mathbf{F}_s, \\ \mathbf{R}_{s+1} &= \mathbf{R}_s + \Delta \mathbf{R}_s. \end{aligned} \quad (2)$$

In equations (2) \mathbf{F} is vector of coupling conditions, \mathbf{R} means calibration parameters, \mathbf{l} is measuring distances and \mathbf{J} is jacobian. The algorithm begins with input of inaccurate calibration parameters \mathbf{R}_0 . Iterative calculation is carried out in a loop, until $\|\mathbf{F}\| \geq \varepsilon$ or $\lambda \geq \varepsilon$, where ε is sufficiently small number. In our method we chose the halving of step method (if it should occur in $s + 1$ iteration divergence ($\|\mathbf{F}_{s+1}\| \geq \|\mathbf{F}_s\|$), we will decrease step from λ to half of λ , so long as this condition is true).

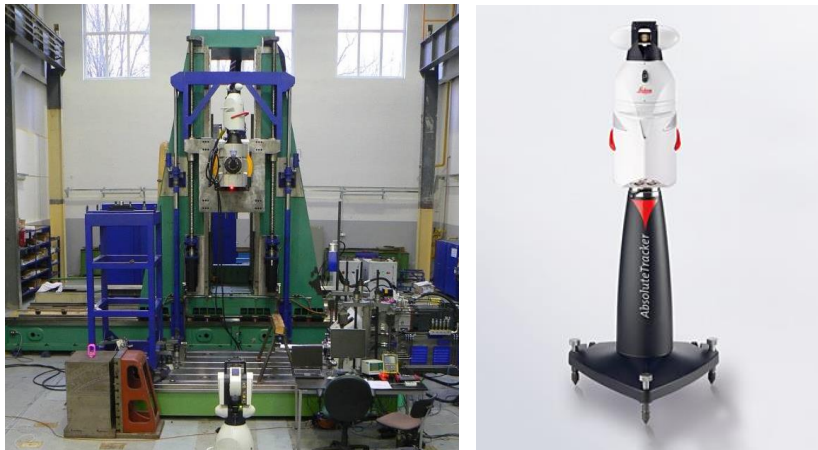


Fig. 2. Machine Grata in TOS Varnsdorf and detail of laser tracker Leica AT901 (right)

For experimental tests, there was chosen the machine Grata in TOS Varnsdorf (see Fig. 2 – left) and measuring device the laser tracker Lieca AT901 (see Fig. 2 – right). Number of reflectors was 17 and number of position of trackers was 32.

There was up to six-fold improvement in measurement accuracy.

References

- [1] Štembera, J., Vliv vícenásobné redundance měření na přesnost kalibrace a měření, Praha: Faculty of mechanical engineering, CTU in Prague. (in Czech)
- [2] Valášek, M., Nečas, M., Švéda, J., Zařízení pro redundantní optické měření a/nebo kalibraci polohy tělesa v prostoru, Užité vztahy, Czech republic 25815, 2013. (in Czech)

Investigation of aeroelastic bridge instabilities using the multidimensional Fokker-Planck equation and wind-tunnel experiment

R. Král^a

^a*Institute of Theoretical and Applied Mechanics, v.v.i., Prosecká 76, 190 00 Prague, Czech Republic*

Stability of bridges and other line-like engineering structures is an important part of their overall design. It is also still of great interest nowadays due to a higher demand on increasing the span while maintaining an economical cost and service. During the previous decades sophisticated methods for the aeroelastic instability prediction have evolved and successfully applied to the real structures and many questions have been adequately answered.

The majority of the methods is based on the knowledge of the aerodynamic and aeroelastic coefficients that can be obtained using wind-tunnel experiment or increasingly often numerically. If experimental testing is considered, a special experimental set-up designed to allow two component independent motion (vertical and torsional response) with a linear behaviour should be employed that enables studying both one component bridge instabilities (vortex shedding, torsional flutter) and coupled motion instabilities (classical flutter), see e.g. [3]. The numerical simulation treats the bridge stability effectively using various types of computational models. For reliable description of the fluid dynamics, fluid-structure interaction with an appropriately selected turbulent model is usually preferred, see for instance [1]. In this paper, the dynamic bridge response is investigated using a combination of the Fokker-Planck equation and experimental bridge testing that gives the solution of cross probability density function (PDF) $p(\mathbf{x}, t)$ by solving the following differential system:

$$\frac{\partial p(\mathbf{x}, t)}{\partial t} = - \frac{\partial}{\partial x_j} (\kappa_j(\mathbf{x}, t) \cdot p(\mathbf{x}, t)) + \frac{1}{2} \frac{\partial^2}{\partial x_j \partial x_k} (\kappa_{jk}(\mathbf{x}, t) \cdot p(\mathbf{x}, t)), \quad (1)$$

$j = 1, \dots, 2n$, n – dynamic degrees of freedom.

In Eq. (1), the drift coefficients $\kappa_j(\mathbf{x}, t)$ represent the modal properties of the bridge including external harmonic forces with variable frequencies, and the diffusion coefficients $\kappa_{jk}(\mathbf{x}, t)$ are referred to intensity of the stochastic excitation of the turbulent wind flow, be considered as a Gaussian white noise. The input values for the external forces both the deterministic and stochastic character are determined experimentally using the wind tunnel testing.

A large number of monographs and papers have been published concerning this widely known partial differential equation which has mostly the linear character, see for instance [5], [4]. Besides indisputable strengths of these methods they include very unpleasant shortcomings which consist predominantly in very limited dimensionality of FPE, configuration of boundary conditions and problematic possibility to analyze any non-stationary problem. In the present approach, FE method as a main solution tool is accommodated involving two or four independent

space variables depending on what aeroelastic instabilities are considered. Due to the harmonic external force, a periodic solution of PDF arises with a time period close to the excitation frequency. By averaging of PDF values over the computational time, the resulting probability function of a response is achieved. Comprehensive description of the multidimensional FPE solution using FEM published by present authors can be found in [2].

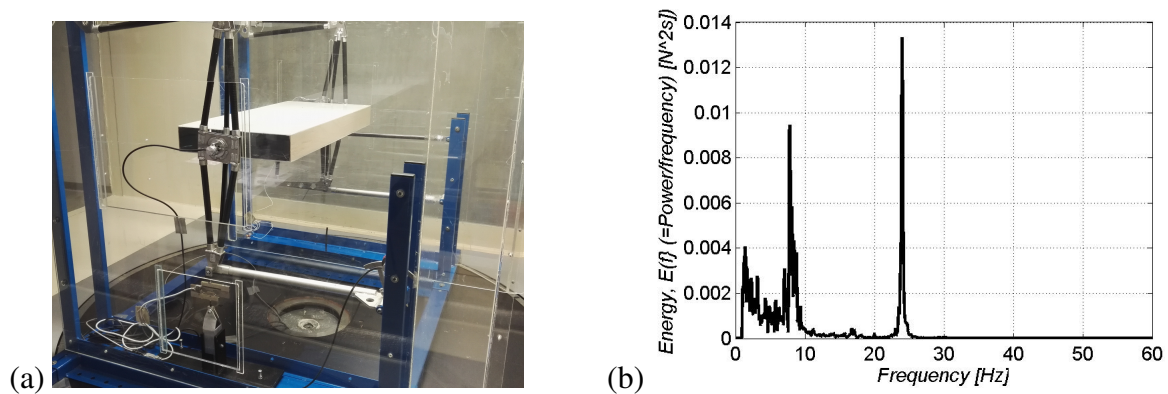


Fig. 1. (a) View of experimental set-up with scale bridge deck; (b) power spectrum of lift force

The experimental tests are carried out on a bridge deck in the shape of a rectangular prism with aspect ratio of 1:5, see Fig. 1a. First, aerodynamic forces in heave and torsion are acquired separately on the nearly motionless deck at velocities ranging from 0.2 m/s to 7 m/s. For the measurement purposes, ultra-sensitive dynamometer and accelerometer are used by means of which, when assuming the measured signals and known mass/stiffness parameters, the resulting aerodynamic forces are evaluated as a sum over all terms in the equation of motion. In Fig. 1b, a representative power spectral density of the heave force component is presented with a dominant peak at the Strouhal frequency. In the next experimental phase, free vibration measurements are performed both for each degree of freedom separately and the coupled system. These records are then used for the comparative study with the numerical FE results. In order to determine the effect of turbulence, two types of oncoming air flow with the turbulent intensities 0.6% and 12% are examined for all the tests.

Acknowledgments

The kind support of the Czech Science Foundation - projects No. 14-34467P, and RVO 68378297 institutional support are gratefully acknowledged.

References

- [1] Král, R., Náprstek, J., Analysis of stability conditions of a slender beam under wind effects using numerical model, Proceedings of the 10th World Congress on Computational Mechanics, Sao Paulo, Brazil, 2012.
- [2] Král, R., Náprstek, J., Theoretical background and implementation of the finite element method for multi-dimensional Fokker-Planck equation analysis, Journal of Advances in Engineering Software, 2016. (in press)
- [3] Král, R., Pospíšil, S., Náprstek, J., Wind tunnel experiments on unstable self-excited vibration of sectional girders, Journal of Fluids and Structures 44 (2014) 235-250.
- [4] Lin, Y.K., Cai, G.Q., Probabilistic structural dynamics – Advanced theory and applications, McGraw-Hill, New York, 1995.
- [5] Pugachev, V.S., Sinitsyn, I.N., Stochastic differential systems – Analysis and filtering, Willey, Chichester, 1987.

Experimental redundantly actuated cable-driven manipulator

K. Kraus^a, P. Beneš^a, Z. Šika^a, P. Polach^b

^a Faculty of Mechanical Engineering, CTU in Prague, Technická 4, 160 00 Praha 6, Czech Republic

^b Faculty of Applied Sciences, University of West Bohemia, Univerzitní 8, 306 14 Plzeň, Czech Republic

Cable-driven manipulator, in general, offers many advantages, such as low weight of load components, easily variable workspace or the possibility of placing actuators (winches) outside the workspace. Therefore the workspace size growth is also not necessarily rapidly increasing the price.

In this case cable-driven manipulator (Fig. 1) consists of higher count of cables than the number of DOFs is, which – if cables properly placed – removes need of the gravity force in order to cover the whole required workspace and also increases the range of platform movement in each axis. Along with that the cable mutual collision probability and the control system complexity increase. Since every actuator can be driven with respect to the position or to the applied force but never to both of those, there are few options how to manage the problem. First of them is simply based on kinematics, which supplies the control system with required position of every single actuator. But in the world of non-rigid materials and noisy measurements there would be no way to achieve such a state accurately and actuators would mutually “fight” each other [3] in order to reach their own position values. Second option could be a system, which controls as many actuators with respect to the position as the number of DOFs is. The rest of cables are then pre-loaded by predetermined forces, but it does not take the full advantage of optimal load distribution either. Therefore this paper deals with the control system, which drives all of the actuators with respect to applied force, and with low-cost design of such an experimental manipulator.

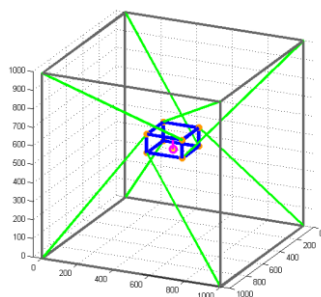


Fig. 1. Manipulator scheme

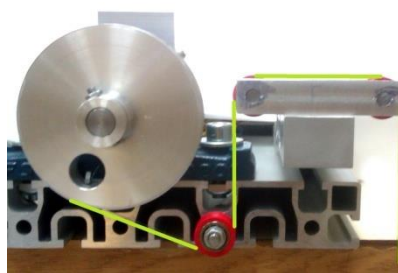


Fig. 2. Modular winch

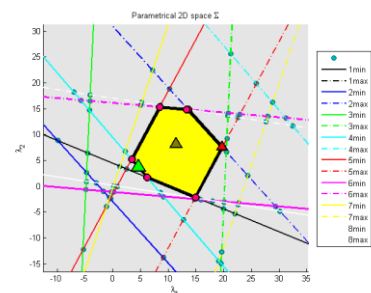


Fig. 3. Parametrical polygon

The whole control system is based on centralized model (Fig. 4). Although it contains position measurement, it does not actually use measured values to directly control actuators, but – in order to maintain low-cost requirement of the experimental manipulator – only gives information about platform position in workspace as well as would any external (e.g. laser) sensor do. Since there are more cables than DoFs, Newton iteration is included, which also averages measurement errors of each cable.

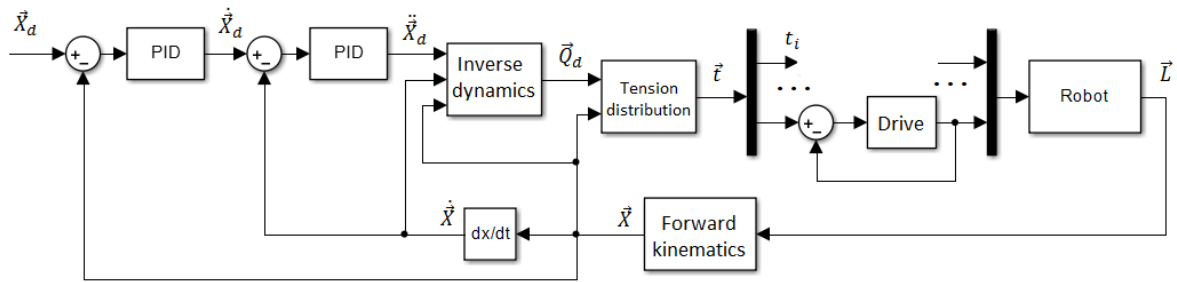


Fig. 4. Centralized model of control system

The tension distribution is then provided using an approximate dynamic model of manipulator and kinematic model as well. The inverse dynamics [2] allows us to transform kinematic variables into desired global forces, which can be later redistributed among all of the cables using Moore-Penrose pseudoinversion while minimizing [3] applied forces. Since such a control system is not aware of cable nature of the mechanical system so far, it is necessary to provide tension forces only. That can be achieved [1] with parametrical solution of system of inequalities (the number of parameters is as high, as the kinematical redundancy is), which along with cable force limits (a range between zero and maximum value) can be graphically illustrated as a line segment (1-param. sol.), convex polygon (2-param. sol. – see Fig. 3), convex polyhedron (3-param. sol.), etc.

The base of the experimental manipulator is a cube built from aluminium profiles. That allows us to easily mount modular winches into various configurations. Each winch is composed of a DC motor with an encoder, a winch drum and a strain gauge. The cable is then led through the strain gauge using a system of pulley (Fig. 2) to get a force feedback for the control system.

Computational hardware consists of low-cost platforms, such as Arduino or RoboClaw boards and soldered circuits containing operational amplifiers (in order to measure tensions using bridge circuits). Main advantage of Roboclaw board is high performance in double DC motors control and encoders reading among other features. Arduino provides all necessary communication among RoboClaws, strain gauges and PC, which runs the main algorithm. In order to increase performance Arduino board also runs an inner loop of force feedback actuating.

Acknowledgements

The work has been supported by the Czech Science Foundation project GA15-20134S – Multi-Level Light Mechanisms with Active Structures.

References

- [1] Gouttefarde, M., Lamaury, J., Reichert, Ch., A versatile tension distribution algorithm for n -DOF parallel robots driven by n+2 cables, *IEEE Transactions on Robotics* 31 (6) (2015) 1444-1457.
- [2] Stejskal, V., Valášek, M., *Kinematics and dynamics of machinery*, Dekker, New York, 1996.
- [3] Valášek, M., Bauma, V., Šika, Z., Belda, K., Píša, P., Design-by-optimization and control of redundantly actuated parallel kinematics sliding star, *Multibody System Dynamics* 14 (3) (2005) 251-267.

Parametric CFD analyses of coolant flow in nuclear reactor VVER 440

V. Kutiš^a, J. Jakubec^a, J. Paulech^a, G. Gálik^a, J. Murín^a, J. Hrabovský^a

^a Department of Applied Mechanics and Mechatronics, Institute of Automotive Mechatronics, Faculty of Electrical Engineering and Information Technology, Slovak University of Technology in Bratislava, 812 19 Bratislava, Slovakia

During the phase of considering safety aspects of the nuclear power plant, one of the fundamental criterions rests in determination of the thermohydraulic conditions in the active zone of the nuclear reactor [1]. In reactor VVER440, there are 6 inlet nozzles for cold coolant water at the reactor pressure vessel (RPV). The paper deals with the influence of nuclear reactor components design on coolant mass flow and velocity distribution during nominal project conditions and with the influence of orifice diameter change on coolant mass flow distribution. The nominal project conditions are defined as isothermal and equal mass flow conditions of coolant in all 6 RPV inlet nozzles. The inlet nozzles of fuel assemblies and control rods are set up as output region of the simulation model.

Because only downcomer of the nuclear reactor VVER 440 is investigated by CFD [2], only three geometry parts were created, namely reactor pressure vessel (RPV), reactor shaft core barrel and bottom of reactor shaft core barrel. Fig. 1 shows negative volume of geometry model, which represents volume of coolant in downcomer of reactor.

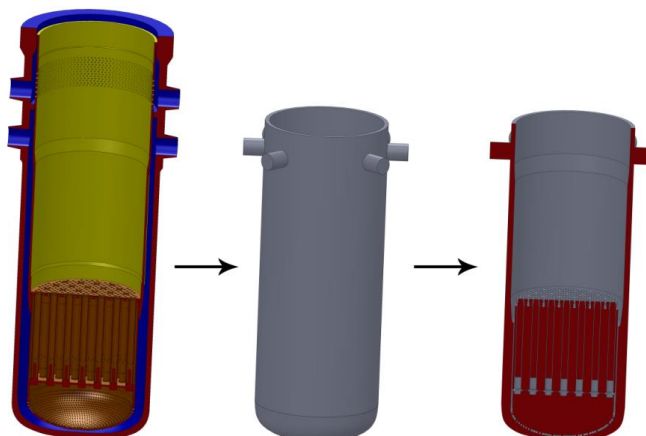


Fig. 1. Negative volume of reactor - volume of coolant in downcomer

In presented CFD analyses of coolant flow in downcomer of nuclear reactor VVER 440, nominal project conditions are considered. They can be described as follows: coolant mass flow through nuclear reactor: 33 383 t/hour, coolant mass flow through each of 6 inlet nozzles are equal with value: 1545.5 kg/s, coolant temperature in all 6 inlet nozzles: 268.0 C, coolant bypass of core: 6.3%, coolant output pressure: 12.25 MPa

All boundary conditions of CFD model were set up according the nominal project conditions. The simulation was performed by CFD code ANSYS CFX. The goal of the CFD analyses is to determine the distribution of coolant velocity in downcomer, the distribution of

coolant mass flow at the individual inlet fuel assembly (FA) nozzles and to investigate the influence of orifice diameter change on mass flow distribution through individual orifices, when boundary conditions are set up according nominal project conditions.

Distribution of coolant velocity in downcomer of nuclear reactor VVER 440 in two different vertical planes is shown in Fig. 2.

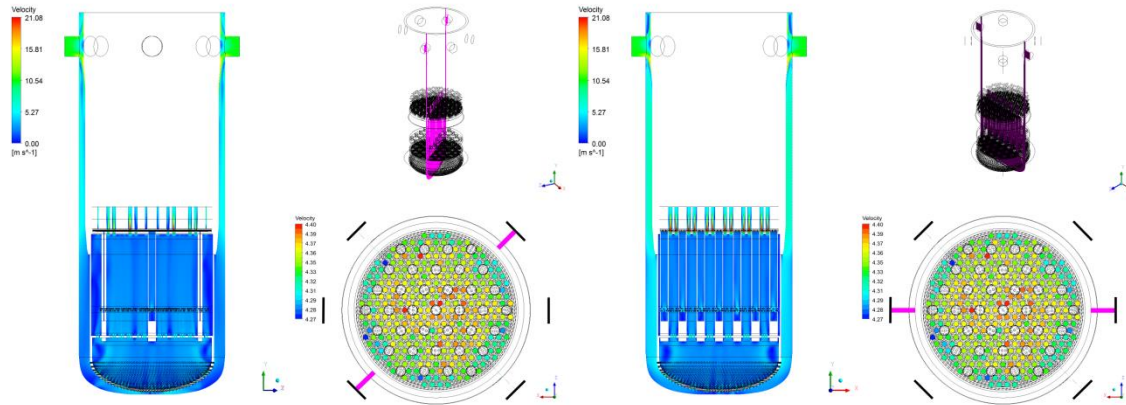


Fig. 2. Distribution of coolant velocity in downcomer in two different vertical planes

The influence of orifice diameter change on mass flow distribution through individual orifices was investigated in three different orifices, which also represents inlet into three different FA (Fig. 3 left): FA 174 - FA in the central area next to HRK (safety rod), FA 154 - FA in the central area between HRK, FA 167 - FA in peripheral area next to HRK.

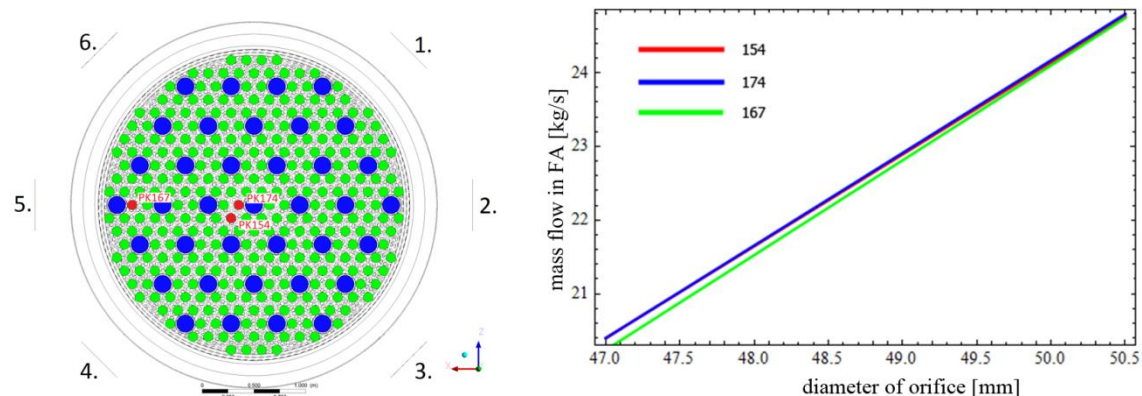


Fig. 7. Dependence of mass flow on diameter of selected orifices

Acknowledgements

This work was supported by the Slovak Research and Development Agency under the contract No. APVV-0246-12 and APVV-14-0613, by Grant Agency VEGA, grant No. 1/0228/14 and 1/0453/15. Authors are also grateful to the HPC Centre at the Slovak University of Technology in Bratislava, which is a part of the Slovak Infrastructure of High Performance Computing (SIVVP project, ITMS code 26230120002, funded by the European Regional Development Funds), for the computational time and resources made available.

References

- [1] Todreas, N. E., Kazimi, M.S., Nuclear systems volume I: Thermal hydraulic fundamentals, 2nd edition, CRC Press, 2011.
- [2] Versteeg, H., Malalasekera, W., An Introduction to computational fluid dynamics: The finite volume method, 2nd edition, Prentice Hall, 2007.

Determination of velocity of propagation of Lamb waves in aluminium plate using piezoelectric transducers

Z. Lašová^a, R. Zemčík^a

^a*Faculty of Applied Sciences, University of West Bohemia, Univerzitní 8, 306 14 Plzeň, Czech Republic*

Propagation of Lamb waves and their interaction with material damage is one of the most promising methods in structural health monitoring (SHM). It requires a minimum of sensors for relatively large areas and enables to inspect visually inaccessible spots of structures. On the other hand, multimodal character and geometric dispersion of the Lamb waves complicate interpretation of collected data.

Two types of modes of Lamb waves exist – symmetric and antisymmetric. In low frequency range two zero-order modes dominate (denoted as S_0 , A_0). With increasing frequency higher modes occur. The Lamb waves are dispersive, which means their velocity depends on frequency (or wavenumber). These dependencies are called dispersion curves. The analytical solution for infinite plate can be obtained by a numerical solution of Lambs equations [2]. Thanks to fact that Lamb waves are periodical both in temporal and spatial domain, two dimensional Fast Fourier Transform (2D-FFT) can be used to obtain approximate dispersion curves [1, 3]. 2D-FFT is defined as

$$H(k, f) = \int_{-\infty}^{\infty} \int_{-\infty}^{\infty} u(x, t) e^{-i(kx+ft)} dx dt, \quad (1)$$

where k is wavenumber, f is frequency, ω is angular frequency. To collect the data for 2D-FFT, a finite element model of the plate was created. The model was a cross-section of the plate (plain strain assumed) of thickness 2 mm, loaded at one end by Hann pulse to excite broadband frequency response. The load was in form of time-dependent displacement with amplitudes and direction referring to the induced wave mode. The time histories of x-displacement at 4096 positions on the surface of plate were ordered as columns of a matrix transformed by 2D-FFT to frequency-wavenumber domain (see Fig. 1). The group velocity c_g defined by $\partial\omega/\partial k$ was calculated as difference $\Delta\omega/\Delta k$ for selected frequencies in range 100-500 kHz.

The measurement of Lamb waves velocities was performed using Acellent ScanSentry and piezoelectric patch transducers. The patches were applied to the aluminum plate of dimensions $800 \times 800 \times 2$ mm, one actuating the Lamb waves in the middle of the plate and a pair of sensors placed along the investigated direction. The Lamb waves were induced by windowed 5-period sine bursts, each having frequency between 100-500 kHz with step 50 kHz. The temporal signals were processed by wavelet transform to separate the significant (input) frequency. The velocities of zero-order modes (S_0 , A_0), calculated by comparison of peaks in time-frequency domain were compared to the results of 2D-FFT, as is presented in Fig. 2. The analytic dispersion curves were calculated in DC Toolbox [2].

Average error of 2D-FFT method in comparison with analytic solution is 3.4% (S_0) and 1.2% (A_0), the precision can be further increased by refinement of finite element mesh and

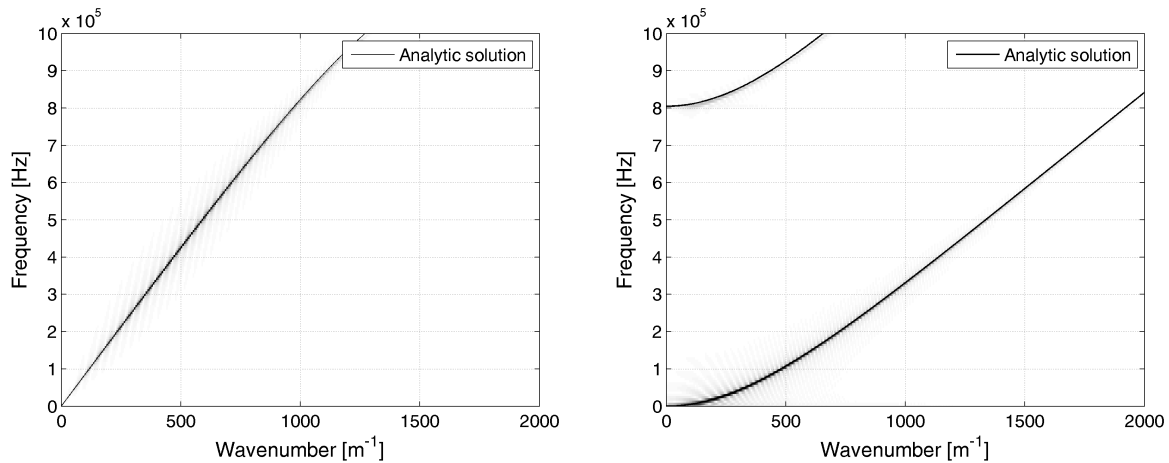


Fig. 1. Dispersion in wavenumber/frequency domain obtained by 2D-FFT (shaded) and analytic solution: symmetric modes (*left*) and antisymmetric modes (*right*)

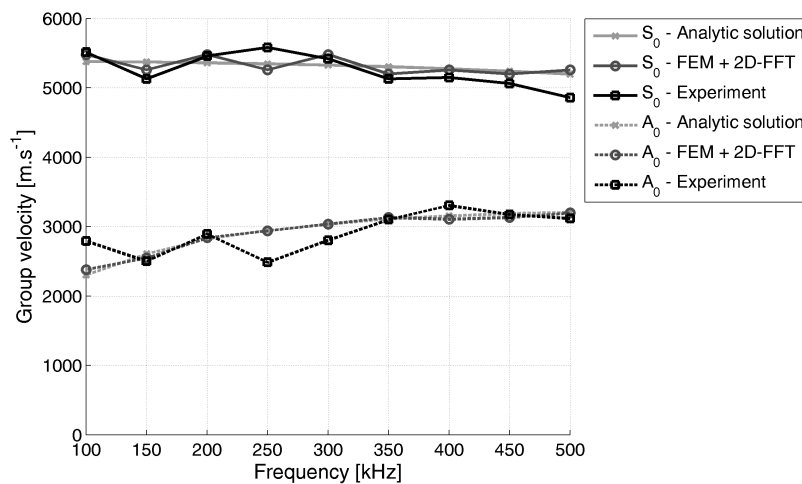


Fig. 2. Dependency of group velocity on frequency of zero-order modes calculated by analytic solution, FEM + 2D-FFT and measured

higher number of evaluated nodes. Average error of experimental results is 3.4% (S_0) and 6.6% (A_0).

Acknowledgement

This publication was supported by the project LO1506 of the Czech Ministry of Education, Youth and Sports.

References

- [1] Alleyne, D.N., Cawley, P., A two-dimensional Fourier transform method for the measurement of propagating multimode signals, *Journal of the Acoustical Society of America* 89 (3) (1991) 1159-1168.
- [2] Hora, P., Thick plate toolbox I., Research Report No. Z13xx/02, Laboratory of Material Diagnostics, Institute of Thermomechanics AS CR, v. v. i., Pilsen, 2002. (in Czech)
- [3] Hora, P., Červená, O., Determination of Lamb wave dispersion curves by means of Fourier transform, *Applied and Computational Mechanics* 6 (2012) 5-16.

Computational aspects of RBFN meta-models for reliability problems

M. Lepš^a, M. Šmejkal^a

^a*Czech Technical University in Prague, Faculty of Civil Engineering, Thákurova 7, 166 29 Prague 6, Czech Republic*

The reliability-based design optimization (RBDO) [1] seeks such designs that are cheap but still reliable. Despite the growing performance of computers, evaluation of reliability measures is still computationally expensive especially for small failure probabilities. In simulation techniques often used for the computation of reliability, the largest part of the computational time is devoted to a repeated evaluation of a performance function represented by a finite element model (FEM). In our approach, the original FEM model is replaced by a meta-model that has a similar response but it is faster to evaluate. Several samples still have to be evaluated with the original model; these samples are used for the meta-model construction. Radial basis functions (RBF) interpolation meta-models [3] are still computationally expensive since every construction sample increases a dimension of a linear system. This contribution focuses on a reduction of the computational effort spent on the RBF model evaluation during RBDO. In comparison to our previous versions, the resulting system of equation is factorized subsequently with the adaptive updating of the meta-model leading to substantial computational time reduction.

Radial basis functions is a special type of a neural network (NN) that is designed to simulate a black-box function $f(\mathbf{x})$ by its interpolation $F(\mathbf{x})$ given by the sum of basis functions multiplied by appropriate weights:

$$f(\mathbf{x}) \approx F(\mathbf{x}) = \sum_{i=1}^N b_i(\mathbf{x})w_i, \quad (1)$$

where \mathbf{x} is a vector of unknowns, $b_i(\mathbf{x})$ is a basis function of the i -th neuron, w_i is a weight of the i -th neuron and N is the total number of neurons creating the neural net. We have best experiences with “Gaussian” shape basis functions given by

$$b_i(\mathbf{x}) = e^{-\|\mathbf{x}-\mathbf{c}_i\|^2/r^2}, \quad (2)$$

where \mathbf{c}_i is a vector of coordinates of the center for the i -th basis function and r is a norm. Normalization ensures that basis functions will produce similar values for different scales in multidimensional spaces. The selection of the norm r is not crucial and therefore the most common form is used:

$$r = \frac{d_{max}}{\sqrt[dim]{dimN}}, \quad (3)$$

where d_{max} is a maximal distance within the domain, dim is the number of dimensions and N is the number of neurons. The weights $\mathbf{w} = [w_1, w_2, \dots, w_N]$ are obtained from the equality

between function values of a black-box function $\bar{\mathbf{y}} = [\bar{y}_1, \bar{y}_2, \dots, \bar{y}_N]$ and its NN approximation in the function basis centers:

$$[\mathbf{A}]_N \mathbf{w} = \bar{\mathbf{y}}. \quad (4)$$

This is a system of *linear* equations and if no other assumption is applied the matrix $[\mathbf{A}]_N$ is generally a full matrix. Note that for some given norm r and given positions of basis functions' centres the resulting system of linear equations is always the same.

However, the starting positions of RBF centres are rarely sufficient for the accuracy of RBF approximation. Therefore, more sampling points must be added as new centres to add more information to the system [2]. Thus the system of equations is growing with the added points:

$$\begin{bmatrix} A & A_{ij}^* \\ A_{ij}^{*T} & A^* \end{bmatrix}_{N+N^*} \begin{Bmatrix} w \\ w^* \end{Bmatrix} = \begin{Bmatrix} \bar{\mathbf{y}} \\ \bar{\mathbf{y}}^* \end{Bmatrix}, \quad (5)$$

where terms with asterisk $*$ are the added new terms. Since the original part, i.e. the matrix $[\mathbf{A}]$ and the vector $\bar{\mathbf{y}}$ does not change if the norm r remains the same, the factorization of the matrix $[\mathbf{A}]$ can save a lot of time if the updating procedure is repeated several times.

To show a potential of the proposed procedure, the scenario obtained during a commercial project has been simulated. The starting set contains 200 uniformly spaced centres in a 10D space, the updating procedure adds at each iteration another 200 random samples up to the total number of 2000 points. A simple LU factorization algorithm in Matlab is used. This new version is compared to the algorithm which factorizes the whole system of equations after each update. The starting times are the same for both versions, however, to solve the last update with 2000 points (the matrix $[\mathbf{A}]$ contains 4 millions entries), the proposed procedure is five times faster than the original one.

Of course, there is “no free lunch” and hence the proposed procedure has several limitations. The most important one is that the matrix $[\mathbf{A}]$ must be same for all updates and, therefore the norm r must be same for all updates. Note that in our previous version, this parameter was changing to reflect the increased number of points through the number N in Eq. (3).

Acknowledgement

This work was supported by the Grant Agency of the Czech Technical University in Prague, grant No. SGS16/037/OHK1/1T/11.

References

- [1] Dubourg, V., Adaptive surrogate models for reliability analysis and reliability-based design optimization, Ph.D. thesis, Blaise Pascal University - Clermont II, 2011.
- [2] Pospíšilová, A., Lepš, M., Multi-objective reliability-based design optimization utilizing an adaptively updated surrogate model, Proceedings of the 4th International Conference on Soft Computing Technology in Civil, Structural and Environmental Engineering, Prague, Czech Technical University, 2015, doi: 10.4203/ccp.109.8.
- [3] Waszczyszyn, Z., Ziemianski, L., Neural networks in the identification analysis of structural mechanics problems, In: Z. Mróz, G. E. Stavroulakis (eds.), Parameter identification of materials and structures, Springer, 2005, pp. 265-340.

Numerical simulation of a human body in aircraft crash scenarios

L. Lindstedt^a, J. Vychytil^b, T. Dziewonski^a, L. Hynčík^b

^a*Institute of Aeronautics and Applied Mechanics, Warsaw University of Technology, Nowowiejska 24, 00-665 Warsaw, Poland*
^b*New Technologies – Research centre, University of West Bohemia, Univerzitní 8, 306 14 Plzeň, Czech Republic*

Certification of seats for use in aircrafts includes their dynamic testing under conditions of emergency landing. In this work, we focus on tests prescribed by Federal Aviation Regulations (FAR), Part 23.562 and 25.562 [1]. The first one applies for normal, utility, acrobatic and commuter airplanes, while the latter one applies for transport airplanes. The test conditions in both regulations are generally similar. They simulate the aircraft crash with ground with the airplane's longitudinal axis canted downward 30° with respect to the horizontal plane. Since horizontal sleds are used in experimental setting, the seat/restraint system must be oriented in such a way, that the horizontal plane of the airplane is pitched up 60°, see Fig. 1. Acceleration pulse corresponding to the emergency landing is prescribed on the sled. In case of 23.562 test, the peak acceleration is 19g, while in the 25.562 test, the peak acceleration is 14g. The tests are performed using anthropometric test device (ATD) representing human body. For successful certification of seats, mechanical response of ATD has to satisfy certain conditions. Namely, spinal compression load, head injury criterion, femur compressive load and safety belts load shall not exceed defined limit values.

It is allowed to use computer modeling analytical techniques validated by dynamic tests to provide all pass/fail criteria identified above. Therefore, we perform numerical simulations using VIRTHUMAN model as a human body representative. Its skeleton is formed of rigid bodies interconnected via joints into a multi-body structure. Its surface is formed of deformable segments to account for deformations of soft tissues. Extensive validation has been performed concerning individual body parts as well as whole-body tests to ensure biofidelity of the model [3]. That is, mechanical response of the VIRTHUMAN model represents the response of a real human body. Calculation of standard injury criteria, as demanded for these particular tests, is possible via an automatic algorithm embedded in the model.

The model is seated in the sled with the pitch 60°. For both tests, rigid seat is considered. In addition, 14g test is performed also with cushioned seat, see Fig. 1. Two-points safety belt is used in accordance with experimental settings. Acceleration pulse is prescribed in horizontal direction, see Fig. 2. Results of the simulations in terms mechanical response of the VIRTHUMAN model are compared to experimental data provided in literature [2]. In this case, we focus on the overall kinematics of the human body and maximum spinal compression load in the lumbar area. Concerning 14g test with the rigid seat, simulation suggests less rotation of the body compared to experiments with ATD. However, maximum value of the lumbar compressive load is in a good agreement with experiments as the relative difference is approximately 4.2 %. In case of 19g test with rigid seat, maximum rotation of the VIRTHUMAN model is significantly lower than the ATD in experiment. The shape and phase of the lumbar force time-history is in correlation with experiment. However, the magnitude predicted by simulation is lower compared to experiment with the difference of approximately 31.5 %. Finally, 14g test with

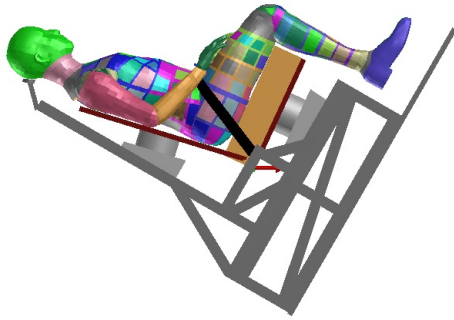


Fig. 1. Initial position of VIRTHUMAN model seated in a horizontal sled

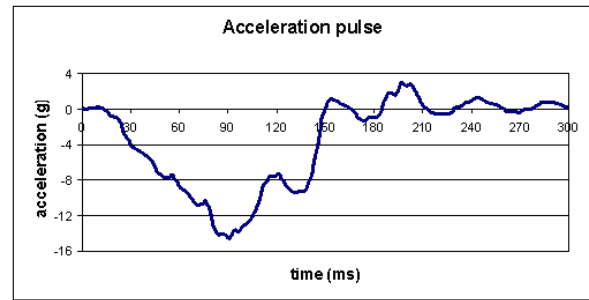


Fig. 2. Acceleration pulse prescribed for 14g test

the cushioned seat results in a clear difference between the rotation of VIRTHUMAN model and the ATD. This might be a result of the different seating procedure. On the other hand, time history of the lumbar compression is in a good correlation with experiment in both shape and phase. Good agreement is obtained also for magnitude; the difference of maximum values predicted by simulation in comparison with experiment is approximately 8.3 %.

An interesting result of the simulations is the increase of lumbar spine force for the cushioned seat in comparison with rigid one. However, such prediction is in correlation with experimental results. There is an experimental evidence proving the increase of force affecting the lumbar spine when the cushion is used. Hence, numerical simulations suggest VIRTHUMAN as a suitable tool for investigation of chosen aircraft crash scenario including the effect of lumbar force increase.

Acknowledgements

The work has been supported by the project SGS-2016-059.

References

- [1] Federal Aviation Administration, Methodology for dynamic seat certification by analysis for use in parts 23, 25, 27 and 29 airplanes and rotorcraft, Advisory Circular 20 - 146, FAA web page, 19.05.2003.
- [2] Lindstedt, L., Vychytil, J., Dziewonski, T., Hyncik, L., Numerical tests of the Virtual human model response under dynamic load conditions defined in Federal Aviation Regulation part 23.562 and 25.562 – preliminary study, Archive of Mechanical Engineering, 2016. (in press)
- [3] Vychytil, J., Mañas, J., Čechová, H., Špírk, S., et al., Scalable multi-purpose Virtual human model for future safety assessment, SAE Technical Paper 2014-01-0534, 2014.

Validation tests for gravity casting simulations

L. Lobovský^a, T. Mandys^a, J. Sklenička^b, O. Bublík^a, J. Vimmr^a

^aNTIS, Faculty of Applied Sciences, University of West Bohemia, Univerzitní 8, 306 14 Plzeň, Czech Republic

^bRTI, Faculty of Mechanical Engineering, University of West Bohemia, Univerzitní 8, 306 14 Plzeň, Czech Republic

Experimental investigation of real casting processes is challenging as the casting process often involves free surface flow of hot molten material inside a solid mold. Furthermore, heat transfer between the liquid and the mold and solidification of the cast material plays an important role. Nevertheless, it is possible to perform in situ measurements of casting flow patterns using e.g. X-ray radiography and to analyse heat transfer using e.g. thermocouple wires. In situ analysis of aluminium casting may be found e.g. in [3, 4], where a mass flow and heat transfer is studied in a simplified planar mold as suggested at 7th Conference on Modelling of Casting, Welding and Advanced Solidification Processes in 1995.

In order to provide an extensive data set measured under well controlled laboratory conditions, a water analogue model is often applied, such as in [1, 2]. In such cases, the mold can be made of transparent polymethylmethacrylate (PMMA) which allows for an application of standard optical measurements methods.

Within this study, a dedicated experimental test setup which enables execution of well-controlled benchmark tests is designed. These tests are then used for validation of an in-house developed gravity casting computational model.

Three benchmark tests are considered, two of them are focused on a gravity flow in a vertical labyrinth and the third one captures the flow in a long horizontal channel. One of the vertical labyrinth setups is displayed in Fig. 1 (left) and corresponding results of the in-house implemented computational software are shown in Fig. 1 (right).

Both vertical labyrinths as well as the horizontal channel are milled in transparent PMMA sheets. The tested fluid is originally at rest in the reservoir which is attached to the channel. The reservoir and the channel are separated by a removable gate. That is abruptly removed at time zero (the removal time is less than 0.03 s and the fluid is free to move within the rigid channel. The vertical labyrinth in Fig. 1 is designed so that the gate slides in a horizontal direction and the fluid experiences a free fall initially. The labyrinth channel cross-section is $10 \times 10 \text{ mm}^2$ in general. At the end, the channel opens to a $30 \times 30 \text{ mm}^2$ large chamber. The outer dimensions of the labyrinth and reservoir fit within the $110 \times 100 \text{ mm}^2$ box. The vertical labyrinth is designed so that an air does not get entrapped in the channel, except for the large bubbles in the free-fall area on the left.

The second vertical labyrinth (not depicted in this abstract) is designed so that the gate obstructs a horizontal channel and slides in vertical direction. Thus there is no free fall of the surge front and the fluid initially starts to move along the horizontal channel. This second labyrinth consists of channels of various cross-sections ranging from $3 \times 10 \text{ mm}^2$ to $10 \times 10 \text{ mm}^2$.

The horizontal labyrinth is also designed so that the fluid moves along the horizontal channel immediately after the gate removal. The horizontal channel winds in a 1 160 mm long spiral. The invariant channel cross-section is $3 \times 10 \text{ mm}^2$, where 3 mm is the height of the channel.

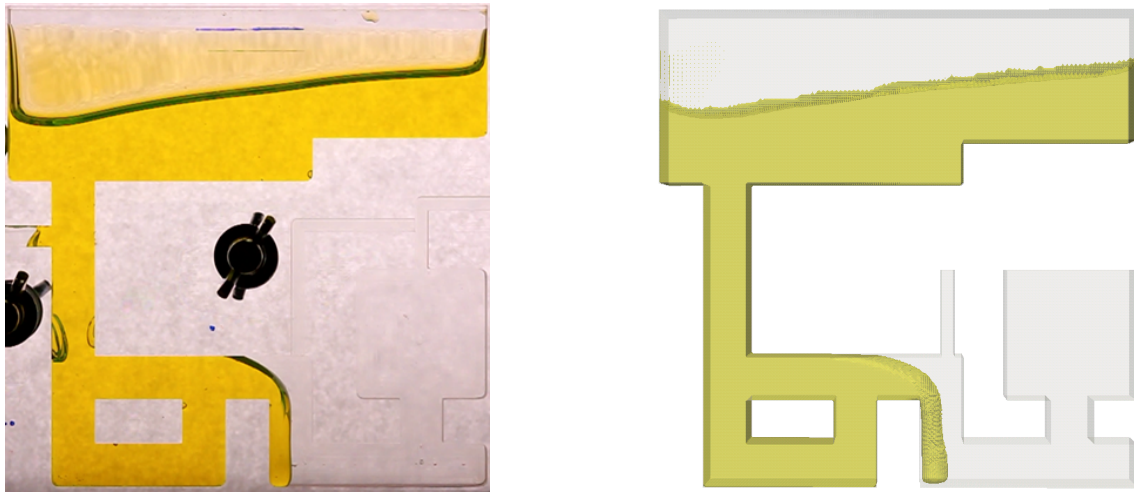


Fig. 1. Experimental (*left*) and computational (*right*) solution of gravity casting flow in a rigid vertical labyrinth

The benchmark tests are performed for viscous fluids at standard room temperature. A special attention is paid to propagation of the fluid through the channel and to the free surface shape evolution. Heat transfer as well as solidification are not considered. Physical properties (viscosity, surface tension, density) of the tested fluid are precisely assessed. Viscosity and surface tension are measured for both a fresh unused sample and a sample that was used for gravity casting inside the labyrinth.

For each labyrinth geometry, a series of 10 gravity casting experiments is conducted. After each run, the physical properties of the tested fluid are examined. The results of fluid propagation are consistent within the test series and show little variation. The largest deviations in results are achieved for the vertical labyrinth with initial free fall (Fig. 1). They may be attributed to variations of the initial free surface shape that is strongly influenced by the gate removal time.

The recorded data clearly show a sensitivity of the flow propagation on the value of fluid viscosity. In the narrow channels, an influence of surface tension is pronounced. The recorded evolution of the surge front profile and all results of the experimental analysis provide an extensive data set for benchmarking of the in-house developed computational software.

Acknowledgements

This work was supported by the grant project TA ČR, no. TA03010990, Josef Sklenička was supported by the project LO1502 of the Czech Ministry of Education, Youth and Sports.

References

- [1] Ha J., Cleary P., Ahuja V., Nguyen T., Simulation of die filling in gravity die casting using SPH and MAGMASoft, Proceedings of the 2nd International Conference on CFD in the Minerals and Process Industries, CSIRO, Melbourne, Australia, 1999, pp. 423-428.
- [2] Kowalewski T.A., Cybulski A., Sobiecki T., Experimental model for casting problems, Computational Methods and Experimental Measurements X, WIT Transactions on Modelling and Simulation 30 (2001) 179-188.
- [3] Sirrell, B., Holliday, M., Campbell, J., Benchmark testing the flow and solidification modeling of Al castings, JOM 48 (3) (1996) 20-23.
- [4] Zhao H., Ohnaka I., Zhu J., Modeling of mold filling of Al gravity casting and validation with X-ray in-situ observation, Applied Mathematical Modelling 32 (2008) 185-194.

Some results of simulations of flows with internal permeable walls

P. Louda^a

^a*Institute of Thermomechanics, Czech Academy of Sciences, Dolejškova 5, Praha 8, Czech Republic*

The work deals with the numerical modeling of compressible flow in a domain containing permeable walls in its interior, i.e. submerged in the fluid. The aim is to exclude direct simulation and find a model approximating the flow through a permeable plate driven by the static pressure difference between the sides of the wall.

The wind tunnel facility of the Institute of Thermomechanics AS CR is used in investigation of various types of blade cascades in transonic regimes. Different outlet angles, blade dimension and numbers lead to the use of perforated plates located inside the tunnel with the purpose of stream-lining the flow near model cascade boundaries, diminishing both shock wave reflections from tunnel walls and shear layers and expansion waves, formed on concave boundaries, penetrating the measured area [3, 5]. The plates are formed of sheet metal with staggered rows of holes with diameter comparable to their thickness. In 2D simulation, obviously a model of the plate is needed.

As a first attempt the model of Bohning/Doerffer [1] is used to compute the local flow rate through perforated plate from known pressure difference Δp . The flow rate is expressed as

$$\dot{m} = S_{aero} \rho_h v_h, \quad (1)$$

where ρ_h is density of fluid in the holes and v_h velocity in the holes related to Mach number M_h which is obtained from implicit relation for pressure difference. The model parameter for the type of porosity is S_{aero} which reached maximum of 25% in the original study. It should be noted that the model has been calibrated on surfaces with holes of small diameter compared to length of the hole and with low density of holes. The application to present perforated plates is therefore more a numerical experiment because no experimental calibration for S_{aero} nor the model itself exists.

The numerical simulation is based on Favre-averaged Navier-Stokes equations with the SST turbulence model [4]. The domain boundary approximates part of the wind tunnel with model cascade. The system is solved by cell-centered finite volume method with implicit discretization in time. The grid is of multi-block type with quadrilateral finite volumes. The inviscid flux is computed by AUSMPW+ scheme [2] and higher accuracy achieved by linear interpolation with van Leer limiter. The linear system is solved by a combination of direct block tri-diagonal solver and over-relaxation method.

As an example of numerical results, Fig. 1 shows computed schlieren images for 3 configurations with tip profile cascade in wind tunnel. In the case without internal walls the flow behind the cascade is disturbed by shock waves reflected on the shear layer from the end of bottom inlet channel boundary. Moreover expansion waves spread from this corner. In measurements, perforated plate is appended to the trailing edge of the second blade from below, and another plate prolongates the top inlet channel wall. The simulation where the plates are modelled as

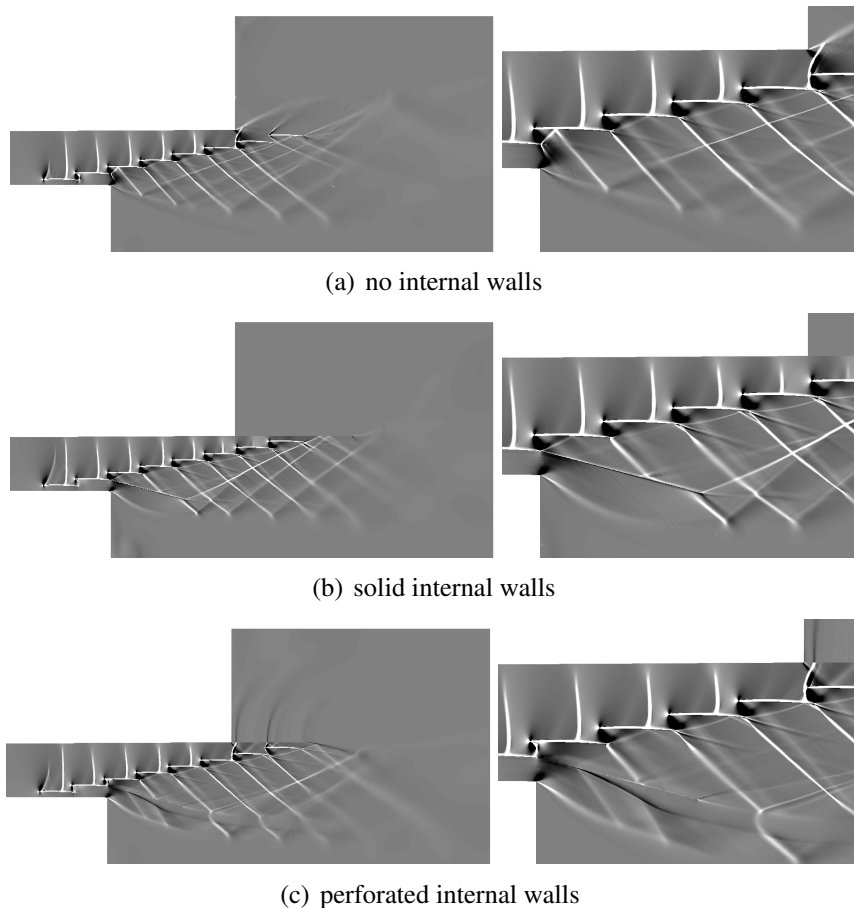


Fig. 1. Tip profile cascade in wind tunnel, outlet Mach number $M_{2is} \approx 1.88$

impermeable (solid) walls changes the angle of reflected shock waves. The permeable bottom wall shows weaker reflexions and little improved periodicity of the middle 3 blade channels. The S_{aero} has been set 0.5 here.

The numerical experiments so far enable to understand better forming of parasitic wave structures in the measuring section of the wind tunnel. The model of permeable wall needs further verification.

Acknowledgements

The work has been sponsored by the institutional support RVO 61388998 and by the Czech Science Foundation under grant 13-00522S.

References

- [1] Doerffer, P. P., Bohning, R., Modelling of perforated plate aerodynamics performance, *Aerospace Science and Technology* 4 (2000) 525-534.
- [2] Kim, K. H., Kim, C., Rho, O.-H., Methods for accurate computations of hypersonic flows I. AUSMPW+ scheme, *Journal of Computational Physics* 174 (2001) 38-80.
- [3] Luxa, M., Synáč, J., Šafařík, P., Šimurda, D., Causes and solution of aperiodicity of supersonic flow field downstream of a profile cascade, *Komunikacie* 14 (4A) (2012) 23-28.
- [4] Menter, F. R., Two-equation eddy-viscosity turbulence models for engineering applications. *AIAA Journal* 32 (8) (1994) 1598-1605.
- [5] Šimurda, D., Luxa, M., Šafařík, P., Synáč, J., Rudas, B., Measurements on supersonic turbine cascades – Methodical approach, In: *Proceedings of the XXII Symposium on Measuring Techniques in Turbomachinery*, Lyon, 2014.

Semi-automatic finite element mesh generation using medical imaging data

V. Lukeš^a, M. Jiřík^a

^aFaculty of Applied Sciences, University of West Bohemia, Univerzitní 8, 306 14 Plzeň, Czech Republic

The patient specific computational modeling based on the finite element method requires tools for generating geometrical models of body organs using data acquired from computed tomography (CT), magnetic resonance imaging (MRI) or positron emission tomography (PET) scans. The medical imaging data are stored as a series of DICOM files which contain body scans in parallel planes. This multi-frame image set has to be processed by a segmentation algorithm to obtain 3D volumetric data that are further used for generation of finite element meshes. We use a semi-automatic segmentation approach based on the graph-cut method, see [2] and [1], which combines advantages of region and edge segmentation algorithms.

The segmentation process results in a 3D voxel array that can be directly transformed into a stair-step shaped FE mesh. It is the fast and easiest way of generating FE meshes but the usage is usually limited only for testing purposes or as a quick preview of tissue geometry. The marching cubes algorithm [4] is used to generate a smooth triangular surface meshes of the segmented body part. To improve the quality of the resulting meshes the Taubin smoothing filter [6, 7] can be applied. This filter is able to preserve the total volume of the segmented tissue represented by the mesh. This feature is essential for the credibility of the FE model and its results.

A volumetric FE mesh is obtained by applying a tetrahedral (or hexahedral, if the geometry is suitable for that) meshing function to the generated surface mesh. We use the meshing tool called *gms* [3], it is an open source 3D finite element grid generator which allows to control meshing process by a wide set of parameters.

We demonstrate the segmentation process and mesh generation on the liver parenchyma, see Fig. 1 and [5]. In general, the automatic liver segmentation is a complex task due to a low density contrast to adjacent organs like the stomach or hearth. The way from medical scans to a FE mesh is more straightforward in the case of bones or well distinguishable body parts.

Acknowledgment

This publication was supported by the project LO1506 of the Czech Ministry of Education, Youth and Sports.

References

- [1] Boykov, Y., Funka-Lea, G., Graph cuts and efficient N-D image segmentation, *International Journal of Computer Vision* 70 (2006) 109-131.
- [2] Boykov, Y., Veksler, O., Zabih, R., Fast approximate energy minimization via graph cuts, *Pattern Analysis and Machine Intelligence* 23(11) (2001) 1222-1239.

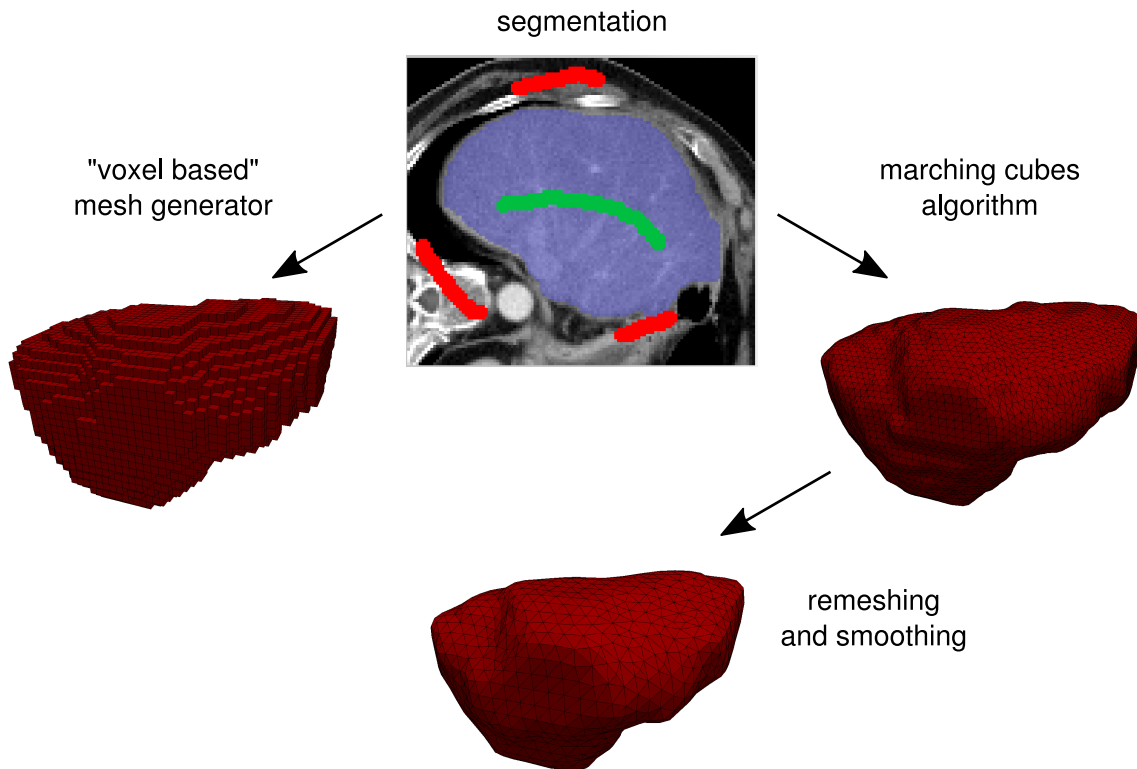


Fig. 1. Finite element meshes of the liver parenchyma generated by the "voxel based" generator and marching cubes algorithm

- [3] Geuzaine, C., Remacle, J.-F., Gmsh: A three-dimensional finite element mesh generator with built-in pre- and post-processing facilities, *International Journal for Numerical Methods in Engineering* 79(11) (2009) 1309-1331.
- [4] Lorensen, W. E., Cline, H. E., Marching Cubes: A high resolution 3D surface construction algorithm, *Computer Graphics* 21(4) (1987) 163-169.
- [5] Lukeš, V., Jiřík, M., Jonášová, A., Rohan, E., Bublík, O., Cimrman, R., Numerical simulation of liver perfusion: From CT scans to FE model, *Proceedings of the 7th European Conference on Python in Science (EuroSciPy 2014)*, Cambridge, 2014, pp. 79-84, <https://arxiv.org/abs/1412.6412>.
- [6] Taubin, G., A signal processing approach to fair surface design, *Proceedings of the 22nd annual conference on Computer graphics and interactive techniques – ACM SIGGRAPH 95*, New York, 1995, pp. 351-358.
- [7] Taubin, G., Geometric signal processing on polygonal meshes, *Proceedings of the conference Eurographics 2000 – State of the Art Report*, 2000, doi: 10.2312/egst.20001029.

Surface sensitivities computation for turbine blades using OpenFOAM

F. Moravcová^a, V. Lukeš^a, E. Rohan^a

^aFaculty of Applied Sciences, University of West Bohemia, Univerzitní 8, 306 14 Plzeň, Czech Republic

The computation of surface sensitivities is an essential step of the shape optimization process since they are correlated with the normal displacements of the geometry boundary [2]. Here we apply the continuous adjoint method [1] to incompressible flows around turbine blades [3]. The constrained optimization problem, which consists of minimizing the cost function $J = J(\beta, \mathbf{v}, p)$ subject to the constrains $\mathcal{R}(\beta, \mathbf{v}, p) = 0$, is tackled by introducing a Lagrange function \mathcal{L}

$$\mathcal{L} := J + \int_{\Omega} (\mathbf{u}, q) \mathcal{R} d\Omega, \quad (1)$$

where β represents the design variables, \mathbf{v} and p are the velocity and pressure, respectively, and \mathbf{u} and q the Lagrange multipliers, also called adjoint variables. The constrains \mathcal{R} denote the state problem; in our case, the incompressible, steady-state Navier-Stokes equations in the flow domain Ω with appropriated boundary conditions on $\partial\Omega$ which consists of five parts: inlet, outlet, blade wall and periodic boundaries. For computing the sensitivity of the cost function, we have to compute the total variation of \mathcal{L} ; $\delta\mathcal{L} = \delta_{\beta}\mathcal{L} + \delta_{\mathbf{v}}\mathcal{L} + \delta_p\mathcal{L}$. If, moreover, the Lagrange variables are chosen such that

$$\delta_{\mathbf{v}}\mathcal{L} + \delta_p\mathcal{L} = 0, \quad (2)$$

then, the total variation of \mathcal{L} reduces to

$$\delta\mathcal{L} = \delta_{\beta}\mathcal{L} = \delta_{\beta}J + \int_{\Omega} (\mathbf{u}, q) \delta_{\beta}\mathcal{R} d\Omega. \quad (3)$$

The condition (2), i.e. the vanishing of the variation of \mathcal{L} w.r.t. the state variables, leads to a system of equations, the adjoint problem, which fixes the solution (\mathbf{u}, p) . On the other hand, if the cost function J is formulated as integrals over inlet and/or outlet (and do not contain a contribution from the domain interior nor do not involve the flow quantities on the blade wall) the local contribution of (3) at some specific point on the blade wall is given by

$$s_{wall} = -\nu(\mathbf{n} \cdot \nabla) \mathbf{u} \cdot (\mathbf{n} \cdot \nabla) \mathbf{v}. \quad (4)$$

Both the primal and the adjoint problems are solved using the open-source OpenFOAM toolbox, and the sensitivities (4) are evaluated in a post-processing step using an user-defined utility. The cost function is commonly chosen as the the dissipated power,

$$J := - \int_{\Gamma_{inlet} \cup \Gamma_{outlet}} \left(p + \frac{1}{2} v^2 \right) \mathbf{v} \cdot \mathbf{n} d\Gamma, \quad (5)$$

and two different blade geometries are tested. As a result, the distribution of adjoint velocity in the flow domain and the distribution of sensitivities over the blade wall are shown in Fig. 1.

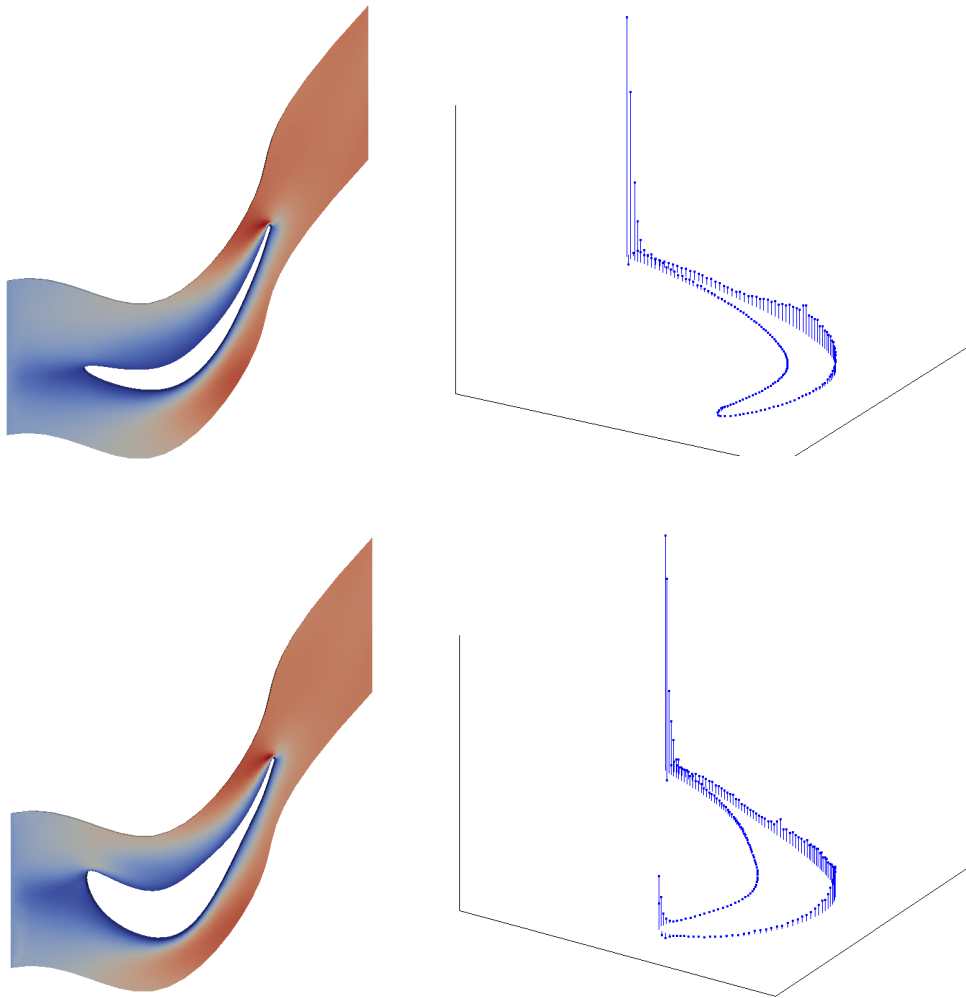


Fig. 1. Adjoint velocity magnitude $|\mathbf{u}|$ in flow domain Ω and surface sensitivity over blade wall for two selected geometries (normalized values in range from 0 to 1)

Acknowledgements

This work was supported by the projects MSMT LO1506 and TA ĀR 01020068.

References

- [1] Othmer, C., A continuous adjoint formulation for the computation of topological and surface sensitivities of ducted flows, *International Journal for Numerical Methods in Fluids* 58 (2008) 861-877.
- [2] Pironneau, O., *Optimal shape design for elliptic systems*, Springer, Berlin, 1984.
- [3] Rohan, E., Lukeš, V., *Methods for the parametric description of the shape of turbine blades and the formulation of optimization problem*. Research Report No. 0009/2014 of the project TA ĀR TE01020068, University of West Bohemia, Pilsen, 2014. (in Czech)

Comparison of local and global critical time step size estimators in explicit dynamics

M. Mračko^a, A. Tkachuk^b, R. Kolman^a, J. Plešek^a, D. Gabriel^a

^a*Institute of Thermomechanics, The Czech Academy of Sciences, Dolejškova 1402/5, 182 00 Praha 8, Czech Republic*

^b*Institute for Structural Mechanics, University of Stuttgart, Pfaffenwaldring 7, 70550 Stuttgart, Germany*

Nowadays, a standard tool for simulations of dynamic response or impact-contact problem of bodies and structures is the explicit Finite Element Analysis [3]. Generally, explicit time integration is only conditionally stable. For the central difference method in time, the stable/critical time step size is limited by the highest eigenfrequency of the system of interest. Since the critical time step size is inversely proportional to this maximum eigenfrequency, as $\Delta t_{cr} = 2/\omega_{max}$, a task of stable determining of time step size leads to numerical solving of a maximum eigenvalue. Several global methods for accurate computation of the highest eigenfrequency exist, for examples, Power iterations, methods based on Rayleigh quotient, Lanczos algorithm, etc. But these methods are extremely computationally expensive and practically it is not possible to use them in real computations. For that reason, a set of cheaper local estimators (e.g. Courant–Friedrichs–Lewy condition, based on the Gerschgorin theorem, etc.) have been proposed. These estimators of stable time step size use only nodal or elemental data.

As it is shown in this contribution, global and local estimates for regular meshes with lumped mass matrix give the same time step sizes. However, this is not true for irregular finite element (FE) meshes or significantly distorted elements. In this contribution, the main attention is paid to comparison of these mentioned methods for estimations of time step size for explicit integration in one-dimensional FEM computations on different meshes with/without boundary conditions.

Numerical tests for five different meshes (see Table 1) were performed on a truss with the following parameters: length of the truss $L = 10$ m, cross section area $A = 0.1$ m², mass density $\rho = 7850$ kg/m³, Young’s modulus $E = 210$ GPa. Two cases of boundary conditions were taken into account: a free-free truss and a fixed-free truss, 2-node elements were used.

Table 1. Partition of a truss; numbers mean finite element lengths

Regular mesh	1.667	1.667	1.667	1.667	1.667	1.667
Irregular mesh 1	1.68	1.65	1.67	1.65	1.67	1.68
Irregular mesh 2	1	0.5	3	1.5	2	2
Irregular mesh 3	0.5	1	1.5	2	2	3
Irregular mesh 4	3	2	2	1.5	1	0.5

For computation of the exact maximum eigen-value, the solving of generalized eigen-value problem respecting boundary conditions was used. However, one can substitute this strategy, for e.g., the Power iterations method [5] or Rayleigh quotient [1], which numerically solve only the maximum eigen-value. One of often used local method is based on Courant number [2] and

it estimates maximum eigen-value of one-dimensional linear FE with the lumped matrix matrix [3] from $\omega_{max}^e = 2c/l_e$, where $c = \sqrt{E/\rho}$ is the wave speed in a truss and l_e is the element length (in 1D). Another approach is a method based on the Gerschgorin's theorem [4]. This leads to nodal estimation

$$\omega_{max}^{Ger} \leq \max_i \sqrt{\frac{\sum_{j=1}^n |K_{ij}|}{M_{ii}}},$$

where K is stiffness matrix, M is lumped mass matrix and n is number of degrees of freedom of the problem of interest. This strategy can be performed both on local and global level.

All the results are normalized with respect to exact maximum eigenfrequency given by "Eig". Results of time step size estimation are presented in Table 2, where "Ger." stands for the Gerschgorin's theorem based method, "w/o BC" and "w BC" means "without" and "with boundary conditions", respectively. Based on the numerical tests, we can say than the global Gerschgorin's theorem based method produces stable time step size for each tested FE mesh.

Table 2. Normalized estimations ω_{max} with respect to the exact value "Eig"

Mesh	max $\frac{2c}{l_e}$	Local		Global w/o BC		Local			Global w BC	
		Ger.	Eig	Ger.	Eig	Ger.	Eig	Ger.	Eig	
Regular	1.000	1.000	1.000	1.000	1.000	1.009	1.009	1.009	1.009	1.000
Irregular 1	1.010	1.010	1.010	1.038	1.000	1.019	1.019	1.019	1.013	1.000
Irregular 2	1.706	1.706	1.706	1.207	1.000	1.814	1.814	1.814	1.171	1.000
Irregular 3	1.202	1.202	1.202	1.202	1.000	1.916	1.916	1.916	1.106	1.000
Irregular 4	1.202	1.202	1.202	1.202	1.000	1.202	1.202	1.202	1.202	1.000

Acknowledgements

The work has been supported by the Czech Science Foundation (Gr. No. 16-03823S and 15-20666S), the Technology Agency of the Czech Republic, (Gr. No. TH01010772) and the bilateral mobility project No. DAAD-16-12 within institutional support RVO:61388998.

References

- [1] Benson, D.J., Stable time step estimation for multi-material Eulerian hydrocodes, *Computer Methods in Applied Mechanics and Engineering* 167 (1) (1998) 191-205.
- [2] Flanagan, D.P., Belytschko, T., Eigenvalues and stable time steps for the uniform strain hexahedron and quadrilateral, *Journal of Applied Mechanics* 51 (1) (1984) 35-40.
- [3] Hughes, T.J.R., *The finite element method: Linear and dynamic finite element analysis*, Dover Publications, New York, 2000.
- [4] Kulak, R.F., *Critical time step estimation for three-dimensional explicit impact analysis*, Elsevier, Amsterdam, 1989, pp. 155-163.
- [5] Salkuyeh, D.K., Toutounian, F., Optimal iterate of the power and inverse iteration methods, *Applied Numerical Mathematics* 59 (7) (2009) 1537-1548.

Non-uniform torsion modal analysis of thin-walled open cross-sections with effect of axial force

J. Murín^a, M. Aminbaghai^b, J. Hrabovský^a

^aDepartment of Applied Mechanics and Mechatronics, IAMM FEI STU in Bratislava, Ilkovičova 3, 812 19 Bratislava, Slovakia
^bVienna University of Technology, Institute for Mechanics of Materials and Structures, Karlsplatz 13, A-1040 Vienna, Austria

In this contribution, the paper [1] is extended on uniform and non-uniform torsional analysis of the beams with longitudinal continuously varying axial force. The differential equation of beam with longitudinally variation of axial forces are formulated for Saint-Venant and non-uniform torsional deformations including the inertial line moments. In non-uniform torsion, the part of the bicurvature caused by the bimoment is taken into account as the warping degree of freedom, and the Secondary Torsional Moment Deformation Effect (STMDE) is also considered. A general semi-analytical solution of the differential equation is presented and the transfer matrix relation is established, from which the finite element equations of the two nodal straight beam finite element are derived. Omitting the external load the FEM equation for torsional natural free vibration are obtained. The torsional modal analysis of the thin walled beams with open I cross-section (Fig. 1) is done. Our results are compared with the ones obtained by commercial FEM code. The effect of axial force is evaluated.

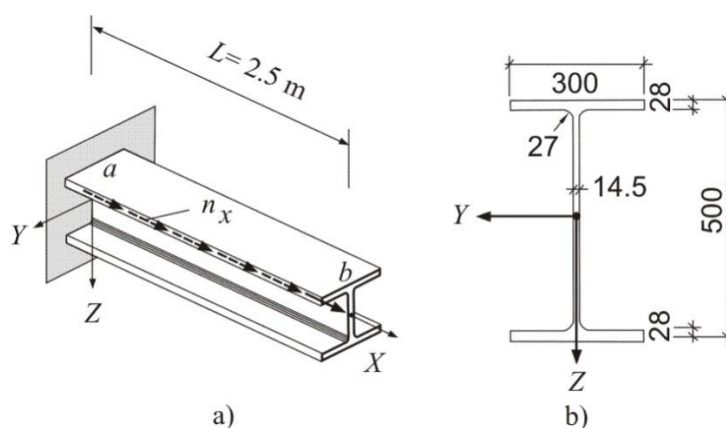


Fig. 1. Cantilever beam with an I cross-section: a) system, axial force, torsional moment, b) cross-section

Table 1 shows the comparison of the results for the eigenfrequencies obtained by proposed method and with corresponding results obtained by ANSYS [2] with 3D solid finite elements (16080 of SOLID168 elements) for a cantilever beam with an I cross-section and varying axial force $N^{\text{II}}(x) = n_x(L - x)$, $\forall n_x \in [-3000, 3000]$, kN/m.

As shown in Table 1, an excellent agreement of our non-uniform torsion results with the benchmark ANSYS solution is obtained. As expected, the Saint-Venant solution produces incorrect eigenfrequencies. The main novelty of this contribution is:

- inclusion of the varying axial force and the STMDE into the differential equation for non-

Table 1. Comparison of the results for the eigenfrequencies for a cantilever beam with an I cross-section and varying axial force

n_x	-3000				-2000			
	Saint-Venant torsion		Warping torsion:		Saint-Venant torsion		Warping torsion:	
	proposed method	ANSYS	proposed method	ANSYS	proposed method	ANSYS	proposed method	ANSYS
f_1	11.92	---	42.35	41.39	16.23	---	43.33	42.02
f_2	43.16	---	217.03	213.24	52.74	---	218.08	213.86
f_3	72.88	---	543.14	550.76	88.41	---	544.33	551.55

n_x	-1000				0				1000			
	Saint-Venant torsion		Warping torsion:		Saint-Venant torsion		Warping torsion:		Saint-Venant torsion		Warping torsion:	
	proposed method	ANSYS	proposed method	ANSYS	proposed method	ANSYS	proposed method	ANSYS	proposed method	ANSYS	proposed method	ANSYS
f_1	19.14	---	44.28	42.63	21.50	---	45.21	43.26	23.55	---	46.12	43.83
f_2	59.24	---	219.12	214.49	64.51	---	220.16	215.24	69.07	---	221.19	215.72
f_3	98.96	---	545.52	552.34	107.51	---	546.70	553.49	114.90	---	547.88	553.91

n_x	2000				3000			
	Saint-Venant torsion		Warping torsion:		Saint-Venant torsion		Warping torsion:	
	proposed method	ANSYS	proposed method	ANSYS	proposed method	ANSYS	proposed method	ANSYS
f_1	25.38	---	47.02	44.42	27.06	---	47.89	44.96
f_2	73.16	---	222.22	216.33	76.89	---	223.24	216.93
f_3	121.51	---	549.05	554.70	127.54	---	550.22	555.48

uniform torsion of thin walled beams with open and closed cross-sections according to the second order torsional warping theory;

- formulation of the transfer matrix method and the finite element method equations for elastic and modal analysis of non-uniformly twisted beams according the second order torsional warping theory.

Acknowledgements

This paper has been supported by the Slovak Grant Agencies VEGA No. 1/0453/15.

References

- [1] Aminbaghai, M., Murin, J., Hrabovsky, J., Mang, HA., Torsional warping eigenmodes including the effect of the secondary torsion moment on the deformations, Engineering Structures 106 (2016) 299–316.
- [2] ANSYS Swanson Analysis System, Inc., 201 Johnson Road, Houston, PA 1534/1300, USA.

Structural dynamic modification of the vibrating beam structures

M. Nad^a

^a Faculty of Materials Science and Technology in Trnava, Slovak University of Technology in Bratislava, J. Bottu 25,
917 24 Trnava, Slovak Republic

Structural dynamic modification (SDM) has become one of the popular and perspective tool applied in the design, resp. modification of the structure to achieve the required dynamic properties. The main objective of SDM, the modification so-called spatial properties (mass, stiffness, damping) of computational model of the mechanical system by means of changes in the structural design parameters are expected. As a result of spatial properties modification is a change in the modal properties of the structures.

The general equation of motion of the vibrating damped mechanical system with a finite number of degrees of freedom n , which is in the original structural state, i.e. in the state before the structural modification, has the form

$$\mathbf{M}_0 \ddot{\mathbf{v}} + \mathbf{B}_0 \dot{\mathbf{v}} + \mathbf{K}_0 \mathbf{v} = \mathbf{f}, \quad (1)$$

where \mathbf{M}_0 , \mathbf{B}_0 , \mathbf{K}_0 are coefficient matrices of the system before its structural modification.

Using the modal matrix Φ_0 , determined from the eigenvalue problem solution for equation (1), the modal transformation from physical space to the so-called modal space is made by

$$\mathbf{v} = \Phi_0 \mathbf{q}_0, \quad (2)$$

and

$$\ddot{\mathbf{q}}_0 + \Gamma_0 \dot{\mathbf{q}}_0 + \Lambda_0 \mathbf{q}_0 = \Phi_0^T \mathbf{f}, \quad (3)$$

where Γ_0 is matrix of modal damping coefficients, Λ_0 is spectral matrix and \mathbf{q}_0 ($\dot{\mathbf{q}}_0$, resp. $\ddot{\mathbf{q}}_0$) is the vector of generalized coordinates (velocities, resp. accelerations).

If the vibrating mechanical system does not have the required dynamic properties, the change of selected structural parameters is needed. The changes in structural parameters cause changes of coefficient matrices, i.e. changes in the mass matrix, damping matrix and stiffness matrix. These structural changes can be characterized by the new coefficient matrices of modified vibrating system, which are expressed by

$$\mathbf{M}_M = \mathbf{M}_0 + \Delta \mathbf{M}_{0M}, \quad (4a)$$

$$\mathbf{B}_M = \mathbf{B}_0 + \Delta \mathbf{B}_{0M}, \quad (4b)$$

$$\mathbf{K}_M = \mathbf{K}_0 + \Delta \mathbf{K}_{0M}, \quad (4c)$$

where $\Delta \mathbf{M}_{0M}$ is the modifying mass matrix, $\Delta \mathbf{B}_{0M}$ is the modifying damping matrix, $\Delta \mathbf{K}_{0M}$ the modifying stiffness matrix. These matrices represent the change in vibrating mechanical system from initial state 0 into the modified state of M .

Then the equation of motion of the modified system has the following form

$$\mathbf{M}_M \ddot{\mathbf{v}} + \mathbf{B}_M \dot{\mathbf{v}} + \mathbf{K}_M \mathbf{v} = \mathbf{f} \quad (5)$$

and using the new modal transformation

$$\mathbf{v} = \Phi_0 \mathbf{q}_0 = \Phi_0 \Phi_{0M} \mathbf{q}_M = \Phi_M \mathbf{q}_M, \quad (6)$$

the equation of motion of the modified system is transformed into the following form

$$\ddot{\mathbf{q}}_M + \Gamma_M \dot{\mathbf{q}}_M + \Lambda_M \mathbf{q}_M = \Phi_{0M}^T \Phi_0^T \mathbf{f}, \quad (7)$$

where Γ_M is modified modal damping coefficients matrix and Λ_M is modified spectral matrix.

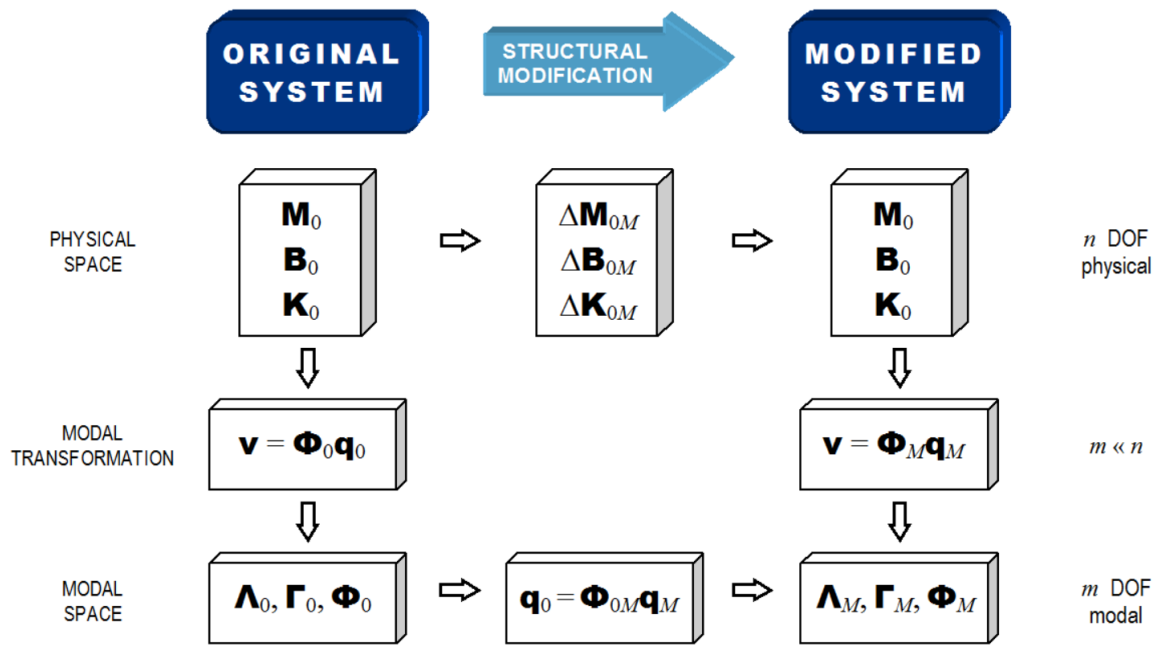


Fig. 1. Process of SDM of vibrating mechanical systems

Since the beam is a fundamental structural component of different structures and technical equipment, many practical ways, which lead to the modification of the modal properties of beam structures can be carried out.

Acknowledgements

The work has been supported by the grant project VEGA-1/0520/16 and institutional project MTF2016/006.

References

- [1] Avitable, P., Twenty years of structural dynamic modification - A review (based on a paper presented at IMAC-XX), Sound and Vibration, 2003, 14-25.
- [2] Izrael, G., Bukoveczky, J., Gulán, L., Influence of nonstandard loads onto life of chosen modules of mobile working machines, Machine Design 3 (1) (2011) 13-16.
- [3] Meirovitch, L., Analytical methods in vibrations, McMillan Company, London, 1987.
- [4] Nađ, M., Modification of modal characteristics of vibrating structural elements, Scientific Monographs, Hochschule Anhalt, Köthen, 2010.
- [5] Rolník, L., Structural dynamic modification of lathe tool body, PhD. Thesis, Slovak University of Technology in Bratislava, 2015.

Subcritical micro-crack growth in particulate ceramic composite with residual stresses

L. Náhlík ^{a,b}, K. Štegnerová ^{a,b}, Z. Majer ^b, P. Hutař ^a

^a Institute of Physics of Materials, Czech Academy of Sciences, Žitkova 22, 616 62 Brno, Czech Republic

^c Faculty of Mechanical Engineering, Technická 2, 616 69 Brno, Czech Republic

In ceramic based materials, typically in glass-ceramic composites filled by alumina particles, can the existing cracks propagate under an applied stress with stress intensity factor K_I lower than the fracture toughness K_{Ic} value [1, 4, 6, 7]. This phenomenon is generally called subcritical crack growth (SCCG) and it is related to fatigue or stress corrosion [9]. The stress corrosion manifests by a hydrolysis reaction occurring between the composite material in the crack tip and the water in the environment [5]. This degradation mechanism is described in many publication [2, 3, 8].

Nowadays, the composite materials are often used in engineering applications. For example in the microelectronics, low temperature co-fired ceramics (LTCC) consisting of ceramic grains (alumina) embedded in a glass matrix (borosilicate glass) are used as substrate material for production of printed circuit boards. The main advantage of LTCC is low sintering temperature (ca 850°C), which is possible due to use of the glass matrix with a low melting point.

Generally, the mechanical behavior of composite is associated with particle size and properties, matrix properties, volume filler fraction, etc. Moreover, the manufacturing process, where both phases (matrix and particles) are sintered at relatively high temperature, leads to the presence of the residual stresses due to mismatch of coefficients of thermal expansion. Note that several effects taking place in this kind of composites have been studied individually in the works.

The present paper is focused on the role of residual stresses in crack propagation process in dependence on used shape of particles. A two-dimensional finite element model was developed in software ANSYS to analyze the crack growth in LTCC composites. The used material data were published in [1]. Several geometric configurations (particle size and shape, position of initial crack, etc. were varied) were numerically analyzed. Two basic states, composite with and without consideration of residual stresses was studied, and corresponding conclusions were formulated.

Finite element (FE) method and commercial system ANSYS were chosen for the numerical modelling of crack propagation. Numerical model of LTCC assumes that alumina particles are homogeneously distributed in the glass matrix. The diameter of the spherical particles is 1 μm and the volume filler fraction (VFF) is 25%. The initial crack is modelled at certain interval from the center line. The initial length a_i was set to 0.05 μm . The stress intensity factors (K_I and K_{II}) are numerically calculated and the direction of next crack propagation (ϕ) is evaluated in each step of the simulations. The crack increment $\Delta a = 0.05 \mu\text{m}$ is considered in all calculations. Fine mesh is created around the crack tip to obtain accurate results. All calculations are performed under condition of plane strain. The model contains from 80 000 to 200 000 PLANE 183 elements in dependence on model geometry.

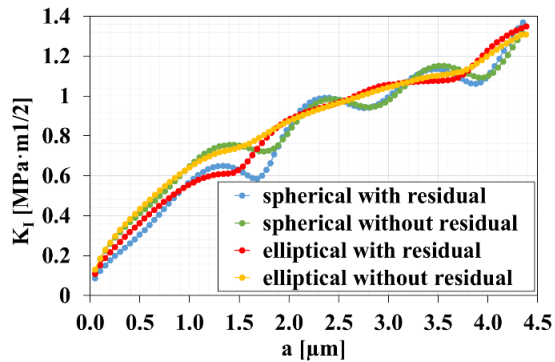


Fig. 1. Dependence of stress intensity factor on the crack length for different particle shapes (VFF = 25%, $c/b = 0.4$)

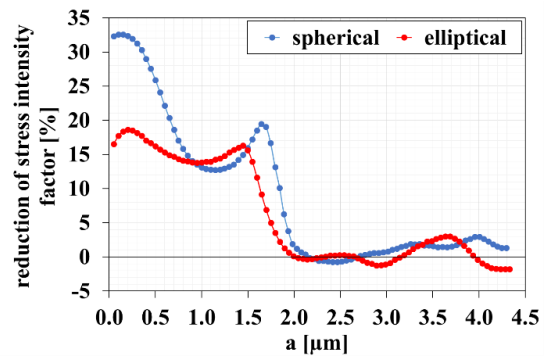


Fig. 2. Reduction of stress intensity factors due to residual stresses in dependence on the crack length for different particle shapes (VFF = 25%, $c/b = 0.4$)

The influence of residual stresses on crack propagation in ceramic particulate composite is evaluated using numerical modelling. Two-dimensional computational model loaded by applied remote stress is developed. Material characteristics of low temperature co-fired ceramics are considered. To determine the influence of residual stresses two states (with and without residual stresses) are considered and crack propagation under both of them is simulated.

The results can be summarized to following points: i) the presence of residual stresses significantly reduces values of stress intensity factors (up to 30% in the studied case, see Figs. 1 and 2), i.e. significantly influence the crack behavior in particulate composite and the crack propagation rate, ii) shielding effect of residual stresses contributes to the crack deflection close to the particle – crack propagates only in the matrix without direct interaction with particles, iii) the shape of the particles influences the reduction effect of residual stresses.

Results obtained contribute to a better understanding of the role of residual stress in the micro-crack propagation in particulate ceramic composite under both unstable and stable crack extensions.

Acknowledgements

This research was supported through grant GA15-09347S of the Czech Science Foundation and by research infrastructure IPMinfra (www.ipminfra.cz).

References

- [1] Bermejo, R., Supancic, P., Krautgasser, C., Morrell, R., Danzer, R., Subcritical crack growth in low temperature co-fired ceramics under biaxial loadig, *Engineering Fracture Mechanics* 100 (2013) 108-121.
- [2] Danzer, R., *Sub-critical crack growth in ceramics*, Pergamon Press, Oxford, 1994.
- [3] Krautgassera, C., Chlup, Z., Supancic, P., Danzer, R., Bermejo, R., Influence of subcritical crack growth on the determination of fracture toughness in brittle materials, *Journal of the European Ceramic Society* 36 (2016) 1307-1312.
- [4] Majer, Z., Pletz, M., Krautgasser, C., Náhlík, L., Hutař, P., Bermejo, R., Numerical analysis of sub-critical crack growth in particulate ceramic composites, *Procedia Materials Science* 3 (2014) 2071-2076.
- [5] Michalske, T.A., Freiman, S.M., A molecular mechanism for stress corrosion in vitreous silica, *Journal of the American Ceramic Society* 66 (1983) 284-288.
- [6] Munz, D., Fett, T., *Ceramics: Mechanical Properties, Failure Behaviour, Materials Selection*, Springer-Verlag, Berlin Heidelberg, 1999.
- [7] Smedskjaer, M.M., Bauchy, M., Sub-critical crack growth in silicate glasses: Role of network topology, *Applied Physics Letters* 107 (2015) 141.
- [8] Schoeck, G., Thermally activated crack-propagation in brittle materials, *International Journal of Fracture* 44 (1990) 1.
- [9] Wiederhorn, S.M., Proof testing of ceramic materials—an analytical basis for failure prediction, *Fracture Mechanics of Ceramics* 2 (1974) 613-646.

Computational simulation of additional effects in the sealing gap

N. Nováková^a, V. Habán^a, M. Hudec^a

^a Faculty of Mechanical Engineering, Brno University of Technology, Technická 2896/2, 616069 Brno, Czech Republic

Sealing gaps are important components of many mechanical machines. Additional effects in these sealing gaps may cause a destruction of the machine when sealing gaps are designed inaccurately. Experimental measurements were performed at the Department of Fluid Engineering Victor Kaplan at BUT in Brno. There were observed additional effects in the sealing gaps. From these measurements were obtained boundary conditions, which were used for simulating of sealing gap in ANSYS Fluent. [2], [3].

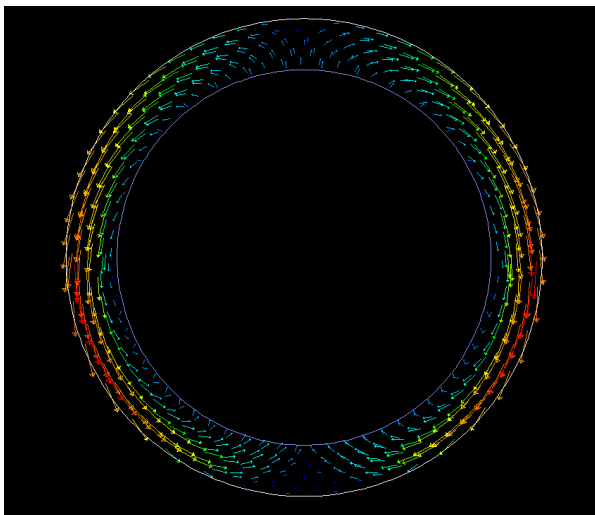


Fig. 1. Velocity in sealing gap

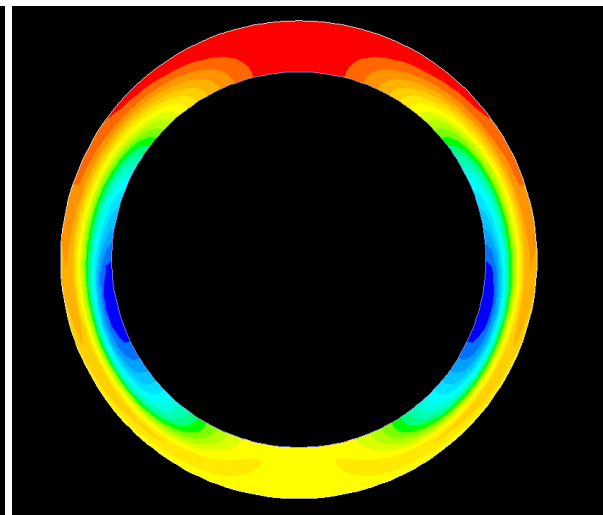


Fig. 2. Total pressure in sealing gap

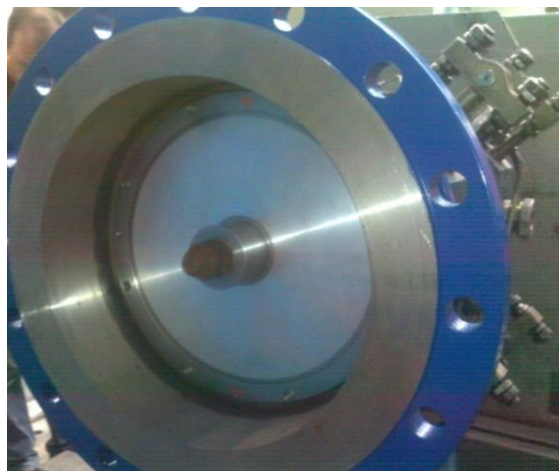


Fig. 3. The test equipment with the sealing gap [2]

The size of the sealing gap was 0.25 mm. It was simulated in 2D with the movement of the rotor in the vertical direction. The rotor was placed eccentrically. Medium flowing through the sealing gap was water. The forces from water were acting to the wall of stator. The aim of calculation was to obtain a force depending on the time. The calculation was performed for several frequencies. The additional weight was calculated from the acquired forces and then was compared with experimentally obtained value. [1], [4].

Acknowledgements

Presented research was supported by centre of competence of Technology Agency of the Czech Republic TE02000232 “Rotary machines” TA13402001.

References

- [1] Gasch, R., Nordmann, R., Pfützner, H., Rotordynamik, Springer Verlag, Berlin, 2002. (page 705)
- [2] Habán, V., et al., Experimentální výzkum přídavných účinků kapaliny v hydrodynamických spárách, Project No. FR-TI3/051 - QR-31-12, Brno: VUT Brno, 2012. (page 23) (in Czech)
- [3] Habán, V., et al., Experimentální výzkum přídavných účinků kapaliny v hydrodynamických spárách, Project No. FR-TI3/051. - QR-32-13, Brno: VUT Brno, 2013. (page 60) (in Czech)
- [4] Liang, Q.W., Rodríguez, C.G., Egusquiza, E., Escaler, X., Farhat, M., Avellan, F., Numerical simulation of fluid added mass effect on a francis turbine runner, Computers & Fluids 36 (6) (2007) 1106-1118.

Experimental analysis of steering shaft with focus on the strength of the bonded joint

Z. Padovec ^a, M. Zbojovský ^a

^a Czech Technical University in Prague, Faculty of Mechanical Engineering, Department of Mechanics, Biomechanics and Mechatronics, Technická 4, Prague, 166 07, Czech Republic

Presented article deals with the description of experimental evaluation of steering shaft loaded with torque with focus on strength of the bonded joint. Steering shaft which will be part of the car for E-Force Fee Prague Formula was designed from composite tube (carbon fiber/epoxy matrix). This tube was bonded to the steering rack through aluminum insert for transmission of torque from the driving wheel to the front axle.

First goal of this work is the measurement of torque which is depicted in Fig. 1. Brake pedal of the car was pressed and mass was added at the end of the beam until the observable deflection was achieved. Then the torque was calculated - $M_k = 10,73 \text{ Nm}$.

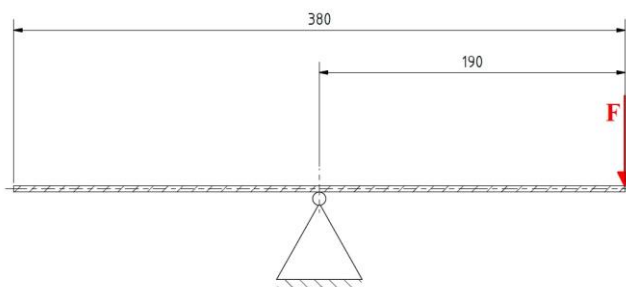


Fig. 1. Torque measurement and its diagram

Next step is the choice of the suitable adhesive. Adhesives from Spabond and Loctite manufacturers were chosen and experiment for shear stress and shear modulus determination was done. Other goal of presented work was the influence of curing process on the bonded joint (long time on lower temperature vs. short time on higher temperature). Experiment was based on ČSN EN 14 65 standard (see [3] for details) and it was done on Tira 2300 universal testing machine. Description of specimens, their number, average shear modulus (see [2] for details) and strength obtained from experiment can be seen in Table 1 (S stands for Spabond, L for Loctite). From the results can be seen that there is almost no influence of curing process and both adhesives achieve similar results in shear strength and shear modulus.

Table 1. Results from the experiment

Curing process	Number of specimens	Average shear modulus [MPa]	Average shear strength [MPa]
S 5 hours on 70°C	4	1,08±0,056	15,13±0,78
S 24 hours on 21°C + 16 hours on 50°C	5	0,99±0,074	15,13±1,1
L 1 hour on 80°C	3	0,97±0,06	16,74±0,77
L 24 hours on 23°C	5	1,03±0,05	15,41±1,4

The last step was the safe design of the tubular joint. Average shear stress in tubular lap joint loaded with torque can be computed as

$$\tau_{ST} = \frac{2M_k}{\pi \cdot (D - t_l)^2 \cdot L_l}, \quad (1)$$

from which we can see that the crucial parameters are length and thickness of the bonded joint. This value remains constant over the entire length of the joint. Next equation (see [1] for details) determines relationship between shear stress in bonded joint and relative length z/L_l of the bonded joint, where $z = 0$ is the edge of the tube and $z = L_l$ is the edge of the insert

$$\tau_T = \frac{2M_k \alpha}{\pi \cdot D_s^2} \left[\left(\frac{1 - \psi (1 - \cosh \alpha L)}{\sinh \alpha L} \right) \cosh \alpha z - \psi \sinh \alpha z \right]. \quad (2)$$

Coefficients α and ψ are computed from material and geometric parameters of the tube, insert and adhesive. Torque load for computation was chosen $M_k = 60$ Nm (almost 6 times higher than measured) for including dynamic and fatigue effects during driving, which were not simulated during torque measurement. Loctite 9466 adhesive was chosen, thickness of the designed joint was chosen 0,2 mm, length of the joint was chosen 25 mm. Safety factor computed as a ratio between evaluated shear stress of the adhesive and average shear stress in adhesive layer is 3,5, which was found sufficient for the safe operation of investigated application. Graph from the experiment and shear stresses obtained from (1) and (2) can be seen in Fig. 2.

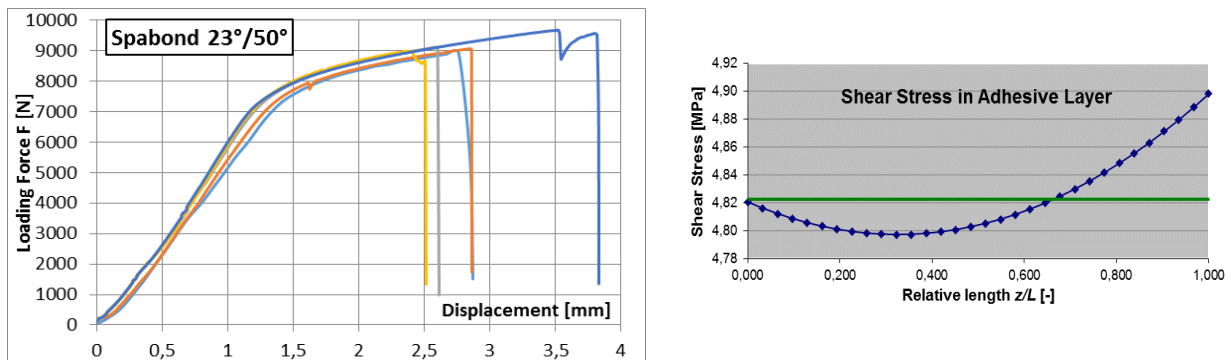


Fig. 1. Graph from experiment and computed shear stress in adhesive layer

Acknowledgements

This work has been supported by the Grant Agency of the Czech Technical University in Prague, grant No. SGS15/188/OHK2/3T/12.

References

- [1] Adams, R.D., Peppiatt, N.A., Stress analysis of adhesive bonded tubular lap joints, *Journal of Adhesion* 9 (1977) 1-18.
- [2] Renton, J.W., Vinson, J.R., On the behavior of bonded joints in composite material structures, *Engineering Fracture Mechanics* 7 (1975) 41-60.
- [3] ČSN EN 14 65, Determination of shear strength in tension of rigid adherends on lap joints. (in Czech)

Single core model in VPS with respect to non-linear static, crashworthiness and internal acoustic

M. Pašek^a, J. Šašek^a

^a MECAS ESI s.r.o., Brojova 2113/16, 326 00 Plzeň, Czech Republic

The presentation will be focus to single core and modular input approach in Virtual Performance Solution (VPS). The software package is industrially used to solve wide range of mechanical applications like linear and non-linear static, crashworthiness, fluid structure interaction or internal and also external acoustic. The VPS contains different numerical methods which are integrated to one single environment. The main advantage of this integration is to have one common solver language to build single core model which can be used for multiple simulation domains. The single core model can be easily combined with modular input which significantly save time for numerical model building. Two application examples will be discussed to show VPS state of art with respect to single core mode approach.

First example is focused to numerical simulations of rail vehicles which are required by various regulations and homologation procedures. One of the requirement defines the crash test procedure for passenger coach. The crash scenario is defined by using of single core model approach, which allows to use same data structure for other load cases like static and dynamic analysis, and modular input. The modular input is used to define the model structure of the coach body, bogies, crash elements and other components. User can easily modify any parts in the modular structure and reflect to other modules (coaches). This modern method of model assembly improves model quality, prevent user errors and brings significant benefits in speed up of model building.

Second example is related to modeling of low-frequency vibro-acoustic. A response at a certain location may have been caused by a remote vibration source. This phenomenon is hard to analyze in complicated structures (with various subassemblies like cars). The energy from a car engine is transmitted into the passenger cavity by a number of different routes (e.g. from engine mounts, wheel suspensions, the exhaust components, drive shafts...). Transfer path analysis offers a methodology to evaluate the contribution along each transfer path from the source to the receiver. The presentation demonstrates usage of TPA tool with VPS 2016. The TPA tool is available as add on to VPS and Visual Environment and can be customized according the user needs.

References

- [1] Pašek, M., Virtual testing and car body development for crashworthiness, Proceedings of VVA 2014, Lázně Bělohrad, 2014.
- [2] Šašek, J., Pašek, M., Beneš, K., Glac, V., Effects of manufacturing process in crash simulations, Applied and Computational Mechanics 4 (1) (2010) 113-120.

- [3] Ullrich, P., van Hal, W., Petitjean, A., Virtual Performance Solution 2016 – Current status and future trends, VPS User Forum 2016, Darová-Břasy, 2016.
- [4] Virtual Performance Solution, 2016, Solver Reference Manual, ESI Group.

Simple parallel implementation of an implicit CFD solver using the Schwarz domain decomposition method

A. Pecka^a, O. Bublík^a, J. Vimmr^a

^a*NTIS – New Technologies for the Information Society, Faculty of Applied Sciences, University of West Bohemia, Univerzitní 8, 306 14 Plzeň, Czech Republic*

One way of decreasing the computational time required to solve a large scale problem is to spread the boundary-value problem over a computer network and solve the problem in parallel. The target of this contribution is to present a simple parallel implementation of an implicit CFD solver for 2D compressible Navier-Stokes equations. The employed CFD solver is based on the discontinuous Galerkin method and the time integration is carried out by the BDF scheme. Note however that the parallel implementation is independent of the particular CFD solver.

In order to distribute the CFD computation onto nodes of a computer network we first convert the boundary-value problem into subproblems. Following the Schwarz method [1, 2, 3] we decompose the domain into a set of overlapping subdomains. We require that the Dirichlet boundary condition is satisfied at the newly created boundary of each subdomain. The resulting subproblems are independent of each other, hence each subproblem can be solved by a different node in the computer network. In order for the unified solution of the subproblems to be equivalent to the solution of the original problem some form of coordination between adjacent subdomains is required. In case of Schwarz method this is achieved by iteratively solving the subproblems and swapping the data from overlap regions between adjacent subdomains until the steady state is reached. Note that the iterating process needs to be performed at each time step. We also analysed the effect of the number of iterations on the solution since increasing number of iterations decreases the efficiency of parallelization. The result of this analysis will be given in the upcoming presentation.

We test the developed parallel implicit CFD solver on a several benchmarks one of which we present in this annotation. Let us consider a transonic flow around the NACA 0012 aerofoil with the angle of attack $\alpha = 5^\circ$, the Reynolds number $Re = 10000$ and the free stream boundary condition with Mach number $M_{inf} = 0.8$. In this benchmark we execute two iterations of the Schwarz method at each time step. We use a triangular mesh of 99 077 elements, see Fig. 1, and quadratic basis polynomials, which correspond to 2 377 848 DOFs. We split the domain with the aid of the software tool METIS, which creates non-overlapping subdomains each with a similar number of elements. The output of METIS for 16 subdomains is displayed in Fig. 1 in the vicinity of the aerofoil. To each subdomain ω , we add k layers of elements that surround ω , thus creating a set of overlapping subdomains. The chosen integer k determines the size of the overlap. The Mach contour of the steady flow in the vicinity of the aerofoil is shown in Fig. 2. This benchmark was designed to analyse the scalability of the solver, i.e. how the elapsed time decreases with increasing number of nodes. The results of the benchmark along with the speedup and efficiency is listed in Table 1. Here the CPU time corresponds to 200 time steps, that means the steady state was not reached during the simulations in order to make the

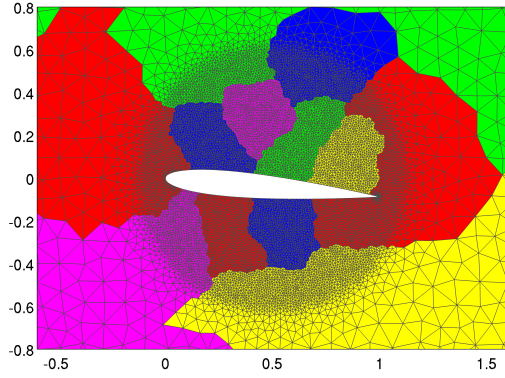


Figure 1. Mesh and domain decomposition

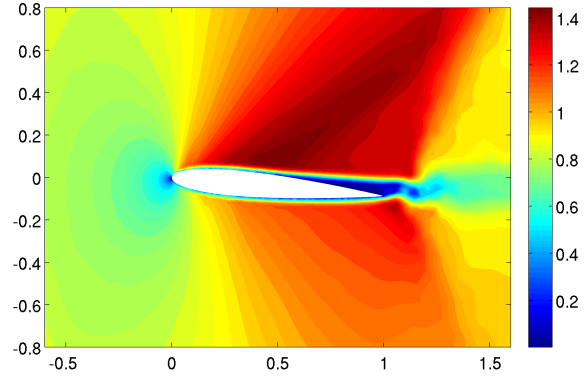


Figure 2. Mach contour of the steady flow

Table 1. CPU time that corresponds to 200 time steps along with speedup and efficiency for various number of nodes (each node was using four cores)

# of nodes	# of cores	CPU [s]	transfer [s]	speedup [1]	efficiency [%]
2	8	6166	23	1.0	100
4	16	3855	37	1.6	80
8	32	1666	17	3.7	92
16	64	905	53	6.8	85

benchmark less time-consuming. The column labelled *transfer* in Table 1 refers to the accumulated time that takes to transfer data between corresponding nodes after each iteration. The benchmark was performed on a heterogeneous network of computers consisting of 16 nodes, each of which exploited four physical cores. Note that the number of subdomains was chosen according to the number of nodes rather than the number of cores. The synchronization and data transfer among nodes is implemented in the Java programming language, which is platform independent and has plenty of simple networking tools available.

As expected with increasing number of nodes the CPU time decreases hence speedup grows. The efficiency varies from 80% to 92%. For more thorough analysis of the dependency of speedup on the number of nodes, more test cases are needed, which will be given in the upcoming presentation.

Acknowledgements

This work was supported by the project LO1506 of the Czech Ministry of Education, Youth and Sports and by the project TE01020068 Centre of research and experimental development of reliable energy production of the Technology Agency of the Czech Republic.

References

- [1] Dryja, M., Widlund, O. B., Additive Schwarz methods for elliptic finite element problems in three dimensions, Proceedings of the 5th International Symposium on Domain Decomposition Methods for Partial Differential Equations, Norfolk, VA, USA, 1992, pp. 3-18.
- [2] Maday, Y., Magoulès, F., Optimized Schwarz methods without overlap for highly heterogeneous media, Computer Methods in Applied Mechanics and Engineering 196 (8) (2007) 1541-1553.
- [3] Schwarz, H. A., On passing to the limit by the alternating process, Vierteljahrsschrift der Naturforschenden Gesellschaft in Zürich 15 (1870) 272-286. (in German)

Friction and fretting wear coefficients between the key and the groove in the lower part of the WWER 440-213 reactor pressure vessel

L. Pečínka ^a, J. Svoboda ^b, V. Zeman ^c

^a ÚJV Řež a. s., Hlavní 130, 250 68 Husince – Řež, Czech Republic

^b CVŘ Řež s. r. o., Hlavní 130, 250 68 Husince – Řež, Czech Republic

^c Department of Mechanics, Faculty of Applied Sciences, University of West Bohemia, Univerzitní 8, 306 14 Plzeň, Czech Republic

The couple key-groove in the lower part of the reactor pressure vessel reactors WWER 440 and WWER 1000MW, see Fig 1 is in normal operation conditions loaded by the force F_N of the order of kN. Relative vertical motion induced by pressure pulsations generated by main circulation pumps result in fretting wear of the surfaces in the contact. The design value of the gap between the key and the groove range from 0.05 to 0.17 m. Due to supposed fretting wear the potential for increasing the gap exist and finally the impacts in the direction of acting force may be induced. The loss of the mass of the sliding surfaces may be predicted using well known Zeman equation [2]

$$\Delta m = \mu \frac{f(\omega)}{f_0} W \frac{t_o}{T} [g], \quad (1)$$

where Δm [g].....loss of the mass in grams,
 μ [g/J].....fretting wear coefficient,
 f_0design value of the friction coefficient,
 $f(\omega)$value of the frictin coefficient as the function of the frequency,
 W [J].....work of the friction force per one cycle,
 t [s].....time of the operation,
 T [s].....period of the pressure pulsation.

The values of the μ and the $f(\omega)$ must be experimentally verified. The values of the friction coefficient will be in the next presented.

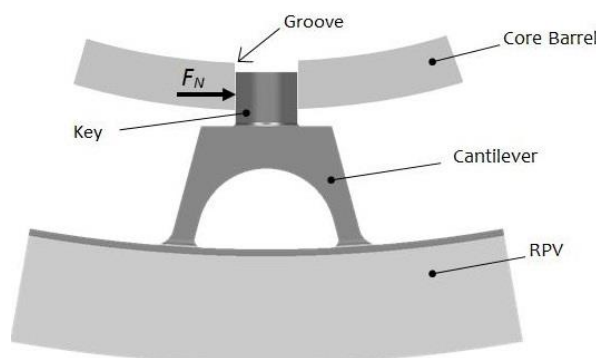


Fig. 1. The couple key-groove



Fig. 2. Experimental Device

Experimental device is illustrated in the Fig.2. Consist of two servocylinders INOVA AH 63, maximal force 63kN and AH 10, maximal force 10kN. For the evaluation of the friction coefficient the following relation has been used

$$f = \frac{F_{exp}}{F_N} + \frac{mX\omega^2}{F_N} \sin \omega t - \frac{2f_p r_p}{l}, \quad (2)$$

where f_pcoefficient of the pin friction,
 r_pradii of the pin,
 llength of the pin,
 F_{exp}measured force,
 F_Npushing force,
 maccelerated mass,
 Xamplitude of the horizontal movement,
 ωfrequency of the horizontal movement.

First set of the experiments has been performed with frequency 25Hz, X=3mm and pushing force 3kN. Total length of the friction movement was 5000m.

Results of the experiments: Coefficient of the friction as the function of the time is illustrated in Fig. 3. It is evident that typical values which influence the fretting wear range from $f=1.0$ to $f=1.3$. Higher values of (1.5:2.) represent cases of the seizure which was observed during the experiment.

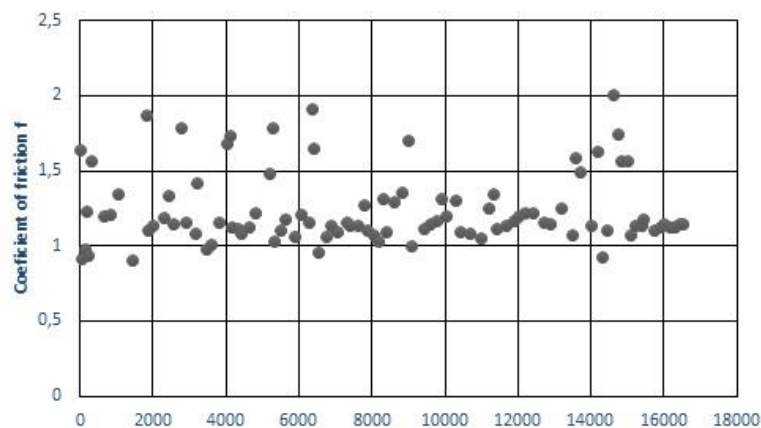


Fig. 3. Results of the experiments

Conclusions: The couple key-groove in the lower part of the WWER reactors pressure vessel is possible to consider as unlubricated. The possible types of the interactions may be according [1] divided into the following three mechanical categories:

- seizure or very high friction, the friction coefficients range from $f=3.0$ to $f=10$,
- strong adhesion, where friction coefficient is equal approximately about 1,
- weak adhesion, where friction coefficient is about $f \sim 0.4$ or lesser.

Results of our experiments confirm this theory. The nature of this one is based on the fact that the pushing force was 3kN. It represents strong adhesion. Only some cases of the seizure were observed. The values of the fretting wear coefficient are under evaluation. Next year these experiments will continue but with another types of materials. We suppose that the obtained results will be similar.

References

- [1] Green, A.P., Friction between unlubricated metals: A theoretical analysis of the junction model, Proceedings of the Royal Society, London, 228 (1173), 1955, pp. 190-204.
- [2] Zeman, V, Dyk, Š., Hlaváč, Z., Mathematical modelling of nonlinear vibration and fretting wear of the nuclear fuel rods, Archive of Applied Mechanics 86 (4) (2016) 657-668.

Numerical simulation of free surface flows using a three-equation model for two-phase flows

S. Plánička ^a, J. Vimmr ^a

^a NTIS - New Technologies for the Information Society, Faculty of Applied Sciences, University of West Bohemia, Univerzitní 8, 306 14 Plzeň, Czech Republic

The main objective of this study is the demonstration of the use of a simple three-equation model for calculation of complex free surface compressible flows. An in-house computational software written in Matlab was developed for the solution of the aforementioned problem. This numerical code was tested for the dambreak problem.

The three-equation model was derived from a seven-equation Baer-Nunziato model for compressible two-phase flows, which was originally designed for solving detonation waves [1]. Amount of tracked fluid per volume is defined by the volume fraction α determined from advection equation. The described model is not suitable for solving dispersed flow, sedimentation, thermodynamics problems etc. due to its characteristics. The approach is applicable for the solution of fluid flow with free surface, wherein the second phase is negligible (vacuum or fluid with significantly lower density). Consequently its foundation could be used also for vacuum casting problems.

The original Baer-Nunziato model contains conservation equations of mass, momentum and energy for both phases and an advection equation of volume fraction. This model was reduced following various simplifications proposed by Dumbser [2]. As suggested above – the second phase is neglected, therefore all the corresponding evolution equations are omitted. The interface pressure is kept on atmospheric pressure ($p_1 = p_2 = p_{ATM} = 0 \text{ Pa}$), when choosing that all pressures value are relative to the atmospheric one. The interface velocity that corresponds to the rate of advection of the volume fraction is set to be equal to the velocity of the primary phase. In other words the interface propagates along with the primary fluid. The system was closed by a simple Tait equation of state, see [3], for the primary phase

$$p = K((\rho/\rho_0)^\gamma - 1), \quad (1)$$

which directly relates pressure p and density ρ . K, γ are constants affecting compressibility and speed of sound a of the fluid and ρ_0 is the density at reference pressure. The density is calculated directly from evolution equations and afterwards pressure is determined from the equation of state. Therefore there is no need for the energy equation. The final mathematical model can be written in one dimension as

$$\frac{\partial}{\partial t}(\alpha\rho) + \frac{\partial}{\partial x}(\alpha\rho u) = 0, \quad (2)$$

$$\frac{\partial}{\partial t}(\alpha\rho u) + \frac{\partial}{\partial x}(\alpha(\rho u^2 + p)) = \alpha\rho g, \quad (3)$$

$$\frac{\partial}{\partial t}\alpha + u \frac{\partial \alpha}{\partial x} = 0, \quad (4)$$

where u denotes the velocity component. The source term on the right hand side represents gravitational force per unit volume with acceleration g . The system is hyperbolic with eigenvalues $u-a, u, u+a$, if the total pressure is positive and the volume fraction is $0 < \alpha < 1$.

The equation (4) was reformulated into a new shape

$$\frac{\partial}{\partial t} \alpha + \frac{\partial}{\partial x}(\alpha u) - \alpha \frac{\partial u}{\partial x} = 0, \quad (5)$$

where the second term is basically a conservative convective flux of volume fraction and the third term a non-conservative source term. The form is utilized by the in-house code. The finite volume method was used for the spatial discretization of Eq. (2, 3, 5) and entire coupled system was time-iterated by an explicit Euler scheme. The conservative convective numerical flux was approximated by the first order scheme in order to damp instabilities of the two-phase flow model. Specifically AUSM scheme was used due to its simplicity, efficiency and accuracy, for more information see [4]. The AUSM scheme does not require the Jacobian. This is a great advantage for two-phase flow simulations in general. The non-conservative term was discretized in the spirit of AUSM scheme due to consistency.

The developed numerical code was verified on the two-dimensional dambreak problem and obtained results were compared with the numerical results published in [2], namely dambreak with bottom step into a wet bed area. Computational domain was $\Omega = ([-5; 5] \times [0; 3]) \setminus ([0; 5] \times [0; 0.2])$ m, the domain covered by fluid was $\Omega_L^0 = ([-5; 0] \times [0; 1.46]) \setminus ([0; 5] \times [0.2; 0.51])$ m. Gravity acceleration was $\vec{g} = [0; -9.81]$ m/s² and parameters of Tait equation were artificially set as $\nu = 1$, $\rho_0 = 1000$ kg/m³, $K = 0.637$ MPa to improve the convergence of the solution. Initial velocities were $u = v = 0$ m/s, pressure was set to be in hydrostatic condition with zero pressure level at $h = 1.46$ m. The following figures compare the results of performed simulation in Fig.1 and original work shown in Fig.2.

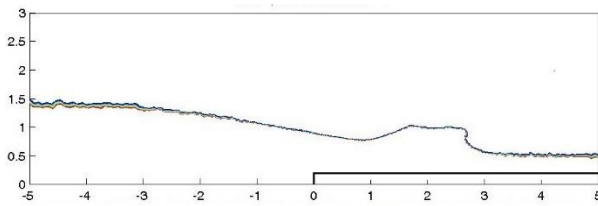


Fig. 1. Dambreak with wet step at the time $T = 1$ s, developed numerical code based on FVM

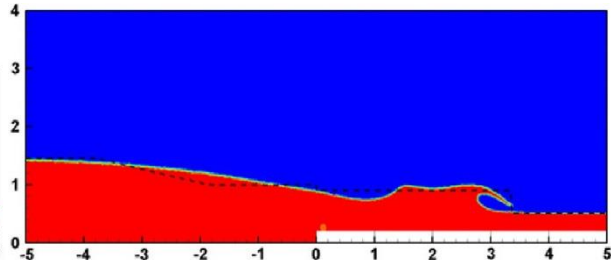


Fig. 2. Dambreak with wet step at the time $T = 1$ s, DGFEM (field) and comparison with SWE (dashed)

The obtained results demonstrate the applicability of three-equation model solved by FVM with the use of the AUSM scheme on free surface flow problems. In comparison with the results using DGFEM higher artificial viscosity is evident. On the other hand more realistic shape of initial breaking wave is observed compare to the results of the Shallow water equations model. More details and numerical results will be shown in the conference presentation.

Acknowledgements

This work was supported by the project TA03010990 of the Technology Agency of the Czech Republic and by the project LO1506 of the Czech Ministry of Education, Youth and Sports.

References

- [1] Baer, M.R., Nunziato, J.W., A two-phase mixture theory for the deflagration-to-detonation transition (DDT) in reactive granular materials, *Int. J. of Multiphase Flow* 12 (6) (1986) 861-889.
- [2] Dumbser, M., A simple two-phase method for the simulation of complex free surface flows; *Computer methods in applied mechanics and engineering*, 2010, pp. 1204-1219.
- [3] MacDonald, R., Some simple isothermal equations of state, *Reviews of modern physics* 38 (4) (1966) 669-679.
- [4] Paillère, H., Corre, C., García Cascales, J.R., On the extension of the AUSM+ scheme to compressible two-fluid models, *Computers and fluids* 32 (2003) 891-916.

The influence of residual stress on fracture behavior of the CRB test specimen

J. Poduška ^{a,b}, P. Hutař ^b, J. Kučera ^c, J. Sadílek ^c, A. Frank ^d, L. Náhlík ^b

^a Faculty of Mechanical Engineering, Brno University of Technology, Technická 2896/2, 61669, Brno, Czech Republic

^b Institute of Physics of Materials, Academy of Sciences of the Czech Republic, Žižkova 22, 61662, Brno

^c Polymer Institute Brno, Tkalcovská 36/2, 60200, Brno

^d Polymer Competence Center Leoben, Roseggerstrasse 12, A-8700, Leoben, Austria

Polymer pipes made of materials like polyethylene or polypropylene are put to use quite frequently nowadays. Polymer materials are very durable, so the predicted lifetimes of plastic pipes are usually quite high, especially in the case of modern polyethylene pipe grades with enhanced mechanical properties. These pipes are predicted to last for more than 100 years in operation. Testing pipe's lifetime is usually done by the hydrostatic pressure test, where pieces of pipes are loaded with internal pressure and times to failure are measured. The predicted lifetime can be estimated by extrapolation of these measured times. However, these tests take very long time to produce satisfactory results. Instead of hydrostatic pressure test, an accelerated method of testing can be used. Accelerated methods are focused on the so-called slow crack growth (SCG), which is the most frequent mechanism of pipe failure in operation. The accelerated tests are carried out by loading notched specimens and measuring the slow crack growth kinetics. These results can be used to calculate an estimation of the lifetime by integrating a modified Paris-Erdogan equation. This method can be used because the plastic deformation during SCG is very small and so the conditions of linear elastic fracture mechanics are met. [2,4,5]

One of the most effective ways to accelerate the slow crack growth without significantly changing its character is to use cyclic loading instead of static loading. The test that uses cyclic loading is the cracked round bar (CRB) test (see Fig. 1), which uses specimen in the shape of round bars with an initial notch in the middle. During the CRB test the crack growth rate da/dt is measured for different R -ratios of stress intensity factors ($R = K_{min}/K_{max}$). However, the requested result is to obtain the crack growth rate for static loading, which means for $R = 1$. This is achieved by extrapolation of the results for cyclic loading. [1,3]

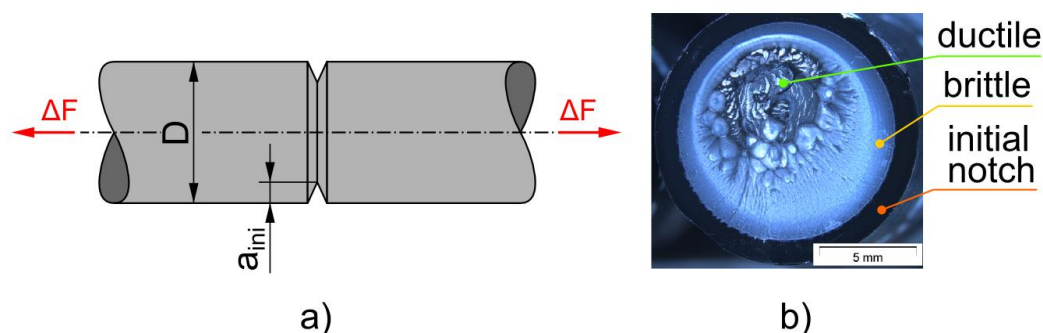


Fig. 1. Scheme of the CRB specimen (a) and the fracture surface after a finished CRB test (b)

Taking a look at the fracture surface of a CRB specimen after a finished test, three distinct regions can be distinguished. At first there is a smooth surface of the initial notch, followed by the slow crack growth fracture surface, described as brittle. The last region is the surface of the final ductile fracture. The whole character of the fracture surface is asymmetrical. The cause of this asymmetry is unknown.

In this contribution, the problem of the asymmetrical fracture surface of the CRB specimen is investigated. Since the CRB specimen are made by cutting the desired shape directly out of the wall of the plastic pipe, one of the causes of the asymmetry could be the residual stress. The residual stress is present in the pipe wall as a result of uneven cooling during the pipe manufacture process. As the specimen is cut out of the pipe, the residual stress releases, causing the cut-out shape to bend. The bent specimen has to be straightened back when finishing it on a lathe and when loading it in the testing device.

A finite element method was employed to investigate this hypothesis. A model of the polyethylene CRB specimen was created (see Fig. 2) with an initial crack front. Using the INISTATE command in ANSYS, the residual stress was included in the model (see [6] for details about residual stress in PE pipes). The model was then loaded with a typical CRB specimen load (10 MPa). Stress intensity factors were calculated in several places along the crack front and a new shape of the crack front was established based on these values. This procedure was repeated and the change of the crack front was recorded and then compared to the photograph of the fracture surface.

It was found that the calculated asymmetry was much more pronounced than the one observed on real specimens. This led to a conclusion that the residual stress included in the model was too high, compared to the residual stress that actually remains in the CRB specimen and also that other effects are probably influencing the asymmetry.

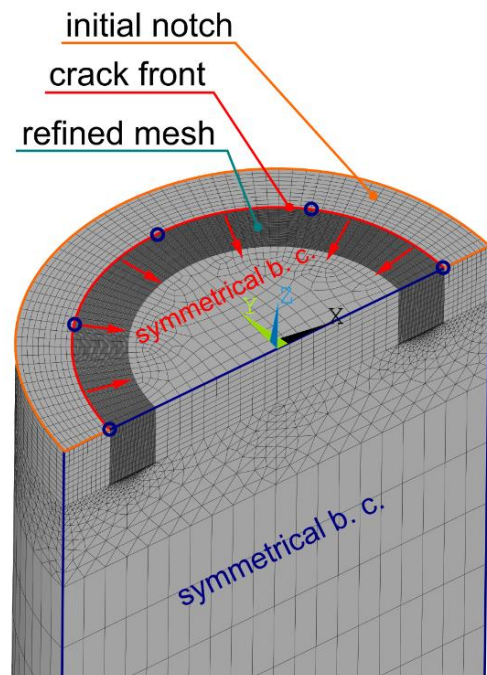


Fig. 2. The FEM model of the CRB specimen with boundary conditions

Acknowledgements

The research has been supported by the specific research project FSI-S-14-2311 provided to Brno University of Technology, Faculty of Mechanical Engineering.

References

- [1] Arbeiter, F., Schrittester, B., Frank, A., Berer, M., Pinter, G., Cyclic tests on cracked round bars as a quick tool to assess the long term behaviour of thermoplastics and elastomers, *Polymer Testing* 45 (2015) 83–92.
- [2] Brömstrup, H., PE 100 pipe systems, 3rd ed., Vulkan-Verlag, Essen, 2009.
- [3] Frank, A., Freimann, W., Pinter, G., Lang, R.W., A fracture mechanics concept for the accelerated characterization of creep crack growth in PE-HD pipe grades, *Engineering Fracture Mechanics* 76 (2009) 2780–2787.
- [4] Hutař, P., Ševčík, M., Náhlík, L., Pinter, G., Frank, A., Mitev, I., A numerical methodology for lifetime estimation of HDPE pressure pipes, *Engineering Fracture Mechanics* 78 (2011) 3049–3058.
- [5] Janson, L.-E., *Plastics pipes for water supply and sewage disposal*, 3., Borealis, Stockholm, 1999.
- [6] Poduška, J., Hutař, P., Kučera, J., Frank, A., Sadílek, J., Pinter, G., et al., Residual stress in polyethylene pipes, *Polymer Testing* 54 (2016). doi:10.1016/j.polymertesting.2016.07.017.

Approaches to the computational modelling of the mechanical systems with cables

P. Polach^a, R. Bulín^a, P. Beneš^b, Z. Šika^b, M. Hajžman^a

^a *New Technologies for the Information Society, European Centre of Excellence, Faculty of Applied Sciences, University of West Bohemia, Univerzitní 8, 306 14 Plzeň, Czech Republic*

^b *Department of Mechanics, Biomechanics and Mechatronics, Faculty of Mechanical Engineering, Czech Technical University in Prague, Technická 4, 166 07 Praha, Czech Republic*

The paper summarizes the possible approaches suitable for the modelling of cable and fibre dynamics in the framework of various mechanical systems. Force representation of a cable, a point-mass model and an absolute nodal coordinate formulation are introduced in more detail.

The motivation is the development of a cable model, which could be efficient for the usage in a mechatronic model of a manipulator consisting of cables and an end-effector, whose motion is driven by cables – particularly for the usage in the model of QuadroSphere (see Fig. 1; e.g. [1]). The QuadroSphere is a tilting mechanism with a spherical motion of a platform and an accurate measurement of its position. The platform position is controlled by four fibres; each fibre is guided by a pulley from linear guidance to the platform. The numerical model of QuadroSphere will serve for the investigation of different possible strategies of the control of this active structure superimposed to the end-effector of the cable-driven mechanism in order to improve the end-effector positioning accuracy and the operational speed.

The cable and fibre modelling should be based on considering the fibre flexibility and the suitable approaches can be based on the flexible multibody dynamics (see e.g. [5]). Many industrial applications can be solved using the proposed flexible multibody dynamics approaches. The studied problems are characterized by general large motion of interconnected rigid and flexible bodies with the possible presence of various nonlinear forces and torques.



Fig. 1. The QuadroSphere tilting mechanism

There are many approaches to the modelling of flexible bodies in the framework of multibody systems.

The simplest way how to incorporate cables in the equations of motion of a mechanism is the force representation of a cable (e.g. [2]). It is supposed that the mass of cables is small to such an extent comparing to the other moving parts that the inertia of cables is negligible. The cable is represented by the force dependent on the cable deformation and its stiffness and damping properties. A variable length of the cable due to wiring

can be easily described using the force approach. This way of the cable modelling is probably the most frequently used in the cable-driven robot dynamics and control.

A more accurate approach is based on the representation of the cable using a point-mass model (e.g. [4]). It has the advantage of a lumped point-mass model. Point masses can be connected by forces or constraints. Wiring of a cable can be also simulated and a detailed model of a wiring mechanism can be observed. In the case of the manipulator mechatronic model consisting of cables and an end-effector, whose motion is driven by cables (e.g. in the case of the QuadroSphere model [1]) utilization of the point-mass model of a cable proved to be very prospective.

A very promising approach usable for the cable modelling is so called absolute nodal coordinate formulation (ANCF), which is based on the discretization of a cable or a fibre to nonlinear finite elements [5]. Absolute nodal positions and slopes are considered to be nodal coordinates of the ANCF elements. The formulation leads to a constant mass matrix and a highly nonlinear stiffness matrix. The model can be efficiently used for the investigation of various contact problems related to cables or fibres.

In order to represent bending behaviour of cables their discretization using the finite segment method or so called rigid finite elements is possible [5]. Other more complex approaches can utilize nonlinear three-dimensional finite elements.

Another approach used for the creation of a general model involving cables with distributed mass and time-varying length is based on Hamilton's principle, which serves for achieving the system of partial differential equations describing the cable dynamics [3]. To solve the system of dynamic equations, the Ritz-mode method with polynomial shape functions is employed and the system of partial differential equations is converted into ordinary differential equations. The accuracy of the cable model depends on the order of the used polynomial mode functions. This approach is suitable for the modelling of the cable-driven manipulators with distributed mass flexible cables.

Future work will be focused on the implementation of the point-mass model of the cable and the modelling of its interaction with the pulley (advantage of this approach is supposed to be in a precise physical interpretation of the problem and in a short computational time).

Acknowledgements

The paper has originated in the framework of solving No. 15-20134S project of the Czech Science Foundation entitled "Multi-level Light Mechanisms with Active Structures".

References

- [1] Beneš, P., Šika, Z., Polach, P., Valášek, M., Zavřel, J., Volech, J., Kinematic analysis of possible concepts of multi-level mechanisms combining active structures and cable-driven mechanisms, Proceedings of Extended Abstract of 31st conference with international participation Computational Mechanics 2015, Špičák, Faculty of Applied Sciences, University of West Bohemia, 2015. (CD-ROM)
- [2] Diao, X., Ma, O., Vibration analysis of cable-driven parallel manipulators, *Multibody System Dynamics* 21 (4) (2009) 347-360.
- [3] Du, J., Agrawal, S.K., Dynamic modeling of cable-driven parallel manipulators with distributed mass flexible cables, *Journal of Vibration and Acoustics* 137 (2) (2015) 021020 (8 pages).
- [4] Ottaviano, E., Gattulli, V., Potenza, F., Rea, P., Modeling a planar point mass sagged cable-suspended manipulator, Proceedings of 14th IFToMM World Congress, Taipei, Chinese Society of Mechanism and Machine Theory, 2015, pp. 2696-2702.
- [5] Shabana, A.A., Flexible multibody dynamics: Review of past and recent developments, *Multibody System Dynamics* 1 (2) (1997) 189-222.

Free vibration modal spectrum of planetary gearing box

L. Půst^a, L. Pešek^a

^aInstitute of Thermomechanics, Academy of Sciences of the Czech Republic, Dolejškova 5, 18200 Praha 8, Czech Republic

Analysis of planetary gearings is of basic importance for reduction of noise and vibrations of these very-often used transmission systems. The planetary gearboxes are always included into a set of aggregates – usually driving motor on the input wheel side and working (braking) aggregate on output wheel side. These I/O subsystems are in the next analysis modelled by one DOF torsional mass-spring elements. Presented paper is oriented on the modelling and solution of spectral and modal properties of the plane type of gearing with four planetary subsystems and with fixed planet carrier.

The scheme of investigated type of gearings is shown in Fig. 1. The axes of central sun wheel and of outer ring wheel are stiff, but the shaft connecting sun wheel Θ_1 (ring wheel Θ_3) with driving aggregate Θ_0 (braking aggregate Θ_4) is elastic with torsion stiffness k_0 (k_4). Planet wheels 2 are pivoted on elastic pins (stiffness k_3), which enable the tangential motion.

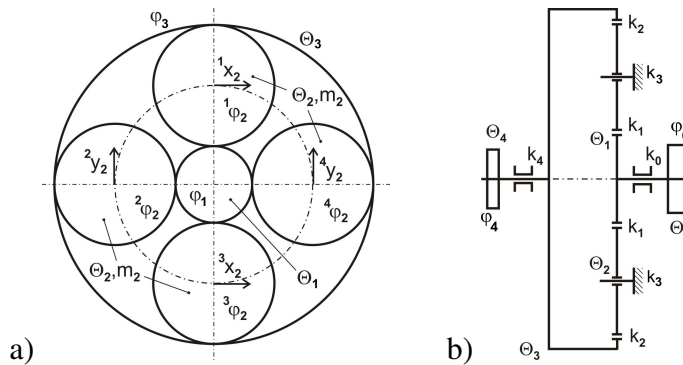


Fig. 1. Four planetary gearbox with I/O aggregates

All the wheels have helical gearings. As this kind of gearings has an essential smaller variation of contact stiffness against the spur gearings, this stiffness variability is not taken into account and teeth contact stiffness is supposed to be constant. Using expressions for kinetic and potential energy and introducing them into Lagrange equations, we get 12 differential equations of motion:

$$\begin{aligned}
 \Theta_0 \ddot{\varphi}_0 + k_0(\varphi_0 - \varphi_1) &= 0, \\
 \Theta_1 \ddot{\varphi}_1 + k_0(\varphi_1 - \varphi_0) + k_1 r_1 [4r_1 \varphi_1 - r_2 ({}^1\varphi_2 + {}^2\varphi_2 + {}^3\varphi_2 + {}^4\varphi_2) - {}^1x_2 - {}^2y_2 + {}^3x_2 + {}^4y_2] &= 0, \\
 m_2 {}^1\ddot{x}_2 - k_1 r_1 \varphi_1 + (k_1 - k_2) r_2 {}^1\varphi_2 + (k_1 + k_2 + k_c) {}^1x_2 + k_2 r_3 \varphi_3 &= 0, \\
 \Theta_2 {}^1\ddot{\varphi}_2 - k_1 r_2 r_1 \varphi_1 + (k_1 + k_2) r_2 {}^1\varphi_2 + (-k_2 + k_1) r_2 {}^1x_2 - k_2 r_2 r_3 \varphi_3 &= 0, \\
 m_2 {}^2\ddot{y}_2 - k_1 r_1 \varphi_1 + (k_1 - k_2) r_2 {}^2\varphi_2 + (k_1 + k_2 + k_c) {}^2y_2 + k_2 r_3 \varphi_3 &= 0, \\
 \Theta_2 {}^2\ddot{\varphi}_2 - k_1 r_2 r_1 \varphi_1 + (k_1 + k_2) r_2 {}^2\varphi_2 + (-k_2 + k_1) r_2 {}^2y_2 - k_2 r_2 r_3 \varphi_3 &= 0, \\
 m_2 {}^3\ddot{x}_2 + k_1 r_1 \varphi_1 - (k_1 - k_2) r_2 {}^3\varphi_2 + (k_1 + k_2 + k_c) {}^3x_2 - k_2 r_3 \varphi_3 &= 0,
 \end{aligned}$$

$$\begin{aligned}
\Theta_2 \ddot{\varphi}_2 - k_1 r_2 r_1 \varphi_1 + (k_1 + k_2) r_2^3 \varphi_2 + (k_2 - k_1) r_2^3 x_2 - k_2 r_2 r_3 \varphi_3 &= 0, \\
m_2 \ddot{y}_2 + k_1 r_1 \varphi_1 + (-k_1 + k_2) r_2^4 \varphi_2 + (k_1 + k_2 + k_c) y_2 - k_2 r_3 \varphi_3 &= 0, \\
\Theta_2 \ddot{\varphi}_2 - k_1 r_2 r_1 \varphi_1 + (k_1 + k_2) r_2^4 \varphi_2 + (-k_1 + k_2) r_2^4 y_2 - k_2 r_2 r_3 \varphi_3 &= 0, \\
\Theta_3 \ddot{\varphi}_3 + k_4 (\varphi_3 - \varphi_4) + k_2 r_3 [4r_3 \varphi_3 - r_2 (\varphi_2^1 + \varphi_2^2 + \varphi_2^3 + \varphi_2^4) + x_2 + y_2 - x_2^3 - y_2^4] &= 0, \\
\Theta_4 \ddot{\varphi}_4 + k_4 (\varphi_4 - \varphi_3) &= 0.
\end{aligned}$$

Eigen-frequencies of investigated planetary gearbox is given by the roots of characteristic determinant $|\mathbf{K} - \Omega^2 \mathbf{M}| = 0$. The program "eig" in system Matlab determines the eigenfrequencies of planetary gearing connected with the driving (input) and braking (output) aggregates. The main parameters of following example of planetary gearbox are:

- mesh stiffness of gearings contacts and planet pin: $k_1 = k_2 = 4 \times 10^9 \text{ N/m}$, $k_3 = 5 \times 10^9 \text{ N/m}$,
- radiuses of gear-wheels: $r_1 = 0.06 \text{ m}$, $r_2 = 0.12 \text{ m}$, $r_3 = 0.3 \text{ m}$,
- torsion stiffness of I/O shafts: $k_0 = 1 \times 10^7 \text{ Nm/rad}$, $k_4 = 3 \times 10^7 \text{ Nm/rad}$,
- moments of inertia of gear-wheels: $\Theta_1 = 0.05 \text{ kg.m}^2$, $\Theta_2 = 0.5 \text{ kg.m}^2$, $\Theta_3 = 200 \text{ kg.m}^2$,
- moments of inertia of I/O wheels: $\Theta_0 = 1 \text{ kg.m}^2$, $\Theta_4 = 3 \text{ kg.m}^2$.

Influence of external I/O shafts torsion stiffness k_0 , k_4 on change of all angular velocities Ω is shown in Fig. 2, where the range of this stiffness is $k_0 = 1 \times 10^4 \text{ Nm/rad}$ up to $k_0 = 1 \times 10^8 \text{ Nm/rad}$ ($3k_0 = k_4$).

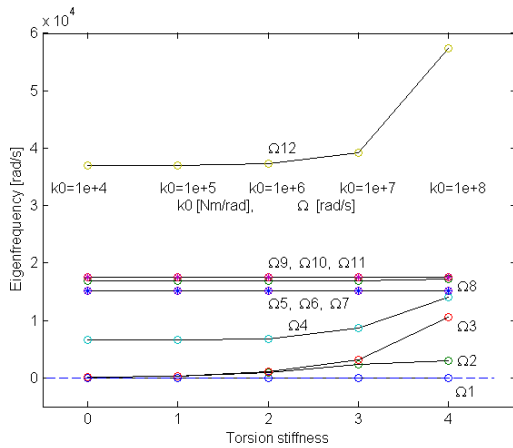


Fig. 2. Dependence of eigenfrequency on I/O stiffness

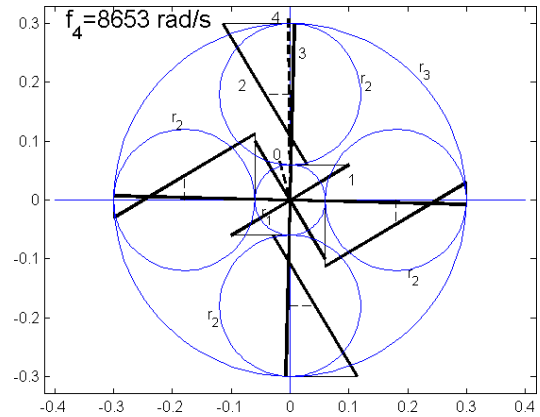


Fig. 3. Mode of vibration at 8693 rad/s

The external torsional stiffness of input and output (I/O) aggregates influences only some of eigenfrequencies of gearing train, but some groups of them (e.g. triple frequencies Ω_5 , Ω_6 , Ω_7 and Ω_9 , Ω_{10} , Ω_{11}) are independent on the increase of I/O shafts stiffness. The simple eigenfrequencies Ω_2 , Ω_3 , Ω_4 , Ω_8 , Ω_{12} are approximately constant up to $k_0 = 100\,000 \text{ Nm/rad}$ and at higher stiffness they rapidly increase. A mode of free vibration of investigated planetary gearings with external torsional stiffness of input shaft $k_0 = 1 \times 10^7 \text{ Nm/rad}$ is shown as an example in Fig. 3.

Results of developed modal analysis will be used for evaluation of measurements data gained on the new gearing box prototypes. More detailed description of modal properties of planetary gearing will be given at presentation.

Acknowledgement

The work has been supported by the grant project CSF No. 16-04546S.

Effect of a soft tissue on vocal tract acoustic resonance properties in vocal exercises using phonation into tubes

V. Radolf^a, J. Horáček^a, A. M. Laukkanen^b

^a Institute of Thermomechanics AS CR, v. v. i., Dolejškova 1402/5, 182 00 Prague, Czech Republic

^b Speech and Voice Research Laboratory, School of Education, Åkerlundink. 5, University of Tampere, 33100 Tampere, Finland

In this contribution a mathematical model is introduced to clarify the influence of the vocal tract soft tissues on the acoustic resonance (formant) frequencies. The influence is studied in the context of voice therapy technique that uses phonation into tubes. Strong acoustic-structural interaction is demonstrated to take place in the vocal tract when it is prolonged by a tube with the distal end in air or submerged 2 cm and 10 cm in water. The numerical results from the model (Fig. 1) are compared with the resonance frequencies measured in humans.

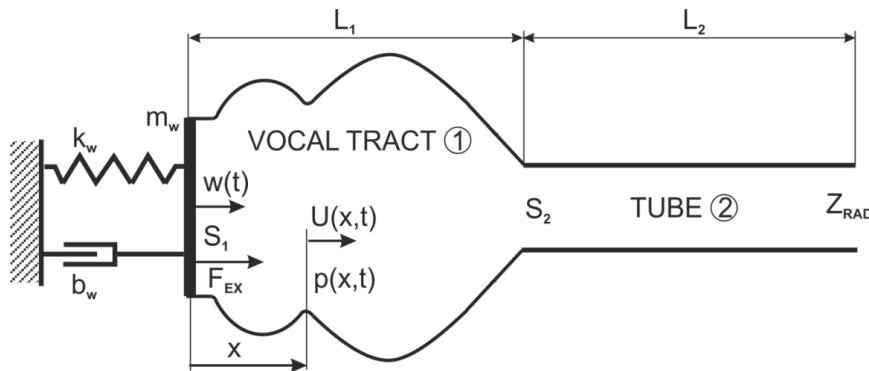


Fig. 1. Scheme of the vocal tract model for vowel phonation through a tube connected to the lips. The inner end of the VT is closed by a yielding wall at the position of the vocal folds. The yielding wall is modeled by a damped dynamic mechanical system with one degree of freedom coupled with the VT tract model. The radiation losses Z_{RAD} are considered at the distal tube end

The transfer function between the output pressure $p(x=L_1+L_2)$ and the external force F_{EX} loading the mass m_w by the harmonic excitation can be derived as

$$\frac{P_{out}}{F_{EX}/S_1} = \frac{Z_{RAD}}{\frac{1}{S_1^2} \left(b_w + \frac{k_w}{j\omega} + j\omega m_w \right) \cdot (A - C \cdot Z_{RAD}) - (B - D \cdot Z_{RAD})}, \quad (1)$$

where A, B, C, D are components of the transfer matrix of the complete acoustical system (VT + tube), which was divided into 30 acoustic elements (29 conical acoustic elements for VT and 1 cylindrical element for the tube), see [2]. The geometrical parameters considered for a glass ‘resonance tube’ were: $L_2 = 26.4$ cm and $S_2 = 0.36$ cm², which corresponds to the inner diameter 6.8 mm, and for a silicon ‘Lax-vox tube’: $L_2 = 35$ cm and $S_2 = 0.785$ cm² for the inner diameter 1 cm. The following parameters for the mechanical system were recalculated from the data published by Liljencrants [1 - Table 4.1]: the eigenfrequency $\omega_w = 2\pi \cdot 66$ rad/s, the damping ratio of the yielding wall $\zeta_w = 0.99$ and the mass $m_w = 1400 S_1^2 = 0.2$ gram.

Considering the mechanical resonance F_m of vocal tract to be 66 Hz, as previously estimated from measurements of a closed vocal tract [1], then according to the mathematical model for the vocal tract prolonged by a rigid glass tube, this frequency drops to 26 Hz, see the thin line in Fig. 2. When the tube is considered to be submerged in water, F_m drops further to $F_m=8$ Hz and to about $F_m=10$ Hz for a silicon Lax-vox tube (longer and wider), see thick lines in Fig. 2. This shows that the mechanical resonance can be near the measured water bubbling frequency $F_b=11-11.5$ Hz. The result, thus, supports the hypothesis of a coalescence of the low frequency mechanical resonance of the human vocal tract and the frequency of water bubbling during phonation into a tube with the other end submerged in water. This could potentially enhance the positive effects of the water therapy procedure, i.e. to intensify a massage like effect that may potentially relax the muscles and improve liquid circulation in the tissue. On the other hand, this coalescence may result in unpleasantly intensive vibrations of the laryngeal tissues which may even cause some vocal fold impairment.

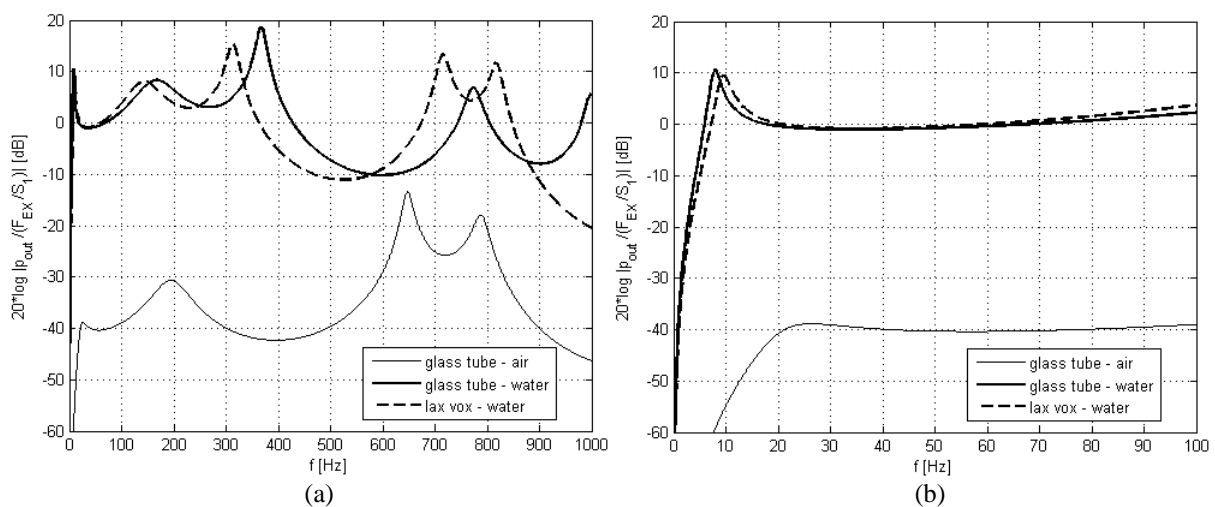


Fig. 2. Computed absolute values of the transfer functions $p_{out}/(F_{EX}/S_1)$ of the VT model for vowel /u:/ prolonged by the resonance tube in air and in water and by the Lax-vox tube in water, with the detail in the frequency range of the first resonance (right)

The first computed acoustic resonance frequency decreased from $F_1=195$ Hz for the tube end in air down to about $F_1=168$ Hz for the tube end in water, which roughly agrees with the first formant frequency ca 179 Hz found experimentally for a human male vocal tract. In these experiments a male subject phonated on [u:] at comfortable pitch and loudness into the resonance tube with the outer end of the tube submerged 2 cm and 10 cm under the water. According to the experiments, the oral pressure variation does not depend on the depth of submersion of the tube with the distal end in water.

Acknowledgements

The work has been supported by the grant project GACR No 16-01246S.

References

- [1] Liljencrants, J., Speech synthesis with a reflection-type line analog, PhD thesis, Stockholm, 1985.
- [2] Radolf, V., Horáček, J., Dlask, P., Otčenášek, Y., Geneid, A., Laukkanen, A.M., Measurement and mathematical simulation of acoustic characteristics of an artificially lengthened vocal tract, Journal of Sound and Vibration 366 (2016) 556-570.

Modelling of wave propagation in phononic plates in frequency and time domain

E. Rohan^a, R. Cimirman^b

^a*European Centre of Excellence NTIS – New Technologies for the Information Society, Faculty of Applied Sciences, University of West Bohemia, Univerzitní 8, 306 14 Plzeň, Czech Republic*

^b*New Technologies Research Centre, University of West Bohemia, Univerzitní 8, 306 14 Plzeň, Czech Republic*

The phononic plates are periodic structures made of elastic components with large differences in their elastic coefficients, the soft phase being distributed in a form of inclusions embedded in a stiff matrix. The homogenization approach of such elastic structures occupying domain Ω with the “dual porosity” type of the scaling ansatz applied in the inclusions [1] leads to the following model

$$-\omega^2 \mathbf{M}(\omega^2) \mathbf{q} + \mathbf{K} \mathbf{q} = \mathbf{f}(\omega^2) \quad \text{in } \Omega, \quad (1)$$

where $\omega \in \mathbb{R}$ is a fixed frequency, $\mathbf{q}(x) \in \mathbb{R}^d$ is the generalized displacements $\mathbf{M} : \mathbb{R}^d \mapsto \mathbb{R}^d$ is the mass tensor (real symmetric, but possibly indefinite, depending on $\omega \in \mathbb{R}_+$) and \mathbf{K} is the 2nd order (elliptic) differential operator, the stiffness. For the 3D elasticity problem (with $\mathbf{q} = \mathbf{u} = (u_i)$, $i = 1, 2, 3$) \mathbf{K} attains the form $(\mathbf{K})_{ij} = -\partial_k D_{ikjl} \partial_j$ with D_{ikjl} being the usual symmetric positive definite elasticity tensor.

Wave equation (1) can be transformed using the spectral decomposition of \mathbf{M} , see [2],

$$-\omega^2 \langle \Lambda \boldsymbol{\xi}, \boldsymbol{\zeta} \rangle_{\Omega} + a_{\Omega}(\boldsymbol{\xi}, \boldsymbol{\zeta}) = \langle \mathbf{b}(\omega^2), \boldsymbol{\zeta} \rangle_{\Omega} \quad \text{for all } \boldsymbol{\zeta} \in W_0(\Omega), \quad (2)$$

where $a_{\Omega}(\cdot, \cdot)$ is an elliptic bilinear form and $\Lambda = \Lambda^+ + \Lambda^-$ is the diagonal spectral matrix associated with \mathbf{M} , decomposed into the positive and the negative parts. This is the basis for introducing two subspaces by solving eigenvalue problems which depend on the imposed frequency. Projections of (2) into these bases yield a system which allows us to resolve the propagating and evanescent modes (when $\Lambda^- \neq \mathbf{0}$).

The homogenization of the phononic Reissner-Mindlin plate [3] leads to a model which attains the same form (1), although \mathbf{q} involves plate deflections and rotations and the \mathbf{K} and \mathbf{M} have a more complex structure. The phononic Timoshenko beam (deflection w , rotation θ) is described in the frequency domain by the following equations, where $x \in]0, L[$, $(\mathcal{M}, \mathcal{N}, \mathcal{G}, \mathcal{D})$ are the homogenized coefficients, h is the thickness),

$$-\omega^2 \frac{h^3}{3} \mathcal{M}(\omega^2) \theta - \frac{h^3}{3} \mathcal{D} \theta'' - h \mathcal{G}(w' - \theta) = 0, \quad -\omega^2 h \mathcal{N}(\omega^2) w - h \mathcal{G}(w'' - \theta') = 0. \quad (3)$$

The beam is clamped at $x = 0$, whereas a kinematic excitation of deflections at $x = L$ is considered, thus $w(0) = 0$, $w(L) = \bar{w}$, $\theta(0) = 0$, and $\theta'(L) = 0$. In Fig. 1, the distributions of deflections and rotations are depicted for the frequency modulation to illustrate qualitative difference of the response for the “pass” and the “stop” bands. Model (3) transformed to the

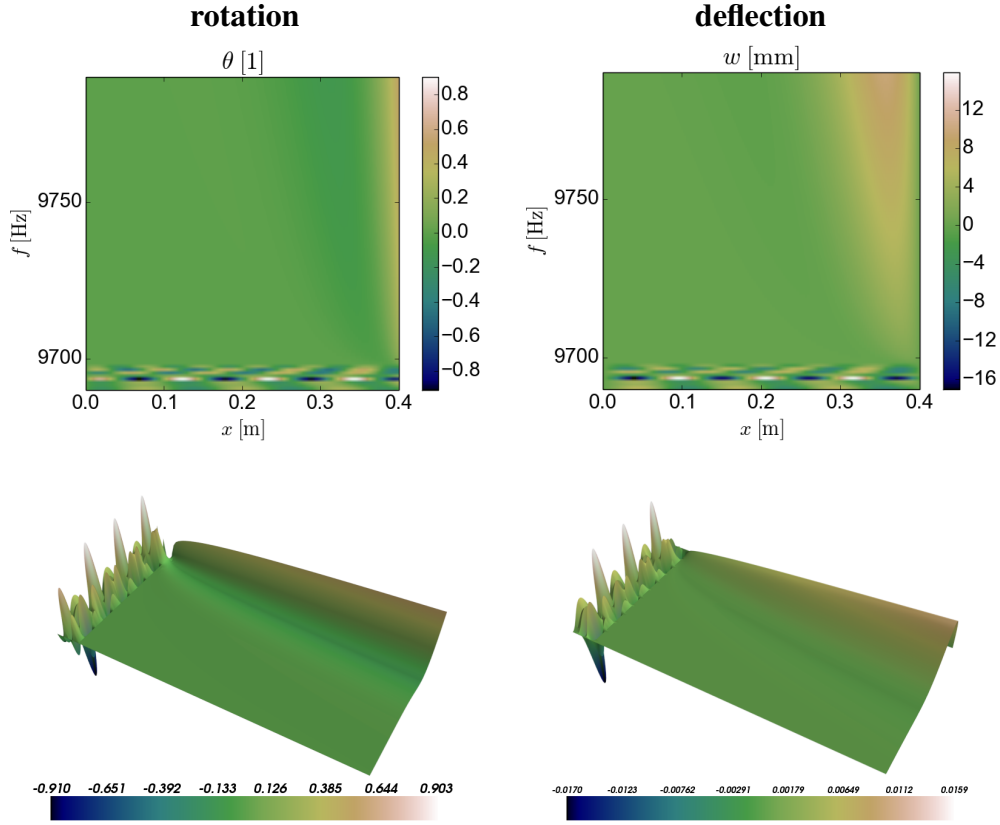


Fig. 1. Modulation between 9.690 and 9.790 kHz (lower bound of band gap is 9.698 kHz)

time domain yields

$$\begin{aligned} \frac{h^3}{3} \int_0^t \mathcal{M}(t-s) \ddot{\theta}(s) ds - \frac{h^3}{3} (\mathcal{D}\theta')' - h\mathcal{G}(w' - \theta) &= 0, \\ h \int_0^t \mathcal{N}(t-s) \ddot{w}(s) ds - h\mathcal{G}(w' - \theta)' &= 0. \end{aligned} \quad (4)$$

In the conference paper, the spectral decomposition approach to the wave dispersion analysis in the phononic media is compared with other methods of modelling the wave propagation in homogenized periodic structures. Numerical solutions of the dynamic problem of the type (4) involving the convolutions in the time is discussed.

Acknowledgments

This work was supported the project GACR P101/12/2315 and by the project LO1506 of the Czech Ministry of Education, Youth and Sports.

References

- [1] Ávila, A., Griso, G., Miara, B., Rohan, E., Multiscale modeling of elastic waves: Theoretical justification and numerical simulation of band gaps, *Multiscale Modeling & Simulation* 7 (1) (2008) 1-21.
- [2] Rohan, E., Cimrman, R., Miara, B., Modelling response of phononic Reissner-Mindlin plates using a spectral decomposition, *Applied Mathematics and Computation* 258 (2015) 617-630.
- [3] Rohan, E., Miara, B., Elastodynamics of strongly heterogeneous periodic plates using Reissner-Mindlin and Kirchhoff-Love models, *ZAMM – Journal of Applied Mathematics and Mechanics* 96 (3) (2016) 304-326.

Contribution to the analysis of higher dimensional dynamical systems

J. Rosenberg^a, V. Adámek^b

^a Faculty of Applied Sciences, University of West Bohemia, Univerzitní 8, 306 14 Plzeň, Czech Republic

^b NTIS - New Technologies for Information Society, University of West Bohemia, Univerzitní 8, 306 14 Plzeň, Czech Republic

In the modelling of mechanical and mainly biomechanical problems we have to deal with dynamical systems having the number of degree of freedom $\text{DOF} > 3$. The analysis of these systems is much more difficult in comparison to problems with $\text{DOF} \leq 3$. In this work we are dealing with the model of the Cajal-like interstitial cell which plays an important role in the bladder wall. This system has five DOFs. It's important to know all the attractors in the physiological range of main parameters.

The model used in this work is developed in [3], where the usage of perpetual points according to [2] was described. While the method of perpetual points is still not verified we tried to develop another simple method allowing to obtain all the attractors. The software developed in Matlab allows to study even systems with higher DOFs. The inspiration was the code written by S. Kolukula and presented in [1]. We compared also the proposed method with the method making the use of the perpetual points [2]. The proposed method involves the following steps:

1. Using the knowledge of some attractors either fixed points (FPs), limit cycles (LCs) or chaotic attractors, we use their coordinates as input to a main control function. In the case of chaotic attractors it is necessary to use three or more arbitrary points of this attractor.
2. We choose the number of grid points and the intervals of coordinates where the basins of attraction should be searched in.
3. The right hand sides of ODEs describing the dynamical system is defined in a separate Matlab function.
4. The basins of attraction are calculated as a set of grid points from which the attractors defined in Step 1 are reached. The basins are then coloured with respect to the type of attractor. The rest of the whole phase space corresponds either to new basins of attraction of not yet known attractors or to the points running to infinity.
5. Starting from this new region we eventually obtain new attractors and the process can be repeated.

The perpetual points are computed in parallel to this procedure. It can be seen that they are lying on the found basins of attraction and that they can probably be used for the finding of hidden attractors. To show this property more deeply some results for the system of Nose-Hoover oscillator with the lower number of DOFs ($\text{DOF} = 3$) are demonstrated.

As an example of a system with $\text{DOF} = 5$, the model of the interstitial cell of Cajal mentioned previously was used. The result is shown in Fig. 1. We see that starting from the unstable FP the LC is reached (self-excited attractor) although this FP is of saddle type. It means that starting from the red basins of attraction we reach even this FP! In Fig. 2 the trajectories starting from different basins of attraction are shown.

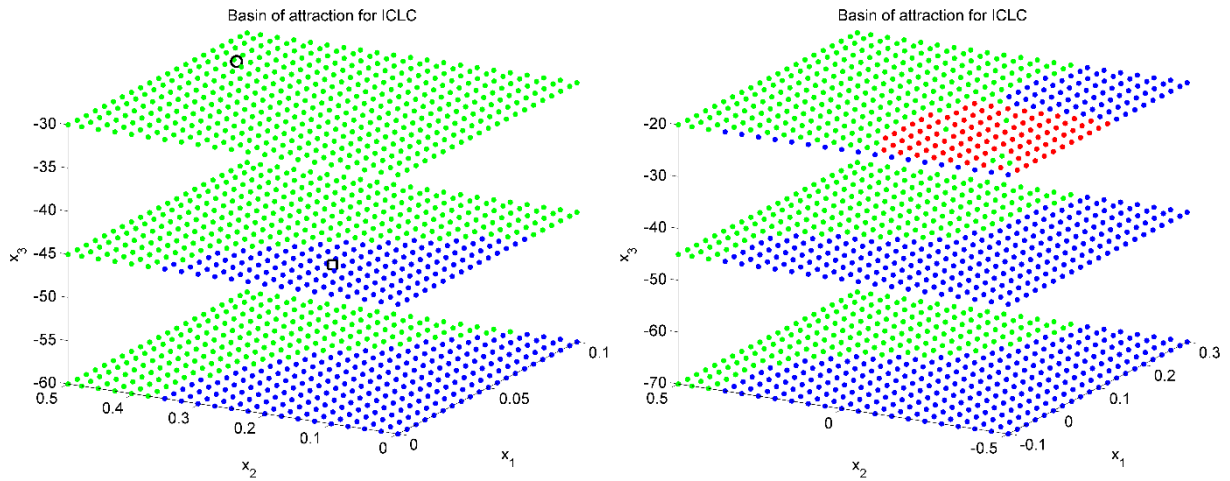


Fig. 1. Basins of attractions for physiological ranges of variables with perpetual point (square) and the unstable fixed point (circle) (left) and the enlarged phase space (right). Blue is the basin of attraction for stable FP, green for limit cycle and red for unstable FP of saddle type

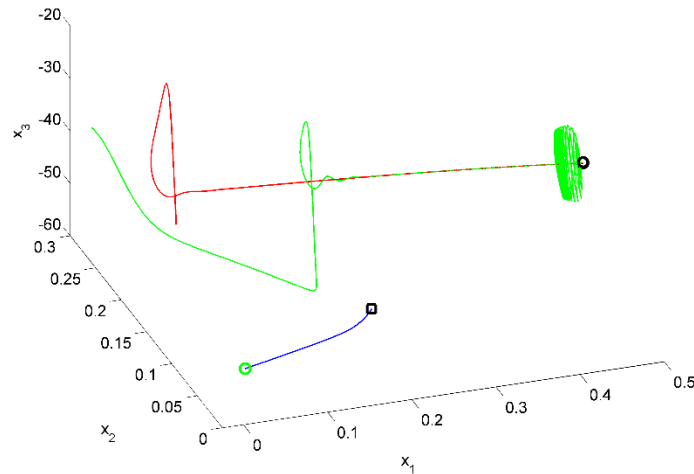


Fig. 2. Trajectories starting from different basins of attraction in the phase space. Colours, FP and PP correspond to the Fig. 1

Acknowledgements

This publication was supported by the project LO1506 of the Czech Ministry of Education, Youth and Sports.

References

- [1] Kolukula, S., <http://www.mathworks.com/matlabcentral/fileexchange/43564-basins-of-attraction>.
- [2] Prasad, A., Existence of perpetual points in nonlinear dynamical systems and its applications, *International Journal of Bifurcation and Chaos* 25(2) (2015), art. num. 1530005.
- [3] Rosenberg, J., Stengl, M., Byrtus, M., Simple model of the Cajal-Like interstitial cell and its analysis, *Applied Mechanics and Materials* 821 (2016) 677-684.

Numerical and experimental study of induction bending of large diameter pipes

M. Sága^a, M. Handrik^a, P. Kopas^a, M. Vaško^a, M. Tropp^a

^a Faculty of Mechanical Engineering, University of Žilina, Univerzitná 1, 010 26 Žilina, Slovakia

Our paper presents FEM application for numerical analysis of the bending process of large scale gas pipes using induction heating. The goal of this study was to obtain relevant information about stress and strain distribution and mainly about ovalization changes. Numerical results were compared with real experiment focused on measuring of the radial thickness change applying ultrasonic method [3].

Induction bending as a technique is relatively quick and cheap (Fig.1), but produces unwanted changes in geometry such as wall thinning at the extrados, wall thickening and wrinkling at the intrados, and steep transitions in wall thickness between tangent and bend. These problems increase in severity as the bend radius is reduced. However, there are a lot of another problems, such as springback and cross-section ovality when bending thinwall pipe with a large diameter. The fundamental tasks which had to be solved we can summarized as follows: material characteristics identification, kinematic analysis of the process, implementation of material characteristics into computational model, finite element modelling (geometry, definition of thermal contact problem, thermo-plasticity and large strain analysis), stress, strain, displacement analysis, computational ovality prediction and comparison [1,3].

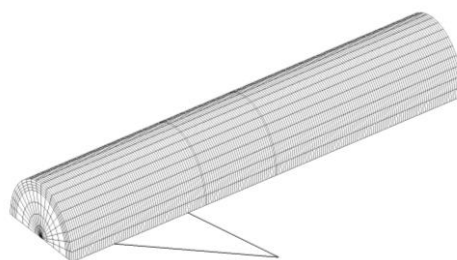
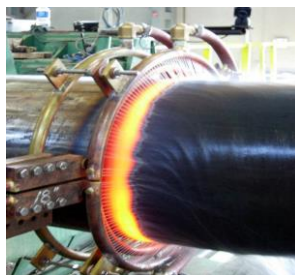


Fig. 1. Bending process of the pipe using induction heating

Fig. 2. FE model of the pipe

Modelling of technological processes of hot tube bending is a complex task involving constrained physical fields, and the following types of subtasks are to be addressed [1]:

- analysis of the state of stress and strain for flexible bodies – modelling the pipe deformation,
- temperature field modelling – modelling of heat propagation in the pipe and its surroundings.

Constraints related to individual physical fields are as follows [1, 2]:

- Analysis of the state of stress and strain vs. temperature fields modelling – changing the material temperature will significantly change the material mechanical properties, and the stress analysis should allow to reflect this change.
- Temperature field modelling vs. electromagnetic fields modelling, heating was modelled by contact with heat transfer in the location of electromagnetic inductor.

- Temperature field modelling vs. fluid dynamics modelling, cooling was modelled by contact with heat transfer in the location of water spray.

Computational models that would include solving all the above-mentioned physical fields and their mutual constraints are extremely challenging in terms of compiling a corresponding mathematical model, and it is also very difficult to solve. When compiling a physical model, we must take into account the fact that all physical fields need to be addressed as dynamic problems involving a change in the tube shape during the bending process. When compiling a computational model, it is appropriate to carry out modifications, namely by simplifying the physical model through reducing the modelled physical fields and their mutual interactions [2, 3]. In terms of modelling the technological process of pipe bending using induction heating, dominant is to preserve the analysis of the state of stress and strain interlinked with the temperature field analysis. The computational model allows us to obtain the following information: nodal points displacements that allow us to display the pipe shape after bending – using the mesh nodal points position at control points we can determine the pipe wall thickness and ovality after bending, stress and strain field distribution including the residual ones, as well as temperature field distribution.

In verifying the created computational model we utilised comparison of the basic geometrical characteristic – pipe wall thickness after bending, found out in experimental measurement using ultrasound [3]. We compared the change in the pipe wall thickness in the middle of the bend where the thickness change is settled, therefore there is a relatively small possibility of error due to incorrect positioning of experimental measurements and the thickness reading site on the computational model. Figure 3 shows the course of the pipe wall thickness changes in the middle of the bend, namely in the radial direction. Maximum difference between the experimentally measured value and the value obtained through numerical computation was found at the inner side of the bend, with the following results: the experimentally measured value was 21.63 mm, and the value determined by numerical computation was 21.022 mm. Thus, the maximum error of the tube wall thickness is 1.81 %.

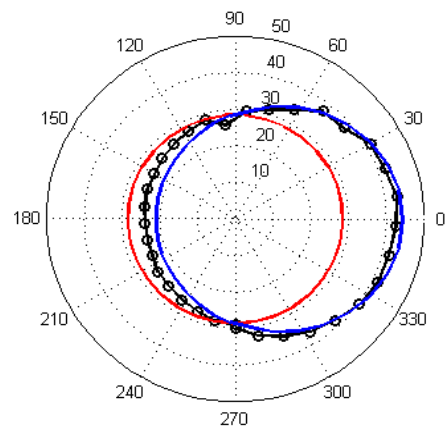


Fig. 3. Behaviour of radial changes of pipe thickness – point 13
- red = reference value
- black = measuring data
- blue = computed data

Acknowledgements

This work has been supported by grant project VEGA No. 1/0234/13.

References

- [1] Hu, Z., Elasto-plastic solutions for spring-back angle of pipe bending using local induction heating, *Journal of materials processing technology* 102 (2000) 103–108.
- [2] Li, X., Wang, M.-T., Du, F.-S., Xu, Z.-Q., FEM simulation of large diameter pipe bending using local heating, *Journal of Iron and Steel Research, International* 13 (5) (2006) 25-29.
- [3] Tropp, M., Handrik, M., Kopas, P., Sága, M., Computer simulation of induction bending process, *Pipeline & GAS Journal* 11 (239) (2012) 3.

Modelling vibration sources of rotating device using MSC.ADAMS

A. Sapietova^a, V. Dekys^a, P. Sulka^a

^a University of Žilina, Faculty of Mechanical Engineering, Univerzitná 1, 010 26 Žilina, Slovakia

Correct operation of machinery inevitably requires alignment of machine geometry in hundredths of millimeters (depending on the shaft speed). Shaft misalignment results in increased reactions, which the bearings must absorb, it induces mechanical looseness, damages to seals, allows fluids and impurities to enter the bearings, which considerably decreases the machine operating life and, consequently, the operating life of the whole machinery [4]. Carrying out purposeful maintenance of machines requires a correct interpretation of malfunction causes. In general, there is a lack of correlation between causes and consequences of malfunctions [2].

One of non-destructive methods allowing identifying and consequently eliminating the problem is vibration diagnostics of rotating machinery. It uses vibrations, which are generated by machines in operation, as a source of information about the way of its working. Using this tool, maintenance of machines is planned according to the actual state, and, therefore, many useless preventive revisions are eliminated, which leads to important savings of spare parts and time for machinery repair [1]. It gives information about regularly monitored machines, by which we can prolong the planned periods of shutdowns or prepare in advance for the repair of specific monitored machine node etc. [2, 3, 5].

However, the above is diagnostics of malfunction caused by experimental method right in the operation. In the recent decades many software products solving dynamic problems of rotating machines were developed, therefore, computer simulation and building of virtual prototypes (VP) is nowadays an essential part of every technical solution [4]. Often, there is a question how to create a VP so that the results of its mathematical solution correspond to physical values or values acquired by experimental measurement.

The paper presents the creation of a virtual prototype of gearing, and this prototype is used to generate and analyze dynamic effects measurable in the place of rotary links between the shaft and the frame. These effects are registered as vibration velocity. We then use the generated courses of vibration velocity to obtain velocity spectrum, and this spectrum will be compared with the spectra from diagnostic measurements. In this way we can verify the created virtual model, adjust its appropriate variables to select a suitable solver in MSC.ADAMS software.

The state of the evaluated transmission system can be determined by observing the properties that are specific for this system configuration. These specific properties are time and frequency spectra of vibration velocities obtained from the time courses of vibration on the shaft bearing housings.

Fig. 1 shows the FFT (fast Fourier transform) frequency spectrum corresponding to the above presented course of velocities in the radial direction. The course shows a dominant first tooth frequency. The spectrum also includes its harmonic multiples with insignificant sidebands.

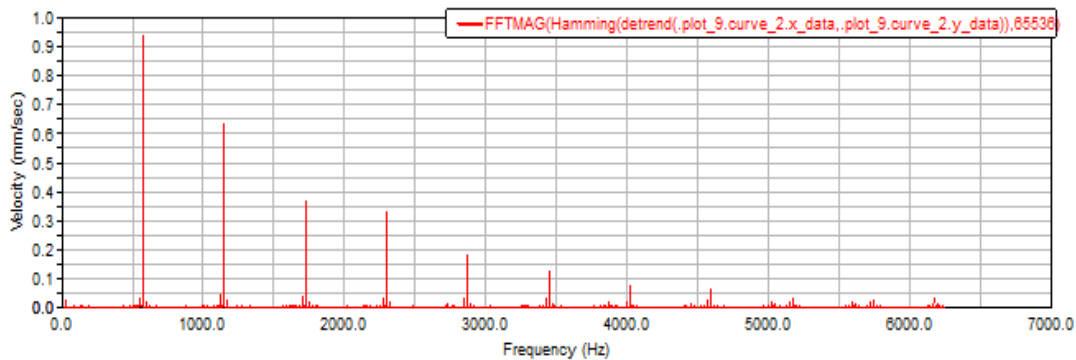


Fig. 1. FFT velocities in the radial direction on the output bearing

Fig. 2 shows a normal spectrum of vibration velocity on the output shaft of a 3-speed gearbox of a cement mill. The spectrum includes lower, but significant multiples of f_{ZUB3} (40.4Hz, 120Hz, 160.4Hz, output gear), two dominant peaks at multiples of f_{ZUB2} (130.4Hz, 259.7Hz), and significant multiples of the tooth frequency f_{ZUB3} (513.3Hz and 1026.6Hz, input gear). This measurement clearly shows a decrease of amplitudes of harmonic tooth frequencies for individual gear speeds.

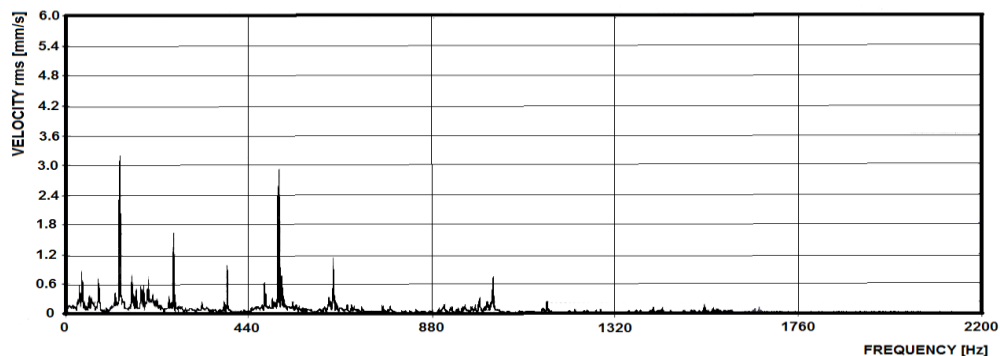


Fig. 2. Normal FFT spectrum of a raw mill gearbox, characterised by decrease in higher multiples of tooth frequencies

In the created VP, the courses of kinematic parameters and FFT spectra were qualitatively identical to the predicted and practically measured ones. This created VP of a gearing may further serve to modelling failure states in the gearing, such as misalignment, damage to teeth, etc. This will allow analysing and mutually comparing, for example, the manifestations of undamaged and damaged gearboxes.

Acknowledgements

This work has been supported by the Slovak Grant Agency VEGA 1/0795/16 and the Slovak Research and Development Agency under the contract No. APVV-0736-12.

References

- [1] Adams, M.L., Rotating machinery vibration from analysis to troubleshooting, Marcel Dekker, New York, 2001.
- [2] Bilošová, A., Biloš, J., Vibration diagnostics, VŠB-TU, Ostrava, 2012.
- [3] Kreidl, M. et al., Diagnostic systems, CVUT, Praha, 2001. (in Czech)
- [4] Saga, M., Kopas, P., Vasko, M., Some computational aspects of vehicle shell frames optimization subjected to fatigue life, Communications scientific letters of the University of Žilina 12 (4) (2010) 73-79.
- [5] Sheffer, D. Girhard, T., Practical machinery vibration analysis and predictive maintenance, Newnes, 2004.

Numerical simulations of flow induced vocal folds vibrations

P. Sváček^a, J. Valášek^a

^a*Department of Technical Mathematics, Faculty of Mechanical Engineering, Czech Technical University in Prague,
Karlovo nám. 13, 121 35 Praha, Czech Republic*

This paper is focused on modelling of fluid-structure interaction problem involved in biomechanics of human voice, see [4]. The mathematical models can be used to provide important information about the voice production. This is why simplified computational models are used using simple mass-spring models coupled with a quasi-1D airflow, see e.g. [1]). However, the simplified flow models do not describe the details of the glottal airflow. In order to address the flow problem more accurately the 2D Navier–Stokes equations can be used, see e.g. [3] or [2]. However, these model describe the flow in the glottal part more precisely, but the other important details of the complex problem of the voice creation are not address (e.g. glottal gap closing or the presence of the contact problem).

In this paper the artificial inlet/outlet boundary conditions are discussed in the context of the closure of the channel due to the vocal folds vibrations. The mathematical model describing the fluid structure interaction problem is given. The choice of boundary conditions and its implementation is discussed. Numerical results are presented.

First, the flow of an incompressible viscous fluid in the domain Ω_t^f is described by the system of the incompressible Navier-Stokes equations written in the ALE form

$$\rho \frac{D^A \mathbf{v}}{Dt} + \rho((\mathbf{v} - \mathbf{w}_D) \cdot \nabla) \mathbf{v} = \text{div } \boldsymbol{\tau}^f, \nabla \cdot \mathbf{v} = 0.$$

Here $\mathbf{v} = (v_1, v_2)$ is the fluid velocity vector, ρ is the constant fluid density, and $\boldsymbol{\tau}^f = (\tau_{ij}^f)$ is the fluid stress tensor given by $\boldsymbol{\tau}^f = -p\mathbb{I} + 2\mu\mathbb{D}(\mathbf{v})$, where $\mathbb{D}(\mathbf{v}) = \frac{1}{2}(\nabla \mathbf{v} + (\nabla \mathbf{v})^T)$, p is the pressure and $\mu > 0$ is the constant fluid viscosity. For the system (1) an initial condition and the appropriate boundary conditions are prescribed. The boundary $\partial\Omega_t^f$ is assumed to be formed by mutually disjoint parts Γ_I - inlet, Γ_O - outlet, Γ_{Wt} - wall whose part (vocal fold surface) may be displaced in time. Here, only the boundary conditions prescribed on the inlet and on the outlet part of the boundary are discussed. Particularly, at the inlet the following two types of boundary condition

$$\text{a) } \mathbf{v} = \mathbf{v}_I \text{ on } \Gamma_I, \quad \text{a') } -\mathbf{n} \cdot \boldsymbol{\tau}^f + \frac{1}{2}\rho(\mathbf{v} \cdot \mathbf{n})^- \mathbf{v} = p_I \mathbf{n} \text{ on } \Gamma_I \quad (1)$$

are considered, where \mathbf{n} denotes the unit outward normal vector to $\partial\Omega_t$, \mathbf{v}_I is the inlet velocity, p_I is a reference inlet pressure value. At the outlet the modified do-nothing boundary condition in the form of (1) is used with different pressure value. The boundary condition allows the inflow of the fluid at the boundary Γ_O . Let us mention here, that the practical realization of particularly the Dirichlet boundary condition (inlet velocity) can differ. The velocity \mathbf{v} can be either expected to approximately satisfy boundary condition 1a) or a penalization concept can be introduced.

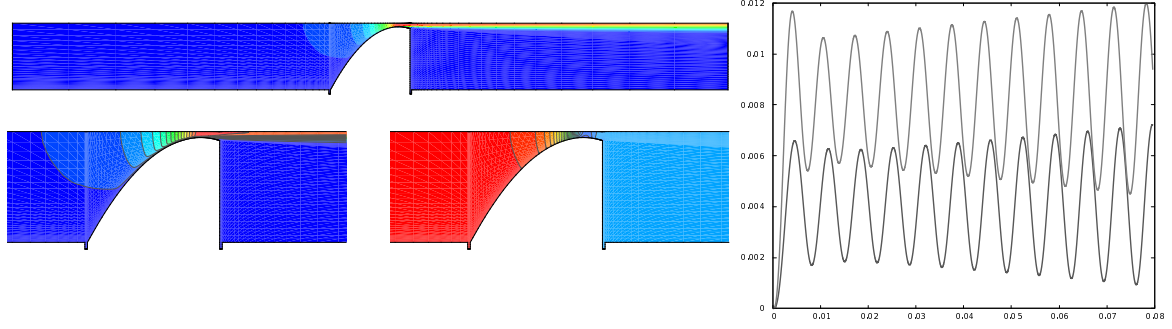


Fig. 1. Numerical results of flow around the vocal fold model: on the left computational domain with flow velocity magnitude, and details of flow velocity magnitude and pressure distribution, on the right the displacement θ_1 and θ_2 in dependence on time t

Further, the vocal folds are assumed to be an elastic structure. For the small displacements its motion can be described by equation

$$\rho^s \frac{\partial^2 \mathbf{u}}{\partial t^2} - \operatorname{div} \boldsymbol{\tau}^s = \mathbf{f} \quad (2)$$

in a bounded open set representing the vocal fold denoted by $\Omega^s \subset \mathbb{R}^2$. Here, \mathbf{u} is the displacement of the structure, $\mathbf{f} = (f_1, f_2)$ is the density of the volume force, ρ^s denotes the density of the structure and $\boldsymbol{\tau}_s$ is the stress tensor dependent on the small strain tensor $\mathbf{e}(\mathbf{u}) = \frac{1}{2}(\nabla \mathbf{u} + (\nabla \mathbf{u})^T)$.

For the computations a simplified aeroelastic two degrees of freedom model is used. The motion of Γ_{Wt} is governed by the displacements $\theta_1(t)$ and $\theta_2(t)$ (upward positive) of the two masses m_1 and m_2 . The displacement vector $\boldsymbol{\theta} = (\theta_1, \theta_2)^T$ is obtained by the solution of the following equations (see [1] for details)

$$\mathbb{M}\ddot{\boldsymbol{\theta}} + \mathbb{B}\dot{\boldsymbol{\theta}} + \mathbb{K}\boldsymbol{\theta} = -\mathbf{F}, \quad (3)$$

where \mathbb{M} is the mass matrix, \mathbb{K} is the diagonal stiffness matrix with spring constants c_1, c_2 on its diagonal and \mathbb{B} is the matrix of the proportional structural damping. The numerical results for a test case from [3] is shown in Fig. 1 in terms of typical flow velocity magnitude distribution and the aeroelastic response.

Acknowledgment

This work was supported by the *Czech Science Foundation* under the *Grant No. 13-00522S*.

References

- [1] Horáček, J., Šidlof, P., Švec, J. G., Numerical simulation of self-oscillations of human vocal folds with Hertz model of impact forces, *Journal of Fluids and Structures* 20 (6) (2005) 853-869.
- [2] Link, G., Kaltenbacher, M., Breuer, M., Döllinger, M., A 2D finite element scheme for fluid-solid-acoustic interactions and its application to human phonation, *Computation Methods in Applied Mechanical Engineering* 198 (2009) 3321-3334.
- [3] Sváček, P., Horáček, J., Numerical simulation of glottal flow in interaction with self oscillating vocal folds: comparison of finite element approximation with a simplified model, *Communications in Computational Physics* 12 (3) (2012) 789-806.
- [4] Titze, I. R., *The myoelastic aerodynamic theory of phonation*, National Center for Voice and Speech, U.S.A., 2006.

Wang tiles with adaptive edges in material engineering

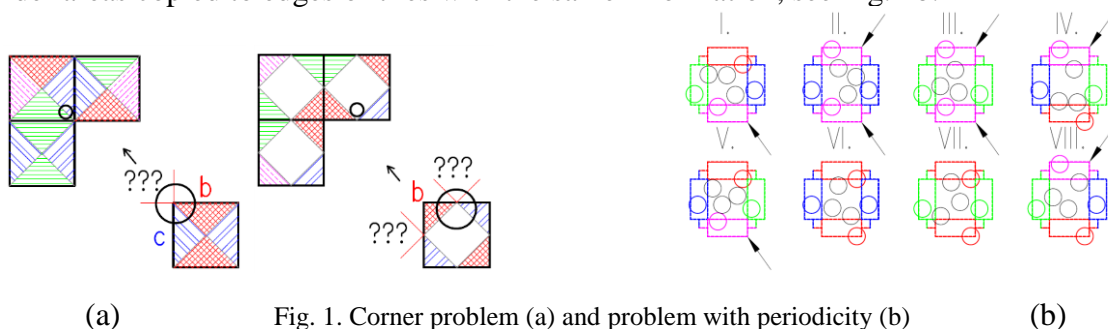
D. Šedlbauer^a

^a Department of Mechanics, Faculty of Civil Engineering, CTU in Prague, Thákurova 7/2077, 166 29 Prague, Czech Republic

The concept of Wang tiling [3] has been used in various fields of interests, e.g. the computational graphics or the biomechanical engineering. The main idea of the Wang tiling is to stack large aperiodic areas with a relative small set of tiles in order to reduce computational efforts for an analysis of the composed domain. The similar tasks can be found within problems of heterogeneous material engineering. For this discipline is not necessary to have strictly aperiodic areas, therefore CSHD [1] algorithm for stochastic tiling is used.

The generation of tile sets are provided via several approaches based on optimization methods, patches or molecular dynamics. The last mentioned technique exhibits potential for material models of large volume fraction without unwanted overlapping particles. In this contribution is presented a modification of the dynamic model for generation of Wang tiles which solves problems with inappropriate copying of tile areas and corner problems of tiling. The modelled material domain consists of hard circular particles of arbitrary radii within a matrix. In general, a set of Wang tiles is visually represented with squares of coloured edges. Considering two different information on vertical and horizontal edges we get minimal set of 8 tiles for stochastic tiling.

Wang tiling doesn't take into account diagonal tile during stacking of a final domain. This issue called corner problem is solved in general with corner tiling [2]. Nevertheless such approach is not sufficient for molecular dynamics in terms of possible particle overlapping, see Fig. 1a. Another problems that cause artificial periodicity are existence and dimensions of border areas copied to edges of tiles with the same information, see Fig. 1b.



The contribution presents upgrade of the dynamic algorithm based on adaptation of tile edges according to moving particles with respect to the rules of stochastic tiling. At the beginning particle centres with random velocity vectors are thrown into tiles related to the required volume fraction of composed material. Each particle during the process grow, bounce of the wall and collide with each other until a stopping criterion is reached.

The tile set consists of eight tiles. Each tile is surrounded with all possible neighbour tiles in terms of stochastic tiling. When particle contour leaves the Master tile, appropriate edges designated with the same colour (information) copies this contour. The particle rebounds

when the particle centre reach the original edge. The similar process runs when a particle reach two edges of a Master tile or interferes diagonal tile. The Master tile than manage adaptation of edges on all Slave tiles via three steps. Within the first step the shape of all edges designated with the same colour as modified Master tile boundaries are unified. In the next step a corner deformation of diagonal tile (in tiling) is copied to all tiles. The most critical issue for proper modification of boundaries is to find all possible neighbour tiling of the Master tile. In the last step corner deformation is copied to opposite side of each tile (either horizontal or vertical but the same for all tiles). This modification reduces inter alia dead spaces. The tiling then represents a puzzle system.

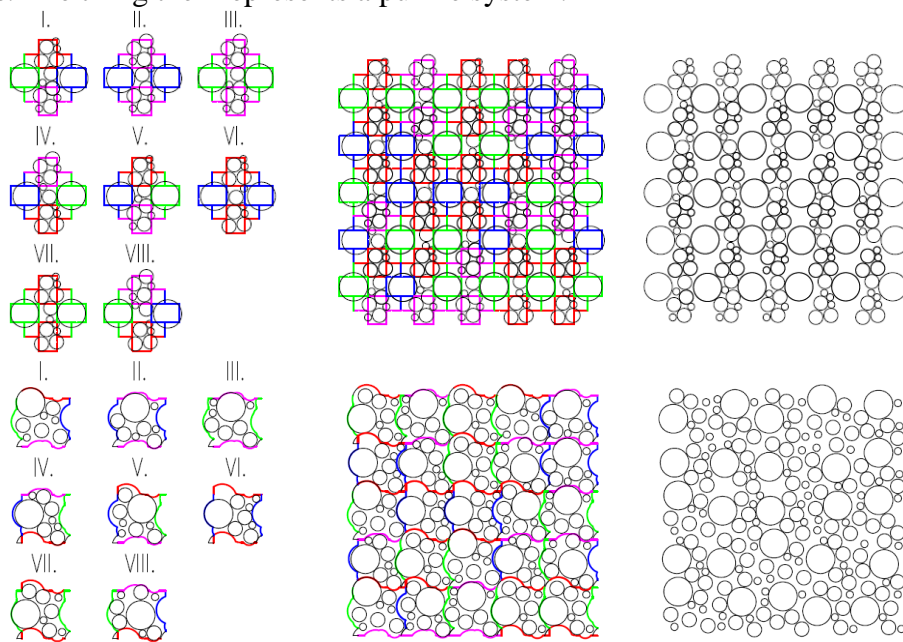


Fig. 2. Generated tiles and tilings a) Tile areas b) Adaptive Edges

For a comparison of previous and modified algorithm was chosen a tiled model with 5x5 tiles, see Fig 2. In here is obvious the periodicity problem of previous algorithm and corner problem of tiling in general. The situation becomes critical with higher volume fraction and with particle radii/tile diameter ratio. The tiling with adaptive boundaries solves these problems. It should be noted that for simplicity and clear representation all tiles of adaptive boundaries approach have just one large particle, therefore these particles follow grid of tiling. Nevertheless each tile of set could have different number of particles in order to reduce grid artefacts but the overall representative elements should follow required volume fraction. Despite improvement in field of tiling problems the concept of adaptive boundaries has larger computer demands that will be resolved within future work.

Acknowledgements

The financial support of the Grant Agency of the Czech Technical University in Prague, grant No. SGS16/037/OHK1/1T/11, is gratefully acknowledged.

References

- [1] Cohen, M., Shade, F.J., Hiller, S., Deussen, O., Wang tiles for image and texture generation, USA: ACM, New York, 2003, pp. 287–294.
- [2] Lagae, A., Ducre, P., An alternative for Wang tiles: Colored edges versus colored corners, ACM Transactions on Graphics 25 (4) (2006) 1442-1459.
- [3] Wang, H., Proving theorems by pattern recognition-II, Bell system technical journal 40 (1) (1961) 76-102.

Planar mechatronic structures with distributed collocated actuators and sensors

Z. Šika^a, R. Krejza^a, P. Beneš^a, M. Hromčík^b

^a Faculty of Mechanical Engineering, CTU in Prague, Technická 4, 166 07 Praha 6, Czech Republic

^b Faculty of Electrical Engineering, CTU in Prague, Technická 2, 166 27 Praha 6, Czech Republic

Distributed control is currently a very promising direction of research in mechatronics [4], [3], thanks to the new possibilities of cheap and miniature hardware implementation and request of efficient applications in industry which requires high scalability and reliability of development procedure. The final target is the concept of easily tunable, scalable, active vibration suppression control laws, defined by a limited number of independent parameters and optimized dominantly based on the local dynamical properties of the compact actuator-sensor-matrices and only finally tuned taking into account the particular global mechanical configurations of the final product (shape; boundary conditions; ...).

The topic of the paper is investigation of the decentralized controllers consisting of simple proportional velocity-feedback loops applied for each **collocated sensor/actuator pair** [1], [5]. Several variants with different densities of collocated pairs (Fig. 1 a)) have been tested. The considered planar mass-spring system is generally nonlinear, control law optimization is done for the linearized variant (Fig. 2) and then tested also for the original nonlinear one (Fig. 3). The simplest conceivable variant comprising the same gain for all pairs isn't optimal. The damping is not improved "uniformly", many of the lower modes become overdamped as the proportional gain is raised to meaningful values to affect the higher modes also. This means that the resulting time-domain responses are sluggish and power consumption is unnecessarily high at the same time.

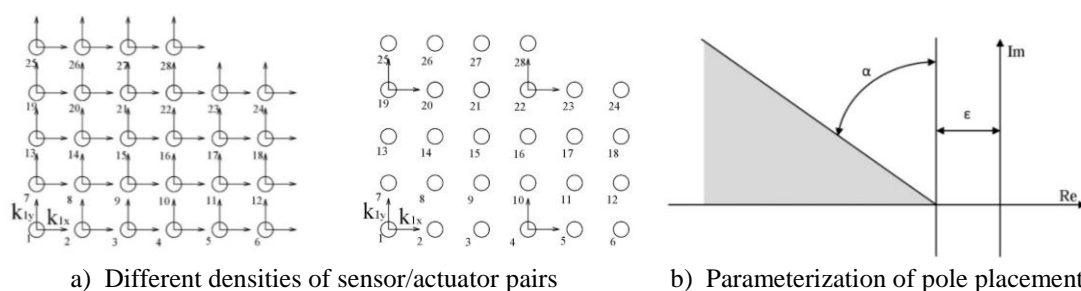


Fig. 1. Conditions of control law optimization

The better results can be achieved e.g. by optimization of the gains of particular collocated sensor/actuator pairs. Two basic versions of optimization formulation have been tested, **minimization of maximum gain** and **maximization of angle α** of pole placement region (Fig. 1 b)). The optimization parameters can be (for both mentioned versions of objective function) either directly the gains of all pairs or coefficients of formulas (linear, bilinear, quadratic, etc.) for gain dependency based on the spatial position of sensor/actuator pair. The further important constraint condition of optimization has been the ratio of number of real

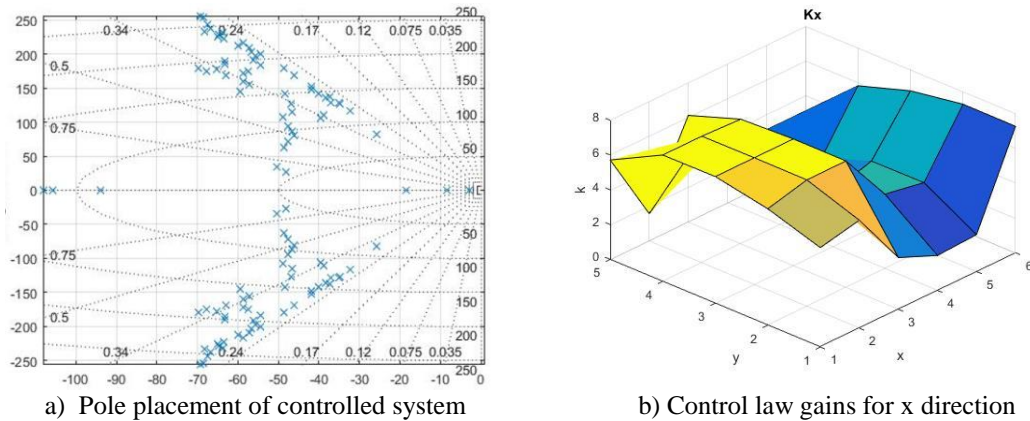


Fig. 2. Example of results of optimization of gains of collocated sensor/actuator pairs

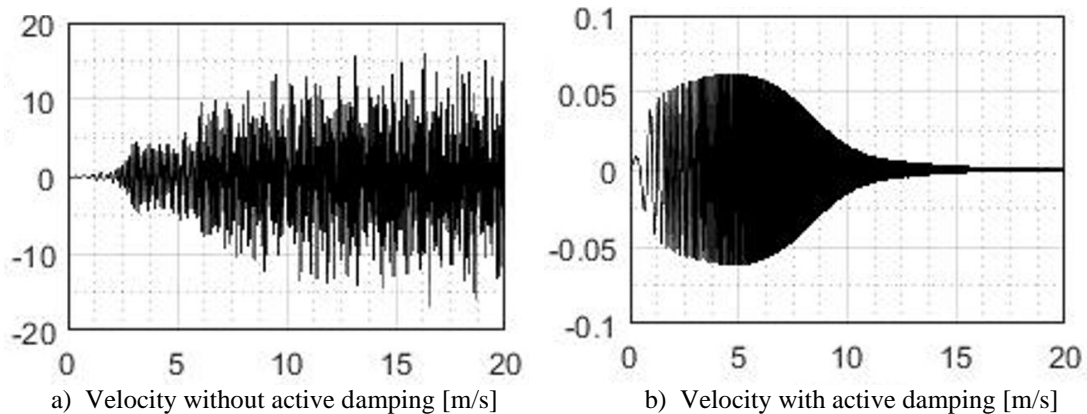


Fig. 3. Example of chirp (0,1 Hz to 50 Hz) disturbance response – velocity of reference point

poles with respect to the total number of poles (Fig. 2 a)) in order to prevent the above mentioned overdamping of the structure. The „distance” ε (Fig. 1 b)) was also constrained.

The optimization results show, that the proposed strategies are capable to tune above mentioned objective functions taken into account the several conditions using relatively small number of optimization parameters. The ongoing research is devoted especially to the distributed control with the nearest neighbor feedback and the combination of the simple controllers with the more complex design methods like LQG, H-infinity [2], mu-synthesis and others. Also the detailed modelling of different variants of piezoactuators and sensors is under intensive development.

Acknowledgements

This work is supported by the grant GA 16-21961S entitled „Mechatronic structures with heavily distributed actuators and sensors “ of Czech Science Foundation.

References

- [1] Gawronski, W.K., Advanced structural dynamics and active control of structures, Springer-Verlag, New York, 2004.
- [2] Gumussoy, S., Henrion, D., Millstone, M., Overton, M.L., Multiobjective robust control with HIFOO 2.0, Proceedings of the IFAC Symposium on Robust Control Design, Haifa, 2009.
- [3] Irschik, H., Nader, M., Actuator placement in static bending of smart beams utilizing Mohrs analogy, Engineering Structures 31 (8) (2009) 1698-1706.
- [4] M. Krommer, M., Irschik, H., Zellhofer, M., Design of actuator networks for dynamic displacement tracking of beams, Mechanics of Advanced Materials and Structures 15 (2008) 235-249.
- [5] Preumont, A., Vibration control of active structures an introduction, Solid Mechanics and its Application, 2nd Edition, Vol. 96, Kluwer Academic Publishers, 2002.

Numerical analysis of a pedestrian to car collision: Effect of variations in walk

J. Špička^a, J. Vychytil^a, L. Hynčík^a, J. Mañas^b

^a*New Technologies – Research Centre, University of West Bohemia, Univerzitní 8, 306 14 Plzeň, Czech Republic*

^b*MECAS ESI s.r.o., Brojova 16, 326 00 Plzeň, Czech Republic*

Purpose of this paper is an investigation of virtual performance in the modelling of the pedestrian to car crash scenario and variation of the pedestrian's initial conditions with respect to the car. This work is focused on the modelling of frontal car to pedestrian crash scenario. Fully validated virtual hybrid human body model VIRTHUMAN [5] as well as simplified model of the car chassis were modelled under Virtual Performance Solution software. The car was simplified onto a model of the car chassis only, which is based on the real geometry data [3]. Main idea of this work is investigation and sensitivity analysis of various initial conditions of the pedestrian during frontal car crash scenario, i.e. position of the extremities due to different step phases and turning angle of the pedestrian around the own axis. Real experimental data of the human gait [2] are used for the sensitivity analysis. The effect of various initial conditions of the pedestrian (positions, translational and angular velocities) on the injuries was monitored. One human step was divided into 9 phases to capture effect of the walk while pedestrian crosses the road, see Fig. 1. Consequently, the influence of different initial conditions on the kinematics and dynamics of the collision together with injury prediction of pedestrian was discussed. The probability of the pedestrian injury for the various body segments was evaluated based on the EuroNCAP injury rating [1].

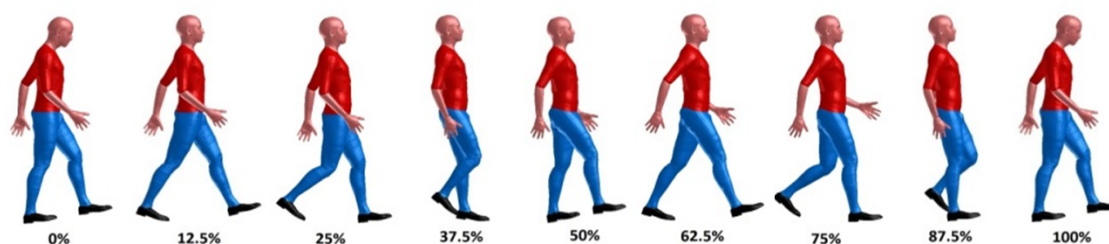


Fig. 1. Human gait phases

The effect of the walk was taken into account within translational velocities of the full human body and rotational velocities of the extremities. The aim of this paper was to assess the effect of the pedestrian motion on crash injury sustained by pedestrian. The results of the injuries for the static cases (zero initial translational velocity of the full human body) and dynamics (non-zero initial velocity) were compared together. Finally, for the considering more

realistic human locomotion, the initial angular velocities of the extremities were defined for the particular human joints.

The car of mass 1200 kg is moving forward with the initial velocity equalling to 45 km/h and impacts the pedestrian from his left side, see Fig. 2. The geometry of the front part of the car is defined based on Kerrigan [3] and modelled within the multibody principle, where 4 rigid elements representing external surface of the chassis are connected to a basic tree structure with the virtual springs and dampers. The specified pedestrian for this analysis is 18 years average (50% percentile) male with weight equalling to 72 kg and height equalling to 178 cm. This selection is based on the statistical analysis [4].

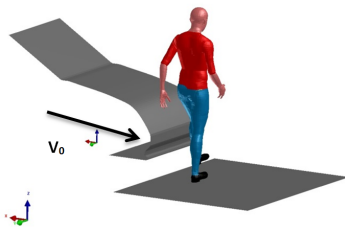


Fig. 2. Crash configuration for the reference step phase and zero turning angle

The human gait can be partitioned and modelled within two ways:

- Translational motion (velocity) of the pedestrian as a complex unit. The initial velocity of the full body equalling 0 km/h, 4 km/h and 6 km/h was applied here.
- Rotational (angular) motion of the extremities. The initial rotational velocity was set up based on experimental measurement [2].

Kinematics and dynamics of the selected car-to-pedestrian crash scenario were monitored here. The main idea of this work is to study the trend, not the absolute values, of the injury for the various body's segments, while varying the initial conditions. Based on the achieved results, the importance or redundancy of modelling locomotion and consideration of different step phases in the car-pedestrian accident can be examined.

References

- [1] EuroNCAP, Assessment protocol – Adult occupant protection, Version 6.0, July 2013.
- [2] Havelková, L., Svoboda, Z., Hynčák, L., Musculoskeletal computer model used for gait analysis of patients with total endoprosthesis, Proceedings of the conference Computational Mechanics 2014, Špičák, 2014.
- [3] Kerrigan, J. R., Murphy, D. B., Drinkwater, D. C. et al., Kinematics corridors for PMHS tested in full-scale pedestrian impact tests, Paper No. 05-0394, Centre for Applied Biomechanics, University of Virginia, United States, 2005.
- [4] Vychytil, J., Hynčák, L., Mañas, J., Pavlata, P., Striegler, R., Moser, T., Valášek, R., Prediction of injury risk in pedestrian accidents using virtual human model VIRTHUMAN: Real case and parametric study (No. 2016-01-1511), SAE Technical Paper, 2016.
- [5] Vychytil, J., Mañas, J., Čechová, H., Špirk, S., Hynčák, L., Kovář, L., Scalable multi-purpose virtual human model for future safety assessment, In: SAE Technical Papers, SAE International, 2014, doi: 10.4271/2014-01-0534.

Simulations of terminal ballistics phenomena

S. Špirk ^a

^a Faculty of Mechanical Engineering, University of West Bohemia, Univerzitní 8, 306 14 Plzeň, Czech Republic

The goal was to carry out computer simulations of ballistics impacts on steel target plates. The problem was formulated using the PAM-SHOCK software and the explicit integration scheme. The 3D geometry model was developed using the NX 9.0 program, based on a longitudinal section through the bullet. In this section, all relevant dimensions, including the jacket thickness, were measured. In contrast to the manufacturer data, the weight of the entire bullet was found to be 12.3 g. This includes the lead core and the bronze jacket. Densities of these materials were found in literature and corrected according to the real specimen.

The bullet velocity was determined from empirical relationships based on the amount of gunpowder and the distance travelled by the bullet. It was verified using a bullet velocity calculator available on the manufacturer's website [5]. The impact velocity is taken as 779 m/s. The bullet spin was derived from the parameters of the barrel. The twist rate of the 308-calibre Winchester rifle is 1:12". Hence, the bullet completes one full revolution in a path of 304.8 mm. At the above velocity, the bullet completes 2.56 revolutions in a millisecond, making a rotation speed of 16.08 rad/ms.

The pressure-volume behavior was defined by a polynomial equation of state. In the equation, the pressure p was a function of the parameter μ .

$$p = C_0 + C_1 \cdot \mu + C_2 \cdot \alpha \cdot \mu^2 + C_3 \cdot \mu^3 + (C_4 + C_5 \cdot \mu + C_6 \cdot \mu^2) \cdot E_i \quad (1)$$

Here, $\mu = \rho / (\rho_0 - 1)$, $C_0..C_6$ are material constants, E_i is internal energy and the coefficient α is equal to zero when $\mu < 0$. Some of the material constants can be derived from fundamental properties of the material, such as volume compressibility, whereas others can be modeled on equivalent terms of the relevant shock equation of state [3]. A comparison between the shock and polynomial equations of state is given in paper [4] as one of its topics.

The plastic behavior is defined by the Johnson-Cook model [2]. The stress equation is as follows.

$$\sigma_y = (C_A + C_B \cdot \varepsilon_p^{C_N}) \cdot (1 + C_C \cdot \ln \dot{\varepsilon}) \cdot (1 - T^{C_M}) \quad (2)$$

Here, $T = (T - T_{room}) / (T_{melt} - T_{room})$, T_{room} denotes ambient temperature, T_{melt} is the melting temperature, ε_p is the equivalent plastic strain, $\dot{\varepsilon}$ denotes dimensionless plastic strain, and C_A , C_B , C_N , C_C and C_M are the Johnson-Cook model coefficients for the particular material, which are available in literature [1].

The first failure criterion used was the maximum plastic strain criterion for element elimination. When the limit value is exceeded, the particular element is practically eliminated by reducing its modulus of elasticity to a negligible value. The limit value is determined by the properties of the material. The second failure criterion involved the deviatoric stress

tensor. This criterion does not affect the volumetric dependence of stress on strain. The total stress is found from the following equation.

$$\sigma = (1 - d(\varepsilon_p))\sigma_o. \quad (3)$$

Here, σ is the damage full stress tensor, $d(\varepsilon_p)$ denotes the isotropic scalar damage function, and ε_p represents plastic strain.

The results of simulations was compared with experiments. The plates made of steel S355 and Hardox 500 with different thickness (8, 10 and 12 mm) was used. The bullet penetration through the plate made of steel S355 with thickness 10 mm is shown (see Fig. 1). One of the advantage of simulations is the possibility to get results, which are difficult to measure (see Fig. 2). The significant advantage of simulations is the repeatability. The experiments are expensive and it is complicated to finding optimal plate thickness or slope.

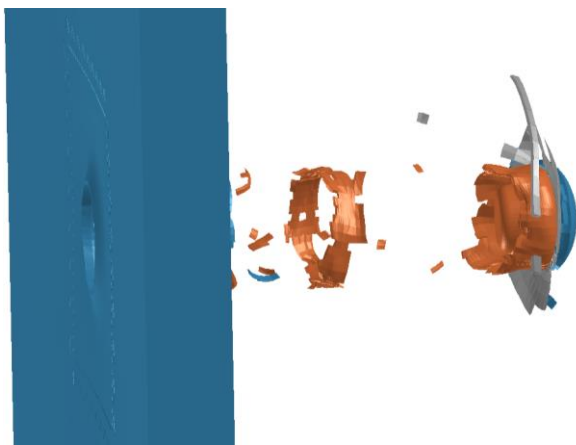


Fig. 1. The bullet penetrating the plate made of steel S355 (thickness 10 mm) in time 0.11 ms

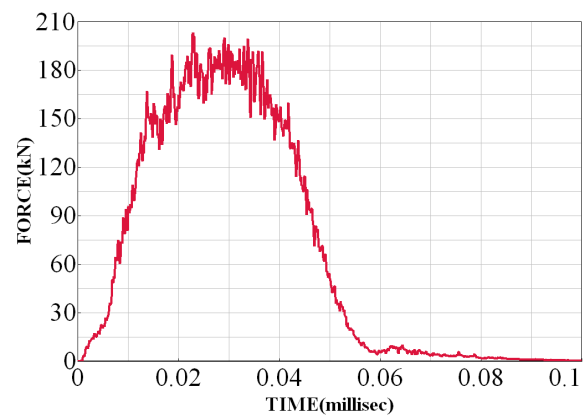


Fig. 2. The contact force magnitude for the plate made of steel Hardox 500 (plate at an angle of 45°)

Acknowledgements

The present contribution was prepared under project POSTDOC supported by University of West Bohemia in Pilsen (Czech Republic) and also by financial support of the institutional funding for long-term strategic development of the University of West Bohemia provided by the Ministry of Education of the Czech Republic.

References

- [1] Borvik, T., Deya, S., Clausen, A.H., Perforation resistance of five different high-strength steel plates subjected to small-arms projectiles, *International Journal of Impact Engineering* 36 (7) (2009) 948–964.
- [2] Johnson, G.R., Cook, W.H., A constitutive model and data for metals subjected to large strains high strain rates and high temperatures, *Proceedings of the 7th International Symposium on Ballistics*, 54 (1983), p. 1.
- [3] Steinberg, D.J., *Equation of state and strength properties of selected materials*, Lawrence Livermore National Laboratory, 1991.
- [4] Churilova, M., Technology of EHIS (stamping) applied to production of automotive parts [WWW] <https://billionbooksbaby.org/pdf-stamping-through-mathematics.html> (13. 06. 2016).
- [5] Sako Ballistics [WWW] <http://luoti.sako.fi/Ballistics/index.jsp> (29. 04. 2015).

Influence of geometric configuration of the acoustic-structural system on deformation characteristics

J. Štorkán^a, T. Vampola^a

^a Department of Mechanics, Biomechanics and Mechatronics, Faculty of Mechanical Engineering, Czech Technical University in Prague, Technická 4, Praha 6, Czech Republic

One of the sources excite of mechanical vibrations can be the acoustic pressure fields. Mechanical vibrations are typically unwanted and it need to minimalize their size. One of possible solution is to use active mechatronics method. Passive solutions of this problem usually do not give as good results, but they are simple, reliable and inexpensive.

In the paper is analyzed the influence of the geometrical configuration to the size of vibration of undamped system exited by acoustic pressure. Examinee system consists of 2D solid continuum, which interact with the acoustic continuum. This system is a model of the cover of oscillating device. The model is solved by finite element method and has been compiled in program Abaqus CAE.

The structural part of the model is a steel plate with a length of 1 [m], a width of 0.75 [m] and a thickness of 0.001 [m]. It was modelled as a shell structure and discretized by four-nodal S4R shell-elements with six degrees of freedom in each node. For calculation was used isotropic material model with a Young Modulus $E=2.1E+11$ [Pa] and Poisson's ratio $\nu=0.3$. Acoustic medium was air defined by density $\rho=1.2$ [kgm^{-3}] and bulk modulus $K=1.4E+5$ [Pa]. Column of air under the structural part of the model was 1 [m] and was discretized by eight-nodal acoustic hexahedrons AC3D8. The structural part is restricted around the circuit on the joints and torsion spring to the frame. Rigidly of the torsion springs was chosen $k_t=1E+8$ [Nm] [1]. The model was excited by pressure boundary condition. Excitation was located in the middle opposite sides of the structural part of the model.

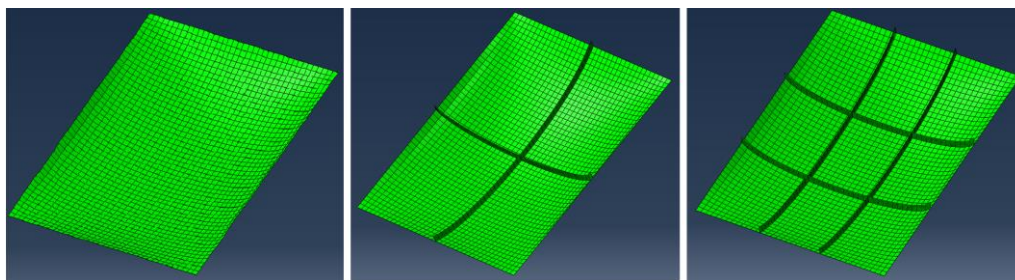


Fig. 1. Structural part of the model is curved in both axes by 0.1 [m] in the variant without and with 2 and 4 ribs

First was performed modal analysis of the structural part of model. It watched the dependence of the first eigenfrequency on the geometric configuration of the system. First it was analysed planar geometry of the structure. Further the structure was with defined curvature. All variations of curvature were created in variants without and with ribs as shown in Fig 1. Fig. 2 shows the dependence of the first eigenfrequency on the deflection for all variants. Furthermore, the figure shows the dependence of the first eigenfrequency based on 1 [kg] weight of model. The fastest growing eigenfrequency with the deflection in both axes.

Ribs increase eigenfrequency by only 30-100 [Hz], deflection increase by hundreds of Hz, while less increases the weight of the system.

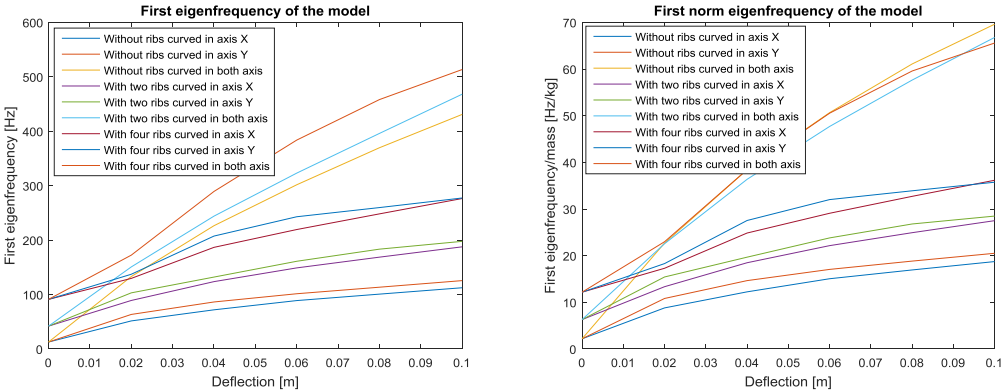


Fig. 2. Dependence of the first eigenfrequency and norm first eigenfrequency on the deflection

With regard to the results of the modal analysis was performed numerical simulation in the time domain for the curvature variant in both axes with deflection 0 [m] and 0.05 [m] without ribs. The simulation was performed for the time interval $\langle 0,1 \rangle$ [s]. The model was excited by harmonic acoustic pressure with frequency equal the first eigenfrequency of planar structure and 100 [Pa] amplitude. Fig. 3 shows the displacement of centre of the structural part. It is seen that displacement for the curved structure is almost $5E+3$ times smaller.

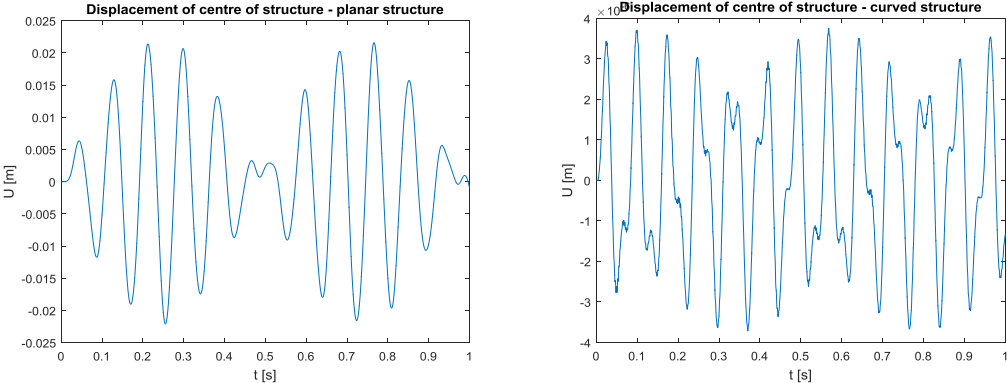


Fig. 3 Course displacement of centre of the structure for the planar and curved structure

FE model interaction of acoustic medium with 2D structure representing the cover of engine of vehicle was created. First was observed influence of changes the geometry of a 2D structure on the first eigenfrequency. The structure was curving independently in different directions and it was completed with a two and four ribs. The value of first eigenfrequency is most influenced by the curvature. Model with a planar structure and a curved structure without ribs was simulated in the time domain. Model was excited by acoustic pressure. Curving reduce the size of the excited displacement of about $5E+3$ times. It was shown that the influence of geometry structure on excited vibrations is significant and only minimally increases the weight of the structure and is very easy to design and manufacturing.

Acknowledgements

The research is supported by the project Josef Bozek Competence Centre for Automotive, TE01020020.

References

[1] Brepta, R., Půst, L., Turek, F., Mechanical vibrations, Sobotáles, Praha, 1994. (in Czech)

Microscopic structural analysis of biological tissues and biomaterials

Z. Tonar^a, T. Kubíková^a, P. Kochová^a, K. Witter^b

^aNTIS, Faculty of Applied Sciences, University of West Bohemia, Univerzitní 8, 306 14 Pilsen, Czech Republic

^bInstitute of Anatomy, Histology and Embryology, Department of Pathobiology, University of Veterinary Medicine Vienna, Veterinärplatz 1, A-1210 Vienna, Austria

The aim of this contribution is to provide practical examples on quantification of inner structures of biological tissue samples and biomaterials. Biological tissues are three-dimensional composite materials produced by biological organisms. The tissues are made of cells and extracellular matrix. The matrix is composed of fibrillar proteins, such as elastin and various types of collagen, and ground substance, which contains mostly highly hydrophilic glycosaminoglycans. Moreover, most of the tissues contain blood microvessels, namely arterioles, metarterioles, precapillaries, capillaries, and postcapillary venules. Although the theoretical resolution of optical microscopy is approx. 200 nm, routine examination of biological tissues can provide morphometric data on structures ranging typically between 1-10,000 μm .

Biomaterials are engineered substances manufactured to interact with biological cells, tissues and organs to provide mechanical support, to accelerate healing, to release drugs or to serve a diagnostic purpose [10]. Both structural and mechanical properties of biological tissues and supporting biomaterials are often evaluated together.

A number of stereological methods [1,2,11,12] are available for statistical determination of the geometric properties of the evaluated structures and objects, using various test probes applied to tissue sections. Using stereology, structural parameters may be quantified as shown in Table 1.

Table 1. Geometric probes used for quantitative estimates of structural features; the sum of the probe dimensions and the structural features is always equal to three

Dimensions of the geometric probe (-)	Dimensions of the structural feature (-)	Example of morphometric parameter estimated
Point (0)	Volume (3)	Volume fraction of collagen, elastin and smooth muscle within arterial wall [7, 13,14]
Line (1)	Surface (2)	Surface density of the trabecular myocardium during systolic and diastolic phase of cardiac cycle [6]
Plane (2)	Length (1)	Length density of the laminal junction of the equine hoof [3,9]
Volume (3)	Number (0)	Numerical density of cells within tissue reference volume [8]

Apart from these first-order stereological characteristics, fibrillar components of biological tissues require assessment of isotropy. Spatial orientation and preferential directions of connective tissue fibres and blood microvessels can be assessed in series of sections [5].

The inner structure of biological tissues and biomaterials can be also quantified using high resolution X-ray microtomography (micro-CT). Whereas the resolution of micro-CT is nowadays comparable with light microscopy, noninvasive scanning provides three-dimensional data that can be evaluated using the same stereological methods as in histological studies. Should a sufficient contrast be provided, a semiautomated and high-throughput evaluation can be performed [4].

Acknowledgements

The work has been supported by the National Sustainability Program I, Project Nr. LO1506 provided by the Ministry of Education, Youth and Sports of the Czech Republic.

References

- [1] Gundersen, H.J., Bagger, P., Bendtsen, T.F., Evans, S.M., Korbo, L., Marcussen, N., Moller, A., Nielsen, K., Nyengaard, J.R., Pakkenberg, B., The new stereological tools: disector, fractionator, nucleator and point sampled intercepts and their use in pathological research and diagnosis, *APMIS* 96 (1988) 857-881.
- [2] Howard, C.V., Reed, M.G., *Unbiased stereology. Three-dimensional measurement in microscopy*, Springer, New York, 1998.
- [3] Jansová, M., Ondoková, L., Vychytil, J., Kochová, P., Witter, K., Tonar, Z., A finite element model of an equine hoof, *Journal of Equine Veterinary Science* 35 (2015) 60-69.
- [4] Jiřík, M., Tonar, Z., Králíčková, A., Eberlová, L., Mírka, H., Kochová, P., Gregor, T., Hošek, P., Svobodová, M., Rohan, E., Králíčková, M., Liška, V., Stereological quantification of microvessels using semiautomated evaluation of X-ray microtomography of hepatic vascular corrosion casts, *International journal of CARS* 11 (2016) 1803-1819.
- [5] Kochová, P., Cimrman, R., Janáček, J., Witter, K., Tonar, Z., How to assess, visualize and compare the anisotropy of linear structures reconstructed from optical sections - a study based on histopathological quantification of human brain microvessels, *Journal of Theoretical Biology* 286 (2011) 67-78.
- [6] Kochová, P., Cimrman, R., Štengl, M., Ošťádal, B., Tonar, Z., A mathematical model of the carp heart ventricle during the cardiac cycle, *Journal of Theoretical Biology* 373 (2015) 12-25.
- [7] Kochová, P., Kuncová, J., Švíglerová, J., Cimrman, R., Miklíková, M., Liška, V., Tonar, Z., The contribution of vascular smooth muscle, elastin and collagen on the passive mechanics of porcine carotid arteries, *Physiological Measurement* 33 (2012) 1335-1351.
- [8] Kochová, P., Tonar, Z., Structural and mechanical properties of gastropod connective and smooth muscle tissue, *Experimental Mechanics* 54 (2014) 791-803.
- [9] Kochová, P., Witter, K., Cimrman, R., Mezerová, J., Tonar, Z., A preliminary study into the correlation of stiffness of the laminar junction of the equine hoof with the length density of its secondary lamellae, *Equine Veterinary Journal* 45 (2013) 170-175.
- [10] Kubíková, T., Kochová, P., Holeček, M., Plencner, M., Prosecká, E., Filová, E., Rampichová, M., Tonar, Z., In vivo microscopic and mechanical characteristics of bioengineered and biodegradable tissue scaffolds and nanomaterials, *Nanobiomaterials in Soft Tissue Engineering - Applications of Nanobiomaterials*, Volume 5, Amsterdam, Elsevier, 2016, pp. 457-490.
- [11] Kubínová, L., Janáček, J., Estimating surface area by the isotropic fakir method from thick slices cut in an arbitrary direction, *Journal of Microscopy* 191 (1998) 201-211.
- [12] Mouton, P.R., *Principles and Practices of Unbiased Stereology. An Introduction for Bioscientists*, The Johns Hopkins University Press, Baltimore, 2002.
- [13] Tonar, Z., Kochová, P., Cimrman, R., Perktold, J., Witter, K., Segmental differences in the orientation of smooth muscle cells in the tunica media of porcine aortae, *Biomechanics and Modeling in Mechanobiology* 14 (2015) 315-332.
- [14] Tonar, Z., Kubíková, T., Prior, C., Demjén, C., Liška, V., Králíčková, M., Witter, K., Segmental and age differences in the elastin network, collagen and smooth muscle phenotype in the tunica media of the porcine aorta, *Annals of Anatomy* 201 (2015) 79-90.

Simulation model of seat with implemented pneumatic spring with consideration of variable pressure in air reservoir

T. Tran Xuan^a, D. Cirkl^a

^aDepartment of Applied Mechanics, Faculty of Mechanical Engineering, Technical University of Liberec, Liberec, Czech Republic

The passenger in moving car is exposed to a certain level of vibrational load what may decrease his comfort. This article deals with description of simulation model of electro-pneumatic mechanical system intended for enhancing vibration isolation capability of car seat. Mechanical part of the system comprises pneumatic spring inserted into seat cushioning what allows to change its hardness in accordance with patented solution [1]. Electro-pneumatic part consists of compressor, reservoir of compressed air, controlled analog and digital pneumatic valves and PID controller. Presented simulation model is based on work done in [2] and describes dynamic behaviour of the system and calculates the displacement and acceleration of mass, pressure inside pneumatic spring, flow rate in controlled solenoid pneumatic valves and needed coil current in case of kinematic excitation of the seat. Consideration of variable pressure of compressed air in reservoir supplied by compressor in this refined version of model allows to perform simulations under conditions which are closer to reality.

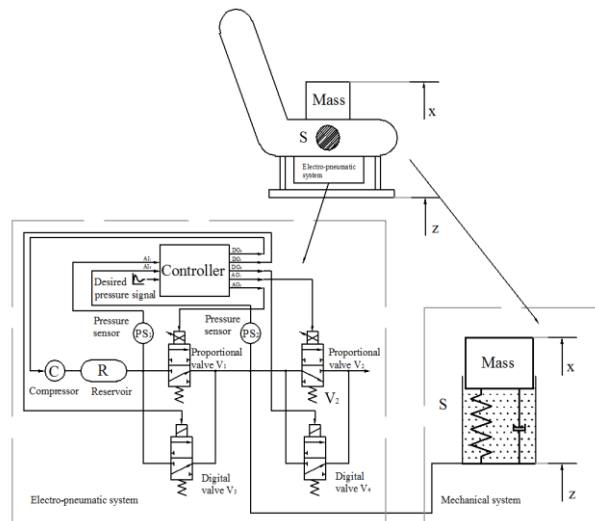


Fig. 1. The scheme of seat with implemented pneumatic spring

Pneumatic circuit comprises two kinds of pneumatic valves. The proportional valves denoted V_1 and V_2 are characterized by dependence of flow rate on pressure difference Δp between input and output pressure, p_1 and p_2 , respectively, and by input coil current i .

$$q_{sj} = k_{00} + k_{10} \cdot i \cdot \Delta p + k_{01} \cdot \Delta p + k_{20} \cdot i^2 + k_{11} \cdot i \cdot \Delta p + k_{02} \Delta p^2 + k_{30} \cdot i^3 + k_{21} \cdot i^2 \cdot \Delta p + k_{12} \cdot i \cdot \Delta p^2 + k_{03} \cdot \Delta p^3 \quad (1)$$

In the pneumatic circuit there are also implemented two digital valves V_3 and V_4 . According with [3], the formulas for the calculation of their flow rate q_{sj} are:

Choked flow

$$\frac{p_2}{p_1} \leq b \rightarrow q_{sj} = 600 \cdot C \cdot p_1 \cdot \sqrt{\frac{293}{273+T}} \quad \text{l/min} \quad (2)$$

Subsonic flow:

$$\frac{p_2}{p_1} \geq b \rightarrow q_{sj} = 600 \cdot C \cdot p_1 \cdot \sqrt{1 - \left(\frac{p_2 - b}{p_1 - b} \right)^2} \cdot \sqrt{\frac{293}{273+T}} \quad \text{l/min} \quad (3)$$

The total air flow q_s is then given by addition of flow rates of all individual valves q_{sj} as it is expressed by equation:

$$q_s = q_{s1} - q_{s2} + q_{s3} - q_{s4} \quad (4)$$

For the control of coil current of proportional valves the PID algorithm is used in form:

$$i(t) = K_p \cdot e(t) + K_I \cdot \int_0^t e(\tau) d\tau + K_D \cdot \frac{de(t)}{dt} \quad (5), \quad \text{where} \quad e(t) = p_s(t) - p_d(t). \quad (6)$$

Model of mechanical part of the system is a simplified representation of seat cushioning with implemented pneumatic spring loaded by mass m . It is possible to set up the equation of motion of mass m in form (7). Pneumatic spring is in a simplified way represented by closed air cylinder with internal pressure p_s . Value of pressure inside the cylinder is given by differential equations (8-9). Mechanical properties of material of flexible cushioning are described by restoring force given by nonlinear progressive function (10) and linear damping force (11). The force in closed air cylinder is given by equation (12).

$$F_k + F_b + F_p - m \cdot g = m \cdot \ddot{x} \quad (7)$$

$$V = S \cdot (h + z - x) \rightarrow \dot{V} = S \cdot (\dot{z} - \dot{x}) \quad (8)$$

$$\dot{p}_s = \frac{\kappa \cdot q_s \cdot R \cdot T}{V} - \kappa \cdot p_s \cdot \frac{\dot{V}}{V} \quad (9)$$

$$F_k = k_1(z-x) + k_2(z-x)^2 + k_3(z-x)^3 \quad (10)$$

$$F_b = b_1(\dot{z} - \dot{x}) \quad (11)$$

$$F_p = S(p_s - p_{out}) \quad (12)$$

Pressure inside the reservoir p_{in} is a parameter which changes in time and influences the system dynamics. According with [2], p_{in} is limited by range $[p_{min}, p_{max}]$ what makes the compressor work just in case of $p_{in} < p_{min}$ and stop in case of $p_{in} > p_{max}$.

The system of equations derived above make up the mathematical model of combined electro-pneumatic mechanical system of the seat. The simulations are performed in Matlab software for two modes of seat operation, the first in the mode of constant stiffness and the second in the mode of constant pressure. The transmission of acceleration is calculated under consideration of harmonic excitation for different setup of desired pressure inside pneumatic spring.

This model allows to investigate the response of the system to kinematic excitation or the change of the desired pressure inside pneumatic spring which is able to set to constant value or defined by deterministic course. Pressure in reservoir is calculated on the basis of real compressor characteristics so it allows to calculate needed compressor capacity to keep desired dynamic behaviour of the system. The analysis of the response helps to find suitable model parameters which represent properties of real parts used for seat construction. Furthermore, the model will be used for evaluation of vibration isolation effect of the system which is possible to represent e.g. in form of curves of transmission of acceleration.

Acknowledgement

This article was written at the Technical University of Liberec, Faculty of Mechanical Engineering with the support of the Institutional Endowment for the Long Term Conceptual Development of Research Institutes, as provided by the Ministry of Education, Youth and Sports of the Czech Republic in the year 2016.

References

- [1] Cirkl, D., Seat, patent no. 303163, 2012.
- [2] Cirkl, D., Tran Xuan, T., Simulation model of seat with implemented pneumatic spring, Proceedings of the 21st International conference on Vibroengineering, Brno, JVE International Ltd., 2016, pp. 154-159.
- [3] 3 Port Solenoid Valve, Series S070, SMC catalog.

Multiscale modeling of ionic transport in deformable porous media

J. Turjanicová^{a,b}, E. Rohan^{a,b}, V. Lukeš^{a,b}

^aFaculty of Applied Sciences, University of West Bohemia, Univerzitní 8, 306 14 Plzeň, Czech Republic

^bNTIS – New Technologies for the Information Society, University of West Bohemia, Univerzitní 8, 306 14 Plzeň, Czech Republic

Modeling of ionic transport is an issue which often arises in building various models in biomechanics, such as modeling cortical bone tissue, or in geoscience. In this paper we focus on simulating the electrokinetics and hydrodynamics in bone tissue, more specifically, its porous structure on the microscopic scale.

On a smaller scale, the cortical bone consists of a tissue carrying surface charges and a system of pores saturated by the bone fluid and interconnected on multiple scale levels. The major focus of this study is devoted to description of the ion transport on the scale of pores with characteristic size of a few hundred nanometers, where the porosity is caused by canalicular-lacunar network. This means that the bone fluid flow takes place in the electric double layer which is formed by an interaction between charged solid-fluid interface and an ionized solution. Our aim is to model the flow of an electrolyte in the presence of an electric field through small pores in the deformable solid matrix.

The porous medium occupies domain Ω and is composed of a fluid filled pore space Ω_f and a solid matrix $\Omega_s = \Omega \setminus \bar{\Omega}_f$ with a solid-fluid interface $\Gamma = \partial\Omega_f \cap \partial\Omega_s$. The system of equations describing deformable porous medium saturated by the incompressible symmetric electrolyte with uniform charge on the solid-fluid interface was introduced in [4] and later also used in [1]. It reads as follows:

Elasticity equation for the elastic displacement \mathbf{u}^s :

$$-\operatorname{div}(Ae(\mathbf{u}^s)) = \rho_s \mathbf{f} \quad \text{in } \Omega_s, \quad (1)$$

where $e(\mathbf{u}^s) = 1/2(\nabla \mathbf{u}^s + (\nabla \mathbf{u}^s)^*)$ is the strain tensor, \mathbf{f} is the external body force and $A_{ijkl} = 2\mu\delta_{ik}\delta_{jl} + \lambda\delta_{kl}\delta_{ij}$ is the elasticity coefficient with Lamé moduli μ and λ . Density of solid matrix is denoted by ρ_s .

Poisson equation for the electrostatic potential Ψ :

$$\mathcal{E}\Delta\Psi = -e \sum_{j=1}^N z_j n_j \quad \text{in } \Omega_f, \quad \mathcal{E}\nabla\Psi \cdot \nu = -\Sigma \quad \text{on } \Gamma, \quad (2)$$

where \mathcal{E} is the dielectric constant of the solvent, e is the elementary charge and Σ is assumed to be the surface charge given at the boundary Γ . The valency and the concentration of i -th ionic species is denoted by z_i and n_i .

Stokes equation for the fluid velocity \mathbf{v} and the pressure p :

$$\nabla p - \eta\Delta\mathbf{v} = \rho_f \mathbf{f} - e \sum_{j=1}^N z_j n_j \nabla\Psi \quad \text{in } \Omega_f, \quad \operatorname{div} \mathbf{v} = 0 \quad \text{in } \Omega_f, \quad (3)$$

where $\rho_f > 0$ is the fluid density and η is the fluid viscosity.

Convection-diffusion equation for the i -th ionic species:

$$\begin{aligned} \frac{\partial n_i}{\partial t} + \operatorname{div}(\mathbf{w}n_i) - \operatorname{div}\left(\frac{n_i D_i^0}{k_B T} (\nabla \mu_i + z_i e \nabla \Psi)\right) &= 0 \quad \text{in } \Omega_f, \\ \frac{n_i D_i^0}{k_B T} (\nabla \mu_i + z_i e \nabla \Psi) \cdot \nu &= 0 \quad \text{on } \Gamma, \end{aligned} \quad (4)$$

where μ_i is the chemical potential, D_i^0 is the diffusion coefficient, k_B is the Boltzmann constant and T is the absolute temperature. The convective velocity \mathbf{w} is defined by the fluid velocity \mathbf{v} and by an extension of solid velocity to the fluid part, so that $\mathbf{w} = \mathbf{v} - \frac{\partial \mathbf{u}^s}{\partial t}$.

We followed the upscaling method proposed by [1]. Firstly, we wrote a system of equations in dimensionless form and we performed linearization. Secondly, the homogenization of electrokinetic system is treated separately, yielding the same results as in the case of the rigid porous medium, studied in [2]. Deformation of the porous medium is considered to be weakly coupled to the electrokinetic flow, thus the homogenization is split in three separate steps: the homogenization of decoupled electrokinetic system, the homogenization of perturbation of potential $\delta\psi^\varepsilon$ and the homogenization of perturbation of displacement $\delta\mathbf{u}^\varepsilon$. Each step of the homogenization introduces its own set of local problems which can be solved on the local periodic cell Y composed of the solid part Y_s and the fluid part Y_f . These local cell problems yield the so-called corrector functions which are necessary for the evaluation of the effective coefficients. The macroscopic homogenized problem is then assembled from the previously obtained decoupled limit equations.

The homogenized model is implemented in the FEM based software *SfePy* [3]. We study the influence of microstructure geometry on both the effective coefficients and the macroscopic solution. In order to observe the behavior on the lower scale, we reconstruct the microscopic variables from the macroscopic solutions.

This approach can be used not only for modeling of the electro-chemo-mechanical coupling in the cortical bone tissue, but also for the modelig of the swelling clays and other tissues.

Acknowledgements

This paper was supported in part by project LO1506 of the Czech Ministry of Education, Youth and Sports and by the Czech Science Foundation through project GA16-03823S. Jana Turjanicová is also grateful for the support of her work by project SGS-2016-059.

References

- [1] Allaire, G., Bernard, O., Dufrêche, J. F., Mikelić, A., Ion transport through deformable porous media: Derivation of the macroscopic equations using upscaling, *Computational and Applied Mathematics*, 2016, pp. 1-32, doi: 10.1007/s40314-016-0321-0.
- [2] Allaire, G., Brizzi, R., Dufrêche, J. F., Mikelić, A., Piatnitski, A., Ion transport in porous media: Derivation of the macroscopic equations using upscaling and properties of effective coefficients, *Computational Geosciences* 17 (3) (2013) 479-495.
- [3] Cimrman, R., *SfePy – write your own FE application*. In: Pierre de Buyl and Nelle Varoquaux, editors, *Proceedings of the 6th European Conference on Python in Science (EuroSciPy 2013)*, Brussels, 2014, pp. 65-70.
- [4] Moyne, C., Murad, M. A., Electro-chemo-mechanical couplings in swelling clays derived from a micro/macro-homogenization procedure, *International Journal of Solids and Structures* 39 (25) (2002) 6159-6190.

On stability of 2D flow-field

V. Uruba ^{a,b}

^a *Institute of Thermomechanics, Czech Academy of Sciences, Dolejškova 5, 182 00 Praha, Czech Republic*

^b *Faculty of Mechanical Engineering, University of West Bohemia, Univerzitní 8, 306 14 Plzeň, Czech Republic*

Stability of a 2D flow-field generated under 2D boundary conditions will be analyzed using various methods. The most practical cases of such flows are found to be highly instable and thus unphysical. The presented paper analyses the situation with help of experiments and mathematical modelling from literature defining an interesting areas for future experimental research, which could extend the published experimental studies and/or verify some recent results of mathematical modelling.

In both external and internal fluid dynamics the flow conditions of practical cases are characterized by 2D boundary conditions very often. Typical examples could be the cross-flow around a prismatic body or flow in channel of circular cross section. The first case could be considered as a plane flow, invariant along the body span (excluding the ends), the second case is rotary symmetrical, invariant variable is the angle.

Such cases are also mathematically modelled as 2D flows, taking into account only a single section, supposing the same flow picture for any value of the invariant parameter (i.e. span position or rotation angle). This approach could provide relevant results only for perfectly stable flows, when no destabilizing factor is present.

Destabilizing factors are namely presence of shear region within viscous fluid and adverse pressure gradient (i.e. positive derivative in flow direction). In flow of real, viscose fluids, the first destabilizing factor is always present. So all real cases of flow-fields have tendency to instability, at least in some extend.

Elementary stability theory relies on harmonic disturbances in the form of waves, which are 2D from definition. As a result this theory gives unrealistic high critical Reynolds numbers, in some cases indicate even always stable flow. The advanced stability theory relies on so-called “optimal perturbation”, which is defined as an initial conditions which yield greatest growth of the total disturbance energy. Such structure is always 3D, well located in space and it is in the form of specific vortices or bundles of vortices very often. To predict such structures the complicated and time exhausting numerical simulation procedure should be applied. However, there are numerous experimental verifications of existence of such structures, see, e.g. [3].

An argument that the 2D approach is sufficient to capture the time-mean flow structure is not relevant. It is known, that the flow structure, which is developed under the instability process, plays fundamental role in the force interaction with submerged bodies and surfaces. Classical example could be cross-flow around prismatic circular cylinder. The classical theory of inviscid, rotation-free flow (so called potential flow) relies on 2D flow-field structure. Those non-physical conditions result in non-physical effect – zero force interaction, known as d’Alembert paradox. The reason of this non-physical behavior is considered vanishing viscosity, which does not allow development of boundary layers on the surfaces. Hoffman and Johnson have demonstrated, that the true reason of the potential theory failure is implicit two-dimensionality of the potential flow-field due to ignoring stability properties of such flow in

reality. In [1, 2] they present the mathematical simulation of the inviscid case of flow around the circular cylinder characterized by 2D boundary conditions, but resolved in 3D space. Distinct streamwise structures, particularly streamwise vortices arise in the body wake, which are of 3D nature and could be by no way captured in any 2D model. The surface pressure distribution gives realistic values of integral forces. The 3D nature of wake behind a circular cylinder is studied in detail in [8], the 2D structure of the wake is shown to be a very special case. Typically, the wake structure is highly 3D, at least on instantaneous basis.

The generation of streamwise vortices and low- and high- velocity streaky structures is studied in [4, 5, 6, 7] in the case of both bluff and streamlined bodies. The preliminary experiments suggest existence of dynamical structures of 3D topology, which are changing considerably both in space and time. The methods based on time-mean flow structure (typically RANS in mathematical modelling or point experimental methods) could not reveal such structures, however their existence play fundamental role in the structure-flow interaction, wake structure and generation of forces exerted on the body.

Acknowledgements

The work has been supported by the grant projects TA04020129 and TA04011437, Technology Agency of the CR.

References

- [1] Hoffman, J., Johnson, C., The mathematical secret of flight, *Normat* 57 (4) (2009) 1–25.
- [2] Hoffman, J., Johnson, C., Resolution of d'Alembert's paradox, *Journal of Mathematical Fluid Mechanics* 12 (3) (2010) 321-334.
- [3] Manneville, P., *Instabilities, chaos and turbulence. An introduction to nonlinear dynamics and complex systems*, Imperial College Press, London, 2004.
- [4] Uruba, V., Force interaction of an airfoil in fluid-flow, 15th conference on Power System Engineering, Thermodynamics & Fluid Flow - ES 2016, Pilsen, Czech Republic, 2016.
- [5] Uruba, V., On aerodynamic forces physical mechanism, SKMTaT 2016, Slovak University of Technology in Bratislava, 2016, pp. 258-262.
- [6] Uruba, V., On 3D instability of wake behind a cylinder, AEaNMiFMaE 2016, University of Žilina, 2016, pp. 253-256.
- [7] Uruba, V., Near wake dynamics around a vibrating airfoil by means of PIV and oscillation pattern decomposition at Reynolds number of 65 000, *Journal of Fluids and Structures* 55 (2015) 372-383.
- [8] Williamson, C.H.K., Vortex dynamics in the cylinder wake, *Annual Review of Fluid Mechanics* 28 (1996) 477-539.

Influence of random factors on pipeline systems

V. Valklovič^a, R. Jančo^a, K. Frydrýšek^b

^a Institute of Applied Mechanics and Mechatronics, Faculty of Mechanical Engineering, Slovak University of Technology in Bratislava, Námestie Slobody 17, 812 31 Bratislava, Slovak Republic

^b Department of Applied Mechanics, Faculty of Mechanical Engineering, VŠB-Technical University of Ostrava, 17. listopadu 15/2172, Ostrava 8, Czech Republic.

Generally, the analysis of bending of beams on an elastic foundation is developed on the assumption that the reaction forces of the foundation are proportional at every point to the deflection of the beam at that point. The vertical deformation characteristics of the foundation are defined by means of identical, independent, closely spaced, discrete and linearly elastic springs. The constant of proportionality of these springs is known as the modulus of subgrade reaction, k_s . This simple and relatively crude mechanical representation of soil foundation was firstly introduced by Winkler, in 1867. The Winkler model, which has been originally developed for the analysis of railroad tracks, is very simple but does not accurately represent the characteristics of many practical foundations. One of the most important deficiencies of the Winkler model is that a displacement discontinuity appears between the loaded and the unloaded part of the foundation surface. In reality, the soil surface does not show any discontinuity (Fig. 1).

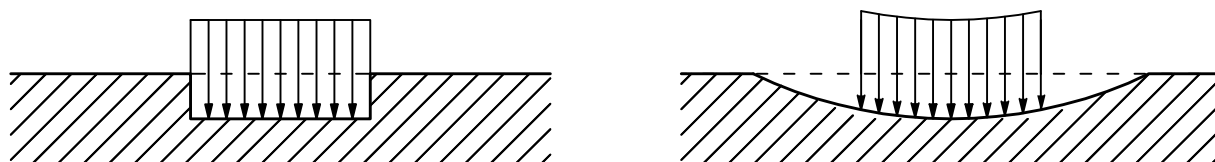


Fig. 1. Deflections of elastic foundations under uniform pressure p ; (a) Winkler Foundation; (b) Elastic solid

This work takes into account the impact of random effects on gas pipelines. All effects such as pipe thickness, Young modulus, Poisson ratio, Yield point, gas pressure, density, foundation, temperature, and many other factors have an impact on the safety factor. Randomly increased value of any of these effects should not normally result in an accident.

The present paper deals with the calculation of stresses and critical points for the pipe system embedded on a flexible substrate using ANSYS program and subsequent statistical evaluation using method SBRA. The work focuses mainly on the parts of the pipeline, which have to be excavated and then backfilled thereby changing the underlying properties.

This work deals with the repairs of the piping system, in which the piping should be excavated. In the subsequent execution of the repair and re-burying the pipeline, there is a change in the deposit, because the background material under the pipeline cannot sufficiently compact to the state before the repair.

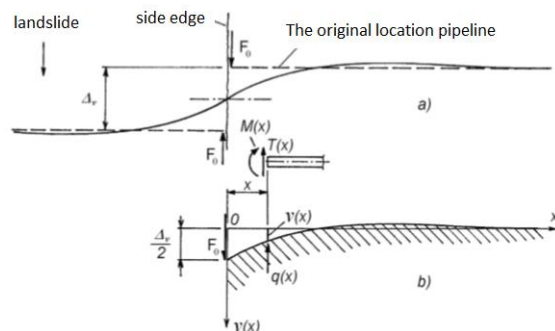


Fig. 2. Schematic pipes with landslides

In resolving the pipeline (beam) on flexible foundation, the change in the properties of the background materials should be also considered. These changes may have the adverse effect on its voltage state. Under these changes we can consider the size of the excavated pipes, air bubbles in the background materials, insufficient reinforcement etc.

Using the Simulation-Based Reliability Assessment (SBRA) Method (i.e. an application of the Monte Carlo probabilistic approach), the probability of failure is obtained mainly by analyzing the reliability function $RF=RV-S$, where RV is the reference value and S is a variable representing the load effect combination. The probability of failure is the probability that S exceeds RV : $p(RV-S \leq 0)$. All inputs and outputs are given by bounded histograms, which include the real (natural) variability of the variables. Application of the SBRA method is a modern and innovative trend in mechanics.

Acknowledgements

The article was supported by the STU Grant scheme for Support of Young Researchers and VŠB in Ostrava.

References

- [1] Frydrýšek, K., Beams and frames on elastic foundation 1, VŠB – Technická univerzita Ostrava, Ostrava, 2006. (in Czech)
- [2] Frydrýšek, K., Jančo, R., Beams and frames on elastic foundation 2, Technická univerzita Ostrava, Ostrava, 2008. (in Czech)
- [3] Frydrýšek, K., Probabilistic calculations in mechanics 1, Technická univerzita Ostrava, Ostrava, 2010, pp. 149. (in Czech)
- [4] Musil, M., Passive and active vibroizolation of machines, Nakladateľstvo STU, Bratislava, 2012. (in Slovak)
- [5] Peciar, P., Eckert, M., Fekete, R., Hrnčiar, V., Analysis of pharmaceutical excipient MCC Avicel PH102 using compaction equations, Journal of Mechanical Engineering – Strojnícky časopis 66 (1) (2016) 65-82.

Influence of the velopharyngeal opening on human voice quality

T. Vampola^a, J. Horáček^b

^a Faculty of Mechanical Engineering, CTU in Prague, Technická 4, 166 00 Prague, Czech Republic

^b Institute of Thermomechanics, Czech Academy of Sciences, Dolejškova 1401/5, 182 00 Praha 8, Czech Republic

Velopharyngeal insufficiency (VPI) is an insufficient closing of nasal cavity (nasopharynx) and its airproof separation from the oral cavity (oropharynx). VPI leads to open nasality (rhinolalia aperta) affecting all oral speech sounds that should not be nasal. Small defects of the velopharyngeal closure become evident first by a different timber of the voice, bigger defects influence formant structure of vowels. According to the literature [1], [3], the VPI influence in particular the production of vowels /i:/ and on the other hand its influence on the production of vowel /a:/ is smaller. Several types of nasal speech are not easily diagnosed even specialized physicians are often not fully aware of the differences. Acoustic analysis of VPI are oriented mainly on differences in voice timbre because the resonant changes are the most essential.

The more precise 3D FE models of adult female vocal tract developed from computer tomography (CT) images for vowels /a:/ and /i:/ were used for the study. The interconnections between the oral and nasal cavities were created according to the anatomical literature. The connecting channels between oral and nasal cavities have got the diameters 3[mm].

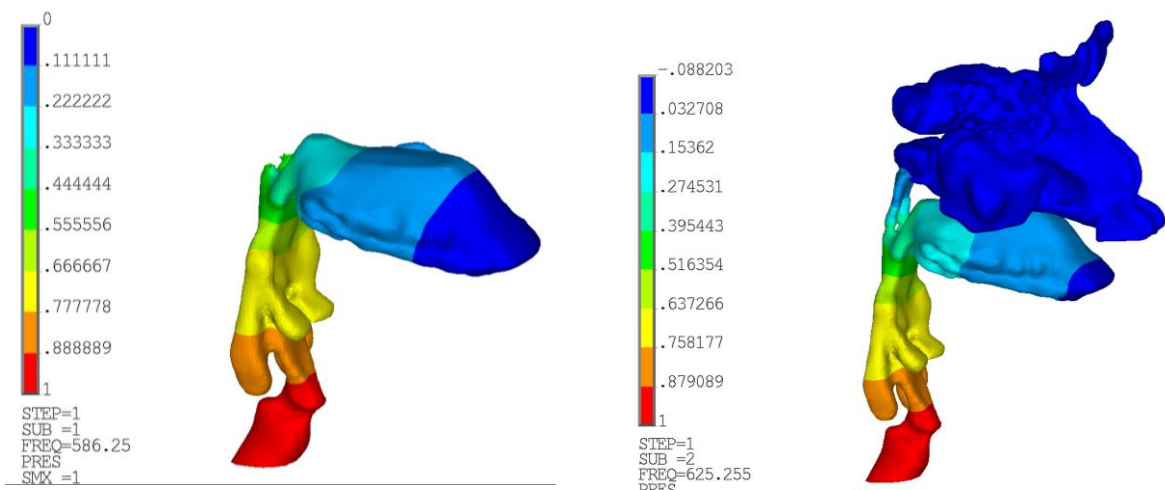


Fig. 1. The first oral mode of the human vocal fold – vowel /a:/ without nasal cavities (left, 586 [Hz]) and with nasal cavities (right, 625 [Hz])

The acoustic frequency - modal characteristics of the FE models were studied by the modal analysis considering air density $\rho_0 = 1.2 \text{ kgm}^{-3}$, sound speed $c_0 = 353 \text{ ms}^{-1}$, coefficient of the boundary admittance $\mu = r/\rho_0 c_0 = 0.0$, where r is the real component of the specific acoustic impedance (see [2]) and the pressure $p = 0 \text{ Pa}$ at the lips and nose.

Table 1. Vowel /a:/ (ON-oral-nasal frequency, O-oral frequency, N-nasal frequency)

	F ₁ [Hz]			F ₂ [Hz]		F ₃ [Hz]	
Without nasal cavities	586			1310		1675	
With nasal cavities	ON 402 1240	O 625	N 1096	O 1326	N 1479	O 1675	N 2016 2488

Table 2. Vowel /i:/

	F ₁ [Hz]			F ₂ [Hz]			F ₃ [Hz]
Without nasal cavities	244			1157			2423
With nasal cavities	ON 306 435	O -	N 1093	ON 1240 2408	O 1164	N 1477	O 2425

Due to the velopharyngeal insufficiency the oro-nasal frequencies f_{nasal} for vowels /a:/ appear below the first formant ($f_{nasal} < F_1$) and between the first and second formants ($F_1 < f_{nasal} < F_2$) of the FE model for a healthy subject. The first pure oral frequency is shifted to second formant.

For the vowel /i:/, two oro-nasal frequencies appear between the first and second formants ($F_1 < f_{nasal} < F_2$) of the normal voice and between the second and third formants ($F_2 < f_{nasal} < F_3$). The first pure oral frequency disappeared.

The results for numerically simulated sound response of the human vocal tract for vowels /i:/ show considerable influence of VPI connecting the acoustic spaces of the vocal and nasal tracts of the FE models on phonation. In contrary, the influence of VPI on the acoustic pressure response for vowel /a:/ is smaller. This is in the qualitative agreement with the clinical acoustic data on velopharyngeal insufficiency. From presented results can be concluded, that for prediction of the voice quality is necessary correctly model the nasal cavities.

Acknowledgements

The research is supported by the Grant Agency of the Czech Republic by project **No 16 01246S** Computational and experimental modelling of self-induced vibrations of vocal folds and influence of their impairments on human voice.

References

- [1] Carney, P.J., Sherman, D., Severity of nasality in three selected speech tasks, *Journal of Speech and Hearing Research* 14 (1971) 396–407.
- [2] Vampola, T., Horáček, J., Vokáříal, J., Cerny, L., FE modeling of human vocal tract acoustics. Part II: Influence of velopharyngeal insufficiency on phonation of vowels, *Acta Acustica united with Acustica* 94 (1) (2008) 448 - 460.
- [3] Vohradník, M., *Communication disorders by velopharyngeal insufficiency*, Dolní Břežany: Scriptorium, Prague, 2001. (in Czech)

Analysis of stress concentration near graphite particles in globular graphite cast iron

M. Vaško^a, M. Handrik^a, P. Kopas^a, M. Sága^a

^a University of Žilina, Faculty of Mechanical Engineering, Department of Applied Mechanics, Univerzitná 1, 010 26 Žilina, Slovak Republic

The paper presents the analysis of stress concentration nearby the graphite particles in cast iron with globular graphite. The quantity and shape of the created graphite particles can be regulated in the production of cast iron with globular graphite. Graphite particle can be considered as random with specific shape and position. The position and shape of graphite particles is randomly generated with predefined properties for the purpose of FEM analyses.

Supporting frames of machines are made from this type of cast iron. Detailed knowledge of the properties and parameters plays an important role in understanding the transmission of forces and vibrations into the concrete basement of construction. A large number of factors (defects, nonmetallic inclusions, notches, etc.) have affect to the characteristics of the materials [5]. The deformation is directly proportional to the stress at the steel under tensile load in the sphere of elastic deformation. The validity of this relationship is not unequivocal in graphite cast iron. It is expected that the modulus of elasticity E is dependent on the stress and it is affected by the presence of graphite. Graphite particles reduce the cross-section of the body (by up to 15 %) and they cause internal notch effect.

In the calculation of stress gradient in the vicinity of graphitic particles is assumed that due to the internal notch effect of graphite grains arise the local stress concentration and multiaxial state of stress [3]. The stress concentration factor

$$\alpha = \frac{\sigma_{max}}{\sigma_n},$$

where σ_{max} is maximum component of the stress, σ_n is nominal stress.

Theoretical calculations of the stress concentration are derived for homogeneous, isotropic and perfectly elastic materials and for single notch with exactly defined shape. In this case the value of the stress concentration factor for the spherical cavity is $\alpha = 3$. But graphite grains in the graphite cast iron have an irregular shape and rugged surface [4]. The value of the stress concentration factor can therefore have a different value. The Finite Element Method (FEM) was used for its calculation [1]. Linear elastic material ($E = 1.69 \cdot 10^5$ MPa) was chosen for the simplification to determine the notch effect of inhomogeneity. In terms of the formulation of FEM the geometrically linear model was chosen for analysis. Sensitivity analysis of the size of model elements had to be done to determine the proper density of the finite element mesh.

The same boundary conditions for the sensitivity analysis and for the stress concentration calculation were chosen. The square area (0.35×0.35 mm) was solved and the double symmetry with unit load in the direction of the y -axis was considered. Size of elements was chosen based on the results of this analysis, its value was determined to 0.0005 mm.

Algorithms in the Octave software were created for the purpose of the model preparation. These algorithms allow generate random models with the following parameters:

- number of inhomogeneities: 200-350 pcs/mm²,

- diameter of inhomogeneity: 0.015-0.08 mm,
- roundness tolerance: 0-0.0075 mm,
- number of nibs: 10-15,
- minimum thickness of the material between inhomogeneities: 0.02 mm.

Twenty areas with inhomogeneities of different sizes and shapes of graphite were generated for the purpose of analysis. Stress analysis was performed on the basis of the proposed algorithm [2].

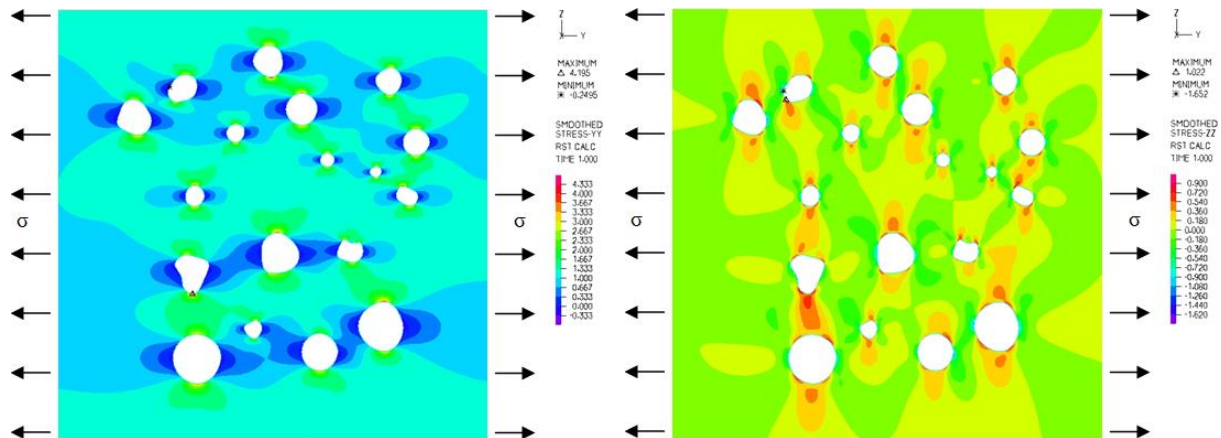


Fig. 1. Stress distribution of σ_{yy} in the y-axis (left) and σ_{zz} in the z-axis (right)

The similarity of experimentally obtained values of stress concentration in the vicinity of graphite particles with an idealized circular shape has been confirmed based on the analysis. The high numbers of graphite particles per unit surface area (mm^2) were included in the analysis on the basis of knowledge of the cast iron structure. This caused a change in the value of stress concentration factor α – from $\alpha = 3.2$ (4 % of graphite) to $\alpha = 3.57$ (12 % of graphite). A greater number of graphite particles in the matrix also relates with the rise of stress fields in the vicinity of neighboring graphite particles.

Different values of stress concentration factor calculated for the equivalent stress (von Mises theory) can be explained by the presence of non-zero components of the stress tensor in the vicinity of graphitic particles. It confirms the assumption of multiaxial stress state in the vicinity of the particles. Performed analyses confirm that the size and the mutual location of inclusions will have a greater effect to the stress concentration as their shape.

Acknowledgements

This work has been supported by grant projects VEGA No. 1/0795/16 and APVV-0736-12.

References

- [1] Bathe, K.J., Finite element procedures, Prentice Hall, 1996.
- [2] Handrik, M., Jakubovičová, L., Kopas, P., Sága, M., Analysis of microplastic areas near graphite particles of nodular cast iron loading below yield stress, *Metallurgy* 49 (2) (2010) 263-267.
- [3] Kopas, P., Vaško, M., Handrik, M., Computational modelling of the microplasticization state in the nodular cast iron, *Applied mechanics and materials* 474 (2014) 285-290.
- [4] Murakami, Y., *Metal fatigue: Effects of small defects and nonmetallic inclusions*, Elsevier, 2002.
- [5] Vaško, A., Microstructure and fracture behaviour of synthetic nodular cast irons, *Materials Engineering* 10 (3) (2003) 179-182.

Calculation of locomotive traction force in transient rolling contact

P. Voltr^a

^aJan Perner Transport Faculty, University of Pardubice, Studentská 95, 532 10 Pardubice, Czech Republic

In numerical simulations of railway vehicle dynamics, wheel–rail contact models are employed to calculate the tangential forces acting between wheels and rails (creep forces). Commonly used creep force algorithms involve the Kalker’s simplified theory (Fastsim) [1] or the Polách’s model [2]. Each model makes use of some simplifications to shorten the computation time.

A common property of all these models is that they assume *steady rolling* which, as opposed to *transient rolling*, means rolling with constant creepage (as well as other parameters which influence the creep force mechanism). This is acceptable in many cases, since the duration of a transient rolling phenomenon is comparable with the time in which the rolling wheel advances by the length of the contact area; for 40 km/h and 15 mm contact length, this is 1.4 ms. For very low vehicle speed, however, the transition is longer and a steady rolling model might result in inaccuracy. In the moment of first motion of the wheel from zero speed, steady rolling is wholly unacceptable. As a consequence, a simulation with a steady rolling model does not allow arbitrarily variable vehicle speed.

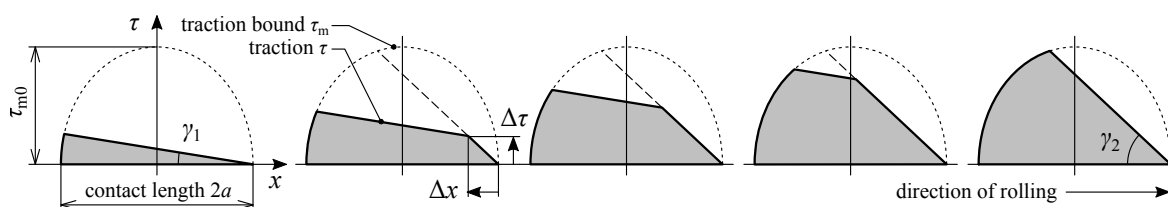


Fig. 1. Evolution of distribution of tangential stress τ in contact area for transient rolling contact – a sketch based on the simplified theory, longitudinal section

To deal with this problem, one might use the algorithm Contact based on the exact theory of Kalker [1]; this would increase the computation time significantly. Also, a simplified model of transient rolling (STR) was proposed and used in locomotive traction simulations [3]. This is basically similar to Fastsim but the program keeps in memory the whole distribution of tangential traction in wheel–rail contact and integrates it without the assumption of steady rolling. The calculation is not slow but requires a lot of programming, and we ask whether this is necessary for simple applications of locomotive traction studies.

As an answer, we propose a simple algorithm of “quasi-transient rolling” that overcomes the inadequacy of steady rolling approach in very low vehicle speed. The design of the method is based on observation of creep force after a step change of creepage in transient rolling: its evolution resembles the behaviour of an exponential smoothing filter which can be expressed as

$$x_f^{(i)} = F \cdot x^{(i)} + (1 - F) \cdot x_f^{(i-1)},$$

where x is any quantity, x_f the same after filtering, i is the time step index. This formula also is not altogether deficient in physical meaning for the transient rolling, because the creep force is a result of tangential stress in the contact area, and there is a part of it (F) that developed during the current calculation step, and the rest ($1 - F$) that is connected with the particles which were present in the contact before. This is illustrated in Fig. 1 where the original steady rolling traction distribution is described by the angle γ_1 , proportional to creepage s_1 . During the transition, this distribution is replaced by a new one with the angle γ_2 for higher creepage.

Having accepted this approach, one has to decide about two points: firstly, which of the quantities describing the creep force mechanism will be subjected to the filtering; secondly, what will be the formulation of the factor F .

After testing several algorithms and comparing their outputs with STR, we conclude that the filtered quantity should be the creep force T or coefficient of adhesion (COA) μ . The smoothing factor F depends on the distance Δx by which the contact advances during the calculation step: with Δx small, F is also small because only a small part of the contact area is filled with new traction distribution. F must, however, depend also on the traction increase $\Delta\tau$.

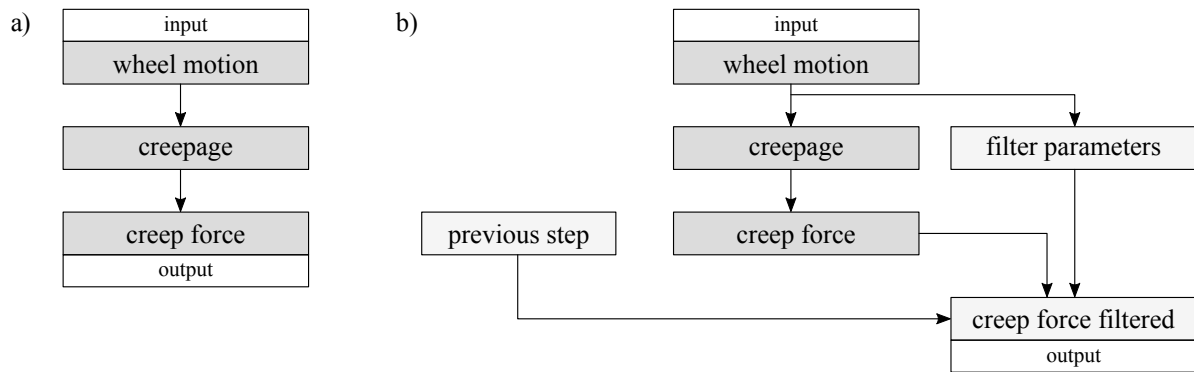


Fig. 2. Creep force calculation: a) steady rolling, e.g. with the model of Polách, b) modification with the proposed method for “quasi-transient rolling”

As a result, we obtain a method of calculation of the creep force in transient wheel–rail contact, the principle of which is given in Fig. 2. The method is approximative in nature and is not intended for the study of transient rolling phenomena. It is, however, fast and readily available to include in simulation code. Testing in simulation of a quite extreme case of locomotive traction (interrupted sliding, change of rolling direction) shows absence of undesirable numerical effects and little difference from the more complex calculation algorithm STR.

Acknowledgements

The research was supported by *Competence Center of Rail Vehicles*, project No. TE01020038, Technology Agency of the Czech Republic.

References

- [1] Kalker, J. J., Three-dimensional elastic bodies in rolling contact, Kluwer Academic Publishers, Dordrecht, 1990.
- [2] Polách, O., Creep forces in simulations of traction vehicles running on adhesion limit, *Wear* 258 (2005) 992-1000.
- [3] Voltr, P., Lata, M., Dynamical behaviour of a locomotive drive system at the adhesion limit – experiment and simulation, *Proceedings of the 22nd International Symposium on Dynamics of Vehicles on Roads and Tracks*, Manchester Metropolitan University, 2011.

Modeling of drive of cable driven mechanism

J. Zavřel ^a, Z. Šika ^a, J. Volech ^a, J. Dupal ^b

^a Faculty of Mechanical Engineering, CTU in Prague, Technická 4, 166 07 Praha, Czech Republic

^b Faculty of Applied Sciences, University of West Bohemia, Univerzitní 8, 306 14 Plzeň, Czech Republic

Drive is an integral part of the mechanism. It is needed to control and achieve the desired motion. Today, drives are controlled by control units with inverters. The most used drive type is the AC synchronous servo motor (drive) with a very high power density. The whole drive system also consists of the drive and the appropriate control unit. Maximum performance requires the drive and control unit to be adapted to each other.

In the first step it is important to tune servo parameters like moment of inertia, resistance and induction of the drive, maximum current and other parameters.

The drive controll unit includes mainly controll loop which can be set by many parameters. It is basically divided into three parts. The first part is the position controller, second is the velocity controller and the last one is the current controller. These parts of the controller can be in many parameters tuned.

Each part of the controller may be switched into two states - the desired value (setpoint) and the ramp (ramp enable signal). The basic scheme of the controller structure is shown in Fig. 1.

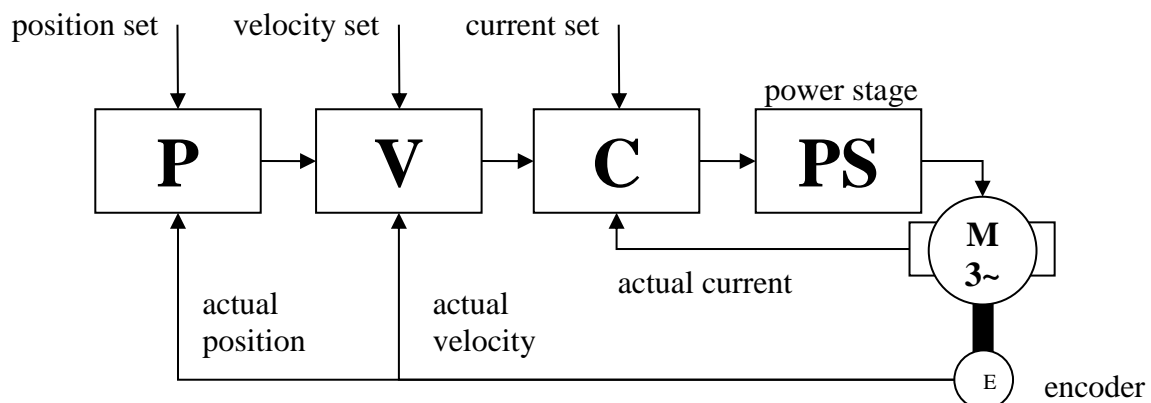


Fig. 1. Overview of the controller structure

In the project are used Schneider drives and control units also. In the product manual there is the control scheme described (Fig. 1). The block “P” denotes position controller, “V” velocity controller and “C” current controller. Position controller use the proportional regulator with the velocity feed-forward control. It is possible to switch the incoming position signal to the set-point or ramp type. The same property has the also the velocity and current controller. The velocity controller scheme is more complex. This velocity controller is PI type with acceleration feed-forward control. Before the evaluation of the regulation deviation there are placed filters. The first one is the overshoot suppression filter (posicast) and then the

velocity value filter (low-pass filter of the first order). These filters play important role in the control process. It affects significantly the controller behaviour. These filters can be set by parameters which are specified in the manufacturer manual. Nevertheless the description is usually very short and detailed description. Especially the mathematical description and terms are mostly missing. Every manufacturer has generally the different setting parameters. The last part of the controller structure is the current controller. It is the integration type controller. It includes the notch filter and the low-pass filter. In the current controller can be set filter parameters only. The main current controller cannot be set directly, it is locked. In the simulation scheme the current controller is usually modelled by the model of the drive including the current backward loop [1].

The outcome signal from the controller is input to the power stage unit. Its phase delay given by the PWM should be basically modelled by the Padde approximation [2]. It can be described by the G_P transfer function (1):

$$G_P = \frac{\frac{T_0^2}{12}s^2 - \frac{T_0}{2}s + 1}{\frac{T_0^2}{12}s^2 + \frac{T_0}{2}s + 1}. \quad (1)$$

The model must be verified by the experiment and then all parameters tuned in a good agreement with the real system. It is very significant in conjunction with cable driven mechanisms. Cables play big role in dynamic behaviour. It is fundamental to catch and filter frequencies which significantly can affect control process.

Modelling of the drive control unit is usually inaccurate because it is often difficult to become the exact description of the control scheme based on the manufacturer's manuals. A simulation model of the drive and control unit was built. The drive Schneider BMH0703P01F2A and a control unit LXM32MD18M2 are used. It is used for simulation model of the cable driven mechanism.

Acknowledgements

The work has been supported by the Czech Science Foundation project GA15-20134S - Multi-Level Light Mechanisms with Active Structures.

References

- [1] Souček, P., Servomechanismy ve výrobních strojích, ČVUT, Praha, 2004. (in Czech)
- [2] Veselý, J., Komplexní modelování dynamiky a řízení NC strojů, Ph.D. Thesis, ČVUT, 2009. (in Czech)

The influence of the slenderness ratio of the composite beam on its bending stiffness

T. Zavřelová^a, T. Mareš^a

^a Czech Technical University in Prague, Faculty of Mechanical Engineering, Department of Mechanics, Biomechanics and Mechatronics, Technická 4, 166 07 Praha 6, Czech Republic

The work is aimed to facilitate the design of composite beams. The usage of composite materials in all kinds of structures is common nowadays. A reliable method for determination the deformation of parts made of the composite material is required. We compare the known methods of bending analysis of composite beams for the different composition of the composite material. This paper presents the influence of the slenderness ratio of the composite tube to its bending stiffness. We used the three different models of FEM analysis to identify the aforementioned dependence and to show the differences between the models.

The results of the deflection of a fixed beam loaded by an isolated force and by an isolated moment, respectively, are presented. The deflection is calculated by the FEM method. The conventional shell, continuum shell and the volume model are used. The geometry of the beam is chosen to meet the expectations of all above mentioned methods of calculation so the results can be easily compared.

The FEM calculations are realised in Abaqus and for the analytical calculations the MATLAB is used. The geometry is the same for all models. The clamped beam is loaded by a single force F or by the momentum M (Fig. 1.).

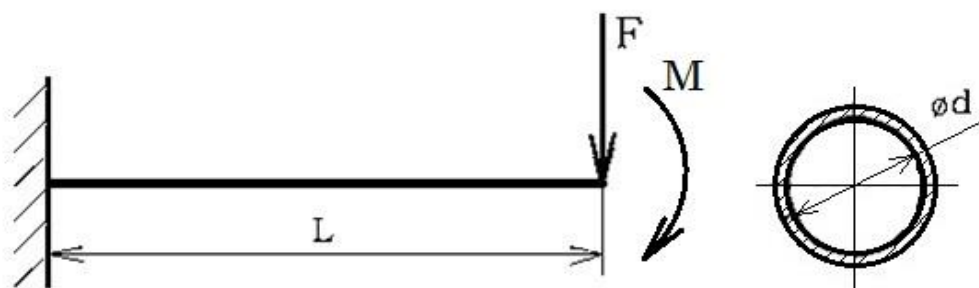


Fig. 1. The geometry of the models and its loads

The composite layup is composed from three layers $[90^\circ, 0^\circ, 0^\circ]t=1\text{mm}$. The diameter $\varnothing d$ and the length L are variables. The material constants and the loads are entered as parameters of the models that do not change.

The thickness of the beam is specified as a parameter of the model by usage both shells. The common elements S4R are used for calculations using conventional shell and SC8R are used for continuum shell. The continuum shell is modelled as a solid body. The real thickness of the beam is specified as the parameter of the model and by the composite layup. The elements of the model are distributed through the whole thickness of the solid body. The advantage of the continuum shell elements is that they can be stacked. According [1] they

yield the exact elastic solution. For calculations using shells, the ratio between shortest surface dimension and the thickness of the material larger than ten is assumed.

For the calculation using the volume model, the full 3-D geometry is specified. Each ply is created separately as a separate solid section with his own anisotropic material specification. The element type C3D8R (three-dimensional hexahedral element) has been used for meshing the tube.

The calculations of the equivalent modules are based on the Bernoulli's theory. The deflection of the beams is obtained from the FEM analysis. Than the equations (1) and (2) are used to obtain the equivalent tensile modules $E_{eq}(\mathbf{F})$ and $E_{eq}(\mathbf{M})$ from the loading by the force F or by the momentum M (Fig. 1).

$$E_{eq}(\mathbf{F}) = \frac{F \cdot L^3}{3 \cdot v \cdot J}, \quad (1)$$

$$E_{eq}(\mathbf{M}) = \frac{M \cdot L^2}{2 \cdot v \cdot J}, \quad (2)$$

where v is the deflection of the beam, J is the moment of inertia and L is the length of the beam. These equations vary in the consideration of the shear. The effect of the shear is evident in the data obtained from the equation (1). The results from the equation (2) are used to obtain the equivalent shear modulus for the whole tube. The shear modulus G is recovered from the formula for calculation of the deflection considering the shear.

$$v = \frac{F \cdot L^3}{3 \cdot E_{eq}(\mathbf{M}) \cdot J} + \beta \frac{F \cdot L}{G \cdot A}. \quad (3)$$

The equivalent tensile and shear modulus of the composite tube are obtained. The examined methods of the calculation of the equivalent tensile modulus show the great influence of the shear in calculation of the deformation of the composite beam.

Furthermore, the data obtained from the continuum shell model and the volume model are close together. We note that the calculation using conventional shell is very sensitive to fulfilling the general conditions for usage of the shells.

Acknowledgment

This work has been supported by project No. SGS15/188/OHK2/3T/12 of the Grant Agency of the Czech Technical University in Prague.

References

- [1] Barbero, E.J., Finite element analysis of composite materials using Abaqus, CRC Press/Taylor & Francis Group, Boca Raton, 2013.

Eigenfrequency analysis of nuclear reactor with clearances in couplings

V. Zeman^a, Z. Hlaváč^a

^aFaculty of Applied Sciences, University of West Bohemia, Univerzitní 8, 306 14 Plzeň, Czech Republic

The original linear discrete model of the WWER 1000 type reactor was derived in co-operation with Nuclear Research Institute Řež and Škoda Nuclear Machinery during the year 2006 [2]. The tongue and groove couplings between the lower part of core barrel and reactor pressure vessel show small assembling side clearances. These clearances are exceeded during the reactor operational period as a result of fretting wear and oxidative process on the contact surfaces.

For a simplification, we neglect the influence of friction in contact surfaces and all damping type. One typical dynamic feature of conservative nonlinear systems is the eigenfrequency-amplitude relationship of the free vibration. In the absence of an exact analytical periodic solution to a vibration of the large reactor model with eight symmetrical nonlinear couplings with clearances, we wish to find at least an approximative solution. Supposing, in the first approximation, harmonic vibration with frequency Ω_ν of the nonlinear mathematical model of reactor. The relative tangential displacements of grooves on lower part of core barrel from central position compared to tongues on pressure vessel can be expressed as

$$u_{i,\nu} = a_{i,\nu} \cos \Omega_\nu t, \quad i = 1, \dots, 8, \quad \nu = 1, \dots, n, \quad (1)$$

where $a_{i,\nu} = \mathbf{d}_i^T \mathbf{v}_\nu$ is the displacement amplitude in coupling i corresponding to eigenvector \mathbf{v}_ν of dimension n (DOF number). Vector \mathbf{d}_i of the same dimension is determined by geometric parameters of the reactor and a position of the concrete coupling.

To linearize the symmetrical nonlinear couplings with clearances included in reactor stiffness matrix, the harmonic balance method is used. Based on this, the term for determination of equivalent stiffness of coupling i with half clearance Δ_i and amplitude $a_{i,\nu}$ according to (1) for nonlinear normal mode corresponding to eigenfrequency Ω_ν can be derived [3] for $|a_{i,\nu}| \geq \Delta_i$ as

$$k_i = \frac{2k}{\pi} \left(\arccos \frac{\Delta_i}{|a_{i,\nu}|} - \frac{\Delta_i}{|a_{i,\nu}|} \sqrt{1 - \frac{\Delta_i^2}{a_{i,\nu}^2}} \right), \quad i = 1, \dots, 8, \quad (2)$$

where k is coupling stiffnesses for $|a_{i,\nu}| \geq \Delta_i$. For $|a_{i,\nu}| < \Delta_i$ is $k_i = 0$. The corresponding reactor equivalent stiffness matrix is

$$\mathbf{K}_e = \mathbf{K} - \mathbf{K}_C(0) + \sum_i k_i \mathbf{K}_i, \quad (3)$$

where \mathbf{K} is reactor stiffness matrix for all clearance-free ($\Delta_i = 0, i = 1, \dots, 8$) couplings, $\mathbf{K}_C(0)$ is stiffness matrix of all clearance-free couplings and \mathbf{K}_i is stiffness matrix of single coupling i with unit stiffness.

Localization of the one nonlinear normal mode [1], corresponding to chosen eigenfrequency Ω_ν and amplitude starting value of the most deformed coupling, can be provided using linear normal mode as the first estimate to start to iterative computation. The eigenfrequency Ω_ν of

the reactor nonlinear model can be investigated depending on relative amplitude $p = \frac{a_{j,\nu}}{\Delta_j}$ of the most deformed coupling j . Amplitudes $a_{i,\nu}$ of others nonlinear couplings are calculated as

$$a_{i,\nu} = \frac{p\Delta_j}{\bar{a}_{j,\nu}} \bar{a}_{i,\nu}, \quad i = 1, \dots, j, \dots, 8, \quad (4)$$

where $\bar{a}_{i,\nu} = \mathbf{d}_i^T \bar{\mathbf{v}}_\nu$ are amplitudes of relative displacements in couplings on reactor free vibration by the ν -th normal mode. The eigenfrequency $\Omega_\nu^{(r)}$ and the eigenvector $\bar{\mathbf{v}}_\nu^{(r)}$ of the linearized reactor model in r -th iteration is calculated from the eigenvalue problem

$$[\mathbf{K} - \mathbf{K}_C(0) + \sum_i k_i^{(r)} \mathbf{K}_i - \Omega_\nu^{(r)2} \mathbf{M}] \bar{\mathbf{v}}_\nu^{(r)} = \mathbf{0}, \quad r = 0, 1, \dots \quad (5)$$

The eigenvector meet the norme $(\bar{\mathbf{v}}_\nu^{(r)})^T \mathbf{M} \bar{\mathbf{v}}_\nu^{(r)} = 1$, where \mathbf{M} is the reactor mass matrix. The calculation procedure can be summarized as follows:

1. Selection of the calculated eigenfrequency Ω_ν and relative amplitude $p_0 \gg 1$ of the most deformed coupling corresponding to state that's near to the reactor with clearance-free couplings.
2. Creation of the linear clearance-free mathematical model of reactor and calculation of eigenfrequency $\Omega_\nu^{(0)}$ and amplitudes $\bar{a}_{i,\nu}^{(0)} = \mathbf{d}_i^T \bar{\mathbf{v}}_\nu^{(0)}$, $i = 1, \dots, 8$ according to (5) for $k_i^{(0)} = k$ at the start (for $r = 0$) of iterative process.
3. Identification of the most deformed coupling j with respect to clearance Δ_j , calculation of ratios $\frac{\Delta_i}{|\bar{a}_{i,\nu}^{(0)}|} = \frac{1}{p_0} \frac{\Delta_i}{\Delta_j} \left| \frac{\bar{a}_{j,\nu}^{(0)}}{\bar{a}_{i,\nu}^{(0)}} \right|$ and equivalent stiffnesses $k_i^{(1)}$ according to (2) in the first iteration.
4. Calculation of eigenfrequency $\Omega_\nu^{(1)}$ and eigenvector $\bar{\mathbf{v}}_\nu^{(1)}$ according to (5) for $k_i^{(1)}$ and continuing in iteration process until satisfaction of condition $\frac{\Omega_\nu^{(r+1)} - \Omega_\nu^{(r)}}{\Omega_\nu^{(r)}} \leq \varepsilon$, where ε is a small dimensionless parameter.

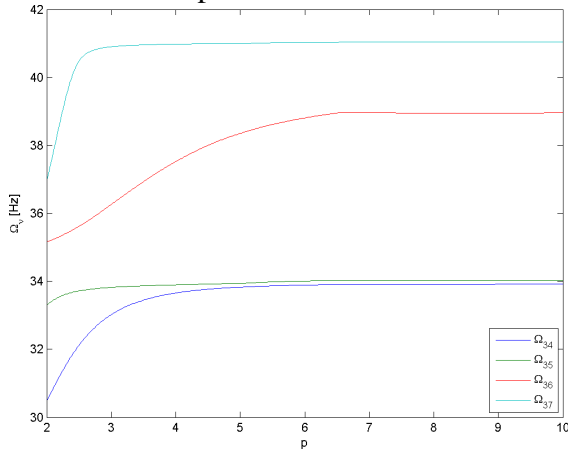


Fig.1. Eigenfrequencies Ω_ν -parameter p plot of the reactor

5. Repetition of iterative process for value $p = p_0 - \Delta p$, whereas the start of every new iteration cycle at interval $p_0 > p > p_{\min}$ appear from the linearized reactor mathematical model with clearances in the end of previous cycle.

The presented method is applied to calculation of the some eigenfrequency-relative amplitude plot of the most deformed tongue and groove coupling providing that all side clearances in couplings $i = 1, \dots, 8$ are same $\Delta_i = \Delta$. For illustration, the plots of the most sensitive reactor eigenfrequencies are presented in Fig.1. The iterative calculation of dependences $\Omega_\nu(p)$ fast tends for $p \in \langle 2, 10 \rangle$ into relative error $\varepsilon = 0.001$.

Acknowledgements

This work was supported by the project LO1506 of the Ministry of Education, Youth and Sports of the Czech Republic.

References

- [1] Byrtus, M., Zeman, V., Z., Alternative methods for vibration analysis of friction blade coupling, Colloquium Dynamic of Machines 2012, Prague, 2012, pp. 23-28.
- [2] Hlaváč, Z., Zeman, V., Vibration of nuclear fuel assemblies, LAP Lambert Academic Publishing, Saarbrücken, 2013.
- [3] Juliš, K., Brepta, R. et al., Mechanics II. – Dynamics, SNTL Praha, 1987. (in Czech)

Dimensioning of the take-up bar on a weaving loom using Winkler's model of soil

J. Žák^a

^aVÚTS Liberec, a. s., Svárovská 619, 460 01 Liberec, Czech Republic

While considered as very solid in comparison with the stiffness of yarns the weaving loom mechanical parts are often subject to so high loads that their deformation may either be comparable to the required precision of the final product either make the production of a product almost impossible. For example high deflection of take-up rollers may cause deformation of a highly setted fabric in its plane due to slipping between the rollers. Care must be taken in order to avoid such situations, nevertheless these parts usually can be dimensioned without any special restriction.

We were in a completely different situation when dimensioning the take-up bar on a special 3D fabric weaving loom. Restricted space limited the overall dimensions of the bar which in turn resulted in a very low stiffness of the latter. This take-up bar is subject to high loads from binding yarns during the loop turn formation while being pulled by a mechanism into a wedge-shaped space between the two plain weave faces [1]. On the other hand the horizontal dimension of the bar determines the minimal length of binding yarns that represents a quality parameter of this fabrics, see Fig. 1.

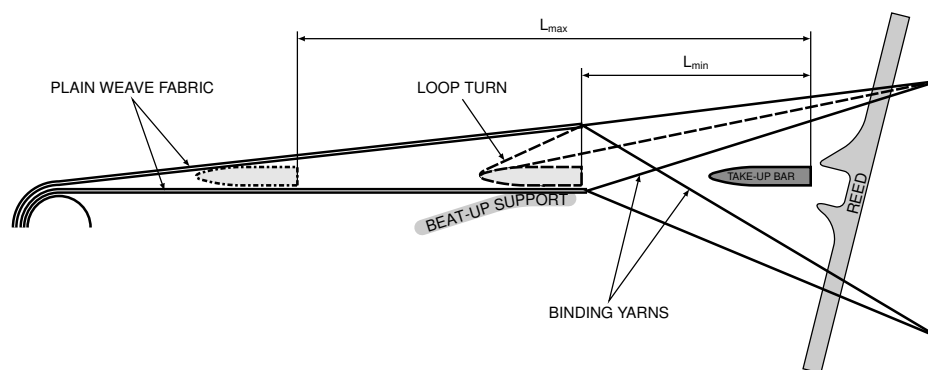


Fig. 1. Schema of take-up bar function

At first glance the classical model of thin beam loaded by distributed linear force was used to determine maximal deflection and stresses in the bar. It soon turned out that a form of interaction of the bar with the pulled binding yarns must be taken into account. It was due to the comparatively equal bending stiffness of the bar and the elongation stiffness of the yarns. Due

to the linearity of the problem, either in material properties either in geometry, the following differential equation could be used:

$$y(x) \cdot K + \left(\frac{d^4}{dx^4} y(x) \right) \cdot EJ = C_7 + C_8 \cdot x.$$

We were supposing linear, yet unknown, distribution of binding yarn pre-tension along the bar. Then a solution in the form:

$$y(x) = y_h(x) + y_p(x),$$

$$y_h(x) = e^{\beta \cdot x} \cdot (C_1 \cdot \sin(\beta \cdot x) + C_2 \cdot \cos(\beta \cdot x)) + e^{-\beta \cdot x} \cdot (C_3 \cdot \sin(\beta \cdot x) + C_4 \cdot \cos(\beta \cdot x)),$$

$$y_p(x) = C_5 + C_6 \cdot x,$$

where $\beta = \sqrt[4]{\frac{K}{4EJ}}$ can be used. By solving a system of linear equations built over appropriate boundary conditions, we obtain a set of eight C_i . The difference between the solutions using the two mentioned approaches is shown on Fig. 2.

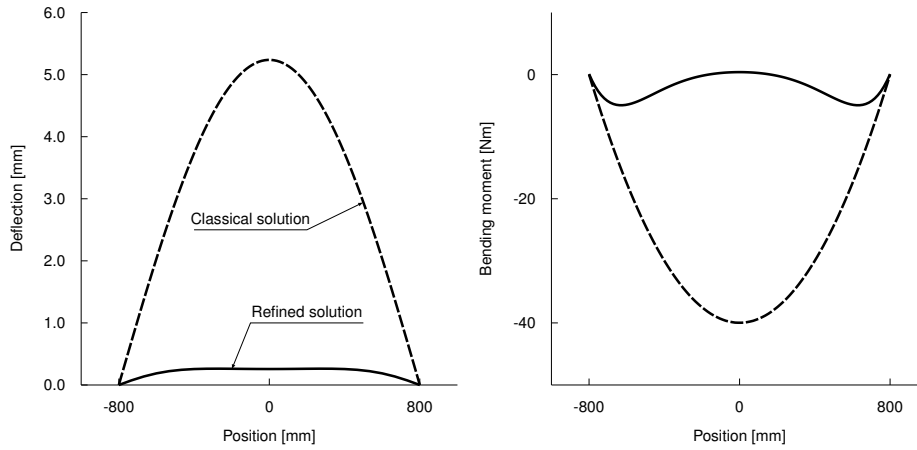


Fig. 2. Comparison of the two approaches

By using the model of elastic soil to represent the take-up bar loading we obtained results which differed sensibly from the simple model using a constant loading. These results also corresponded much better to our experience with a functional model of the bar.

As a side result we demonstrated utility of an analytical method even nowadays, in age of *modern* methods such as FEM.

References

- [1] Teng, Y.-S. et al., Weaving machines and three-dimensional woven fabrics, Patent No. US 2011/0132488 A1 and US 8 015 999 B2, 09/13/2011.